TURBULENT SHEAR FLOW RECOVERY
BEHIND OBSTACLES ON SMOOTH AND ROUGH SURFACES

by

ABDELMONEIM MOHAMED ZEIDAN

Thesis submitted in accordance with the requirements of the University of Liverpool for the degree of Doctor in Philosophy

Department of Mechanical Engineering

August 1980

TO MY WIFE NADIA,

MY DAUGHTER AND MY SON

STATEMENT OF ORIGINALTY

The work described in this thesis was carried out, except where otherwise indicated, by the author in the Fluid Mechanics division of the Department of Mechanical Engineering at the University of Liverpool between October 1976 and August 1980. No part of this thesis has been submitted for a degree in any other university or place of learning.

A M Zeidan

September 1980

ACKNOWLEDGEMENTS

The author wishes to express his sincere thanks to Dr A K Lewkowicz for supervising this project. His excellent guidance, continuous help and constant encouragement have been invaluable at every stage of this resarch.

The author is indebted to the University of Liverpool's Mechanical Engineering Department for sponsoring this project, and for the financial grant that made this study possible.

Thanks are due to Mr D Smith for his technical assistance and Sandra Bargh for the excellent typing of this thesis.

Finally, I am especially grateful to my wife, Nadia, for being so very patient during the last four years.

A M Zeidan

TURBULENT SHEAR FLOW RECOVERY BEHIND OBSTACLES ON ROUGH AND SMOOTH SURFACES

SUMMARY

A turbulent shear flow recovery behind a two-dimensional obstacle was investigated. The main experiment was performed for a turbulent boundary-layer flow, with zero external pressure gradient in a low speed wind tunnel. The main objective of this work was to study:

(i) the boundary-layer recovery downstream of a two-dimensional obstacle;

(ii) the effect of the surface roughness on the mean flow and turbulence properties downstream of the obstacle;

(iii) the effect of the geometry of the obstacle on the recirculating flow region near to the obstacle and on the recovery of the flow downstream of the obstacle.

To study the flow recovery downstream of the obstacle, careful and detailed measurements of both mean velocity and turbulence properties were carried out at many stations in the recovery region. The study of the effect of surface roughness was carried out by placing the two-dimensional obstacle on different plane walls with different surface roughnesses. Therefore, the entire experimental programme was carried out twice: (i) for a smooth plate and (ii) for an irregularly rough surface (the roughness was uniformly distributed over the plate). The study of the effect of the obstacle geometry was carried out using two different geometries for the obstacle - one being a rectangular cross-section bar (ridge) and the other a single hump (hill). The obstacles were roughly half the boundary-layer thickness.

The whole experiment was repeated in a fully developed turbulent flow in smooth and rough pipes. The rough pipe was lined internally with the same non-uniform (irregular) surface roughness. The dynamical similarity between the wall regions of both the pipe and the boundary-layer flow was

arranged. The two-dimensional obstacles in the pipe flow were of the form of suitably scaled internal (rectangular in cross-section) rings. No simple-hump ring profile was used.

The measurements were carried out, in both the boundary-layer and pipe flows, for: (i) mean velocity distribution, turbulent normal and shear stresses downstream of the obstacle; (ii) static pressure distribution around the obstacles and in the separated regions; (iii) turbulence spectra and statistical properties (flatness and skewness factors) of the longitudinal turbulent component across the shear layers and at several stations downstream of the obstacle.

From the above measurements, the following quantities were evaluated: (i) wall friction and roughness function; (ii) typical boundary-layer properties - absolute, displacement, momentum thickness, shape parameters, mixing length and eddy viscosity; (iii) turbulence correlation coefficient (by Fourier transforms); (iv) micro- and macro-scale of turbulence; (v) drag on the obstacle.

It was found that both the surface roughness and the geometry of the obstacle affect the flow recovery downstream of the obstacle. Also it was found that the turbulent quantities $\sqrt{\frac{\overline{u^2}}{u_o}}$, $\sqrt{\frac{\overline{v^2}}{u_o}}$ and the shear stress $\frac{\overline{uv}}{u_o^2}$ need more distance downstream of the obstacle to recovery than the mean velocity. In the boundary-layer flow, the boundary-layer thickness was increased by about 30% for the rough plate and by about 50% for the smooth plate due to the presence of the obstacle. This increase in boundary-layer thickness affects the value of the displacement and the momentum thickness δ^* and θ as well as the shape parameter H. It was found that the shape parameter was reduced by about 10% below the value of H for the rough and smooth plate without the obstacle. In the pipe flow the recovery of the flow downstream of the obstacle occurred at about half the distance needed for the flow recovery in the boundary-layer flow.

A theoretical investigation was carried out to predict the flow around and downstream of the rectangular cross-section bar (ridge). The main flow was divided into two regions: (i) the recirculating flow region which extends from 5 obstacle height upstream to 15 obstacle height downstream of the obstacle and (ii) the boundary-layer region which prevails in front of the obstacle and beyond the recirculating flow region. The stream function ψ and the vorticity ω were the dependent variables in the present investigation. The two equations $k - \varepsilon$ turbulence model was applied in order to specify the turbulent viscosity μ_t. A finite difference technique (Gosman et al (1969)) were used to solve the governing, partial differential equations. A fair agreement was found between the predicted mean velocity and kinetic energy and the experimental measurements for the smooth plate as opposed to the rough plate.

CONTENTS Page No.

NOMENCLATURE

Symbol	Meaning	Equation of First Mention
A	Constant	(3.3)
$A_1(b/h)$	Function of b/h	(2.2)
A_E, A_W, A_N, A_S	Coefficients in convection terms of the finite-difference equation	(6.16b)
a_ϕ	A coefficient in the modified general elliptic equation	(6.14)
$B_1(b/h)$	Function of b/h	(2.2)
B_E, B_W, B_N, B_S	Coefficients in the diffusion terms of the finite-difference equation	(6.16b)
b	Width of the obstacle	
b_ϕ	A coefficient in the modified general elliptic equation	(6.14)
C_E, C_W, C_N, C_S	Coefficient in the general substitution formula	(6.16a)
C_1, C_2	Constants in the dissipation rate equation	(6.13)
C_D	Drag Coefficient	(2.1)
C_{Dc}	Corrected drag coefficient	(2.1)
C_p	Static pressure coefficient	(3.16b)
c_ϕ	A coefficient in the modified general elliptic equation	(6.14)
C_D	Constant	(6.3)
C_μ	A function in the equation for effective viscosity	(6.7)
C_f	Friction Coefficient	(3.4)
D_1	The height of the wind tunnel working section	(2.1)
D	The source term in the general substitution formula	(6.16a)

NOMENCLATURE (cont/d)

Symbol	Meaning	Equation of First Mention
E	Constant depends on the surface roughness	(B.1)
F_f	Flatness Factor	(3.15b)
$F(n)$	Frequency spectrum function	(3.12)
f	Pipe friction factor	(3.7)
G	Clauser parameter	
G_k	The generation term in the kinetic energy equation	(6.13)
H	Shape Parameter (δ^*/θ)	
h	The height of the obstacle	(2.1)
h_s	Equivalent sand-grain roughness height	(3.5)
K	Wave number ($= \frac{2\pi n}{U}$)	
k	The kinetic energy of the fluctuating (turbulent) motion of the fluid (turbulence energy)	(6.7)
L	Length of pipe over which pressure drop is measured	(3.8a)
L_T	Macro-scale of turbulence	(3.14a)
ℓ	Turbulence length scale	(6.7)
ℓ_m	Mixing length	(3.10b)
N	Number of iterations	
n	Frequency	(3.12)
$P(u)$	Probability density distribution	(3.15a)
P	Static Pressure	(3.16a)
P_∞	Free stream static pressure	(3.16b)

NOMENCLATURE (cont/d)

Symbol	Meaning	Equation of First Mention
p'	Fluctuating Pressure	(6.11)
Δp	Pipe pressure drop = $p_1 - p_2$	(3.8a)
R	Pipe radius	(3.2)
R_e	Reynolds number	
$\bar{R}_e$	Reynolds number based on the pipe average velocity $(\frac{V_p . R}{\nu})$	
R_T	Longitudinal spatial correlation coefficient	(3.13a)
S_f	Skewness Factor	(3.15a)
S_w	Source term in the vorticity equation	(6.5)
S_ϕ	Source term in the finite-difference equation	(6.14)
t	Time	
U	Mean velocity in x-direction	(2.4)
U_∞	Free-stream velocity	(2.3)
U_{CL}	Pipe centreline velocity	
u	Component of instantaneous fluctuating velocity in x-direction	(6.11)
u_o	Wall friction velocity $= \sqrt{\frac{\tau_o}{\rho}}$	(2.2)
$\overline{uv}$	Reynolds shear stress	(6.10a)
$\frac{\Delta u}{u_o}$	Roughness Function	(3.3)
$\overline{u^2}$	Mean square value of instantaneous fluctuating velocity in x-direction	(3.15a)
V	Mean velocity in y-direction	(6.1)
V_p	Pipe average velocity	(3.8b)
v	Component of instantaneous fluctuating velocity in y-direction	(6.11)

NOMENCLATURE (cont/d)

Symbol	Meaning	Equation of First Mention
$\overline{v^2}$	Mean square value of instantaneous fluctuating velocity in y-direction	
w	Component of instantaneous fluctuating velocity in z-direction	
w_o	value of $\frac{u_o}{U_\infty}$	(3.4)
$\overline{w^2}$	Mean square of instantaneous fluctuating velocity in z-direction	
X	Cartesian co-ordinate for roughness analysis	
x	Cartesian co-ordinate in longitudinal direction	(3.1)
Δx	Separation distance for R_T	(3.13b)
x_r	Distance from the obstacle to reattachment	
Y	Cartesian co-ordinate for roughness analysis	(A.1)
y	Cartesian co-ordinate in perpendicular to wall	(3.1)
y_o	Roughness length	(2.4)
y^*	Dimensionless wall distance = $\frac{y\, u_o}{\nu}$	(B.3)
α	Eddy viscosity parameter in outer region	(3.11b)
δ	Boundary-layer thickness	(2.3)
δ^*	Displacement thickness	(3.11b)
ε	Turbulent energy dissipation	(6.8)
ε_o	Error in origin of mean velocity distribution	
θ	Momentum thickness	
κ	Von Karman constant	(2.4)
λ	Micro-scale of turbulence	(3.14b)

NOMENCLATURE (cont/d)

Symbol	Meaning	Equation of First Mention
μ	Molecular Viscosity	(6.6b)
μ_{eff}	Effective Viscosity = $\mu + \mu_t$	(6.5)
μ_t	Turbulent Viscosity	(6.6b)
ν	Molecular kinematic viscosity	(3.3)
ν_t	Eddy kinematic viscosity	(3.10a)
ν_{t_i}	Eddy kinematic viscosity in the inner layer	(3.11a)
ν_{t_o}	Eddy kinematic viscosity in the outer layer	(3.11b)
ρ	Fluid Density	(3.8b)
σ_k	Effective Schmidt number for turbulence energy	(6.12a)
σ_ε	Effective Schmidt number for turbulence energy dissipation	(6.13)
τ	Shear Stress	(3.2)
τ_o	Wall Shear Stress	(3.2)
ϕ	Dependent variable of general elliptic equation	(6.14)
χ	Roughness Function	(3.5)
ψ	Stream Function	(6.2)
ω	Vorticity of the fluid	(6.1)
Γ_k	Effective exchange coefficient for turbulence energy	(6.12a)
Γ_ε	Effective exchange coefficient for turbulence energy dissipation	(6.13)
Π	Wake-strength parameter	(3.3)

CHAPTER I

INTRODUCTION

CHAPTER 1

INTRODUCTION

1.1 GENERAL

The behaviour of a turbulent boundary layer perturbed from its equilibrium state has been the subject of several investigations in recent years. For the purpose of experimentation there are two methods of introducing the perturbation into the equilibrium turbulent boundary layer. One by means of a sudden change of pressure gradient or of wall roughness, and the other by means of the introduction of an obstacle into the flow or by the application of injection or suction over a short distance of the wall. In the first method, the boundary layer will change from one equilibrium state to another. In the second method the boundary layer gradually returns to equilibrium as the perturbation declines to a negligible level. Thus the processes that can be usefully studied by the two methods are the response of the boundary layer to a stepwise perturbation, as in the second method. Perturbations are applied to the wall as changes in surface conditions and to the free stream as step change in pressure gradient. Perturbations at the wall; previous researchers have been concerned with the response of a turbulent boundary layer to a step change in surface roughness (e.g., Townsend (1965),(1966); Bradshaw, Ferriss and Atweel (1967); Antonia and Luxton (1971)).

An important type of flow, and an obvious target for extension of the study, is the type of strongly perturbed shear layer (perturbations strong enough to invalidate the boundary-layer approximations. The most common perturbations of this sort are those involving separation and reattachment, which occur when an obstacle is placed on a wall along which a turbulent boundary layer has developed. There have been many investigations of this

type of flow: Tillman 1945, Mueller and Robertson 1963, Good and Joubert 1968, and later by Mikio et al 1975, for an individual roughness element attached to a smooth surface. Most of these investigations have been concerned with the correlation between the pressure and the drag force acting on the obstacle and the local characteristics of the smooth-wall turbulent boundary layer in which the obstacles were immersed, but a few experiments on boundary layer recovery, after reattachment, all are somewhat incomplete.

1.2 REASONS FOR THE PRESENT INVESTIGATION

The flow about obstacles attached to a plane wall is of great practical importance in connection with such diverse applications as the wind load on man-made structures on the ground, the oscillation characteristics and noise of the high-speed vehicles. The structure of the separated eddies behind the body are also of practical importance, especially as the structure of the near wake behind the body is closely related to the shielding effect of the body and the diffusion of heat or mass at the rear of the body. In recent years, this problem has received considerable attention in connection with the diffusion of radioactive release from atomic-energy power plants. Moreover, the knowledge about the mean and turbulent properties in the separated eddies is required to estimate the behaviour of the exhaust fumes from automobiles on roads in built up areas of towns and cities. Whereas the wake behind an immersed body is of basic importance in such professions as marine engineering: Lackenby (1962), in a review of the ship resistance, underlined the importance of this situation which was produced on the hulls of ships by welded and riveted seams. The review includes estimates made by Allan and Cuttand of the effects of roughness on an Atlantic liner (length 294m, speed 29 knots). They showed that there was an increase of 37% in the total resistance due to riveted

seams and only 1½% for welded seams.

There have been many measurements of wakes behind two-dimensional obstacles in turbulent boundary layers. Almost all of it has been made for smooth surfaces, while few are concerned with regular rough surfaces. In practice the results are of limited use to the engineer who is confronted with a flow problem associated with a naturally-rough surface, which may be due to manufacturing processes, deterioration or surface coating, as might be found on a corroded plate or on the inside surface of a concrete pipe line.

With these thoughts in mind, an experimental and theoretical investigation has been carried out to study:

(1) the recovery of a turbulent shear flow downstream of a two-dimensional obstacle;

(2) the effect of irregular surface roughness (uniformly distributed over the plan wall) on the mean flow and turbulence properties downstream of the obstacle;

(3) the effect of the geometry of the obstacle on the recirculating flow region and the recovery of the flow downstream of the obstacle;

(4) the possibility of predicting the flow around and downstream of the obstacle.

It appears more practical, mathematically and experimentally, to investigate the simpler forms of turbulent shear flow - such as fully developed pipe and channel flow. The study of these simpler flows may lead to better understanding of the behaviour of the turbulent boundary layer. Therefore, the experiments have been repeated within the present project for smooth and rough pipes, to study the effect of a two-dimensional obstacle on the fully developed turbulent pipe flow.

1.3 THE PRESENT INVESTIGATION

There have been many measurements of wakes behind two-dimensional obstacles in turbulent boundary layers, both in wind tunnel and in the natural wind. However, the purpose of these measurements has usually been practical rather than scientific and in particular, no detailed turbulence measurements behind a two-dimensional obstacle on an aerodynamically rough surface have been published. Counihan, Hunt and Jackson (1974) studied a two-dimensional obstacle attached to a rough surface, but the roughness they used was the type of regular form (lego sets). In the present investigation, the rough-surface has the property of the irregularity of the distribution of the roughness over the area of the plane. To study the effect of a two-dimensional obstacle attached to the irregular rough surface, two different obstacles have been used: one of a rectangular cross-section bar and the other has the shape of a simple-hump (hill). The obstacles have been roughly half the boundary layer thickness. The present investigation describes the mean flow and turbulence characteristics downstream of the obstacle. The experiments have been repeated for a smooth surface and the respective results are compared and discussed.

The relevant literature is presented in Chapter 2. In Chapter 3 the wind tunnel and the pipes used in the present investigation are described, as well as the instruments and the equipments. The two-dimensional obstacles used for the turbulent boundary layer and pipe flows experiments, the method of investigations and the basic equations to determine the characteristics of the flow downstream of the obstacle are also presented in Chapter 3.

The results of the wind tunnel experiments and the pipe flow experiments are presented in Chapter 4 and 5 respecitvely. Finally, the theoretical study and the numerical solution of the problem are presented

in Chapter 6. The conclusions deduced during the whole investigation together with the suggestions for future work are presented in Chapter 7.

CHAPTER 2

SURVEY OF LITERATURE

CHAPTER 2

SURVEY OF LITERATURE

2.1 INTRODUCTION

The flow of an incompressible fluid over a bluff body is one of the basic problems repeatedly drawing the attention of many research workers. Especially, prediction of the drag and lift forces acting on a body concerned is of great importance for practical purposes. Therefore, a considerable effort has been devoted to this subject. The major part of this effort is concerned with two-dimensional bluff bodies located in a uniform stream of infinite extension. Because of its complex nature, the flow around bluff bodies which are attached to a plane wall still remain in the category of diffcult and interesting problems to be further investigated. Recently the problem of reattachment and redevelopment of boundary layers downstream of a separated region become greatly intensified.

Since the present investigation had as its objective the study, experimentally and theoretically, of the effect of two-dimensional, transverse, blunt obstacles placed on an irregularly rough plate, the literature was surveyed considering the experimental and theoretical investigations.

2.2 EXPERIMENTAL INVESTIGATIONS

Experimental investigations of the flows over two-dimensional obstacle have been made for several geometries which are shown in Figure (2.1). They include an obstacle of square cross-section (Tillman (1945) and Arie et al (1975)), an obstacle that is fully surrounded by fluid (Arie and Rouse (1956)); a backward facing step (Tani et al (1961)), a wedge (Mueller and Robertson (1963) and Bradshaw and Wong (1972)), a a forward facing step (Bradshaw and GAlea (1967)), and a sharp edged normal

plate (Plate (1964), Good and Joubert (1968), and Sakamoto et al (1977)) mounted downstream of the leading edge of a flat plate.

The characteristics of the flow over a two-dimensional obstacle can be described for five regions illustrated in Figure (2.2).

In the far upstream region 1, a boundary layer on the plate develops normally and is uninfluenced by the obstacle. In the near-upstream region 2, an adverse pressure gradient will be produced by the deflection of the flow by the obstacle. The boundary layer will be forced to separate from the plane wall and will reattach on the front face of the obstacle, thereby enclosing a front separation bubble. The flow inside this separation bubble is steady (Good and Joubert (1968)). At the edge of the obstacle the flow separates, and if the mean flow is steady, the streamline which separates from the edge of the obstacle will reattach on the plane wall downstream of the obstacle. Arie and Rouse's (1956) experiments indicate that the rear separation bubble region 3, will be quite long; the bubble behind an isolated bluff plate with a downstream splitter was 17 plate-heights long. In the mid-downstream region 4, which starts at the reattachment line, the boundary layer recovers slowly from the disturbance caused by the obstacle. In the far-downstream region 5, the boundary layer returns to its normal undisturbed behaviour, but it has a greater thickness than the boundary layer which has developed along the plate in the absence of an obstacle.

From an experimental aspect, the most accessible parts of the downstream flow are regions 4 and 5 where no reverse flow exists. Thus reliable measurements of axial mean velocity are possible using a simple pitot tube, and turbulent quantities can be measured by a hot wire-anemometer.

Flow past an obstacle that is fully surrounded by fluid differs in several ways from the above described flow. The former may be considered

to lie in the path of essentially irrotational flow, where as later will be immersed in a boundary layer of indefinite thickness. And the flow in the wake of an isolated plate is free to oscillate about the plane of symmetry, whereas such oscillation is wholly prevented in the vicinity of a rigid longitudinal boundary. Arie and Rouse (1956) considered a situation in which a sharp-edged plate was exposed to uniform normal flow, but the vortex shedding was suppressed by attaching a splitter plate at the mid-height of the back of the plate as shown in Figure (2.1b). The total height, 2h, of the normal plate was 76mm, and the length of the splitter plate, 20h, exceeded the length of the recirculation zone to prevent eddies above and below the splitter plate from joining. The quantities measured in this experiment were the surface pressure on the normal plate, the mean velocity components, U and V, the Reynolds stresses $\overline{u^2}$, $\overline{v^2}$, $\overline{w^2}$, and $\overline{uv}$, and the static pressure distribution within the flow behind the plate. The results of the Reynolds stresses showed the region of maximum turbulence and maximum shear to coincide at the outset with the mean streamline isolating the main flow from that in the zone of recirculating flow. The pressure results showed that the drag coefficient of this arrangement (C_D = 1.4) was only two-thirds that of the isolated normal plate (C_D = 2.1), and the pressure coefficient on the forward face of the normal plate with a splitter plate (C_p = -0.57) was less than half that (C_p = -1.36) for the isolated plate. Such reduction in drag and pressure drop was corresponding to a considerable difference in the length of the mean eddy zone.

Tani et al (1961) carried out an experimental study for the flow downstream of a backward-facing step, Figure (2.1c). The step had an adjustable height (up to 6 cm) made on one side of a flat plate at a distance of 80 cm from the leading edge. The flat plate was spanned across a test section of a low-speed wind tunnel. Measurements of the

static pressure distribution on the step face and on the bottom surface of the plate showed that the pressure distribution was rather insensitive to the change in the step height as well as in the thickness of the approaching boundary layer. In all cases, there was a negative pressure on the step face (negative base pressure), followed initially by a slight drag in pressure downstream of the step, and then by a rather rapid rise of pressure indicating the reattachment of separated flow. The distributions of turbulence intensity $\overline{u}^2$ and turbulent shear stress $-\rho\overline{uv}$ showed the same behaviour as in Arie and Rouse (1956) results in the recirculating zone. The turbulence and shear stress were increased downstream in the mixing region and that the positions of maximum turbulence and maximum shear stress approximately coincide at the outset with the mean dividing streamline, but deviate outwards as the reattachment was approached. The reattachment line for different step height was at $x/h = 7$. All measurements have been carried out only to some distances near the reattachment, and no measurements made in the region of the recovery of the flow downstream of the reattachment.

Bradshaw and Galea (1967) used the normal step flow as means for studying the turbulent boundary layer developing towards separation under a strong adverse pressure gradient caused by the step. The step used in their experiment is shown in Figure (2.1d). A low speed wind tunnel, with step height equal 1.75 times the initial boundary-layer thickness has been used to study the response of the equilibrium turbulent boundary layer approaching upstream of the step. The measurements have been made only for the total pressure, static pressure, and surface shear stress upstream the step and on the step face. The surface pressure gradient decreased considerably just before the separation because of the effect of the increasing displacement thickness on the outer flow. After separation, the pressure gradient continues to decrease and becomes

negative. Very near the step the pressure started to increase rapidly again. This behaviour was consistent with the presence of a layer of reversed flow, emanating from reattachment point part way up the step, turning abruptly at the bottom of the step and then being gradually re-entrained into the separated shear layer. The surface shear-stress also decreased linearly to the value almost zero at the separation point. The point of separation occurred at 1.2 step height upstream of the step.

A similar flow as the one of downstream backward step is that around a wedge mounted on a plane wall with its vertical face backward. Bradshaw and Wong (1972) carried out experiments on a low speed flow downstream a wedge to demonstrate the complicated nature of the flow in the reattachment region, and its effect on the slow non-monotonic return of the shear layer to the ordinary boundary layer state. The study carried out for both, the immediate response to the perturbation, and relaxation back to the thin shear layer state. They defined three strengths of perturbations:

(i) A weak perturbation; the velocity and length scales of the flow are altered without significant change in the dimensionless properties of the turbulence structure.

(ii) A strong perturbation; the turbulence structure is significantly altered and thin-shear layer calculation methods could not predict the flow.

(iii) An overwhelming perturbation; the shear layer changes to one of a different species, as in the change of a boundary layer into a wake or mixing layer.

The authors classified those strengths in terms of h/δ (where h is the height of the obstacle and δ is the boundary-layer thickness). The strength of the perturbation in the Bradshaw and Wong experiment was strong and the conventional boundary-layer calculation methods were inapplicable for many boundary-layer thickness downstream of the reattachment. The velocity profiles presented in their experiments do not follow the logarithmic inner law, not only in the region close to the reattachment, but for many boundary layer thicknesses downstream. The measurements have been made only of the mean velocity distribution downstream the reattachment. The turbulence measurements have been made at one position ($x/h = 10$), and no further measurements have been carried in the region of the redeveloping of the flow. The reattachment point took place at $x/h = 6$ downstream of the step and the last measurements were at $x/h = 52$.

The more difficult perturbation in boundary layer flow is the one shown in Figure (2.2), which involves two separation regions. The first separation zone is upstream the obstacle, and the other is the separation of the flow at the top edge of the obstacle. If the obstacle has a finite width (as a rectangular cross-section obstacle) the separation of the flow will occur at the top edge of the obstacle and the separated stream line will either reattach on the top surface, or downstream the obstacle on the plane wall.

A detailed study of the flow over a sharp-edged obstacle mounted normal to a flat plate was made by Good and Joubert (1968). The experiment was performed mainly for the condition of zero external pressure gradient. The quantities measured included the static pressure distribution and velocity profiles in the whole flow field of Figure (2.2) and the surface pressure distributions on the front face of the normal plate and along the

flat plate. Good and Joubert showed that the drag coefficient of the obstacle and the surface pressure on the front face could be correlated by the independent, dimension less parameter $\frac{u_o}{U_\infty}$, $\frac{h}{\delta}$, and $\frac{hu_o}{\nu}$, . where u_o is the friction velocity and U_∞ is the free stream velocity, both measured at the obstacle position in the absence of the obstacle. The wall-similarity correlation obtained for the pressure on the front face of the normal plate (which was independent of the pressure-gradient hisotry of the boundary layer) indicated that the separation process upstream of the normal plate was sufficiently rapid to be of the type postulated by Stratford (1959) and Townsend (1960), (1962).

For the values of plate height h, to boundary layer thickness δ, ratio less than 0.5, the obstacle was immersed in a thin layer where the law of the wall was valid and the drag coefficient C_D then followed a logarithmic behaviour. For larger h/δ , the outer part of the velocity profile deviated from the logarithmic law and then C_D deviated from the logarithmic behaviour. For zero pressure gradient flows, the correlations obtained allow the form drag, and the actual pressure distribution on the normal plate, to be predicted from a knowledge of the thickness and wall shear stress of the reference profile. The velocity distributions at different stations, upstream and downstream of the normal plate were made. Unfortunately these results were made for height of the normal plate more than the boundary-layer thickness. No attempt was made to measure the turbulent characteristics downstream of the obstacle.

Sakamoto, Mariya and Arie (1975) re-examined the flow over a sharp-edged normal plate attached to a long flat plate, in a field of zero external pressure gradient. Measurements of the surface pressure distributions, static pressure, mean velocity and drag forces acting on the normal plate confirmed the general features shown by Good and Joubert,

but showed a number of detail differences. Sakamoto et al's results reproduced the wall similarity law for the drag coefficient, but showed that a logarithmic variation of C_D with h/δ was applicable upto $h/\delta \simeq 1.2$, compared with Good and Joubert's limit of $h/\delta \simeq 0.5$. Normalised pressure distributions measured on the front face for $0.21 \lesssim h/\delta \lesssim 2.13$ showed an even smaller dependence on Reynolds number than the results obtained by Good and Joubert. The corresponding surface pressure coefficients satisfied the wall law behaviour over the whole range of h/δ tested for values of y/h less than approximately 0.7, in accordance with Good and Joubert's findings. Sakamoto et al attributed to the discrepancies between their own results and those of Good and Joubert to the existence of significant flow blockage in the earlier work.

In support of the conclusions of Sakamoto et al, Ranga and Plate (1976) carried out experiments to study the relation between the form drag on a two-dimensional sharp edged normal plate and the properties of the turbulent boundary layer. The measurements were performed at zero pressure gradient of velocity profiles along smooth, rough and transitional flat plates. They found that after suitable blockage corrections all form-drag coefficients collapsed on a single curve, if they were calculated with the shear velocity as the reference velocity, and plotted against the ratio of the obstacle height to the characteristic roughness parameter of the approaching flow. Ranga and Plate corrected the results obtained by Good and Joubert (1968) for the blockage effect using the formula deduced by Ranga Raju and Garde (1970).

$$C_{D_c} = C_D (1 - h/D)^{2.85} \qquad (2.1)$$

Sakamoto et al (1977) extend their experiments, carried out in (1975), to study the flow around two-dimensional sharp-edged plates attached to a plane wall at different inclinations to the flow. Their experimental data were collected to investigate the effects of (i) inclination of the plate to the flow, (ii) the characteristic of the smooth wall boundary layer in which the plates were immersed, and the pressure forces of the inclined plates. Further, they examined the flow patterns around the inclined plate. The correlations were obtained between the variation of pressure forces and the inclined plate length h, which was analogous in form to the law of the wall of a boundary layer velocity profile.

Most of the obstacles used in the above experiments were of a sharp edged normal plate, whereas obstacles in most practical cases have a considerable thickness. Although the data on the thin normal plates immersed in the turbulent boundary layer may be used as a basic information in this case, the quantitatively correct values of the drag coefficient cannot be estimated from the data of the plate, since the interaction of the separated flow with the after-part of the bodies is not included in the case of the plate. To study this type of flow Mikio et al (1975a) investigated experimentally the pressure distribution on a two-dimensional rectangular cylinder immersed in a turbulent boundary layer, over a smooth wall.

The rectangular cylinders, with various width-to-height ratios, were chosen in this investigation as a representative shape of the bodies which have respectively an after-part behind the fixed separation point.

The pressure distribution and the drag on the rectangular cylinder were correlated with the characteristics of the smooth-wall turbulent boundary layer in which the cylinders were immersed. The correlations obtained were similar in form to the law of the wall for the boundary layer velocity profile.

$$C_D = A_1(b/h) \log_{10} \left(\frac{hu_0}{\nu}\right) + B_1 (b/h) \qquad (2.2)$$

where h is the height of the obstacle, b is the width and the values of A_1 and B_1 are functions of b/h alone.

As continuation of the last paper, Mikio et al (1975b) described the flow patterns around the rectangular cylinders immersed in a turbulent boundary layer. The distributions of the mean velocities, static pressures, longitudinal turbulence intensities and stream functions around the rectangular cylinder with b/h = 2.0 and 4.0 were clarified. The geometrical shape of the rear standing vortex and the reattachment points of the separated flows were also determined. The general shape of the static-pressure distribution was similar to that reported by Good and Joubert (1968). The reattachment point for the ratio of b/h = 2 was at x/h = 9, downstream of the obstacle. The measurements of the mean velocity profiles and the turbulence intensities were measured only for a few stations downstream the reattachment points and no measurements were made to study the recovery of the flow (region 5 in Figure (2.)).

2.3 THEORETICAL INVESTIGATIONS

2.3.1 Review of Approximate Analytical Methods

Analytical methods reported in the literature can be divided into two groups. In the first group, conformal mapping of the velocity potential and stream function are used to obtain stream lines and the pressure distribution around a bluff body; this method is limited to two-dimensional flows. The second group contains methods of analyzing the downstream wake region by solving the linearized equations of motion, assuming small perturbations of the velocity field. These methods have been applied to two- and three-dimensional flows.

The theoretical method developed by Kiya and Arie (1972) was based on a mapping procedure in the complex z-plane. To predict the pressure coefficient on the front surface of an obstacle attached to a flat plate, the non-uniform velocity profile typical of a two-dimensional wall boundary layer (a gradual velocity variation in the outer flow and a steep velocity gradient near the wall) was modelled by a linear velocity profile in the outer flow starting from a non-zero velocity at the wall.

The theoretical results for pressure distribution were compared with the measurements of Good and Joubert (1968) and satisfactory agreement was obtained, although the theory included three or four constants which should be determined on the basis of the experimental information. The number of constants depending upon the shape of the obstacle.

Sakamoto, Mariya and Arie (1975) used a similar theoretical model to predict the pressure distribution and separation streamline for the same situation. In their theory, the front separation bubble, which was predicted by Kiya and Arie, was replaced by a potential vortex. Although this modification simplified the analysis, it introduced a fourth empirical parameter which had to be fixed by experimental conditions. The pressure distribution on the obstacle obtained by this analysis showed good agreement with the authors' own experimental results.

Following the approach used by Steiger and Bloom (1963) and Kuo and Badwin (1966) for the prediction of the far-downstream region of three-dimensional turbulent free wakes, Sforza and Mons (1970) applied such a theory to calculation of a wall wake. Their main interest was to describe how wake-like disturbances from two- and three-dimensional obstacles attached to the leading edge of a flat plate affected the development of the boundary layer along the plate. The linearized equations were used to calculate the velocity defect, defined as the difference in velocity between the undisturbed boundary layer profile and the disturbed profiles

in the wake of the obstacle. The theory used an eddy viscosity which was a function of the streamwise coordinate only, but weighted in the three-dimensional case by a factor proportional to the obstacle dimensions in the cross-stream direction. The predicted velocity defect profiles normal to the plate, and in the three-dimensional wake transverse to the plate, were in good agreement with experiments.

A theory for the flow behind two-dimensional and three-dimensional obstacles immersed in a turbulent boundary layer on a plane surface ($h << \delta$) has been developed and tested by Hunt (1971, 1974, 1980), Smith (1973), Counihan, Hunt and Jackson (1974), Castro and Robins (1977). The objectives of the theories are to predict the distributions of the velocity defect, shear stress and turbulent intensity in the wake, and to relate the velocity defect to the forces on the obstacle. A relation for two-dimensional obstacles was first obtained by Hunt (1971) in laminer flow. A modification of this theory, in which some terms were simplified, was discussed by Smith (1973).

Counihan et al (1974) presented a theory for turbulent flow behind a two-dimensional body in a thick boundary layer. This was based on the following assumptions:

(i) $h_s << h << \delta$, where h_s, h and δ are respectively the heights of the roughness elements (the mean height of the irregular rough surface in the present investigation), the body whose wake is to be studied and the boundary layer.

(ii) Sufficiently far downstream of the body the velocity returns to its value in the undisturbed boundary layer, defined as $(U(y), V(y), 0)$.

(iii) The mean velocity profile, $U(y)$, in the upstream boundary layer can be described by a power law

$$U(y) = U_\infty \ (y/\delta)^n \qquad (2.3)$$

Near the wall, a logarithmic profile is assumed

$$U(y) = \frac{u_o}{\kappa} \ln (y/y_o) \qquad (2.4)$$

where y_o = the roughness length.

(iv) Far downstream of the body the small perturbations to the incident flows caused by the body can be divided into three regions namely: (a) a wall region (W) in which it is assumed that turbulent energy production locally balances dissipation; (b) an adjacent mixing region (M) where the perturbation flow is self-preserving; and (c) an external disturbed region (E) generated by W and M, which can be regarded as inviseid perturbation of the boundary layer flow. In regions (M) and (E) the mean velocity and the mean stresses can be expressed as the sum of an undisturbed mean values and a perturbation values.

Counihan et al predicted that the mean velocity defect would show self-preserving profiles in which the perturbation velocity decays axially as $(x/h)^{-1}$. This self-preservation was confirmed by their own experiments and by the results of Plate and Lin (1965) which involved a different wall roughness and Reynolds number. The predicted behaviour was also supported by the experiments of Sforza and Mons (1960) even though in their case the obstacle was attached to the leading edge of a smooth flat plate, rather than downstream of the leading edge.

Castro (1979) presented detailed measurements in the wakes behind two-dimensional square section blocks mounted in thick wall boundary layer for cases in which $h/\delta << 1$. The experimental data have been compared with the theoretical predictions of Counihan et al (1974). Castro found that, whilst the Counihan et al theory correctly indicates the way in which the wake decay changes with the upstream flow characteristics, was sufficiently realistic to give good predictions of the total flow downstream

of reattachment. The mean velocity perturbations decay initially like $(x/h)^{-1}$, as predicted by the theory, but this decay rate gradually decreases with increasing distance downstream. In the wall region the flow recovered rather more rapidly than elsewhere, in contrast to the theory, and in fact, at a rate which did not seem to depend strongly on the outer flow.

From this review of theoretical treatments of bluff body flows, it is clear that theirapplicability is very limited. The theory of Counihan et al (1974) can describe cross-stream profiles and streamwise decay of the mean velocity defect in the far wake behind bluff bodies in turbulent boundary layers. The theories do not, however, adequately describe the distribution of shear stress and turbulent intensity across the wake. Postential flow situations using conformal mapping have been applied to the flow immediately upstream of a two-dimensional bluff obstacle, but these methods fail in the downstream wake region. The theories developed are also not applicable to other geometries without major modification.

2.3.2 Review of Numerical Methods

Most of the numerical methods applied to the flow around a two-dimensional obstacle were made for a laminar flow. The studies of Greenspan (1969) and Friedman (1972) considered steady, incompressible, laminar flow over a thick rectangular obstacle mounted on one wall of a plane channel. Greenspan solved the equations of motions using the stream function, ψ and vorticity, ω, as dependent variables. He predicted the flow for several ratios of obstacle height to channel height and several Reynolds numbers, found that careful choice of finite difference grid distribution was necessary to secure convergence of the solutions. Freidman modified Greenspan's numerical scheme to extend the range of Reynolds numbers for which convergence could be obtained.

Kiya and Arie (1973) investigated the laminar far wake behind a symmetrical two-dimensional body placed in a uniform shear flow. They solved the equations of motion using the stream function, ψ and the vorticity, ω , as dependent variables. The solution was different from that used by Greenspan (1969), instead of the finite difference method they used the Oseen type of successive approximation, in which the shear was regarded as a small perturbation on a uniform stream. The expression for the stream function was determined up to the third approximation both in and outside the wake region. The stream function was found to contain four constants which cannot be determined from the boundary conditions for the far wake.

Numerical solution of the Navier-Stokes equations, for two-dimensional viscous flow past semicircular and semielliptical projections attached to a plane wall was presented by Kiya and Arie (1975). Numerical solutions were obtained for the range 0.1 - 100 of the Reynolds number, which was defined in term of the approaching velocity at the top of the obstacle and its height. They assumed that the flow was laminar and the height of the obstacle was so small in comparison with the local boundary layer thickness that the approaching flow could be approximated by a uniform shear flow.

For a turbulent boundary layer flow Taulbee and Robertson (1972) investigated such flow toward a normal step. They treated the flow of a turbulent boundary layer into a step as a rotational flow one. The frozen vorticity theory (Robertson (1965)) was used in their investigation. The solution for the stream function and the vorticity was obtained by a successive approximation finite difference method. The thoery used by Taulbee and Robertson predict only the flow pattern upstream the step, but it does not predict the behaviour of the turbulence properties.

From the above review it can be seen that the computation of laminar recirculating flows is possible by the simultaneous solution of the Navier-Stokes and continuity equations in finite difference form. In addition to the obvious difficulties imposed by limited computational facilities, these early solutions were also confined to low flow rates due to numerical instability at higher Reynolds numbers. This limitation has recently been eliminated however, following the development by Gosman et al (1969) and others of improved numerical methods which yield stability and rapid convergence for any Reynolds number. On the other hand, methods for calculating turbulent boundary layers and other thin shear layers are now sufficiently realistic and reliable - Bradshaw et al (1967), Patankar and Spalding (1967), (1972) and Nee and Kovasznay (1969) - for useful attempts to be made to calculate the more complicated flows. There are a number of accurate numerical procedures, mostly finite difference techniques, which have been shown to be successful, and most of the difficulties associated with such predictions relate directly to the lack of total physical understanding and consequent inadequacies in the various turbulence models used. However, in the case of complex turbulent flows, defined as those which fail to satisfy the boundary layer approximation, and which are, therefore, in general elliptic, the situation is not so clear. It is generally recognized that only methods based on modelled forms of the full transport equations are likely to have sufficient physical content to be able to cope with complex flows. Although such models are now being developed - Hanjalic and Launder (1972) and Launder et al (1975) - they have as yet only been extensively tested for the calculation of thin shear flows or, at least, flows which are essentially parabolic; their adequacy for more complex flows remains to be demonstrated.

Vasilic-Melling (1976) solved numerically flows over two- and three-dimensional rectangular obstacles. The method of the solution consisted of a finite-difference procedure for solving the elliptic form of the momentum equation, and two additional conservation equations for the turbulence Kinetic energy and dissipation rate, with the continuity equation. The particular method used was similar to that described by Patankar and Spalding (1972), for solving two- or three- dimensional elliptic equations using velocity and pressure as the main dependent variables. The specific situations examined were two-dimensional turbulent flows over a sharp edged normal plate or square cross section obstacle mounted normal to a flat plate, and three-dimensional flow over a surface-mounted cubical obstacle, oriented with one face perpendicular to the direction of flow. Predictions of two-dimensional flow were compared with measurements of the streamwise velocity component, static pressure, surface pressure and turbulence Kinetic energy reported by some previous researchers. No measurements were made downstream of the square cross section obstacle to compare the predicted flow with such measurements. Instead Vasilic-Melling (1976) made the comparison with Good and Joubert (1968) measurements downstream of a sharp edged normal plate which is different in geometry from an obstacle which has a finite thickness as the one mentioned above. Also, the obstacle he used was partly immersed in the boundary layer which is different than the present investigation.

The accuracy of a numerical prediction rests, however, not only on the excellence or otherwise of the turbulence model but, even more basically, on the accuracy of the numerical techniques used to solve the equations which embody the model. Castro (1979) discussed the numerical accuracy of a finite difference technique typical of many used for the calculation of elliptic turbulent flows. He investigated both analytically and by

direct comparison between prediction and experiments the size of the inevitable truncation terms. Flow down a rearward-facing step and over a two-dimensional obstacle was investigated. A different mesh size was used to performing grid dependency check. In the flow down a rearward-facing step the effect of mesh spacing on mean velocity was small, and the reattachment point was only about 16% further downstream for the finest grid than for the other grids. While for the flow downstream of a two-dimensional obstacle (sharp edged normal plate attached to a plane wall), the point of reattachment was very sensitive to the mesh size in the region of recirculating flow.

2.4 CONCLUSIONS

The survey of experimental data for flow over bluff bodies revealed extensive information for surface pressure, but comparatively little for other quantities (velocity and turbulance intensity) of interest for prediction procedures. At the same time, most of the experimental work has been carried out for two- or three-dimensional obstacles attached to a smooth surface is different from that actually found in the natural ground.

The theoretical treatments of flow around obstacles are basically concerned with regions upstream and far downstream of the obstacle. Analytical methods (Kiya and Arie (1972); Sakamoto et al (1975)) based on conformal mapping have been proposed for two-dimensional flow over obstacle, but they predict only the upstream flow and are not adaptable to other geometries. The other thoeries based on perturbation methods (Hunt (1971); Counihan et al (1974)) have been developed for the wake region downstream of the obstacle. These, however, cannot be applied to the recirculating region in the separation flow near the obstacle since the disturbances of flow properties caused by the body are too large to be treated as linear perturbations.

The numerical solution, most finite difference techniques have been shown to be successful for prediction of such flows. In the present investigation the finite difference technique was employed to predict the flow around the obstacle and downstream of the obstacle. The flow domain can be divided into two regions; the recirculating flow region and a boundary flow region downstream of the separated flow.

CHAPTER 3

APPARATUS AND EQUIPMENT

CHAPTER 3

APPARATUS AND EQUIPMENT

3.1 APPARATUS

3.1.1 Wind Tunnel

The measurements were made in an open circuit wind tunnel. The tunnel had a 122 cms. wide x 61 cms. deep x 366 cms. long working section. The turbulence level at the centre line of the working section was 0.7 percent at a free stream velocity of 21 m/s.

An axial flow fan driven by a 50 HP squirrel cage induction motor was forcing the air to the wind tunnel entry. In order to obtain a condition of zero pressure gradient along the plate, the passage between the tunnel top wall and the plate was made sufficiently divergent to offset the natural fall in pressure due to boundary-layer growth. This was accomplished by an adjustable top wall which could be positioned by screws threaded into the tunnel roof. This adjustment was repeated after placing the obstacle inside the wind tunnel, to satisfy the condition of zero pressure gradient in the whole experimental programme.

Figure (3.1) shows a diagrammatical sketch of the wind tunnel used in the present investigation.

3.1.2 Rough and Smooth Plates

A 367 cms. long x 122 cms. wide, and 0.635 cms. thick hardboard was used as a flat plate. A sheet of abrasive paper of grade 16, was affixed to the plate and mounted on the floor of the working section of the wind tunnel. In order to avoid any effect on the starting boundary-layer thickness, a small rounded wooden piece was mounted parallel to the leading edge of the rough plate.

The wind tunnel was designed with a smooth floor made of a sheet of formica. This smooth floor was used for the smooth plate experiment. The dimension of the plate was 360 cms. long and 110 cms. wide.

3.1.3 Dimensions of the Two-Dimensional Obstacles (RIDGE and HILL)

Two obstacles of different cross-sections were used in the present investigation: one was a rectangular cross-section bar known henceforth as "ridge" and the other had the shape of a simple-hump known henceforth as "hill", (Figure (3.2a). The ratio of the height, h, to the width, b, of the "ridge" was 2.5, and the ratio of the bundary-layer thickness δ to the height of the obstacle h, was 2 at the position of the obstacle "ridge" or "hill". The height of the obstacle was 2 cms. in the case of rough plate and 1.2 cms. in the case of smooth plate. The simple-hump (hill) has the surface which satisfied the equation,

$$y/h = \left[1 + (x/h)^2\right]^{-1} \qquad (3.1)$$

where h is the height of the hump at x = 0. The spanwise length of the obstacle was one metre. This length was a little bit shorter than the width of the wind tunnel to leave some space, so that the rubber tubes which were connected to the static-probes could be easily taken out to the manometer.

The ridge was made of a plate of perspex with a thickness of 2 mm. and the hill was made of a fibre-glass coating with a thickness of 2 mm. The upstream and downsteam edges of the hill were flashed with the plate surface to avoid any step-roughness effect.

A considerable number of 0.5 mm. diameter pizometer holes were drilled at the centre portion of the "ridge" and the "hill", one side had been drilled as well as the top side for the ridge to measure the pressure

distribution on the two obstacles. The side of the obstacle which had the holes can be used as upstream face or downstream face to measure the upstream or downstream pressure distribution. The pressure holes were connected to a multi-tube manometer through 0.71 mm. I.D. stainless tubes and polyvinychloride tubes of various diameters. Figure (3.2a) shows the two obstacles (ridge and hill) used in the wind tunnel experiment. Figure (3.4) shows the position of the obstacles inside the wind tunnel and the boundary-layer thickness developed on the rough plate.

3.1.4 Rough and Smooth Pipes

A 5.08 cms. I.D. (2 in.) and 732 cms. length split pipe was used in the present investigation as a rough pipe. The pipe had three parts of 244 cms. each, with a rectangular cros-section area which could be split to half, and each half contained a longitudinal semi-circular channel of 2.54 cms. in radius. The pipe was lined internally with the same abrasive paper used in the rough plate. The static pressure drop along a length of 244 cms. of the pipe can be measured by means of two static pressure tubes installed concentrically inside the pipe.

A three stage centrifugal blower was used to supply the pipe with the air. The velocity of the air inside the pipe can be controlled by an exit gate valve of the blower. Figure (3.3a) shows the parts of the rough pipe as well as the positions of the static and total head tubes.

For a smooth pipe experiment, a 6 metre perspex pipe with an inside diameter of 3.84 cms. was used. The static pressure drop along the pipe length can be measured by different static pressure taps on the pipe wall.

A small centrifugal fan driven by a variable speed motor was used to drive the air through the pipe. The velocity of the air inside the

pipe can be controlled by changing the speed of the motor. Figure (3.3b) shows the smooth pipe used in the experiment.

3.1.5 Dimensions of the Two-Dimensional Obstacle (RING)

The obstacle in the pipe experiments had a form of suitably scaled internal (rectangular in cross-section) rings. The ratio between the width b to the height h of the ring was ~~0.86~~ 1.163. This ratio was kept constant for both the rough and smooth pipe. The ring was made of wood with a diameter smaller than the internal diameter of the pipe by 1 mm. For the rough pipe the gap between the ring and the pipe surface was sealed by using a blue take, this also protected the irregularity of the rough surface of the pipe from any damage caused by the solid ring. For the smooth pipe the gap between the ring and the pipe was sealed by a foam rubber sealing compound, this made it easy to change the position of the ring and protect the smooth surface of the pipe. Figure (3.2b) shows the rings used for the rough and smooth pipes.

3.2 INSTRUMENTATION

3.2.1 Traverse Mechanism

A special instrument was desinged by El-Samanoudy (1974) for measuring the boundary-layer growth at different stations inside the working section of the wind tunnel. This instrument was used in the present investigation to enable traversing at different positions downstream of the obstacle.

The instrument was made of a stainless steel rod resting on a small rectangular metal block with a rubber pad glued to its underside to protect the surface roughness irregularities. The instrument had a sliding

head carrying the pitot tube which was held tightly by grab screws, the sliding head guided by a groove along the road connected by the traverse outside the wind tunnel by means of a $\frac{1}{16}$ inch steel cord guided by a small pulley and kept under constant tension by an over-hanging weight. A dial clock guage read with an accuracy of 0.01 mm. was used to measure the displacement of the pitot tube or the hot wire probe from the surface up to 50 mm. For boundary-layer thicknesses greater than 50 mm, the scale reading of the traverse gear was used to an accuracy of .05 mm.

The pitot tube had a hypodermic front tube of 0.71 mm. O.D. The static pressure measured by a 0.81 mm. O.D. static tube provided with two static holes. The static tube was held firmly by another head fixed on the instrument road. Figure (3.5) shows in detail the instrument and traverse gear used in the experiment.

A standard pitot -static tube was mounted at the exit of the wind tunnel to measure the exit free stream velocity as well as to control the speed of the working section.

In the pipe flow experiment the pitot tube head was made of a hypodermic tube of diameter 0.57 mm. and was used at the exit of the pipe to measure the velocity profiles. The pitot tube was manually operated by a traverse gear of 0.01 mm. reading accuracy (micro-manipulator).

An inclined multi-tube manometer was used for measurements of pressure. A methylated spirits (S.G. = .815) was used as a manometric fluid.

3.2.2 Hot Wire Equipment

Two different types of standard hotwire were used; one was a single probe 5 micron tangston wire, and 1-1.5 mm. in length. The other was an X - probe (type: DISA 55 A 38). The single probe was used for measuring the skewness, flatness factor and spectrum function. The X-probe was used to measure the turbulence intensities and the shear stress components.

The single probe was connected via a 5 metre cable to a constant temperature anemometer (type: DISA 55M01), the output signal voltage of the anemometer was fed into a linearizer (type: DISA 55M25) to provide a linear function between the output voltage signal and the measured flow velocity. The voltage was read from a digital voltmeter (type: 500 MK III). The output signal from the linearizer was fed to an R.M.S. voltmeter (type: DISA 55D35) to read the fluctuating voltage (related to the longitudinal fluctuation velocity). The square value of that signal could be obtained by the R.M.S. voltmeter. This was squared again by using a turbulence processor (type: DISA 55P25). In order to avoid the fluctuation reading of the square values, the output of the turbulence processor was fed to an integrator (type: DISA 52P30) to give an average value of squared signal. This value was fed to the digital voltmeter to calculate the flatness factor $\left[\frac{\overline{u^4}}{(\sqrt{\overline{u^2}})^4}\right]$. The output of the R.M.S. voltmeter and the squared signal obtained by the R.M.S. voltmeter were fed to an analogue correlator (type: DISA 55D70) to calculate the skewness factor $\left[\frac{\overline{u^3}}{(\overline{u^2})^3}\right]$. A frequency analyser and level recorder (Brüell and Kjaer types 2107 and 2305 respectively with a frequency response of 20HZ to 20KHZ) were used to calculate the frequency spectrum of the longitudinal fluctuation component. The two instruments were mechanically-synchronised by means of a drive cable. The interconnections for the electronic equipment are shown in Fig. (3.6).

The X-probe was connected with two constant temperature anemometer units and two linearizers. The output signals of the linearizers were fed into a random signal correlator and indicator (type: DISA 55A06) to obtain the signals addition and subtraction, which are proportional to longitudinal and tranverse turbulence intensities.

3.3 EXPERIMENTAL MEASUREMENTS AND PROCEDURES

In order to establish a datum from which wall distances were measured for the rough plate and the rough pipe, a flat-headed copper pin was

introduced among the roughness excrescences in the measuring plane. The top of the pin was approximately 0.5 mm. above the local peaks of the roughness. The other end of the pin was connected to one side of a transistorized continuity tester. The other side of the tester was wired to the pitot tube so that when the pitot tube just made contact with the pin the light of the tester came on. For the smooth surface the measurements were started with zero distance from the surface. This was obtained by placing the pitot tube adjacent to its image on the surface.

The datum for the hot-wire traverse could not be established using the above contact method because of possible damage to the probe. A cathetometer, with a vernier scale accurate to within ±10 microns, was used for the pipe experiment in order to measure the distance between a pre-arranged datum just above the surface and either the surface itself (in the case of smooth pipe) or the top of the copper pin. Once the datum had been determined the wall distances were measured using the digital gauge of the traverse gear. For the wind tunnel measurements it was difficult to use the above method. The wall distance was measured as shown in Fig. (3.6b).

The wind tunnel experiments were carried out with free stream velocity in the working section equal to 21 m/s., and in order to take into consideration the variation of the temperature and the atmospheric pressure from one day to another the readings of temperature and the barometric pressure were taken before starting the wind tunnel. The mean velocity profiles and the turbulence quantities were measured for the rough and the smooth plates before placing the obstacle inside the tunnel. These measurements were used to determine the characteristics of the turbulent boundary layer before disturbing the flow. The two-

dimensionality of the flow was checked after the obstacle was introduced inside the working section of the tunnel-velocity and static-pressure distribution were measured at different positions at the top of the obstacle in spanwise direction. The results are shown in Fig. (3.7). For the rough plate, the gap between the obstacle and the surface was sealed by a foam rubber sealing compound. In the case of a smooth surface an abrasive tape was used to close that gap as well as to hold the "ridge" on the surface.

Detailed measurements of the mean velocity and turbulence properties were carried out for both the rough and smooth plates downstream of the obstacle (ridge or hill) to the recovery region of the flow. Two obstacles were used with the rough plate "ridge" and "hill" and only one was used with the smooth plate "ridge" for a comparison. The ratio of the boundary-layer thickness to the height of the obstacle was equal for both the rough and smooth plate experiments. All measurements were made at the centre line of the wind tunnel to avoid the effect of the tunnel side walls. The obstacle was placed at a distance of 135 cms. from the leading edge of the rough and smooth plates.

In the pipe flow experiment the air supply was switched at least 30 minutes before the start of a measurement session for the apparatus to reach equilibrium conditions. The values of the air density and kinamatic viscosity were corrected for daily variations in barometric pressure and air temperature. The value of the Reynold's number $(\frac{V_p h}{\nu})$ was approximately 5.8×10^5 for both the rough and smooth pipes, where h was the height of the ring and V_p the pipe average velocity.

The smooth pipe was used to calibrate the hot-wire probe before the probe was used for the rough pipe measurements. Additionally, the response of the wire to a square wave input was checked on the oscilloscope so that any necessary adjustments to the bridge balance of the anemometer

could be made. The distribution of the turbulence shear stress $\frac{-\overline{uv}}{\overline{u^2_0}}$ was measured in the smooth pipe and compared with the linear distribution:

$$\frac{\tau}{\tau_0} = 1 - \frac{y}{R} \qquad (3.2)$$

as well as with some previous measurements as Lauf er (1955).

The mean velocity, the three components of turbulence normal stresses and the shear stress distribution were measured at different positions downstream of the ring to the recovery condition of the flow. All the measurements were made at the exit section of the pipes. The position of the ring could be changed with respect to the measurement section by pushing the ring inside the pipe to the desired distance.

Measurements of the skewness, flatness and the spectrum function of the longitudinal normal stress were carried out by using a single hot-wire probe. The spectrum functions were measured at wall distances of $\frac{y}{R}$ equal to 0.02, 0.35, 0.68 and 1.0 for both the rough and smooth pipes.

3.4 METHODS OF INVESTIGATION

The main objective of the present investigation was to study how a two-dimensional obstacle attached to a rough surface affect the turbulent boundary-layer developed on the surface. The experiments were carried out for rough and smooth surfaces as well as for a rough and smooth pipe to study the recovery of the flow downstream of the obstacle. The mean velocity profiles and the turbulence properties were measured before and after placing the obstacle in the wind tunnel or in the pipe.

The measurements of the mean velocity profiles were used to determine the wall friction coefficient c_f for the disturbed and undisturbed flows. The graphical method developed by Parry and Joubert (1963) was used to determine the values of c_f for the rough surfaces. Using the usual law of

the wall combined with the law of the wake (Coles, 1956),

$$\frac{U}{u_o} = \frac{1}{\kappa} \ln \frac{y u_o}{\nu} + A - \frac{\Delta u}{u_o} + \frac{\Pi}{\kappa} W(y/\delta) \qquad (3.3)$$

a multiplication of both sides by $\frac{u_o}{U_\infty}$ $\left[\hat{w}=(\frac{1}{2} c_f)^{\frac{1}{2}}\right]$ leads to the form

$$\frac{U}{U_\infty} = \frac{\hat{w}}{\kappa} \ln (\frac{yu}{\nu}) + \hat{w} \left[\frac{1}{\kappa} \ln \hat{w} + A - \frac{\Delta u}{u_o}\right] + \frac{\hat{w}\Pi}{\kappa} W(\frac{y}{\delta}) \qquad (3.4)$$

For a smooth surface ($\frac{\Delta u}{u_o}$ = o) the above equation gives a family of straight lines of ($\frac{U}{U_\infty}$) versus ($\ln \frac{yU_\infty}{\nu}$) - Clauser (1954) - each line corresponding to a given value of w. Thus a chart may be constructed, and by plotting the experimental points on such a chart the line upon which they fall gives the appropriate value of w. The accuracy of the result may be confirmed by two properties of the line, these being its slope and its placement on the chart. In the case of a rough surface difficulties arise, these being that the origin for y is not known and also, since the roughness of the surface causes a shift in the logarithmic profile, the value of c_f is confirmed only by the slope of the logarithmic line and not its position. Perry and Joubert (1963) assumed that the origin was located at distance $\hat{\varepsilon}$, below the crests of the elements used to simulate the rough surface. In the present investigation that distance was below the crest of the artifical datum (the top of the copper pin). The value of, ε, was determined by adding a small distance to the value of, y, such that the experimental values of ($\frac{U}{U_\infty}$) gives a best fit to a straight line in the logarithmic inner region. Once the value of $\hat{\varepsilon}$ was known, the value of c_f could be determined from the slope of the logarithmic line.

The values of the roughness function $\frac{\Delta u}{u_o}$ could be determined for different values of Reynolds numbers by plotting the equation (3.3) for a smooth surface ($\frac{\Delta u}{u_o}$ = o) and for a rough surface, the results of the rough surface will shift from that of the smooth surface by value equal

to $\frac{\Delta u}{u_o}$ at a certain Reynolds number.

Nikuradse (1933) used the logarithmic law in slightly different form. He defined an alternative roughness function, χ , such that

$$\frac{U}{u_o} = \frac{1}{\kappa} \ln \frac{y}{h_s} + \chi \tag{3.5}$$

where $\chi = \frac{1}{\kappa} \ln \frac{h_s u_o}{\nu} + A - \frac{\Delta u}{u_o}$ (3.6)

and h_s is the equivalent sand roughness height of the rough surface, and it depends on the roughness height and the roughness geometry of the surface. For the fully rough flows function factor is independent of Reynolds number) Nikuradse (1933) found that

$$f = (2 \log \frac{R}{h_s} + 1.74)^{-2} \tag{3.7}$$

The value of the friction factor f was determined for the pipe experiments by measuring the pressure drop over a known length of the pipe

$$\tau_o = \frac{\Delta P}{4} \frac{D}{L} \tag{3.8a}$$

where τ_o is the value of the wall shear stress, the respective friction factor is

$$f = \frac{8\tau_o}{\rho V_p^2} \tag{3.8b}$$

where V_p is the average velocity of the pipe defined as

$$V_p = \frac{2}{R^2} \int_o^R U(R-y)\, dy \tag{3.9}$$

The value of the roughness height h_s determined from equation (3.7) was compared with that determined by the statistical examination of the rough surface (see Appendix A) and it was found that no substantial difference between the ten-point height and Nikuradse's equivalent sand roughness height.

The measurements of the turbulence normal and shear stresses were used to determine the turbulent eddy viscosity and the mixing length distribution downstream of the obstacle for both the boundary-layer flow and the pipe flow. The formulae used for this purpose were

$$\nu_t = \frac{(\tau/\rho)}{(\partial U/\partial y)} \tag{3.10a}$$

and

$$\ell_m = \frac{(\tau/\rho)^{1/2}}{(\partial U/\partial y)} \tag{3.10b}$$

The value of the mean velocity gradient $(\frac{\partial U}{\partial y})$, was calculated from the local velocity distribution. The experimental values of the eddy viscosity obtained from the above equation (3.10a) were compared with Clauser's model of the eddy viscosity in the inner and the outer regions of the boundary layer.

$$\nu_{ti} = \kappa\, y\, u_o \tag{3.11a}$$

and

$$\nu_{to} = \alpha\, U_\infty\, \delta^* \tag{3.11b}$$

where α is an eddy viscosity proportionality constant, which assumed to be equal 0.018 for an equilibrium boundary-layer. This value was determined for the disturbed flow downstream the obstacle, where the flow was in non-equilibrium condition.

The frequency spectrum of the longitudinal turbulence normal stress was calculated for both boundary-layer and pipe flow. If u is the component of the fluctuation velocity at a fixed point of turbulent motion in the direction of the main stream resolved into harmonic components, the mean value of u may be regarded as being the sum of contributions from all frequencies and $\overline{u^2}F(n)\,dn$ is the contribution from frequencies between n and n + dn, then

$$\int_0^\infty F(n)\,dn = 1 \tag{3.12}$$

If F(n) is plotted against n, the diagram so produced is a form of the spectrum curve.

For two points in a turbulent flow, separated by a distance, Δx, in the x direction, the longitduinal spatial correlation, R_T, is defined to be

$$R_T = \frac{\overline{u(x)\ u(x + \Delta x)}}{\overline{u^2}} \qquad (3.13a)$$

where $u(x)$ and $u(x + \Delta x)$ represents the instantaneous values of the longitudinal fluctuating velocity at x and $(x + \Delta x)$ respectively. The value of $u(x)$ and $u(x + \Delta x)$ can be measured using a two single hot wire separated horizontally by a distance, Δx. This method is not accurate because the wake of the upstream probe is bound to affect the flow near the downstream probe.

Taylor (1938) postulated that the sequence of changes in u at a fixed point is due to the passage of a 'rigid' turbulent eddy past the point, and if the velocity of the air stream, U, which carries the eddies is very much greater than the turbulent velocity, u, the fluctuations at the point may be imagined to be caused by the whole turbulent flow field passing that point with a constant velocity, U. Then the correlation $\overline{U(t)\ U(t + \Delta t)}$ averaging with respect to, t, must then be identical with the correlation $\overline{u(x)\ u(x + \Delta x)}$ averaging with respect to x. The advantage of this model is the fact that the space correlations can be deduced from time correlations. The latter can be measured either directly, using a time-delay unit, or indirectly by calculating the Fourier transform of the measured frequency spectrum function. The Fourier transform method was used throughout the present investigation. The required relation between the spatial correlation coefficient and the frequency spectrum function are:

$$R_T = \int_0^\infty F(n) \cos \frac{2\pi n}{U} \Delta x \; dn \qquad (3.13b)$$

$$F(n) = \frac{4}{U} \int_0^\infty R_T \cos \frac{2\pi n}{U} \Delta x \; d(\Delta x) \qquad (3.13c)$$

The PDP8 computer program written by Musker (1977) was used to calculate the values of R_T and $F(n)$.

The above calculations were used to determine the integral length scales of the turbulence field downstream of the obstacle. Taylor (1938) described two length scales of turbulence, macro-scale and micro-scale of turbulence. The macro-scale of tur bulence is a measure of the size of the largest eddies and it can be defined in terms of the longitudinal spatial correlation coefficient by

$$L_T = \int_0^\infty R_T \; d(\Delta x) \qquad (3.14a)$$

The micro-scale of turbulence λ is a measure of the size of smallest eddies of the turbulent flows responsible for the dissipation of energy, Taylor defined, λ , in terms of the curvature of R_T curve at its vertex.

$$\frac{1}{\lambda^2} = 2 \lim_{\Delta x \to 0} \left| \frac{1 - R_T}{(\Delta x)^2} \right| \qquad (3.14b)$$

Using equation (3.13b) after applying a series of expansion for the cosine term, as $\Delta x \to 0$, leads to:

$$\frac{1}{\lambda^2} = \frac{4\pi^2}{U^2} \int_0^\infty n^2 \; F(n) \; dn \qquad (3.14c)$$

Hence λ can be calculated from the second moment of the frequency spectrum function.

In the homogenous turbulent flow, the probability density distribution curve of the fluctuating velocity then shows a symmetry with respect to an axis (in the case of a point source) or with respect to a plane (in the case of a line source) the shape of these distribution curves will be

determined by the characteristics of the turbulence and by spatial distribution of the velocity. To study the homogeneity of the flow, two factors are provided by measurements, skewness and flatness factor defined by Klebanoff (1954) as:

$$S_f = \frac{\int_{-\infty}^{\infty} u^3 P(u)\, du}{\left[\int_{-\infty}^{\infty} u^2 P(u)\, du\right]^{3/2}} = \frac{\overline{u^3}}{(\overline{u^2})^{3/2}}, \qquad (3.15a)$$

$$F_f = \frac{\int_{-\infty}^{\infty} u^4 P(u)\, du}{\left[\int_{-\infty}^{\infty} u^2 P(u)\, du\right]^{2}} = \frac{\overline{u^4}}{(\overline{u^2})^2}, \qquad (3.15b)$$

where P(u) du is defined as the fraction of total time the fluctuation spends between u and u + du and,

$$\int_{-\infty}^{\infty} P(u)\, du = 1, \qquad (3.15c)$$

Townsend (1947) has found that the probability density distribution of all three fluctuating velocity components at an arbitrary point and at a given time of decay in the turbulence flow behind a square-mesh grid are approximately normally distributed. He found that the flatness factor, F_f, lies between 2.9 and 3.0 as compared with the value 3.0 appropriate to a normal distribution. The skewness factor, S_f, is found to be zero as the value for a normal distribution or any symmetrical distribution.

At last the force acting on the obstacles (for the boundary-layer flow) was determined by measuring the pressure distribution on the obstacle walls. The values of the drag coefficient, C_D, were obtained by integrating the areas under the curves of the static pressure coefficient C_P versus y/h, where y is the distance on the wall of the obstacle. The

values of C_D and C_P were calculated using the formulae

$$C_D = \int_0^{y/h} C_P \, d(y/h) \qquad (3.16a)$$

$$C_P = \frac{P - P_\infty}{\frac{1}{2} \rho U_\infty} \qquad (3.16b)$$

where P_∞ and U_∞ are the free stream static pressure and velocity respectively.

CHAPTER 4

WIND TUNNEL EXPERIMENTS

CHAPTER 4

WIND TUNNEL EXPERIMENTS

4. INTRODUCTION

An experimental study of the effect of a two-dimensional obstacle attached to a plane wall, on which a turbulent boundary-layer was developed, is considered in this chapter. Two types of geometry were used in these experiments. These two-dimensional obstacles were described in Chapter 3: one was a rectangular cross-section bar (ridge) and the other was a single-hump (hill). In the present study two different plane walls were used: one was a rough plane and the other was a smooth plane. The comparison of the results of these experiments are presented in due course.

The rough plate described in Chapter 3 was used in these experiments. The average height of the irregular rough plate, h_s, calculated from the statistical examination of the surface was 0.98 mm (see Appendix A). This average height is smaller than the height, h (= 20 mm), of the obstacles used in the rough plate experiments. The boundary-layer thickness, δ, above the obstacles (ridge or hill) was 40.5 mm.

For both the surfaces (rough and smooth), the ridge used was of the same width-to-height ratio (i.e., $b/h = 2.5$), and of the same height-to-boundary-layer thickness ratio (i.e., $h/\delta = 0.5$). The boundary-layer thickness above the obstacle (ridge), attached to the smooth plate, was 25 mm. For both of the surfaces, the position of the obstacle was 1350 mm from the leading edge of the plate. The length of all the obstacles in both cases was 1000 mm.

The condition of zero pressure gradient in the working section of the wind tunnel was checked before and after inserting the obstacle inside the working section. The free stream velocity in the working section was 21 m/s for both the experiments rough and smooth plates. The measurements

were carried out at different stations downstream of the obstacle, no measurements were made in the separation regions because of the difficulties of measuring the flow direction in such regions. The measurements were taken at x = reattachment, 50, 69, 86, 116, 139 and 185 cms. from the position of the obstacle.

4.2 STATIC PRESSURE DISTRIBUTIONS

The two-dimensional obstacle in these experiments can be considered as a bluff body immersed in a turbulent boundary-layer, such that an adverse pressure gradient will be produced upstream of the obstacle. The boundary-layer will be forced to separate from the plane boundary wall and will reattach on the front surface of the obstacle, thereby producing a separation bubble on the upstream side of the obstacle. The mean flow inside and outside the front separation bubble is quite steady (Good and Joubert (1968) and Sakamoto et al (1975)). Figures (4.1) and (4.2) show the static pressure distribution on the front and rear surfaces of the ridge and the hill attached to the rough plate. It can be seen that the point of the reattachment (the point of maximum pressure on the front surface) occurs at the range of $0.5 < y/h < 0.6$ in the case of the ridge. This value is different from that in the case of the hill which occurs at $y/h = 0.25$. This difference is due to the fact that in the case of the ridge, the front surface behaves as a normal plate attached to the rough surface creating a severe adverse pressure gradient (same as found by Good and Joubert (1968) who carried out an experiment on normal plates attached to a plane wall, or as found by Bradshaw and Galea (1967) on the upstream forward facing step), which is much more than the one created by a gradually increasing surface-height such as the hill used in the present investigation. Moreover, the length of the front separation bubble in the case of the ridge is bigger than that for the hill.

The flow will separate again at the upstream top edge of the obstacle, producing a free shear layer, reattached on the plane wall downstream of the obstacle. The static pressure distribution on the rear surface (base pressure) for the ridge and the hill are substantially constant as shown in Figs. (4.1) and (4.2).

The separation point in the case of the hill is not known and Fig. (4.2b) represents the static pressure distribution on the front and rear surfaces of the hill with respect to the non-dimensional streamwise direction, x/h. It can be predicted that the flow will separate near the top of the hill, at x/h = -0.3, which corresponds to y/h = 0.9. At this point the pressure decreased to the value of the base pressure on the downstream surface of the hill.

The static pressure distribution, on the front and rear surfaces for an obstacle (ridge), attached to the smooth plane are shown in Fig. (4.1). It can be seen that the point of the maximum pressure (reattachment on the front surface) occurs at $0.5 < y/h < 0.6$ as in the case of the ridge attached to the smooth plane. The values of the static pressure coefficient on the front surface are higher on the ridge attached to the smooth plane than that for the ridge attached to the rough plane. On the other side, the base pressure is lower in the former case than the latter. Although the ratio, h/δ, is the same for both cases, the velocity components close to the ridge on the rough plane are different than if the ridge is attached to the smooth plane by the value of the velocity shift Δu. In smooth surfaces no velocity shift, Δu , occurs and therefore, the ridge attached to the smooth boundary will obstruct higher velocity components compared to the rough wall boundary. It is expected then that the drag force on the ridge attached to the smooth plate is higher than that on the ridge attached to the rough plate. .The drag force on the obstacle was calculated by integrating the pressure difference profile, from which the values of the drag coefficient C_D, were obtained. The drag coefficient, C_D,

for the ridge attached to the rough plate was 0.48 and for the ridge attached to the smooth plate was 0.629. For the hill attached to the rough plate, C_D was 0.41 which is less than that for the ridge attached to the same plate. This is possible because the adverse pressure gradient created upstream of the ridge is more than the one created upstream of the hill. Moreover, the flow separates at the top edge of the ridge (i.e., y/h = 1) whereas in the case of the hill, the flow separates at y/h = 0.9.

These values of the drag coefficients were corrected for the blockage effects, using Ranga Raju et al (1972) formula,

$$C_{D_c} = C_D \left(1 - \frac{h}{D_1}\right)^{2.85} \qquad (4.1)$$

where, D_1, is the height of the wind tunnel working section and, h, is the obstacle height.

Figure (4.3) shows the static pressure distribution on the upper surfaces of the ridge attached to the rough and smooth plates. The pressure distribution on the upper surface has approximately similar shapes for the ridge on the rough and smooth plate.

A static tube was used to measure the static pressure distributions downstream of the ridge and the hill. In fact these readings are in doubt because the actual direction of the flow is not known in the separation bubbles, but it may give some indication about the behaviour of the static pressure in such a region. However, these measurements can be used to predict the point of reattachment of the flow on the plane wall downstream of the obstacle (ridge or hill). Figures (4.4a), (4.4b) and (4.4c) show the static pressure distribution in the separation bubbles behind the ridge and the hill on the rough plate and for the ridge on the smooth plate respectively. The static pressure distributions are shown in the form of the static pressure coefficient at different stations

against the non-dimensional distance y/h. The edge of the shear layer is marked on each curve, it can be seen that the pressure field caused by the obstacle does not end at the edge of the shear layer.

Near reattachment, the static pressure is recovered and, thereby, is returned to a constant value within the boundary-layer thickness. The value of the static pressure downstream of the obstacle, in the separation bubble, is dependent upon the geometry of the obstacle. This can be seen from the measurements downstream of the ridge which show that the ridge causes a severe effect in the static pressure more than in the case of the hill. The distribution of the static pressure downstream of the ridge, on the smooth plate, does not differ too much from that on the rough plate; but it returns more readily to the free stream value.

The reattachment points predicted by using the static pressure measurements, are 25.0 cms. and 18 cms. downstream of the ridge and the hill on the rough plate respectively. For the ridge on the smooth plate the point of reattachment is 13.5 cms. downstream of the ridge.

4.3 BOUNDARY-LAYER MEAN FLOW CHARACTERISTICS

4.3.1 Mean Velocity Distributions

Mean velocity profiles at different stations downstream of the obstacles (ridge or hill) were measured to study the local boundary-layer characteristics after the shear layer was disturbed by the obstacles. The measurements of the mean velocity in all the experiments, for the rough and the smooth plates, were started after the points of the reattachment. The reason for that is the difficulty of measuring the flow direction in the region of the separated flow (inside the bubble). However, the main aim of the present investigation is the study of the recovery of the turbulent shear layer downstream of the obstacle.

The characteristics of the turbulent boundary-layer on the rough and smooth plates were determined before inserting the obstacle inside the working section of the wind tunnel. Figures (4.5a) and (4.5b) represent the mean velocity distribution on both of the rough and smooth plates without the obstacle, the figures include the mean velocity profile at the position of the obstacle, x = 135 cms. from the leading edge of the plates.

The mean velocity profiles downstream of the ridge and the hill attached to the rough plate are shown in Figs. (4.6a) and (4.6b). The first three profiles measured at the top of the ridge and the hill, x = 7 cms. and at x = 9 cms. are shown without the negative velocity values inside the separated flow (bubble), where x is the distance downstream of the ridge and the hill. These profiles give an idea about the size of the re-circulated flow region downstream of the obstacle. The points of the reattachment could be determined by moving the pitot tube very near to the plane wall, downstream of the ridge or the hill, inside the recirculated flow reg ion. The values of x_r (distance from the obstacle to the reattachment) were found to be equal to 22.5 (11.25) cms. and 18 (9) cms. in the case of the ridge and the hill, respectively. From this result, it can be said that the length of the separated region is affected by the shape of the obstacle. Also it is expected then that the recovery of the boundary-layer does depend appreciably on obstacle shape. It is found that the reattachment downstream of the ridge attached to the smooth plate to occur at x_r = 11.5 (9.6) cms.

The measurements in the wake regions downstream of the reattachment indicate that the turbulent boundary-layer exhibits x - wise stability and the violent distortion in the velocity profiles disappear as the boundary-layer proceeds downstream of the obstacle. It can be seen that the inner portion of the boundary-layer returns much more quickly to its

natural shape; this recovery depends on the geometry of the obstacle (ridge or hill). It is faster for the hill than for the ridge. The mean velocity profiles downstream of the ridge attached to the smooth plate are shown in Fig. (4.6c). It can be seen that the inner portion of the boundary-layer returns more speedily to its natural shape than in the case of the ridge attached to the rough plate. It can be concluded that the recovery of the inner portion of the boundary-layer depends on the geometry of the obstacle and the surface roughness which the obstacle is attached.

The logarithmic profiles for the mean velocity distributions are shown in Figs. (4.7a) to (4.7c). The redevelopment of the boundary-layer downstream of the reattachment is clearly evident. The present results for the smooth plate, approach closer to the Coles (1956) formula.

$$\frac{U}{u_o} = 5.75 \log \left(\frac{u_o y}{\nu}\right) + 5.1 \qquad (4.2)$$

It is important to know that the value of traversing distance, y, for the rough plate is equal to the displacement distance of the traverse gear plus the virtual origin of the boundary-layer, ε, determined using the Parry and Joubert method (1963).

For the rough plate, it is known that the value of the roughness function $\frac{\Delta u}{u_o}$ is constant for a certain Reynold's number in the working section of the wind tunnel. This value was checked downstream of the reattachment for the ridge and the hill attached to the rough plate. Figure (4.8) shows the value of $\frac{\Delta u}{u_o}$ against x-wise Reynold's number ($x \frac{u_o}{\nu}$), the values of $(\frac{h_s u_o}{\nu})$ are included in some stations. It is clear that the value of $\frac{\Delta u}{u_o}$ is high near the reattachment, where the value of u_o is very low. The value of $\frac{\Delta u}{u_o}$ reduces downstream of the reattachment to a

minimum value for both ridge and hill experiments. Further downstream of the reattachment the roughness function $\frac{\Delta u}{u_o}$ increases towards the value of $\frac{\Delta u}{u_o}$ for the rough plate without the obstacle. The rate of increase of $\frac{\Delta u}{u_o}$ in the case of the hill is greater than for the ridge, which indicates that downstream of the hill, the wall friction velocity, u_o, returns to its value for the rough plate without the obstacle faster than for the ridge attached to the same plate.

4.3.2 Wall Friction Coefficient

The wall friction coefficient, determined from the local mean velocity profiles is shown in Figs. (4.9a) and (4.9b). The values of the friction coefficient for the rough and smooth plates without the obstacle are also shown in the above figures. Because of the difficulties of measuring the local velocity profile in the separated flow downstream of the obstacles, the values of the friction coefficient was determined downstream of the reattachment. Figure (4.9a) represents the friction coefficient downstream of the ridge and the hill attached to the rough plate. It is clear that the values of the friction coefficient, downstream of the hill are returned more rapidly, than in the case of the ridge, to the ordinary turbulent boundary-layer value on the rough plate. Figure (4.9b) shows the same results for the friction coefficient values downstream of the ridge on the rough and smooth plate. It can be seen that for the rough plate with the ridge attached to it, the flow is not fully recovered at the end of the plate, but for the smooth plate the flow has reached the recovery condition.

The points of the reattachment downstream of the obstacles, on the rough and the smooth plates, can be predicted by extrapolating the wall friction curves. The values of x_r (distance from the obstacle to the

reattachment) determined by this method were 20 cms. and 16 cms. for the ridge and the hill on the rough plate respectively. For the ridge on the smooth plate the value of x_r was 10.8 cms. from the ridge.

4.3.3 Integral Quantities

The boundary-layer integral quantities for the rough and smooth plates without the obstacle (ridge or hill) are shown in Fig. (4.10a). The boundary-layer thicknesses, before and after the flow was disturbed by the obstacles, are also included in the Figure. It can be seen that the edge of the shear layer (boundary-layer thickness) is displaced outward. Therefore, the boundary-layer developed downstream of the obstacle has a thickness δ, greater than that developed on the rough or smooth plates without the obstacles.

Figure (4.10b) shows the boundary-layer integral quantities downstream of the obstacle (ridge or hill) attached to the rough plate. Since the displacement thickness is that distance by which the external potential field of flow is displaced outwards as consequence of decrease in velocity in the boundary-layer, it is expected then that the value of the displacement thickness, δ^*, just behind the reattachment is very large. On the other hand, the momentum thickness, θ does not vary much. Thus the shape parameter, H, has a very large value behind the reattachment. This value of H, decreased to a constant value of 1.41, which is different than the constant value of H, for the rough plate without the obstacle (H = 1.55). This is because the boundary-layer thickness δ, is changed, also the integral values of the displacement and momentum thicknesses δ^* and θ are changed. The same results were shown for the case of the smooth plate, and Fig. (4.10c) shows the shape parameter and the boundary-layer displacement and momentum thicknesses. Also included are results from other

investigations for different but related flow configurations (Muller et al (1964) results for flow downstream a step; Ota and Itosaka (1976) data for flow over a flat plate with finite thickness and blunt leading edge). The constant value of H for the smooth plate downstream of the ridge was 1.29, which is lower than the value of H for the flow on the smooth plate without the obstacle (H = 1.44), for the same reasons as above.

The most useful single parameter for measuring the departure of a turbulent boundary-layer from equilibrium is Clauser parameter G. The value of G for an equilibrium boundary-layer with constant pressure gradient is 6.8. The value of G was calculated using the equation

$$G = (2/c_f)^{1/2}(H - 1)/H \qquad (4.3)$$

Figure (4.11) shows the variation of G with downstream distance x/h. It is very large just behind the reattachment and decreases sharply downstream, becoming nearly constant at a distance of about 70 obstacle heights for the rough plate and about 40 obstacle heights for the smooth plate. The value of 6.9 obtained at x/h = 80 for the smooth plate is almost equal to the accepted value of 6.8 for the equilibrium fully developed constant pressure boundary-layer. For the rough plate the value of 5.5 and 5.9 obtained at x/h = 100, for the hill and the ridge respectively, are smaller than the value of 6.8. It may be concluded from these results that the recovery of the boundary-layer occurs very slowly for the rough surface and a sufficiently long test section is needed in order to observe the increase of G at the long distance, downstream of the reattachment. Further it seems plausible that G = 5.5 and 5.9, for the hill and ridge, respectively, represent the corresponding states of equilibrium being different from that for a ridge on a smooth plate.

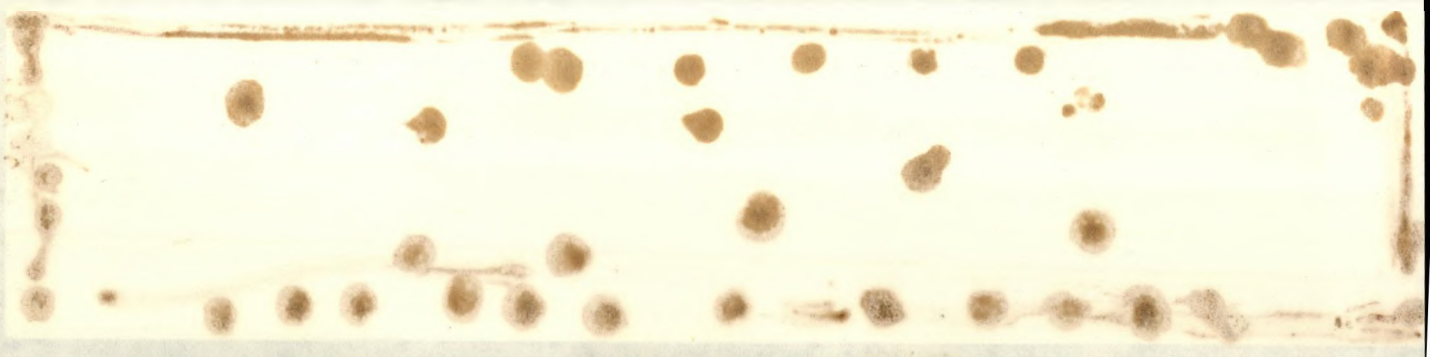

4.4 BOUNDARY-LAYER TURBULENCE MEASUREMENTS

4.4.1 Normal Stresses

Figures (4.12a) and (4.12b) represent the distributions of the longitudinal turbulent normal stress, $\sqrt{\overline{u^2}}/u_o$, against the non-dimensional distance, y/h, downstream of the ridge and the hill attached to the rough plate. Near the reattachment the values of, $\sqrt{\overline{u^2}}/u_o$, are very high and the maximum value occurs at non-dimensional distance y/h = 1.5 for both the ridge and the hill. The maximum value is decreased downstream of the reattachment, but the rate of changing of $\sqrt{\overline{u^2}}/u_o$, in the streamwise direction is very slow. This behaviour is the same for the transverse turbulent normal stresses, $\sqrt{\overline{v^2}}/u_o$, which can be shown in Figs. (4.13a) and (4.13b). Comparison of the results of the ridge on the rough plate with those on the smooth plate are shown in Figs. (4.14a) to (4.15b) for the values of, $\sqrt{\overline{u^2}}/u_o$, and $\sqrt{\overline{v^2}}/u_o$, respectively. It is found that the maximum values of $\sqrt{\overline{u^2}}/u_o$, and $\sqrt{\overline{v^2}}/u_o$, for the smooth plate to occur at y/h = 1.5, which is the same as the value of y/h in the case of the rough plate.

4.4.2 Shear Stresses

Turbulent shear stress distribution at different stations downstream of the reattachment is shown in Figs. (4.16a) to (4.16c). In these figures a comparison between the results of the ridge and the hill attached to the rough plate are shown. Near the reattachment the shear stresses rise from a very small value, at the surface, to a maximum value near to the top of the obstacle. This maximum value of the shear stress takes place at y/h = 1.5 for the ridge (attached to the rough or smooth plate), and at y/h = 1.4 for the hill. Downstream of the reattachment a new inner layer will grow up until a fully developed turbulent boundary-layer having a maximum shear stress at the surface is established

at some distance from the reattachment. It can be seen that the values of the turbulent shear stress downstream of the hill are much less than that downstream of the ridge (at x/h = 25, 43, 58 and 69.5). At the last station, x/h = 92.5; there is still some difference in the values of the turbulent shear stress. Therefore, to reach a complete recovery for the turbulent shear stress, more distance is needed downstream of the ridge. It is clear that the geometry of the obstacle affects the turbulent shear stress distribution downstream of it. Near the wall and at the edge of the boundary-layer thickness the values of the turbulent shear stress are equal for both the ridge and the hill. In the middle portion of the boundary-layer, where the shear layer is spread at the top of the obstacle, the values of the turbulent shear stress are different for different geometry of the obstacle.

A comparison between the results of the turbulent shear stress distributions for the ridges attached to the rough and the smooth plates is shown in Figs. (4.17a) to (4.17c). The behaviour of the shear stress distribution downstream of the ridge attached to the smooth plate is the same as that downstream of the ridge attached to the rough plate, near the reattachment. The maximum value of the turbulent shear stress for both cases, occurs at y/h = 1.5. It can be seen that there is a change in the values of the shear stress between the stations x = 139 cms. and x = 185 cms. This change is very small for the smooth plate results. Therefore, it can be concluded that, for the ridge attached to the smooth surface, the flow recovery occurs in a distance less than that for the ridge attached to the rough plate.

4.4.3 Distribution Properties (skewness and flatness factors)

To study the probability density distribution of the longitudinal velocity fluctuation, a series of flatness and skewness factor measurement downstream of the reattachment were made. The measurements were carried out only for a comparison between the effects of the two-dimensional obstacle (ridge) attached to a different surface - rough or smooth. For the isotropic turbulence, the probability density distribution is a Gaussian error curve. For turbulent shear flow - generally when the mean velocity is not uniform but is a function of the space coordinates - the distribution will be more or less skew. For a normal distribtuion the flatness and skewness factors are equal to 3 and 0 respectively (Townsend (1947)).

Figure (4.18) shows the skewness factor distribution downstream of the ridge. In the region of the recirculating flow (separated bubble), the skewness factor is positive near the wall and changes to a negative value away from the wall. However, these measurements are in doubt because of the reverse flow and the unknown direction of the velocity. Downstream of the reattachment, the distribution of the skewness factors across the boundary-layer thickness is not changing much for both the rough and smooth plates. In the non-intermittent region - near the wall - the distributions are very nearly Gaussian. Near the edge of the boundary-layer the probability density is strongly negatively skewed because of the lower velocity fluctuations within the turbulent regions.

The distributionsof the flatness factor are shown in Fig. (4.19). It can be seen that the flatness factor has a constant value for all the stations, downstream of the reattachment, up to y/h = 3. The values obtained are in the range of 2 - 2.5. These values are lower than the corresponding Gaussian value of 3.0. The flatness factor is increased

in the outer portion of the boundary-layer, where the intermittency value is low,"a small value of the intermittency factor, defined as the fraction of time that turbulence occurs, yields a large value of the flatness factor" Ueda and Hinze (1975).

4.4.4 Spectral Properties

A significant advance in dealing with the energy spectrum was made in the domain of homogeneous and isotropic turbulence (Kolmogroff (1941)). The basic concept underlying this advance is that energy enters the spectrum through the large eddies and is then transferred through the spectrum to the smaller eddies where it is finally dissipated. If the lower wave numbers are excluded there exists a range in which the eddies are in a state of equilibrium, governed by the rate at which they transfer and dissipate energy. When the Reynolds number is high enough, inertial forces will predominate in the lower wave numbers of this equilibrium range, and a relatively pure transfer region will exist. By dimensional reasoning Kolmogroff (1941) found that the spectrum will vary as $K^{-5/3}$ in this range. Heisenberg (1948) extended this concept by assuming that the transfer of energy at wave number K was caused by a turbulence friction produced by eddies with wave number greater than K. He found that in the equilibrium range the spectrum will vary as $K^{-5/3}$ for low wave number and for the high wave number end where viscous forces predominate, as K^{-7}. In the presence of shear flow the situation is complicated by such factors as production, diffusions, convection and the absence of isotropy and homogeneity. Any conclusions as to the effects of the diffusion and convection are difficult to draw (Klebanoff (1954)). It may be assumed that such effects are confined to the very low wave numbers which lie outside the equilibrium range. In addition, the convection may be considered negligible across most of the layer. An

attempt to assess the influence of the production term in the equilibrium range of the spectrum was made by Tchen (1953). By considering the influence of the mean velocity gradient the conclusion is reached that a range of K^{-1} will exist in the wave-number region where $K^{-5/3}$ normally exists when there is no gradient.

The results of the spectrum function at different values of y/δ are shown in figures (4.20a) to (4.21e). It can be seen that the -7 law is approached asymptotically in all distances except at y/δ = 1.27 which exhibits a severe disturbance near the ridge. The effect reduces gradually downstream of the ridge. The spectrum curves for the points not too close to the wall even contain a rather wide range where -5/3 law is closely followed. The curves for the points very close to the wall contains a region where the -1 law is closely followed.

The measurements of the correlation coefficient R_T are shown in Figs. (4.22a) to (4.22d). These measurements are used to calculate the macro-scale of turbulence downstream of the ridge, on the rough and smooth plates. The micro-scale of turbulence is related to the area under the second-moment curve (Taylor (1938)). Figures(4.23a) to (4.23d) show the values of the second-moments of the frequency spectra plotted in the form of a product of the wave-number and the first-moment of the spectrum function, against the wave-number. The results are obtained for different values of y/δ downstream of the ridge attached to the rough or smooth plates.

4.5 RESULTANT BOUNDARY-LAYER TURBULENCE PROPERTIES

4.5.1 Length Scales

Measurements of the macro-scale of turbulence - scale of the largest eddies in the flow - are shown in Fig. (4.24). The measurements were carried out in the streamwise direction and at different values of y/δ.

Near the reattachment and at y/δ = .06, the values of the macro-scale, L, are very small. These values are increased in the case of the smooth plate in streamwise direction. For the rough plate the values of the micro-scale, L_T at y/δ = .06, are almost constant in the streamwise direction. The macro-scale measurements for other ratios of y/δ behave similarly for both the rough and the smooth plates, where there are small values near the reattachment which increase downstream to almost constant values. These constant values are 30 mm. for the rough plate and 20 mm. for the smooth plate.

The measurements of the micro-scale of turbulence - the size of the smallest eddies in the flow - are shown in Fig. (4.25). Near the region of the reattachment the values of the micro-scale of turbulence λ, are small. These values are increased in the streamwise direction to the value of 2-3 mm. for both the rough and smooth plates. At y/δ = .06, near the wall, for the rough plate the values of λ are almost constant and equal to about 1 mm. The high fluctuating values of λ, at y/δ = 1.27 for both the rough and the smooth plates are expected, because the measurements are in the intermittent region. In this region the boundary-layer travels downstream with an outline constantly changing in an irregular manner, and the intermittency is characterized by a large-scale diffusion process, carrying with it small- scale turbulent motions.

4.5.2 Turbulent Eddy Viscosity

Measured Reynold's shear stress $-\overline{uv}$, together with experimental mean velocity gradient $\frac{\partial U}{\partial y}$ were used to obtain the eddy viscosity ν_t and the mixing length ℓ_m. Figures (4.26a) and (4.26b) represent the non-dimensional turbulent eddy viscosity (ν_t/ν), versus y/δ downstream of the obstacle (ridge or hill) attached to the rough plate. For equilibrium boundary-layer Clauser assumed that the eddy viscosity in the inner portion of the

boundary-layer can be determined by the formula,

$$\nu_{t_i} = \kappa\, y\, u_o \qquad (4.1)$$

This assumption for the eddy viscosity is also shown in the above figures. It can be seen that near the reattachment the experimental values of the eddy viscosity are higher than that calculated using the above equation. This is due to the fact that Clauser assumed that the mixing length hypothesis is valid, but in this case the size of the eddies is not proportional to the distance from the wall, and the value of $\tau/(\partial U/\partial y)$ is different from that of $\tau_w/(\partial U/\partial y)$ which Clauser used to get the straight line. Downstream of the reattachment, the inner region is changing toward the equilibrium condition, where the experimental eddy viscosity is equal to the value determined using Eqn. (4.1). In this region a fully developed turbulent boundary-layer having a maximum shear stress at the surface is established. This region starts at x = 86 cms. downstream of the hill and at x = 139 cms. downstream of ridge.

The turbulent eddy viscosity for the ridge attached to the rough and smooth plates is shown in Figs. (4.27a) and (4.27b). The behaviour of the inner layer of the boundary-layer for the smooth plate is the same as on the rough plate, except that on the smooth plate the inner layer recovery is faster, at 116 cms. This is due to the fact that the recovery of the mean velocity and shear stress for the inner layer on on the smooth plate is faster than that on the rough plate. Since a new inner layer will grow up downstream of the reattachment, the surface roughness will affect this layer when its thickness is at the same order as the average height of the surface roughness.

Study of the outer region of the flow carried out by calculating the eddy viscosity proportionality constant α- from Clauser's assumption

for the turbulent eddy viscosity in the outer layer of the boundary-layer,

$$\nu_{t_o} = \alpha \, U_\infty \, \delta^* \qquad (4.2)$$

Figure (4.28) represent the values α at different distance x, non-dimensionalized by the height of the obstacle. The value α (=.018) calculated by Clauser for an equilibrium flow is also shown in the Fig.(4.28). It can be seen that the outer flow region in the smooth plate, is more disturbed and the value of α downstream of the ridge is higher than the equilibrium value .018. The behaviour of α downstream of the ridge and the hill on the rough plate is the same, except that in the case of the hill, the value of α decreased to the equilibrium value faster than in the case of the ridge.

4.5.3 Mixing Length

The measurements of the mixing length downstream of the reattachment are shown in Figs. (4.29a) and (4.29b). The measurements are compared with Prandtl's hypothesis ($\ell_m = 0.4 l y$), which calculate the mixing length in the constant shear stress region. The figures show that the distribution of the mixing length downstream of the ridge or the hill is the same for all distances. Near the reattachment, the mixing length is completely different from the value of 0.4ly. This indicates that the mixing length is not proportional to the distance from the wall in such regions. The mixing length distribution for the ridge on the rough and smooth plates is shown in Figs. (4.30a) and (4.30b). The behaviour of the mixing length is the same for the smooth plate.

4.6 SUMMARY AND CONCLUSION

The effect of the surface roughness on the recovery of the flow downstream of a two-dimensional obstacle was studied. Two types of geometry were used for the obstacle; one being a bar of rectangular corss-section (ridge) and the other a single-hump (hill). The experiments were once again repeated on a smooth surface. The characteristics of the flow on both the rough and smooth plates were determined before and after the obstacle was introduced onto the plate concerned. All the experiments were carried out for a zero external pressure gradient with a free stream velocity of 21 m/s.

The adverse pressure gradient created upstream of the ridge is greater than that created upstream of the hill. Therefore the size of the front separation region upstream of the ridge is greater than that upstream of the hill. It may be concluded that the pressure distribution on the obstacle and the front separation region depends on the geometry of the obstacle itself. The drag force on the ridge attached to the rough surface is less than that on the ridge attached to the smooth surface. This is due to the velocity shift, $\Delta u/u_o$, caused by the plate surface roughness.

Both the geometry of the obstacle and the surface-roughness affect the recovery of the inner portion of the turbulent boundary-layer. For different geometry of the obstacle (ridge or hill) attached to the same rough surface, the inner layer recovers at $x = 86$ cms. downstream of the hill while the ridge recovers at $x = 139$ cms. But with the same ridge attached to the smooth surface, the recovery of the inner layer occurs at $x = 86$ cms.

The coefficient of friction, c_f, assumes an almost zero value near the reattachment but at a far downstream region (i.e. downstream of the

obstacle) it catches up the undisturbed value of the flow without the obstacle. For example, in the case of the hill, the value of c_f reaches the undisturbed flow value at nearly x = 186 cms. but in the case of the ridge an additional distance downstream of the ridge is needed for c_f to reach the undisturbed flow value.

The presence of the obstacle increases the absolute boundary-layer thickness by about 30% and 50% for the rough and smooth plates respectively. This increase in the boundary-layer thickness affects the values of the boundary-layer integral thicknesses δ^* and θ downstream of the obstacle.

The variations of the turbulence quantities $\sqrt{\frac{\overline{u^2}}{u_o}}$, $\sqrt{\frac{\overline{v^2}}{u_o}}$ and $\frac{\overline{uv}}{u_o^2}$ (Figs. (4.12) to (4.17)) show that these quantities require a greater distance downstream of the obstacle than the mean velocity to recover. In the near wake region the shear stress distribution has a maximum value at y/h = 1.5 for all the obstacles on the rough or smooth plate. This maximum value depends on the shape of the obstacle itself. At x = 50 cms. downstream of the ridge attached to the rough plate, the maximum value of the shear stress is about 70% higher than that for the hill at the same downstream position. In the far wake region the shear stress distribution downstream of the hill reaches the full recovery at about x = 139 cms., while the shear stress downstream of the ridge needs a greater distance to reach the same. For the smooth plate the recovery of the shear stress occurs at distance x = 139 cms. downstream of the ridge. It can be concluded that the recovery of the turbulent shear stress downstream of a two-dimensional obstacle attached to a plane wall depends on the geometry of the obstacle and the surface roughness of the plane wall.

Downstream of the reattachment the distributions of the skewness factor in the non-intermittent region (near the wall) are nearly Gaussian for both the rough and smooth plates. Because of the lower fluctuating

velocities in the outer region of the boundary-layer the probability density distribution is negatively skewed. The distribution of the flatness factor is found to vary between 2 and 2.5 which is less than the Gaussian value of 3.0.

The macro- and micro-scales of turbulence show that the rough surface has a smaller streamwise integral length scale in the inner layer, than the smooth wall counterpart. In the outer region these values lie between 5 - 30 mm. and between 1 - 3 mm. respectively, for both the rough and smooth plates. This behaviour indicates that the outer layer of the flow is unaffected by the surface roughness of the plane wall.

CHAPTER 5

PIPE FLOW EXPERIMENTS

CHAPTER 5

PIPE FLOW EXPERIMENTS

5.1 INTRODUCTION

In Chapter 5 the effect of a two-dimensional obstacle attached to a rough and smooth boundary was discussed. In this Chapter the experiments were repeated in a fully developed turbulent flow in a rough and smooth pipe. The rough pipe has the same background roughness as on the rough plate in the wind tunnel experiment. The two-dimensional obstacles taking the form of suitably scaled internal (rectangular in cross-section) rings, are described in Chapter 4.

The pipe flow average velocity was chosen such that the flow dynamic similarity in the inner region of the pipe flow and that on the rough plate is well preserved. This requires the roughness Reynold's number ($u_o h_s/\nu$) to be identical in both cases.

For a fully rough turbulent pipe flow the friction factor f as given by Nikuradse (1933) is

$$f = (1.74 + 2 \log \frac{R}{h_s})^{-2} \qquad (5.1)$$

where $f = 8 \frac{\tau_o}{\rho V_p^2}$, R = pipe radius, τ_o = wall shear stress, V_p = pipe average velocity, h_s = equivalent sand grain roughness, and for a fully rough flat plate the Prandtl -Schlichting (1934) relation for the local coefficient of friction c_f is

$$c_f = (2.87 + 1.58 \log \frac{X}{h_s})^{-2.5} \qquad (5.2)$$

Preserving the dynamic similarity

$$(\frac{u_o h_s}{\nu})_{\text{pipe}} = (\frac{u_o h_s}{\nu})_{\text{plate}} \qquad (5.3)$$

The two relationships result in the following ratio of the pipe average velocity to the free stream velocity in the wind tunnel, (Preston and Lewkowicz (1973)):

$$\frac{V_p}{U_\infty} = \frac{(h_s)pL}{(h_s)pi} \quad \frac{\nu pL}{\nu pi} \quad \frac{3.48 + 4 \log_{10}[\frac{R}{h_s}] pi}{[2.87 + 1.58 \log_{10}(\frac{X}{h_s})pL]^{1.25}} \qquad (5.4)$$

where X is the position of the obstacle on the rough plate from the leading edge, U_∞ the free stream velocity of the boundary-layer and V the average velocity in the pipe flow.

The pipe, rough and smooth and the two-dimensional obstacle (ring) used in these experiments were described in Chapter 3. The two-dimensional obstacle that was used in the pipe will be referred to as 'the ring' during this Chapter.

The measurements were carried out at the exit section of the pipe, and the ring was placed at different positions, to monitor the flow properties as they recovered downstream of the ring. Since the ring occupies a considerable amount of area of the pipe section, the centre line velocity of the pipe changed with the ring inside the pipe. The velocity on the upstream side of the ring was less than that for the pipe without the ring. So the upstream velocity was adjusted to the undisturbed velocity value (velocity of the pipe without the ring), to make sure of the flow similarity before and after putting in the ring.

All the characteristics for the rough and smooth pipes were determined before the insertion of the ring in the pipes. For the flow recovery investigation, only one ring of rectangular cross-section was used in both the rough and smooth pipe. The same ratios of r/h and b/h (where h and b are the height and the width of the rectangular cross-section of the ring) were maintained for both pipes as well as the Reynold's number, $\frac{DV\rho}{\nu}$ (= 4.5×10^4) used was also the same for both pipes.

5.2 AVERAGE VELOCITY

The average velocity for both the rough and smooth pipes are shown in Fig. (5.1). This was calculated by integrating graphically the velocity profiles using Simpson's rule. The ratio of the average velocity to to the centre line velocity is about 0.76 for the rough pipe and 0.87 for the smooth pipe.

5.3 FRICTION FACTOR AND ROUGHNESS FUNCTION

Figure (5.2) shows the graph of Reynold's number R_e versus f, the friction factor for both the pipes. It is seen that the value of the friction factor for the rough pipe is constant and equal to 0.058 for $R_e > 2.4 \times 10^4$, which indicates that fully rough regime was attained. In this region Nikuradse's formula Eqn. (1.5) can be used to evaluate the value of the equivalent sand grain roughness h_s. The ratio of r/h_s is found to be 16. In the case ofasmooth pipe the friction factor is decreased with the increasing Reynold number.

The alternative roughness function, χ, defined by Nikuradse (1933), for the rough pipe is shown in Fig. (5.2). The method of determining the roughness function $\frac{\Delta u}{u_o}$ is shown in Fig. (5.3). The values obtained from this figure were used in Eqn. (3.5) to evaluate the value of χ . It is found that the value of χ is almost constant and equal to 7.5 in the range of Reynold's numbers that were used.

5.4 MEAN VELOCITY DISTRIBUTION

The mean velocity profiles downstream of the ring in the rough pipe for two-different Reynold's numbers based on the average velocity are shown in Figs. (5.4a) and (5.4b). The mean velocity profiles downstream of the ring, in the case of the smooth pipe are shown in Fig. (5.4c). The shape of the disturbed mean velocity profiles in the pipe flow is the same as

that downstream of the obstacle in the turbulent boundary-layer flow. Violent distortions in the velocity profiles are observed immediately after the ring, but they die out as the flow proceeds further downstream of the ring. It can be seen that the reattachment occurs at $9.9 < x/h < 11.9$ for the rough pipe and at $3.95 < x/h < 7.9$ for the smooth pipe.

The undisturbed mean velocity profile for the rough and smooth pipe is also included in the above figures. It can be seen that near the reattachment (at $x/h = 7.9$ and 11.9) the velocity is smaller than the undisturbed velocity in the pipe without the ring. Downstream of the position $x/h = 11.9$ the mean velocity increases to a value greater than the undisturbed velocity profile. This increase in the velocity produces a region of a negative wake effect downstream of the ring in both the rough and smooth pipe. This negative wake effect is explained by the existance of secondary flow in this region. In the boundary-layer flow the situation is different because of the increase in the thickness of the shear-layer downstream of the obstacle. The influence of the secondary flow in the mean velocity profile end at $x/h = 126$ for both the rough and smooth pipes. Downstream of position $x/h = 126$ the mean velocity profile returns to its undisturbed profile.

The logarithmic profiles of the mean velocity are shown in Figs. (5.5a) and (5.5b). For the rough pipe the virtual origin of the profile, ε, was determined by using Perry and Joubert (1963) method. It is clear from the figures that the presence of the ring has distorted the outer part of the velocity profile. The wake parameter is high nearer the ring, this is due to the fact that the flow just reattaches from the separation condition. Downstream of the reattachment the value of the wake parameter decreases and reaches a negative value. This behaviour of the wake parameter associates with the negative wake effect which is shown in the velocity

profiles (see Figs. (5.4a) to (5.4c). Downstream of the position x/h = 94.9 the wake parameter increases again to reach the value of the undisturbed flow. Figure (5.6) shows the above mentioned behaviour of the wake parameter.

As mentioned in section (5.1), the presence of the ring changes the centreline velocity and this change is abrupt just downstream of the ring. Further downstream, however, this change dies out and the centreline velocity becomes equal to the reference velocity upstream of the ring. Figure (5.7) shows the ratio of the centreline velocity downstream of the ring to that reference velocity upstream of the ring, $\frac{U}{U_{ref}}$, against the non-dimensional distance, x/h. It can be seen that the maximum value of the velocity-ratio appears near the ring, and this reduces to a minimum value, below the value of 1.0, at a distance of about x/h = 50. Further downstream of x/h = 50, the velocity ratio increases to reach the value of 1.0, at this point the centre line velocity is equal to the centre line velocity upstream of the ring. It can be seen that for the same Reynold's number of 4.6×10^4, the centreline velocity for the smooth pipe recovers earlier than in the case of the rough pipe.

5.5 WALL FRICTION COEFFICIENT

The wall friction coefficient, c_f, calculated from the local mean velocity profiles are shown in Fig. (5.8) for the rough and smooth pipes. The wall friction coefficient has a very low value near the reattachment and attains a maximum value in the vicinity of the minimum velocity ratio as shown in Fig. (5.7). The wall friction coefficient returns to a constant value at the same x/h for the rough and smooth pipes. The point of the reattachment downstream of the ring can be determined from the friction coefficient distribution curve, by ascerting the value of x/h where c_f becomes zero. This can be accomplished by extending the curve of c_f versus

x/h. The values of x/h = 11 and 6 were determined to be the reattachment points for the rough and smooth pipe respectively.

5.6 TURBULENCE MEASUREMENTS

5.6.1 Turbulent Normal Stresses

The measurements of the turbulence quantities were carried out for the undisturbed rough and smooth pipes flow, and the results were compared with those of some previous authors. Figure (5.9) shows the comparison between present measurements in the rough pipe and those of Townes et al (1972) and El-Samanoudy (1974). The smooth pipe measurements were compared with the measurements of Laufer (1955). There is a good agreement between all the measurements.

Then the turbulence quantities were measured in the flow recovery after the ring was placed in the pipes. The distributions of longitudinal, radial and peripheral turbulent normal stresses are shown in Figs. (5.10a) to (5.12b). The measurements were carried out at different stations downstream of the ring and at the same x/h ratio for both the rough and smooth pipes. Near the reattachment the values of $\sqrt{\overline{u^2}}/u_o$ and $\sqrt{\overline{v^2}}/u_o$ have maximum values at y/R = 0.4, which is corresponding to y/h = 1.5 for the rough and smooth pipe. This value of y/h is the same as in the turbulent boundary-layer discussed in Chapter 4. Between x/h = 11.9, and x/h = 63.3, the values of the normal stresses are different from one station to another. Beyond x/h = 63.3, the values of $\sqrt{\overline{u^2}}/u_o$, $\sqrt{\overline{v^2}}/u_o$ are almost the same for all downstream stations. Comparison of the results with that for undisturbed pipe flow, the recovery of the normal stresses can be detected at $94.9 < x/h < 126.6$

5.6.2 Turbulent Shear Stress

The turbulent shear stress distribution downstream of the ring for both the rough and smooth pipes are shown in Figs. (5.13a) and (5.13b). The results are shown with respect to the linear shear stress distribution:

$$\tau = \tau_o (1 - y/R) \qquad (5.5)$$

Just downstream of the ring the flow behaves like a free jet. The turbulent shear stress $\overline{uv}/u_o^2$, has a maximum value near the separated stream line which isolates the jet flow and the recirculating flow region. This maximum value decays downstream of the reattachment and the flow reaches the equilibrium condition of Eqn. (5.5). The maximum values of the shear stress takes place at y/R = 0.4 which corresponds to y/h = 1.5. Downstream of the position x/h = 47.4 the distribution of the shear stress is lower than the linear distribution of Eqn. (5.5), where the region of the negative wake effect appears in the mean velocity distribution. Moreover the value of the wall shear stress reaches the maximum (c_f is maximum). Downstream of the position x/h = 47.4 the shear stress starts increasing to reach a fully developed pipe flow distribution at x/h = 166.1.

5.6.3 Distribution Properties (skewness and flatness factors)

The probability density distribution of the longitudinal velocity fluctuation can be studied by knowing the flatness and skewness factor. A series of measurements of these two factors downstream of the reattachment are shown in Figs. (5.14) and (5.15) for the rough and smooth pipes. It is known that for the isotropic turbulence the probability density distribution is a Gaussian error curve, and for turbulent shear flow (where velocity gradient exist) the distribution will skew from Gaussian distribution. The measurements of the skewness factor are shown in Fig. (5.14). It can be seen that there is no substantial difference between the values of the skewness factor for the rough and smooth pipes. At all values of x/h, except near the reattachment (x/h = 11.9) the skewness factor has zero value near the wall and changes to a negative value as the centre of the line of the pipe is approached. At x/h = 11.9, the skewness factor is positive near the wall; this is due to the presence of high values of the

longitudinal turbulence intensity.

Figure (5.15) shows the values of the flatness factor at different stations downstream of the reattachment. The values of the flatness factor for both the pipes do not differ too much from the Gaussian value of 3.0. The present values lie between 2.5 and 3.0 for the rough and smooth pipes.

5.6.4 Spectral Properties

The frequency spectra of the longitudinal fluctuating velocity $\overline{u^2}$ are shown in Figs. (5.16a) to (5.17e). The results were obtained at the relative distance y/R = 0.02, 0.35, 0.68 and 1.0 from the pipe wall. It can be seen that the frequency spectra near the reattachment (x/h = 11.9) follows the -5/3 law, where the energy is transferred from large to small eddies without being influenced significantly by either the production or dissipation mechanism. At the point y/R = .02 (inner region of the flow) the frequency spectra follows the -7 law at high wave-numbers (small wave lengths), where the energy received from lower wave-numbers (large wave lengths) is dissipated by the action of molecular viscosity. Downstream of the reattachment the three ranges of the energy (production-intermediate subrange-dissipation) are clearly defined at all stations. In the rough pipe the range of -7 law is approached asymptotically in all stations for a wider range of wave-numbers than in the smooth pipe. The general figure of the frequency spectra does not differ from that for the rough and smooth pipes without the ring.

The second moments of the frequency spectra are shown in Figs. (5.18a) to (5.18e) for the rough and smooth pipes. The results are plotted in the form of a product of the wave-number and the first moment of the spectrum function against the wave-numbers. These results are used to calculate the micro-scale of turbulence, which is related to the area

under the second-moment curve (Eqn.(3.14b)). Near the reattachment for both rough and smooth pipes the results show a poor collapse at y/R = 0.35, 0.68 and 1.0. This indicates that the micro-scale is affected by the high turbulence and the large eddies of turbulence due to the flow separation. The longitudinal spatial correlation coefficient calculated using Eqn. (3.13b) are shown in Figs. (5.19a) to (5.19e).

5.7 RESULTANT PIPE FLOW TURBULENCE PROPERTIES

5.7. Length Scales (Micro- and Macro-Scale of Turbulence)

Figure (5.20a) shows the values of the micro-scale of turbulence downstream of the reattachment. The results were obtained at relative distance y/R = .02, 0.35, 0.68 and 1.0 from the pipe wall. The values of the micro-scale of turbulence at the same relative distances, for the rough and smooth pipes without the ring, are also shown in the above figure. From these results it can be seen that at y/R = .02 (inner region) the small eddies have a minimum value near the reattachment and reaches to maximum value at x/h = 40. Downstream of position x/h = 40 the micro-scale of turbulence reduce to reach the value for the pipe flow without the ring. At y/R > .02 the values of the micro-scale have almost constant values of 1.5 mm. for both the rough and smooth pipes.

The macro-scales of turbulence are shown in Fig. (5.20b). The results show the same trend as the micro-scale of turbulence.

5.7.2 Turbulent Eddy Viscosity and Mixing Length

From the mean velocity distribution and shear-stress distribution, the turbulent eddy viscosity, ν_+, and the mixing length ℓ_m, were calculated. Figures (5.21a) to (5.21c) show the resultant turbulent eddy viscosity calculated using Eqn. (3.10a).

The values of the eddy viscosity are small near the wall, where the molocular viscosity dominates. Away from the wall the turbulent shear

stress increases and so the eddy viscosity is increased. Near the centre line of the pipe the turbulent shear stress has a small value and the velocity gradient is also decreasing, thus the eddy viscosity is reduced. In all the stations downstream of the reattachment this behaviour of the eddy viscosity exists, except that the maximum value of the eddy viscosity is higher near the reattachment because of the high value of the shear stress and low velocity gradient. Comparing the results with those for the pipe flow without the ring, the distribution of the eddy viscosity is returned to its undisturbed flow distribution at distance of x/h = 126.6 for the rough and smooth pipe.

The results of the mixing length distribution are shown in Figs. (5.22a) to (5.22c) for the rough and smooth pipe. Near the reattachment the flow is far from the equilibrium condition and the experimental mixing length, in the inner layer, is higher than that calculated for equilibrium flow ($\ell = \kappa y$). Downstream of the reattachment the inner layer increased and the flow returns to its original mixing length distribution at x/h = 126.6.

5.8 SUMMARY AND CONCLUSIONS

In this Chapter the effect of a two-dimensional obstacle on a fully developed turbulent flow is studied. The experiments were carried out for a rough and smooth pipe. The two-dimensional obstacles were in the form of suitably scaled internal (rectangular in cross-section) ring. The height-to-width ($\frac{h}{b} = .86$) and the radius-to-height ($\frac{R}{h} = 4.0$) ratios were the same for both smooth and rough pipes. The same Reynold's numbers of 4.5×10^5 was also maintained for both the pipes. The rough pipe was lined internally with the same background roughness used on the boundary-layer flow experiments. The results of the friction factor, f, and the roughness function, χ , for the rough pipe, show that the experiments were carried out for a fully rough region.

The mean velocity distribution downstream of the position x/h = 23.74 has higher values than the undisturbed velocity distribution (pipe without the ring). This due to the negative wake effect caused by the secondary flow downstream of the obstacle. This effect does not exist in the boundary-layer flow where the the flow has the tendency to increase the absolute thickness downstream of the obstacle.

The recovery of the mean velocity distribution occurs between the positions $94.9 < x/h < 126.6$ for both the rough and smooth pipes. These positions are corresponding to 59.8 cms. $< x <$ 79.6 cms. for the rough pipe and to $47.5 < x < 63.3$ for the smooth pipe. These positions when compared with those obtained for the boundary-layer flow, 116 cms. $< x <$ 139 cms. for the rough plate and $86 < x < 116$ for the smooth plate, show that the position of the recovery on the flat plate is about 1.8 times the distance of the recovery in the pipe flow. It must be noted that the ratio of R/h in the pipe flow is twice the ratio of δ/h on the boundary-layer.

The recovery of the shear stress distribution in the pipe flow occurs at $126.6 < x/h < 166$ which corresponds to 79.8 cms. $< x <$ 104 cms. for the rough pipe and to 63.3 cms. $< x <$ 83 cms. for the smooth pipe. For the rough plate this recovery occurs at 139 cms. $< x <$ 185 cms.; for the smooth pipe at 116 cms. $< x <$ 139 cms. Comparing this recovery of the shear stress for the pipe flow with that obtained for the boundary-layer yields the same conclusion as obtained for the recovery of the mean velocity distribution.

The effect of the secondary flow in the pipe flow reduced the shear stress below the linear distribution of the shear stress ($\tau/\tau_o = 1 - y/R$). Near the reattachment the maximum shear stress occurs at $y/h = 1.5$ which is the same for the boundary layer experiments.

The results of the spectrum function downstream of the ring for the rough and the smooth pipe show that the behaviour of the frequency spectra is the same for all stations downstream of the ring. The three ranges of the energy (production - intermediate sub-range - dissipation) are clearly defined at all stations downstream of the ring. This behaviour is also shown for the boundary-layer results.

The distribution of the skewness factor downstream of the ring shows that the probability density distribution is less skewed in the centre-line of the pipe, than in the outer layer of the boundary-layer flow. This is due to the fact that in the pipe flow there are two shear layers whereas in the boundary-layer flow there is only one shear layer near the flat plate. It is also found that the flatness factor is nearly Gaussian (varies between 2.5 and 3.0) for both the rough and smooth pipe. The values of the skewness and flatness factors near the reattachment are not Gaussian where these values are affected by the separation and reattachment of the flow.

The micro-scale of turbulence (small eddy size) downstream of the ring has a constant value downstream of the position $x/h = 40$, which is similar to the undisturbed flow distribution (pipe without ring). Upstream of $x/h = 40$, the micro-scale of turbulence has high values because of the effect of the separation of the flow. The macro-scale of turbulence (large eddy size) has a different behaviour than that for the micro-scale. At the position $x/h \lesssim 40$ the values of the macro-scale are the same for all the values of y/R (= 0.35, 0.68 and 1.0). Downstream of $x/h = 40$ the values of the macro-scale tend to catch up the undisturbed values. It can be concluded from the above discussion that the presence of the ring inside the pipe affects the large eddies more than the small eddies.

The recovery of the mixing length and the turbulent eddy viscosity occurs at the same distance $126.6 < x/h < 166$, for both the rough and the smooth pipe.

CHAPTER 6

EQUATIONS OF MOTION AND NUMERICAL PROCEDURE

CHAPTER 6

EQUATIONS OF MOTION AND NUMERICAL PROCEDURE

6.1 INTRODUCTION

In the present chapter the differential equations which govern turbulent flows and their finite difference forms are discussed. The method of solution for the resulting algebraic equations are also described. The velocity components U and V were replaced along with the pressure by both vorticity and the stream function. The turbulent flux terms which appear in the vorticity equation were calculated through the use of a two-equation turbulence model consisting of differential equations for the kinetic enegy of turbulence and its dissipation rate.

The predicted points of separation and reattachment, are compared with the experimental results of the rectangular cross-section obstacle (ridge) attached to both the smooth and rough plates. Similar comparisons are made for the velocity distribution and turbulent kinetic energy downstream of the reattachment.

6.2 DIFFERENTIAL EQUATIONS

6.2.1 Stream Function and Vorticity Equations

The dependent variables in the present numerical solutions are the stream function ψ and the vorticity ω. The vorticity ω is a measure of the amount of anticlock-wise rotation and deformation which the fluid possesses. Its definition is:

$$\omega = \frac{\partial V}{\partial x} - \frac{\partial U}{\partial y} \qquad (6.1)$$

where U and V are the velocity components at direction x and y respectively.

The stream function is a scalar quantity defined by:

$$\psi = \int \rho U dy = -\int \rho V dx \tag{6.2}$$

The relation between the vorticity and the stream function which play a central part in the present calculation procedure, can be obtained by combination of Eqns.(6.1) and (6.2); its simple form is:

$$\frac{\partial^2 \psi}{\partial x^2} + \frac{\partial^2 \psi}{\partial y^2} = -\rho\omega \tag{6.3}$$

Equation (6.3) is the stream function equation. The vorticity equation is derived from the two differential equations which relate to the momentum in x and y direction respectively:

$$\rho U \frac{\partial U}{\partial x} + \rho V \frac{\partial U}{\partial y} = - \frac{\partial p}{\partial x} + \frac{\partial \tau_{xy}}{\partial y}, \tag{6.4a}$$

$$\rho U \frac{\partial V}{\partial x} + \rho V \frac{\partial V}{\partial y} = - \frac{\partial p}{\partial y} + \frac{\partial \tau_{xy}}{\partial x}, \tag{6.4b}$$

with the continuity equation

$$\frac{\partial U}{\partial x} + \frac{\partial V}{\partial y} = 0 \tag{6.4c}$$

By eliminating the pressure from the momentum equations (6.4a) and (6.4b), the two equations can be replaced with one equation for the vorticity. The result is:

$$\rho U \frac{\partial \omega}{\partial x} + \rho V \frac{\partial \omega}{\partial y} = \frac{\partial^2}{\partial x^2} (\mu_{eff}\, \omega) + \frac{\partial^2}{\partial y^2} (\mu_{eff}\, \omega) + S_\omega \tag{6.5}$$

where

$$S_\omega = 2 \frac{\partial^2}{\partial x \partial y} \left| \mu_{eff} \left(\frac{\partial V}{\partial y} - \frac{\partial U}{\partial x} \right) \right| + 2 \frac{\partial^2}{\partial x^2} \left(\mu_{eff} \frac{\partial U}{\partial y} \right) - 2 \frac{\partial^2}{\partial y^2} \left(\mu_{eff} \frac{\partial V}{\partial x} \right) \tag{6.6a}$$

and $\mu_{eff} = \mu + \mu_t$ (6.6b)

where μ is the molecular viscosity and μ_t is the turbulent eddy viscosity, the value of S_ω is zero in the uniform viscosity flow and boundary-layer flows (Wolfshtine (1967)). The final equations for the stream function ψ, and the vorticity ω, are Eqns. (6.3) and (6.5).

6.2.2 Turbulence Model

The value of the turbulent eddy viscosity μ_t, which is needed to calculate μ_{eff}, can be calculated in a number of ways (Launder and Spalding (1972)). The necessary algebraic or differential equations collectively constitute a 'turbulence model'.

The standard for the choice of a turbulence model include economy of computer time, accuracy, width of applicability and simplicity. A classification for tur bulence models and some examples of their applications are provided by Launder and Spalding (1972). Turbulence models can be classified according to the number of additional differential equations which they contain. Most zero-, one- and two-equation models represent the Reynold's shear stress by means of the turbulent viscosity concept.

The turbulent viscosity is taken to be proportional to the product of a velocity scale and length scale characteristic of the local turbulent flow. Zero-equation models employ the mixing length hypothesis (Prandtl, (1925)) in which the length scale is specified by a "mixing length" ℓ_m and the velocity scale is of the form $\ell_m \left|\frac{\partial U}{\partial y}\right|$; the velocity gradient $\frac{\partial U}{\partial y}$ is calculated from local mean flow conditions. This model is applicable to simple two-dimensional boundary-layer flows (Patankar and Spalding (1970)) where ℓ_m is easily prescribed empirically and the predominant mean velocity gradient does not change sign.

In one- and two-equation models, the turbulent eddy viscosity μ_t, is related to the kinetic energy of turbulence, $k = \frac{1}{2}(\overline{u^2} + \overline{v^2} + \overline{w^2})$ and a length scale ℓ, by the experssion:

$$\mu_t = C_\mu \rho k^{1/2} \ell \tag{6.7}$$

where C_μ is an empirical coefficient. The value of k can be obtained by solving the differential transport equation for kinetic energy, but sufficient knowledge of the length scale, ℓ, distribution is required.

Two-equation models provide a more general approach by solving transport equations for both k, and a quantity related to the length scale ℓ. In practice, it proves to be more satisfactory to solve for the turbulent dissipation, ε, rather than for the dissipation length scale ℓ. The two variables are related (Launder and Spalding (1974)) by the equation:

$$\varepsilon = C_D \frac{k^{3/2}}{\ell} \tag{6.8}$$

where C_D is a constant to be determined from experimental data. By combining equations (6.7) and (6.8) the turbulent viscosity can be linked to k and ε, thus:

$$\mu_t = C_\mu \rho \frac{k^2}{\varepsilon} \tag{6.9}$$

"Two-equation models are the simplest available means of calculating turbulent stresses in recirculating or separated flows where the length scale distribution cannot be prescribed algebraically" (Launder and Spalding (1972)). Such models have been applied to wall boundary-layers (Pope and Whitelaw(1975)) and two-deminsional recirculating flows over a backward facing step (Minh and Chassainy (1978)) and flow over a rectangular cross section obstacle (Vasilic-Melling (1977), Durst and Rastogi (1979)).

More elaborate turbulence models exist which do not employ the turbulent viscosity concept, but solve differential equations for the Reynold's stresses. In a study of a two-dimensional channel flow, Hanjalic and Launder (1972), solved an equation for one shear stress component in addition to equations for the kinetic energy and dissipation. This model was later extended by replacing the turbulence energy equation by transport equations for the three normal stresses and solving these along with equations for shear stress and dissipation.

In the present study, the two-equation $k-\varepsilon$ turbulence model was applied to predict the flow over a two-dimensional obstacle. This flow is characterised by a region of recirculation and wake. Zero- and one-equation models are inadequate for such flow because of their dependence on prescribed length scale distribution.

As described above, the turbulence model used in the present investigation is the two-equation model, for the transport equations for both the turbulent kinetic energy k, and the dissipation rate ε . The transport equation for turbulent kinetic energy first derived by Kolmogorov (1942) is obtained using the equations for the turbulent velocity and pressure fluctuations in the momentum equations (Eqns. (6.4a) and (6.4b) and averaging with respect to time the two-dimensional turbulent flow equation can be written as:

$$\rho U \frac{\partial U}{\partial x} + \rho V \frac{\partial V}{\partial y} = - \frac{\partial p}{\partial x} + \mu\left(\frac{\partial^2 U}{\partial x^2} + \frac{\partial^2 V}{\partial y^2}\right) + \rho \frac{\partial}{\partial y} \overline{uv} \qquad (6.10a)$$

$$\rho U \frac{\partial V}{\partial x} + \rho V \frac{\partial V}{\partial y} = - \frac{\partial p}{\partial y} + \mu\left(\frac{\partial^2 U}{\partial x^2} + \frac{\partial^2 V}{\partial y^2}\right) + \rho \frac{\partial}{\partial x} \overline{uv} \qquad (6.10b)$$

It may be shown that after some lengthy algebra, that the turbulence energy equation is:

$$\rho U \frac{\partial k}{\partial x} + \rho V \frac{\partial k}{\partial y} = -\rho \overline{uv} \frac{\partial U}{\partial y} - \frac{\partial}{\partial x} \overline{(p' + k) v} + \mu\left(\frac{\partial^2 k}{\partial x^2} + \frac{\partial^2 k}{\partial y^2}\right)$$

$$-\mu \left| \overline{\frac{\partial u}{\partial x} \frac{\partial u}{\partial x}} + \overline{\frac{\partial v}{\partial y} \frac{\partial v}{\partial y}} \right| \qquad (6.11)$$

The steps to get the above equation are given by Hinze (1975). The physical meaning of the various terms in the equation may be identified as follows:

$\rho U \frac{\partial k}{\partial x} + \rho V \frac{\partial k}{\partial y}$ ≡ convection of the turbulence energy by the mean motion

$-\rho \overline{uv}$ ≡ the Reynold's shear stress

$-\rho \overline{uv} \frac{\partial U}{\partial y}$ ≡ production of the turbulence energy

$-\frac{\partial}{\partial x} \overline{(p + k) v}$ ≡ turbulent diffusion of the turbulence energy

$\mu\left(\frac{\partial^2 k}{\partial x^2} + \frac{\partial^2 k}{\partial y^2}\right)$ ≡ viscous diffusion of the turbulence energy

$-\mu \left| \overline{\frac{\partial u}{\partial x} \frac{\partial u}{\partial x}} + \overline{\frac{\partial v}{\partial y} \frac{\partial v}{\partial y}} \right|$ ≡ viscous dissipation

The above terms have to be approximated in terms of quantities which could be known or can be determined. These approximation forms are presented by Launder and Spalding (1972) and when Eq. (6.11) is rearranged the final equation becomes:

$$\rho U \frac{\partial k}{\partial x} + \rho V \frac{\partial k}{\partial y} = \frac{\partial}{\partial x}\left(\Gamma_k \frac{\partial k}{\partial x}\right) + \frac{\partial}{\partial y}\left(\Gamma_k \frac{\partial k}{\partial y}\right) + G - \rho\varepsilon \qquad 6.12a$$

where Γ_k is the exchange coefficient = $\mu + \frac{\mu_t}{\sigma_k}$

and

$$G = \mu_t \left| 2\left(\frac{\partial V}{\partial y}\right)^2 + 2\left(\frac{\partial U}{\partial x}\right)^2 + \left(\frac{\partial V}{\partial x} + \frac{\partial U}{\partial y}\right)^2 \right| \qquad 6.12b$$

By a similar procedure to that used above, the equation for the dissipation rate, ε , can be derived. The resulting equation is long and complicated, and it will suffice here to state a modelled form (Launder and Spalding (1974)):

$$\rho U \frac{\partial \varepsilon}{\partial x} + \rho V \frac{\partial \varepsilon}{\partial y} = \frac{\partial}{\partial x}\left(\Gamma_\varepsilon \frac{\partial \varepsilon}{\partial x}\right) + \frac{\partial}{\partial y}\left(\Gamma_\varepsilon \frac{\partial \varepsilon}{\partial y}\right) + C_1 \frac{\varepsilon}{k} G - C_2 \rho \frac{\varepsilon^2}{k} \qquad (6.13)$$

where

$$\Gamma_\varepsilon = \mu + \frac{\mu_t}{\sigma_\varepsilon}$$

The values of the constants σ_k , σ_ε , C_1 and C_2 appearing in Eqns. (6.12a) and (6.13) were determined approximately from data for simple turbulent flows. Then these constants were optimised by predictions for a different flow situation. Details of the evaluation of these constants were given by Launder and Spalding (1972). These constants take the values given in table (6.1).

Table 6.1

The values of constants in the k - ε model.

C_μ	C_1	C_2	σ_k	σ_ε
0.09	1.44	1.92	1.9	1.3

6.2.3 Conservation Equation for Property ϕ

As shown in the last section (6.2.2), the differential equations which control the flow are the Eqns. (6.3), (6.5), (6.12a) and (6.13). All of these equations can be regarded as possessing the common form for dependent variable, ϕ , (Gosman et al (1969)):

$$a_\phi \{\frac{\partial}{\partial x}(\phi \frac{\partial \psi}{\partial y}) - \frac{\partial}{\partial y}(\phi \frac{\partial \psi}{\partial x})\} - \{\frac{\partial}{\partial x}(b_\phi \frac{\partial c_\phi \phi}{\partial x}) - \frac{\partial}{\partial y}(b_\phi \frac{\partial c_\phi \phi}{\partial y})\} + S_\phi = 0 \quad (6.14)$$

where the terms in the first curly brackets represent the transport of ϕ by convection. The terms in the second curly brackets represent the diffusion of ϕ. The "source" term S_ϕ, contains quantities related to the generation or destruction of ϕ, as well as any other terms which are not accounted for in the convection and diffusion expressions. The new coefficients a_ϕ, b_ϕ and c_ϕ are shown in table (6.2):

Table 6.2

The functions a_ϕ, b_ϕ, c_ϕ and S_ϕ associated with Eqn.(6.14)

ϕ	a_ϕ	b_ϕ	c_ϕ	S_ϕ
ω	1.0	1.0	μ_{eff}	$\{2 \frac{\partial^2}{\partial x \partial y} \mu_{eff} (\frac{\partial V}{\partial x}) + 2 \frac{\partial^2}{\partial x^2} (\mu_{eff} \frac{\partial U}{\partial y})$ $-2 \frac{\partial^2}{\partial y^2}(\mu_{eff} \frac{\partial V}{\partial x})\} \approx 0$
ψ	0	1.0	1.0	$-\rho\omega$
k	1.0	$\Gamma_{k,eff}$	1.0	$-(G - \rho\varepsilon)$
ε	1.0	$\Gamma_{\varepsilon,eff}$	1.0	$-(C_1 \frac{\varepsilon}{k} G - C_2 \rho \frac{\varepsilon^2}{k})$

.2.4 Boundary Conditions

The differential equations of the form of (6.14) are second-order elliptic equations. Therefore, information must be provided to specify the value of each variable (or its first derivative, normal to the boundary) on each boundary. The boundaries of the solution domain may coincide with an upstream location at which a specified inflow, solid walls, a free boundary and a downstream location where outflow takes place.

At the upstream boundary, it is necessary to provide distributions of all variables, including ψ, ω, k and ε. The values of the stream function and the vorticity were calculated using a mean velocity profile whose outer region was modified by Moses (1964) and Finly (1966). This mean velocity profile satisfies the condition that the cross-stream mean velocity gradient should be zero at the edge of the boundary-layer:

$$\frac{U}{u_o} = \frac{1}{k} \log_e \frac{y u_o}{\nu} + A - \frac{\Delta u}{u_o} + \frac{\Pi}{k} \left[6 \left(\frac{y}{\delta}\right)^2 - 4 \left(\frac{y}{\delta}\right)^3\right] + \frac{1}{k} \left[\frac{y}{\delta}\right]^2 \left[1 - \frac{y}{\delta}\right] \qquad (6.15)$$

where Π is the wake-strength parameter and δ is the absolute boundary-layer thickness. The value of $\frac{\Delta u}{u_o}$ is the roughness function, which is equal to zero for smooth surface. The above values can be determined experimentally in the upstream location.

The application of the boundary conditions at walls in turbulent flow requires a more elaborate treatment than at the upstream boundary. Thus, although the velocity components are zero (ψ = const and $(\frac{\partial \psi}{\partial y}) = 0$), special formulae are necessary to calculate the resultant wall shear stresses. These, together with the boundary conditions on the turbulence kinetic energy, k , and dissipation rate ε, are deduced from wall function approximation to the transport equations in the near wall region. Details of these practices are shown in Appendix C.

At the free boundary, the conditions are known from the distribution of velocity, turbulence energy, etc.. However, this information is not always available in complete detail, especially if the flow was disturbed by an obstacle. Therefore, it is required to locate the computational free boundary sufficiently far from the obstacle. If this precau tion is taken, constant values of stream-wise velocity (or constant stream function ψ), k and ε can be specified along the free boundary. The vorticity and the normal velocity are set equal to zero.

Finally, the outlet plane boundary was located downstream of the obstacle, where the velocity normal to the boundary is directed everywhere outwards. All the derivatives with respect to the stream-wise direction, x, were set to zero ($\frac{\partial \phi}{\partial x} = 0$).

6.3 FINITE DIFFERENCE EQUATIONS

In section (6.2) the differential equations which have to be solved are presented. Generally, there is only one practical method to obtain solutions of these equations; this is by finite-difference techniques. The control volume was covered with a mesh, which is rectangular in the present work. In each mesh point the differential equation was replaced with a finite-difference, algebraic equation. The control volume and the mesh are shown in Fig. (6.19).

As mentioned in section (6.2), all the differential equations were represented by the general conservation Eqm. (6.14). The finite-difference form of this equation is then obtained by integration of Eqn. (6.14) over small rectangles, surrounding each mesh point. These rectangles are so defined that their sides lie half-way between the mesh points and the parallel to the x and y axes (see Fig. (6.1b)).

Details of the integration of Eqn. (6.14) over the control are given by Gosman et al (1969). Here it will suffice to present the final result, for the value of ϕ at point p surrounded by the points E, W, N and S as follows:

$$\phi_p = C_E \phi_E + C_W \phi_W + C_N \phi_N + C_S \phi_S + D \qquad (6.16a)$$

where

$$C_E = (A_E + B_E C_{\phi,E})/\Sigma_{AB}$$

$$C_W = (A_W + B_W C_{\phi,W})/\Sigma AB$$

$$C_N = (A_N + B_N C_{\phi,N})/\Sigma_{AB} \qquad (6.16b)$$

$$C_S = (A_S + B_S C_{\phi,S})/\Sigma_{AB}$$

$$D = (S_{\phi,p} V_p/\Sigma_{AB}$$

$$\Sigma_{AB} = A_E + A_W + A_N + A_S + C_{\phi,p} (B_E + B_W + B_N + B_S)$$

and

$$V_p = \frac{1}{4} (x_E - x_W) (y_N - y_S) \qquad (6.16c)$$

$$A_E = \frac{a_{\phi,p}}{\theta} \left[(\psi_{SE} + \psi_S - \psi_{NE} - \psi_N) + | \psi_{SE} + \psi_S - \psi_{NE} - \psi_N | \right] \qquad (6.17)$$

and the A_W, A_N, A_S are similar expressions.

$$B_E = \frac{b_\phi + b_{\phi,p}}{4} \frac{y_N - y_S}{x_E - x_p} \qquad (6.18)$$

and B_W, B_N, B_S are similar expressions.

The expressions of the terms A_E, A_W, A_N and A_S describe the transport of ϕ by convection. Those of B_E, B_W, B_N and B_S describe the ϕ transport by diffusion. A further discussion of the equation (6.16a) was presented by Gosman et al (1969).

Equation (6.16a) represents the finite-difference, algebraic equations, for all the dependent variables (ϕ): ω , ψ, k and ε . Once the algebraic equations were derived, a procedure must be found for solving them. When the equations are linear and few in number, standard matrix-inversion

techniques can be used. Usually, either because the equations are very numerous, or because of non-linearities, successive substitution techiniques must be employed (Gosman et al (1969)). In these, initial guesses for the values of the variables are substituted into successive substitution formulae which were derived from the algebraic equations and, new values are computed; then these values are used as new guesses to the solution. Such procedures are commonly referred to as iterative, and each set of calculations of new values is terms a cycle of iteration.

As mentioned before (section (6.2.4)) the solution of these finite-difference equations needs information for the boundary domain (boundary conditions). At the upstream boundary, the appropriate conditions are supplied by assigning the specified distributions of ϕ at all grid nodes in the entry plane of the solution.

At the solid boundary the value of ψ was set to zero, the vorticity was taken as varying linearly with the normal distance from the wall, this assumption made by Gosman et al (1969), which give the vorticity at the wall boundary as

$$\omega_p = -\left[\frac{3(\psi_{NP} - \psi_D)}{y_{NP}^2\, p} + \frac{\omega_{NP}}{2}\right] \qquad (6.19)$$

where ψ_{NP} and ω_{NP} are the value of the stream function and the vorticity at the near wall boundary.

At the free boundary specific values were assigned to all variables as described in section (6.2.4). At the outlet plane, the stream-wise diffusion was set to zero, i.e., $\frac{\partial \phi}{\partial x} = 0$, for all the properties ψ, ω, k and ε.

The important boundary is the corner marked, p, in Fig. (6.1c). A fixed separation stream line method was used. This method used by Gosman et al (1969), and by Debenham and Duggins (1977). It is based on the assumption that the separating streamline leaving the corner continues forward to the

next grid point (p in Fig. (6.1c)). The finite-difference equation for ψ_p using the notation of Eqn. (6.16a) is:

$$\psi_p = C_E \psi_E + C_W \psi_W + C_N \psi_N + C_S \psi_S + C_p W_p \qquad (6.20)$$

where $\psi_S \equiv \psi_p = \psi_{wall}$ and the last term on the right-hand side represents, D, in Eqn. (6.16a). Utilising the above assumption, ψ_p is known (= ψ_{wall}) and Eqn. (6.20) is rearranged to give an expression for W_p.

The complete flow domain can be divided into two regions: the recirculating flow region which extends from 5h upstream of the obstacle to 15h downstream of the obstacle (where h is the height of the obstacle) and the boundary-layer region which prevails in front of the obstacle ($x/h < -5$) and beyond the recirculating flow region. In the region around the obstacle diffusion is equally important in both x- and y-directions; there exists no dominant direction of flow, and the flow is influenced by the downstream conditions. In the region beyond the separated flow, there exists a dominant direction of flow and diffusion is important only in the cross-stream direction. This region is governed by the differential Eqns. (6.3), (6.5), (6.12) and (6.13) without the diffusion terms in the x-direction.

6.4 CONVERGENCE AND ACCURACY OF THE SOLUTION

Gosman et al (1969) found that when Eqn. (6.19) is used explicitly for the calculation of the wall vorticities, and when the spacing between the grid lines parallel to the wall is non-uniform, divergence may occur. The source of the divergence appears to be the linkage of the vorticity and stream function equations throw the vorticity boundary conditions.

This divergence may be averted by the following two measures:

(i) Near the wall, the ratio of the intervals between the nodes would be kept as close to unity as possible.

(ii) The wall vorticity should be removed from the substitution formulae for the near-wall nodes by once-and-for-all algebraic elimination. Thus for example, if p is the interior node which lies adjacent to a wall node S, and equation (6.19) is the vorticity boundary condition, then the following modified substitution formula should be used (Gosman et al (1969)):

$$W_p = \frac{C_E W_E + C_W W_W + C_N W_N - 3 C_S(\psi_p - \psi_S)/y_p^2 + D}{1 + C_S/2} \qquad (6.21)$$

The divergence may also occur when the source term D in Eqn (6.16a) is a function of ϕ. This can be seen in the kinetic energy equation and the dissipation rate equation. To avert this divergence the source term was modified. Pun and Spalding (1977) linearised forms for the source terms in the kinetic energy and dissipation rate equations were used in the present solution.

The factors which affect the accuracy of the predictions are the degree to which the solution satisfies the differential equations, the degree to which it satisfies the finite-difference equations, the location of and conditions imposed on the boundaries and the adequacy of the turbulence model.

The first factor results from truncation error which is the difference between the solution of the differential equations and the solution of the finite-difference equations. It arises because of the approximations involved in the replacement of the differential coefficients by the finit-difference ones. These errors can be minimised by reducing the spacing between nodes to an acceptable level, preferably by using a non-

uniform grid with modes concentrated in regions of high gradients. Concerning the second factor, the extent to which the current solution satisfies the finite-difference equations can be assessed by that the difference between the variables at N and N + 1 iterations is very small.

Errors caused by inappropriate location of boundaries or specification of boundary conditions can be detected by adjusting the location conditions of the boundary and determining the sensitivity of the solution to such changes. If all the latter factors are eliminated, the adequacy of the turbulence model may then be assessed by comparing the solution with the experimental data.

6.5 COMPARISON OF NUMERICAL RESULTS WITH EXPERIMENTAL DATA

6.5.1 Recirculating Flow Region

Computations were carried out to solve Eqns. (6.3), (6.5) (6.12a) and (6.13) upstream and downstream of the two-dimensional rectangular cross-sectional bar (ridge) attached to the rough and smooth plates. The computations were carried out to solve these equations at between 5 and 15 obstacle heights upstream and downstream of the obstacle respectively. The recirculating flow program was used for this purpose. A 51 x 17 finite-difference grid for the smooth plate and a 48 x 20 finite-difference grid for the rough plate was used. The initial conditions at $x/h = -5$ for ψ, ω, k were taken from the experimental data while the dissipation rate was assumed to follow the mixing length hypothesis. About 6000 iterations and 500 secs. of computing time were required to obtain the converged solutions. The time required for the solution of the rough plate was 630 secs. for the same number of iterations.

Figures (6.2) shows the computed stream line pattern around the obstacle attached to both the rough and the smooth plates. The separated stream line determined experimentally is also shown in the same figure.

Agreement between the predicted value of the reattachment length and the experimental is not too good. This discrepancy may be attributed to the unsteady flow in the reattachment zone. The experiments carried out by Abbott and Kline (1962) for flow patterns over backward facing steps showed that the overall length of the separation region was unsteady and periodically changing in size. The above results were obtained by solving the kinetic energy and dissipation rate equations with the constants of table (6.1).

The recirculating flow region upstream of the obstacle is also shown in the above mentioned figure. Due to the negative pressure gradient created upstream of the obstacle, the flow will separate from the wall boundary and reattach again on the front surface of the obstacle. The agreement between the predicted and the experimental point of reattachment on the front surface is good. The point of reattachment occurs at y/h = 0.6 for the ridge on the rough plate and at y/h = 0.55 for the ridge on the smooth plate

The solution was repeated for different values of the constants C_1 C_2, C_μ, σ_k and σ_ε in the kinetic energy and dissipation rate equations. The effects of this change are shown in Figs. (6.3) and (6.4). These results show that these constants affect the general behaviour of the flow around the obstacle. The constants which give a reasonable agreement are those recommended by Launder and Spalding (1974).

6.5.2 Boundary Layer Flow Downstream of Reattachment

Downstream of the reattachment, there exists a dominant direction of the flow and diffusion is important only in the cross-stream direction. This region is governed by the differential equations used in the recirculating flow, without the diffusion terms in the x-direction. A different computer program was used to obtain the solutions for this flow.

The boundary condition for ψ, ω, k and ε were taken from the experimental data. A 51 x 18 finite-difference and for the smooth plate was used. For the rough plate, two finite-difference grids were used, one was 51 x 22 and the other 29 x 26. The solution was obtained for a ratio $x/h = 50$ downstream of the reattachment.

Figure (6.5) shows the measured velocity distributions superimposed on the theoretical ones. The latter were calculated from the stream function results. For the smooth plate, the wall function (the law of the wall is valid between the near grid points and the solid wall), which is discussed in Appendix B, was used in the near-wall region. As this figure shows, the numerical solution with and without the wall function is almost the same for the mean velocity and kinetic distributions. The two solutions with the wall function and without it are in reasonable agreement with the experimental results. The wall friction coefficients determined from the wall function is shown in Fig. (6.6). It can be seen that the agreement between the experimental and prediction distribution is good in near region downstream of the reattachment.

The results of the mean velocity distribution obtained for the rough plate do not agree well with the experimental results. To improve the solution for the rough plate several computational attempts were made and the following possibilities were considered:

(i) the effect of the finite-difference grid;

(ii) the effect of the number of iterations.

It was found that the solution was independent of the finite-difference grids used in the present analysis. Also the solution was independent of the number of iterations when the latter exceeded 6000.

The discrepancy between the theoretical and experimental results was due to the fact that the surface roughness was not considered. Also the wall function could not be used, except if the relationship between

the constant E in Eqn. (I.C) and the values of the wall friction velocity u_o is known.

The kinetic energy distributions are shown in Fig. (6.7) for both rough and smooth plates. It can be seen that there is a good agreement between the predicted and the experimental profiles for the smooth plate. However, the agreement for the rough plate proved to be less satisfactory. Neither the change of the finite-difference grid nor the number of the iterations improved the results.

The boundary-layer integral thicknesses δ^* and θ and the shape parameter H calculated from the theoretical and measured mean velocity profiles are shown in Fig. (6.8). The smooth plate results are seen to be in good agreement with their experimental counterparts. Because of the poor agreement of the predicted and measured velocity profiles on the rough plate, there is a noticable difference between the theoretical and experimental boundary-layer integral thicknesses δ^* and θ. Inspite of this, the shape parameter H, is predicted fairly well.

6.6 SUMMARY AND CONCLUSION

This chapter has presented the equations of motion and a method for their solution for a two-dimensional turbulent flow of uniform property fluid. The dependent variables in the solution were the stream function ψ and the vorticity ω. A two-equation $k - \varepsilon$ turbulence model was used to calculate the value of μ_{eff}. A general conservation equation for any property ϕ was formulated. Then finite-difference version was derived by integrating the partial differential equations over a small control volume centred at a representative node of the finite-difference grid. The flow was divided into two regions, a recirculating flow region around the obstacle, and a boundary-layer flow downstream of the reattachment.

The prediction of the recirculating flow region is good compared with the available experimental data. The solution can predict the separation bubble upstream of the obstacle. The change in constants C_1 C_2 , C_μ , σ_k and σ_ε in the kinetic energy and dissipation rate equations affect the solution of the recirculating flow region. Downstream of the reattachment the agreement between the predicted and experimental results is acceptable for the smooth plate. For the rough plate there is a disparity between the predicted and the experimental results. This disparity is probably due to the omission of surface roughness and must be taken into consideration if the solution is to be improved. This may be achieved by using the wall function formula in the near wall region.

CHAPTER 7

CONCLUSIONS AND SUGGESTIONS FOR FUTURE WORK

CHAPTER 7

CONCLUSIONS AND SUGGESTIONS FOR FUTURE WORK

7.1 SUMMARY

This thesis investigated, experimentally and theoretically, the recovery of a turbulent shear flow downstream of a two-dimensional obstacle, the effect of an irregular surface roughness on the mean flow and turbulence properties downstream of the obstacle. The experiments were carried out for turbulent boundary-layers developed on smooth and rough plates. Two types of geometry were used for the obstacle: one being a rectangular cross-section bar (ridge) and the other a single hump (hill). The characteristics of the flow, on both the rough and smooth plates, were determined before and after the obstacle was introduced into the working section of the wind tunnel. All the experiments were made for a zero external pressure gradient with a free stream velocity of 21 m/s.

The experiments were repeated, within the present project, for a fully developed turbulent pipe flow. Study of the pipe flow may lead to a better understanding of the behaviour of the turbulent boundary-layer flow. The shear stress distribution is already known for a fully developed pipe flow. The pipe flow experiments were carried out for both rough and smooth pipes. An abrasive paper sheet, of grade 16, was used to simulate the irregular rough background for both the boundary-layer and pipe flows. The two-dimensional obstacle used with the pipe experiments was a rectangular cross-section ring.

A theoretical investigation was carried out to predict the separation zone upstream and downstream of the obstacle (rectangular cross-section bar) in addition to the flow recovery downstream of the obstacle. The main flow was divided into two regions: (a) the recirculating flow region upstream

of the obstacle $x/h > -5$ to $x/h \lesssim 15$ downstream of the obstacle and (b) the boundary-layer region which prevails in front of the obstacle ($x/h < -5$) and beyond the recirculating flow region. The stream function ψ and the vorticity ω were the dependent variables in the present investigation. The k-ε turbulence model was employed to specify the turbulent viscosity μ_t. The available finite difference calculation procedures for recirculating flow and boundary-layers (Gosman et al (1969)) were used to solve the governing, partial differential equations.

7.2 CONCLUSIONS

The following important conclusions can be arrived at:

(a) Wind Tunnel Experiments

(1) The pressure distribution on the obstacle depends upon the shape of the obstacle itself. For the ridge and the hill attached to the rough plate, the adverse pressure gradient, created upstream of the ridge, is greater than that created upstream of the hill. This pressure gradient affects the size of the front separation bubble (upstream of the obstacle). Due to this adverse pressure gradient, the flow separates from the plane boundary and reattaches on the front surface of the obstacle. At this reattachment the static pressure distribution on the front surface reaches its maximum value. For the same geometry (ridge), with the same aspect ratio ($b/h = 2.5$) and the same boundary-layer-to-obstacle height ($\delta/h = 2$), attached to rough and smooth plates the reattachment of the flow on the front surface occurs at $0.5 < y/h < 0.6$. For different geometry (ridge or hill) with the same δ/h, the reattachment on the front surface of the hill occurs at $0.2 < y/h < 0.3$.

(2) The flow separates at the top of the obstacle and reattaches at the wall boundary downstream of the obstacle. In the case of the rectangular cross-section bar (ridge), the separated flow from the wall boundary

(upstream of the ridge) is reattached on the front surface of the obstacle and separates again at the top edge of the front surface of the obstacle. The static pressure distribution on the front surface will be decreased to the base pressure value (c_p = -0.26 ridge and -0.36 hill) on the rear surface of the obstacle at the separation point of the flow. This separation occurs at y/h = 1.0 for the ridge and in the case of the hill the separation occurs at y/h = .9.

(3) For two obstacles, with the same boundary-layer thickness-to-obstacle height - δ/h and the same aspect ratio - b/h, attached to smooth and rough surfaces, the drag force on the obstacle attached to the smooth plate is higher than that on the obstacle attached to the rough plate. This is due to the velocity shift - $\Delta u/u_o$ - caused by the plate surface roughness.

(4) The size of the recirculating flow region, downstream of the obstacle, depends on the geometry of the obstacle itself and the surface roughness of the plane wall. The length of the recirculating flow region downstream of the rectangular cross-section bar (ridge) is about 25% more than that downstream of the hill. For the same geometry of the obstacle, the length of the recirculating zone on the rough plate is about 15% more than that on the smooth plate.

(5) Downstream of the reattachment, the mean velocity distribution recovery depends on both the geometry of the obstacle and the surface roughness. For different geometries of the obstacle attached to the same rough surface, the velocity recovers at 116 cm < x < 139 cms in the case of the ridge, while in the case of the hill-shaped obstacle the recovery occurs at 86 cms < x < 116 cms. For different surfaces and the same obstacle geometry, the recovery of the mean velocity occurs at 116 cms < x < 139 cms for the rough surface and at 86 cms < x < 116 cms for the smooth surface.

(6) The results obtained for the wall friction coefficient c_f, and Clauser parameter G, confirms the above conclusion (5). Figure (4.9a) shows the friction coefficient found downstream of the reattachment for both the ridge and the hill. It is clearly noticeable that the value of c_f increases from a near zero value, near the reattachment, to reach the value of c_f, for the undisturbed flow in the case of the hill. In the case of the ridge, an additional distance downstream of the reattachment is needed for c_f to reach the value of c_f for undisturbed flow. A similar behaviour occurs for the ridge on both the rough and smooth surface (Fig. (4.9b)), with the exception that c_f reaches its undisturbed value much earlier with the smooth plate than with the rough one. Clauser parameter, G, (Fig. (4.11)) shows the same sequence of recovery which occurs firstly, downstream of the ridge on the smooth plate, secondly, downstream of the hill on the rough plate and, thirdly, downstream of the ridge on the rough plate.

(7) The presence of the obstacle in a turbulent shear flow increases the absolute boundary-layer thickness downstream of the obstacle.

(8) In the far region, downstream of the obstacle, the mean flow characteristics are different than those for the flow without the obstacle. The main changes in these characteristics are:

(a) the boundary-layer thickness is considerably increased. This increase is about 30% for the rough plate and about 50% for the smooth plate.

(b) both the boundary-layer integral thicknesses δ^* and θ are changed downstream of the obstacle. These changes affect the value of the shape parameter H - which decreases from 1.55 for the rough plate, without the obstacle, to 1.4 for the rough plate with the obstacle. The same behaviour for the smooth plate occurs where the value of H decreases from 1.44 for the smooth plate, without the

obtacle, to 1.3 for the smooth plate with the obstacle. The decrease in the value of H is about 10% for both the rough and smooth plates.

(9) The variation of the turbulent quantities plotted as a function of the positions downstream of the reattachment (Figs. (4.12) to (4.17)) shows that these quantities require a greater distance downstream of the obstacle than the mean velocity to recover.

(10) In the near wake region the turbulent shear stress increases from low values, near the wall, to a maximum value near the top of the obstacle. This maximum shear stress occurs at $y/h = 1.5$ for all the obstacles. This is because the shear flow in this region is dominated by the turbulence generated, in the initial mixing process, near the top edge of the obstacle. The value of the shear stress in this region depends upon the shape of the obstacle itself. At $x = 50$ cms downstream of the ridge attached to the rough plate, the maximum value of the shear stress is about 70% higher than that for the hill at the same downstream position. In the far wake region the shear stress distribution downstream of the hill reaches the full recovery at about $x = 139$ cms., while the shear stress downstream of the ridge needs a greater distance to reach the full recovery. For the smooth plate the recovery of the shear stress occurs at distance $x = 139$ cms downstream of the ridge. The main conclusion from this discussion is that the recovery of the shear stress downstream of a two-dimensional obstacle, attached to a plane wall, depends on the geometry of the obstacle and the surface roughness of the plane wall.

(11) The skewness and flatness factors which are used to express the probability density distribution of the fluctuating velocity component, at an arbitrary point, were also measured. Downstream of the reattachment the distribution of the skewness and the flatness factors in the non-intermittent region (near the wall) are nearly Gaussian for both the rough

and smooth plate, (flatness factor changes from 2 to 3 and the skewness factor is zero). Because of the lower fluctuating velocity in the outer region of the boundary-layer, the probability density distribution is negatively skewed and the flatness factor increases to more than the value of 3.

The behaviour of these two factors is the same for both the rough and smooth plates with and without the obstacle.

(12) The distributions of the spectrum function downstream of the reattachment show that there is no substantial difference between all the measurement stations. This indicates that the energy transfer from the large eddies to the small eddies and the production and the dissipation of energy follow the same laws of $k^{-5/3}$ and k^{-1} and k^{-7} as the one without the obstacle.

(13) The macro- and micro-scale of turbulence (Figs. (4.24) and (4.25)) show no substantial difference between the values determined for the rough and smooth plates respectively. Except in the inner region $y/\delta = .02$, the rough surface has smaller streamwise values of macro- and micro-scales of turbulence than that on the smooth surface.

(14) Clauser's assumption of the distribution of the turbulent eddy viscosity in the inner layer is not valid near the reattachment - where the experimental turbulent eddy viscosity is much higher than the one calculated from:

$$\nu_{t_i} = \kappa\, y\, u_o$$

This invalidity is due to the high shear stress values near the reattachment and low velocity gradient in the near wake region. Downstream of the reattachment, the inner portion of the flow returns to the equilibrium , boundary-layer state and follows the distribution according to the above equation. The variation of the mixing length is similar to that observed for the eddy viscosity.

(b) Pipe Flow Experiments

(1) The presence of the ring increases the centre-line velocity by about 100% just downstream of the ring. Further downstream, however, this increase dies out.

(2) The measurements of the mean velocity profiles downstream of the ring show that the recovery of the flow is almost at the same x/h for both the rough and smooth pipes. This recovery occurs between the positions $94.9 < x/h < 126.6$ for both the rough and smooth pipes. Comparison between these positions with those obtained for the boundary-layer flow shows that the position of the recovery on the flat plate is about 1.8 times the distance of the recovery in the pipe flow.

(3) The mean velocity distribution, downstream of the position $x/h = 23.74$, has higher values than the undisturbed velocity distribution (pipe without the ring). This is due to the negative wake effect caused by the secondary flow downstream of the obstacle. This effect does not appear in the boundary-layer flow where the flow has the tendency to increase the absolute thickness downstream of the obstacle.

(4) The friction coefficient has a minimum value near the reattachment and increases to a maximum value in the region of the negative wake effect. It then decreases again to reach its value for a pipe flow without ring at $x/h = 100$.

(5) The shear stress distribution and the turbulence intensities $\sqrt{\overline{u^2}}/u_o$, $\sqrt{\overline{v^2}}/u_o$ and $\sqrt{\overline{w^2}}/u_o$ have very high values near the ring where the flow behaves like a free jet flow. The maximum value of these intensities occurs at $y/R = 0.4$ which corresponds to $y/h = 1.5$ in the boundary-layer flow. Downstream of the ring, these maximum values of the turbulence quantities considerably decrease to reach the undisturbed value for the pipe flow without the ring.

(6) Due to the negative wake effect, the turbulent shear stress distribution reduces below the linear distribution of equation

$$\frac{\tau}{\tau_o} = 1 - \frac{y}{R}$$

This effect appears at x/h = 47.4 and end when the flow recovers to the fully developed pipe flow at x/h = 166.1.

(7) The measurements of the skewness and flatness factors is the same for all measurement positions downstream of the reattachment as those obtained for the pipe flow without the ring. These distributions are near to the normal distribution where the flatness factor is about 3.0 for the rough and smooth pipes and the skewness factor is about zero in the inner region of the flow. The probability density distribution is less skewed at the centre-line of the pipe than in the outer layer of the boundary-layer flow. This is due to the fact that in the pipe flow there are two shear layers - whereas in theboundary-layer flow, there is only one shear layer near the flat plate. Because of the high velocity fluctuating very near to the reattachment, (x/h = 11.9), the probability density distribution is positively skewed near the wall and then changes to a negative skew at the centre-line of the pipe where the law velocity fluctuation is present.

(8) The frequency spectra of the longitudinal fluctuating velocity $\overline{u^2}$ are determined downstream of the ring for both rough and smooth pipes. The three ranges of the energy (production k^{-1} - intermediate sub-range $k^{-5/3}$ - dissipation k^{-7}) are clearly defined at all stations. All the measurements are also nearly collapsed in a curve similar to the frequency spectra for the pipe flow without the ring. This behaviour shows that the transfer of energy from the large eddies to the small eddies and the dissipation of the energy into heat at high frequency is not changed by the flow

disturbance caused by the presence of the ring.

(9) The micro-scale of turbulence (small eddy size), downstream of the ring, has constant values downstream of the position x/h = 40 - which is similar to the undisturbed flow distribution (pipe without ring). Upstream of x/h = 40, the micro-scale of turbulence has high values because of the effect of the separation of the flow which is expected to have large eddies than the downstream positions. The macro-scale of turbulence (large eddy size) has a different behaviour from that for the micro-scale of turbulence. At the position x/h $\leq$ 40, the values of the macro-scale are the same for all the distance from the wall (y/R = .35, .68 and 1.0). Downstream of x/h = 40, the values of the macro-scale tend to catch up the undisturbed values. It can be concluded the upstream of x/h = 40, the flow has large eddies of the same order for the whole distance y/R. Downstream of x/h = 40, the large eddies are related to the distance from the wall. Also the presence of the ring inside the pipe affects the large eddies more than the small eddies. The effect of the surface roughness on the large and small eddies is essentially near the wall y/R = .02 - where the surface roughness reduces the size of the eddies in this region compared to that near the smooth surface.

(10) The distribution of the mixing length and the turbulent eddy viscosity behaves the same as the boundary-layer flow downstream of the reattachment. The mixing length and the eddy viscosity return to the fully developed distribution for the flow without ring at 126.6 < x/h < 166 for both the rough and the smooth pipes.

(c) Numerical Predictions

The results presented in Chapter 6 show that:

(1) In the region around the obstacle diffusion is equally important in both x and y directions; there exists no dominant flow direction. In

the region beyond the separated flow, there exists a dominant direction of flow and diffusion is important only in the cross-stream direction. Thus, for numerical convenience, the complete flow domain must be divided into two regions: (a) the recirculating flow region which extends from about 5 obstacle heights upstream of the obstacle to 15 obstacle heights downstream and (b) the boundary-layer region which prevails in front of the obstacle and beyond the recirculating flow region.

(2) The present numerical solution in the region of the recirculating flow proves to be satisfactory in predicting the general flow behaviour around the obstacle. The front separation (upstream of the obstacle) and the downstream separation are quite clear in the present solution. However, the length of the separated flow downstream of the obstacle (reattachment length) is not the same as the one obtained experimentally. This disparity exists in the case of both the rough and smooth surfaces. The numerically predicted, reattachment length is about 40% more than the length obtained experimentally, in the case of the rough plate and that of about 60% for the smooth plate. This disparity could be due to the unsteady flow in this region (Abbott and Kline (1962)). The point of the reattachment on the front surface of the obstacle is in good agreement with the experimental results.

(3) Any change of the constant C_1, C_2, σ_k and σ_ε in the kinetic energy and dissipation rate equations affects the stream line pattern around the obstacle. This affect is seen in the length of the separation zones upstream and downstream of the obstacle (Figs. (6.3) and (6.4)). The nearest prediction to the experimental results is obtained by the constants recommended by Launder and Spalding (1974).

(4) In the boundary-layer flow region the predicted mean velocity and kinetic energy distributions for the smooth plate are in good agreement

with the experimental results. In the smooth plate case, the wall function (law of the wall) applied in the near wall region does not affect the solution for the mean velocity and the kinetic energy. The value of the friction factor calculated, numerically from the wall function is in good agreement with the experimental results up to $x/h = 20$ downstream of the reattachment. Further downstream $x/h = 20$, the disparity between the predicted friction coefficient and the experimental one increases. In this region the predicted value is less than the experimental one by about 25%.

(5) The prediction of the velocity and kinetic energy distributions for the rough plate is poor. This may be due to the omission of the effect of the surface roughness in the present analysis.

(6) Considering the disparity between the calculated and measured mean velocity profiles for the rough surface, the boundary-layer integral thickness δ^* and θ are not well predicted (about 60% more than the experimental results). The values of δ^* and θ for the smooth surface are in good agreement with the experimental results. The predicted shape parameter H for both the rough and smooth plates is in good agreement with experimental data. It can be concluded that the present numerical solution gives a satisfactory agreement with respect to the experimental data for the smooth surface more than in the case of the rough surface.

7.3 SUGGESTIONS FOR FUTURE WORK

(1) To provide more complete experimental data against which to compare predicted flow patterns and, thereby, enabling improvements in the calculation procedures and turbulence modelling - extension of the experimental study is recommended along the following lines:

(a) In the recirculating flow region and inside the separated bubble, measurments of all three mean velocity components be encouraged. A laser-Doppler anemometer is the convenient instrument for performing these measurements. This laser-Doppler anemometer has the advantage of not disturbing the flow and having a better response time for detecting turbulent fluctuations. These measurements should be directed to providing information on the boundary of the recirculating flow, region flow, and the flow near the top edges of the obstacle where the shear layer emanates from these edges.

(b) Experiments for different geometrical parameters, such as the aspect ratio or the boundary-layer to the obstacle height ratio are recommended. These experiments would provide a wide choice of data for testing the predictions around the obstacle.

(c) The influence of the surface roughness on the recirculating flow region and the recovery of the flow can be detected by using a different surface roughness in both boundary-layer and pipe flow. Therefore, an extension of the experimental study is recommended for different rough surfaces (or different h_s/h, where h_s is the surface roughness height and h is the height of the obstacle)

(2) In the present numerical solution the stream function ψ and the vorticity ω were used as the dependent variables. It is interesting to use the method proposed by Patankar and Spalding (1972) where the dependent variablesin their method are the velocities U, V and the pressure P. This method may provide a better solution especially for the rough surface.

APPENDIX A

Statistical Examination of the Rough Surface

Method for calculating the statistical properties of the rough surface was made by Musker (1978) in the University of Liverpool. This method can be evaluate four different roughness heights, skewness and flatness of the surface profile. The method can be summarized in the following paragraphs.

A thixotropic (free flowing) silicon rubber post was used to obtain the profile of the surface roughness. The correspoinding rubber negative was cut through the seam and laid out on a flat board with its rough side uppermost. The rubber was then cut, with an unused surgical scalpel, along the lines coded by Z1, Z2, Z3 and Z4 as shown in Fig. (A.1). By this method there were two profiles in the direction of the flow and the other two were perpendicular to the flow direction. The four rectangular strips of the rubber containing the four profiles to be measured were mounted individually on a flat blockboard. A thin film of adhesive was used to hold the rubber on the blockboard.

A shadowgraph machine with a magnification factor of 25 was used during the tracings of the surface profiles. The length of each sample was 50mm corresponding to a trace of length 1.25m. The four profiles are shown in Fig. (A.1). Digital records of the profiles were obtained using a Marconi digitising table. A rectangular 'window' measuring 40mm by 1250 mm, was drawn around each tracing of a profile and the tracing paper was then fixed to the digitising table. The table could be regarded as a Cartesian mapping space and the coordinates of a point were sent to a buffer register by means of a cross-wire cursor. Before the profile was digitised the corner points of the rectangular window

were sent to the registers using a push-button on the cursor. These were used to apply a transformation from the table, coordinates to window-coordinates. Each point registered by the cursor was sent automatically to a tape-punching machine. A total of at least one thousand points were recorded for each profile. The paper tape records were used to create data files onto the disc storage system of the 1906S computer.

The first part of the computer program used to analyse the profiles consisted of the determination of a mean line through the profile. An interpolation procedure was used to convert the profile points so that they corresponded to 1001 equally spaced intervals of length so microns in the direction. Then a least-squares straight line was computed. The Y axis referred to surface height in microns. Then all data needed to calculate the roughness height of the surface was available. The peak-to-valley height is defined as the difference between the highest peak and lowest valley. The ten point height is the difference between the average of the five highest peaks and the five lowest valleys. The centre line average height is defined to be the quantity:

$$\frac{1}{n} \sum_{i=1}^{i=n} |Y_i| \qquad (A.1)$$

where n is the number of sampled height coordinates per profile (= 1001). Finally, the root-mean square height is simply the standard deviation of the profile about the mean line:

$$\left[\frac{1}{n-1} \sum_{i=1}^{i=n} Y_i^2 \right]^{1/2} \qquad (A.2)$$

The skewness of the height distribution is the quantity,

$$\frac{\frac{1}{n} \sum_{i=1}^{i=n} Y_i^3}{\left[\frac{1}{n-1} \sum_{i=1}^{i=n} Y_i^2 \right]^{3/2}} \qquad (A.3)$$

and the flatness is the quantity,

$$\frac{\frac{1}{n}\sum_{i=1}^{i=n} Y_i^4}{\left[\frac{1}{n-1}\sum_{i=1}^{i=n} Y_i^2\right]^2} \qquad (A.4)$$

For a Gaussian height distribution the skewness and the flatness are known to be 0 and 3.0 respectively. A positive skewness implies that the peaks are more prominent than the valleys (and vice versa for negative skewness). A flatness greater than 3 describes profiles with exaggerated peaks and valleys. For flatness less than 3 the surface is associated with rather flat profiles.

The results for the four heights of the surface roughness, the skewness and flatness factors are shown in table (A.1).

TABLE (A.1)

Results of the analysis of the rough surface

PROFILE CODE	PEAK-TO-VALLEY HEIGHT	TEN-POINT HEIGHT	CENTRE-LINE AVERAGE HEIGHT	STANDARD DEVIATION	MAXIMUM PEAK FROM MEAN	MINIMUM VALLEY FROM MEAN	SKEWNESS	FLATNESS
21	929	913	120	177	573	-356	1.0	3.82
22	944	920	120	157	551	-393	0.57	3.8
23	1282	881	138	172	422	-860	.086	3.2
24	1226	1204	165	215	885	-341	1.256	5.3
AVERAGE	1095	980	136	180	608	488	0.728	4.03

APPENDIX B

The Wall Function

Close to the solid walls, since the variations of flow properties are much steeper, the momentum transport processes were modelled through the wall function (Launder and Spalding (1974)). The first feature of the method is to locate all the finite-difference grid nodes in the fully turbulent region. Thus the nearest - to wall node - is located sufficiently far from the wall where the Reynold's number of the turbulence ($\equiv \rho k^{1/2} \ell / \mu_e$, where $\ell \equiv k^{3/2}/\varepsilon$) is much greater than unity. It is then assumed that a logarithmic velocity profile prevails in the region near the wall. For a smooth wall, this law can be expressed (Schlichting, 1968) as:

$$\frac{U}{u_o} = \frac{1}{\kappa} \ell n \, (Ey^*) \tag{B.1}$$

where E is a constant dependent on the surface roughness.

$$u_o = (\tau_w/\rho)^{1/2} \tag{B.2}$$

and

$$y^* = \frac{y_p u_o}{\nu} \tag{B.3}$$

Here, u_o is the "friction velocity, τ_w is the wall shear stress and y_p is the normal distance from the wall. κ is the von Karman constant with a value of 0.4. E is a function of the wall roughness, approximately equal to 9.0 for a smooth wall.

Further, in the uniform shear stress layer, the general and dissipation of k are nearly in balance and can be shown that

$$\tau_p = \tau_w = \rho \, C_\mu^{1/2} k_p \tag{B.4}$$

where τ_p and k_p are the values of the shear stress and the kinetic energy at the nearest node to the wall.

By the use of Eqn. (4-C) in conjunction with (1.8) the shear stress can be related to the kinetic energy of the turbulence through the relation

$$\tau_p = \frac{\rho \kappa C_\mu^{1/2} k_p^{1/2} U_p}{\ell n \left[E y_p C_\mu^{1/4} \rho k_p^{1/2} / \mu\right]} \tag{B.5}$$

The energy dissipation rate ε_p near the wall is fixed by the requirement that the length scale varies linearly with the distance from the wall; thus:

$$\varepsilon_p = C_\mu^{1/2} k_p^{3/2} / \kappa y_p \tag{B.6}$$

The near wall turbulence energy k_p is obtained from the direct solution of the regular energy equation, but with the following modifications:

(i) the diffussion of k to the wall is set to zero: i.e.,

$$\left(\frac{\partial k}{\partial y}\right)_{wall} = 0 \tag{B.7}$$

(ii) the general term G, defined by Eqn. (6.14b) is modified to account for the wall shear stress, as defined by Eqn. (6-C), by noting that for a finite-difference cell of volume δV,

$$\int_V \mu_t \left(\frac{\partial U}{\partial y} + \frac{\partial V}{\partial x}\right)^2 dv \simeq \tau_w (U_p - U_w) \, \delta V / y_p, \tag{B.8}$$

where U_p is the velocity at the near wall node and U_w is the velocity at the wall.

APPENDIX C

A COMPUTER PROGRAM FOR THE RECIRCULATING FLOW REGION

This Appendix presents a computer program for the calculation of turbulent shear flow around a two-dimensional obstacle (rectangular cross-section bar) attached to rough and smooth surfaces.

The following list contains information about only the more important variables used in this program.

List of Fortran Symbols

Fortran Symbol	Meaning
BNK, BSK, BEK, BWK	Coefficients in the diffusion terms of the finite-difference equation for the turbulent Kinetic energy
BNE, BSE, BEE, BWE	Coefficients in the diffusion terms of the finite-difference equation for the turbulent energy dissipation
CNS, CSS, CES, CWS	Coefficient in the general substitution formula (Eqn. (6.16a)) for the stream function
CNK, CSK, CEK, CWK	Coefficient in the general substitution formula (Eqn. (6.16a)) for the turbulent Kinetic energy
CNE, CSE, CEE, CWE	Coefficient in the general substitution formula (Eqn. (6.16a)) for the turbulent energy dissipation
CK1, CK2, CM	Constants C_1, C_2 and C_μ
D1	σ_k Eqn. (6.12a)
D2	σ_ε Eqn. (6.13)
E(I, J)	Turbulent energy dissipation
L	Number of grid lines (in y-direction) above the obstacle
MM	Number of gride lines in y-direction
NN	Number of grid lines in x-direction

Fortran Symbol	Meaning
S(I, J)	Stream function ψ
SE	Source term for the turbulent energy dissipation
SEP	Coefficient in the linear form of the source term appearing in the finite-difference equation for the turbulent energy dissipation
SK	Source term for the turbulent Kinetic energy
SKP	Coefficient in the linear form of the source term appearing in the finite-difference equation for the turbulent Kinetic energy
W(I, J)	Vorticity ω

Program Listing

The following Fortran statements are a complete listing of the used program of Appendix C.

Note:

The computer program shown below is the one used for the calculation of the turbulent shear flow around the two-dimensional obstacle (ridge) attached to the rough plate.

```
JOB EM28AR,,RMJAP,CP76(TD1280,P2000,SP)
ATTACH(MYLIB,LIBNAGFTNSCM,ID=LIBAPPL)
LIBRARY(MYLIB)
FTN(R=3)
LDSET (MAP=R/ZZZZMP,PRESET=NGINF)
LGO(PL=10000)
####S
      PROGRAM ABDA4(INPUT,OUTPUT,TAPE5=INPUT,TAPE6=OUTPUT)
      DIMENSION K(48,20),E(48,20),X(48),Y(20),U(48,20),AQ(48,20)
      DIMENSION S(48,20),W(48,20),V(48,20),KE(48,20),DK(48,20)
      DIMENSION DE(48,20),KT(48,20),QS(48,20),QK(48,20),SE(48,20)
      DIMENSION Q(48,20),DUX(48,20),DUY(48,20),DVX(48,20),DVY(48,20
      DIMENSION SK(48,20),SKP(48,20),SEP(48,20),EK(48,20)
      INTEGER H
      REAL K,KE,KT,NE
      KKK=6000
      N=47
      M=19
      NN=N+1
C     ROUGH PLATE
      MM=M+1
      H=0
C     NULL VARIABLES
C**********************
      DO 12 I=1,NN
      DO 14 J=1,MM
      W(I,J)=0.0
      S(I,J)=0.0
      K(I,J)=0.0
      E(I,J)=0.0
      U(I,J)=0.0
      V(I,J)=0.0
      DUX(I,J)=0.0
      DVX(I,J)=0.0
      DUY(I,J)=0.0
      DVY(I,J)=0.0
   14 CONTINUE
   12 CONTINUE
C*****CONSTANTS
C******************
      CK1=1.35
      CK2=1.85
      CM=0.095
      D1=1.0
      D2=1.3
C*****GRID POINTS
C******************
      X(1)=0.0
      Y(1)=0.0
      DO 1 I=2,6
```

```
      X(I)=X(I-1)+0.01
    1 CONTINUE
      DO 2 I=7,13
    2 X(I)=X(I-1)+0.005
      DO 3 I=14,18
    3 X(I)=X(I-1)+0.002
      DO 4 I=19,20
    4 X(I)=X(I-1)+0.004
      DO 15 I=21,22
   15 X(I)=X(I-1)+0.006
      X(23)=X(22)+0.008
      DO 17 I=24,25
   17 X(I)=X(I-1)+0.006
      DO 19 I=26,30
   19 X(I)=X(I-1)+0.002
      X(31)=X(30)+0.004
      DO 21 I=32,33
   21 X(I)=X(I-1)+0.006
      DO 23 I=34,37
   23 X(I)=X(I-1)+0.01
      DO 24 I=38,41
   24 X(I)=X(I-1)+0.02
      DO 25 I=42,46
   25 X(I)=X(I-1)+0.03
      X(47)=X(46)+0.01
      X(48)=X(47)+0.01
      DO 26 J=2,6
   26 Y(J)=Y(J-1)+0.002
      Y(7)=Y(6)+0.004
      DO 27 J=8,12
   27 Y(J)=Y(J-1)+0.002
      DO 28 J=13,15
   28 Y(J)=Y(J-1)+0.004
      Y(16)=Y(15)+0.006
      DO 29 J=17,18
   29 Y(J)=Y(J-1)+0.008
      DO 30 J=19,20
   30 Y(J)=Y(J-1)+0.01
      U1=21.0
      D=.042
      DO 5 J=2,16
      U(1,J)=3.14*(ALOG(Y(J)*0.842*1.E5)-1.23+0.3*(6.*(Y(J)/D)**2
     1-4.*(Y(J)/D)**3)+(Y(J)/D)**2-(Y(J)/D)**3)
      W(1,J)=-(3.14*(1./Y(J)*.3*(12.*Y(J)/D**2-12.*(Y(J)/D)**2/D)
     1+2.*Y(J)/D**2-3.*(Y(J)/D)**2/D))
    5 CONTINUE
      DO 6 I=17,MM
      U(1,I)=U1
      W(1,I)=0.0
    6 CONTINUE
```

```
      DO 34 J=2,MM
      K(1,J)=0.001*U1**2
   34 E(1,J)=(0.09)**0.75*K(1,J)*SQRT(K(1,J))/(0.41*Y(J))
      S(1,1)=0.0
      DO 444 J=2,MM
  444 S(1,J)=S(1,J-1)+U(1,J)*(Y(J)-Y(J-1))
      WRITE(6,77)(I,K(1,I),E(1,I),S(1,I),U(1,I),W(1,I),I=1,MM)
   77 FORMAT(1H ,I5,5F20.5)
      DO 7 I=1,20
      V(1,I)=0.0
    7 CONTINUE
      DO 8 I=1,NN
      U(I,MM)=U1
      V(I,MM)=0.0
      W(I,MM)=0.0
      S(I,MM)=S(1,MM)
      K(I,MM)=K(1,MM)
      E(I,MM)=E(1,MM)
    8 CONTINUE
      DO 9 I=1,MM
      V(NN,I)=0.0
    9 CONTINUE
      DO 10 I=1,17
      DO 16 J=28,NN
      U(I,1)=0.0
      U(J,1)=0.0
      V(I,1)=0.0
      V(J,1)=0.0
      S(I,1)=0.0
      S(J,1)=0.0
      K(I,1)=0.0
      K(J,1)=0.0
      E(I,1)=0.0
      E(J,1)=0.0
   16 CONTINUE
   10 CONTINUE
      DO 11 I=17,28
      DO 18 J=1,10
      U(I,J)=0.0
      V(I,J)=0.0
      S(I,J)=0.0
      K(I,J)=0.0
      E(I,J)=0.0
      W(I,J)=0.0
   18 CONTINUE
   11 CONTINUE
      DO 20 I=1,NN
      DO 22 J=1,MM
      KE(I,J)=1.53E-5
      DK(I,J)=KE(I,J)
```

```
      DE(I,J)=1.18E-5
      KT(I,J)=1.53E-5
   22 CONTINUE
   20 CONTINUE
      DO 51 I5=2,N
      K(I5,18)=K(1,18)
      K(I5,19)=K(1,19)
   51 CONTINUE
      DO 53 I4=2,N
      E(I4,18)=E(1,18)
      E(I4,19)=E(1,19)
   53 CONTINUE
C     SOLUTION
C     VORTICITY
C*********************
  105 DO 306 I=2,N
      DO 307 J=2,M
      IF(I.GE.29) GOTO 116
      IF(I.GE.17) GOTO 117
  116 DV=0.25*(X(I+1)-X(I-1))*(Y(J+1)-Y(J-1))
      AN1=S(I+1,J+1)+S(I+1,J)-S(I-1,J+1)-S(I-1,J)
      AS1=S(I-1,J-1)+S(I-1,J)-S(I+1,J-1)-S(I+1,J)
      AE1=S(I+1,J-1)+S(I,J-1)-S(I+1,J+1)-S(I,J+1)
      AW1=S(I-1,J+1)+S(I,J+1)-S(I-1,J-1)-S(I,J-1)
      AN=0.125*(AN1+ABS(AN1))
      AS=0.125*(AS1+ABS(AS1))
      AE=0.125*(AE1+ABS(AE1))
      AW=0.125*(AW1+ABS(AW1))
      G=AN+AS+AE+AW
      BN=0.5*((X(I+1)-X(I-1))/(Y(J+1)-Y(J)))
      BS=0.5*((X(I+1)-X(I-1))/(Y(J)-Y(J-1)))
      BE=0.5*((Y(J+1)-Y(J-1))/(X(I+1)-X(I)))
      BW=0.5*((Y(J+1)-Y(J-1))/(X(I)-X(I-1)))
      F=BN+BS+BE+BW
      CN=(AN+BN*KE(I,J+1))/(G+F*KE(I,J))
      CS=(AS+BS*KE(I,J-1))/(G+F*KE(I,J))
      CE=(AE+BE*KE(I+1,J))/(G+F*KE(I,J))
      CW=(AW+BW*KE(I-1,J))/(G+F*KE(I,J))
      IF(J.EQ.2)GO TO 405
      W(I,J)=CE*W(I+1,J)+CW*W(I-1,J)+CN*W(I,J+1)+CS*W(I,J-1)
      GO TO 406
  405 VD=3.0*CS*(S(I,J)-S(I,J-1))/(Y(J)-Y(J-1))**2
      W(I,J)=CE*W(I+1,J)+CW*W(I-1,J)+CN*W(I,J+1)-VD
      W(I,J)=W(I,J)/(1.0-0.5*CS)
  406 DO 220 L=2,M
      W(NN,L)=W(N,L)
  220 CONTINUE
      DO 50 I3=1,N
      W(I3,M)=W(I3,MM)
   50 CONTINUE
```

```
C       STREAM
        CSN=BN/F
        CSS=BS/F
        CSE=BE/F
        CSW=BW/F
        Q(I,J)=W(I,J)*DV/F
        S(I,J)=CSN*S(I,J+1)+CSS*S(I,J-1)+CSE*S(I+1,J)+CSW*S(I-1,J)+Q(I,J
        DO 260 LL=2,M
        S(NN,LL)=S(N,LL)
  260   CONTINUE
C       VELOCITY
        CY1=(Y(J)-Y(J-1))/(Y(J+1)-Y(J))
        CY2=1.0/CY1
        CY3=CY1/(Y(J+1)-Y(J-1))
        CY4=CY2/(Y(J+1)-Y(J-1))
        U(I,J)=CY3*(S(I,J+1)-S(I,J))+CY4*(S(I,J)-S(I,J-1))
        CX1=(X(I)-X(I-1))/(X(I+1)-X(I))
        CX2=1.0/CX1
        CX3=CX1/(X(I+1)-X(I-1))
        CX4=CX3/(X(I+1)-X(I-1))
        V(I,J)=(CX3*(S(I+1,J)-S(I,J))+CX4*(S(I,J)-S(I-1,J)))
        DO 41 II1=2,N
        U(II1,M)=U(II1,MM)
        V(II1,M)=V(II1,MM)
   41   CONTINUE
        DO 710 L1=2,M
        V(NN,L1)=0.0
        V(N,L1)=0.0
        V(N-1,L1)=0.0
        U(NN,L1)=U(N,L1)
  710   CONTINUE
        DO 44 J9=2,10
   44   U(16,J9)=0.0
C       KINETIC ENERGY
        IF(J.GE.18)GOTO 589
        IF(J.LE.2)GOTO 589
        BNK=((DK(I,J+1)+DK(I,J))/4.0)*(BN/0.5)
        BSK=((DK(I,J-1)+DK(I,J))/4.0)*(BS/0.5)
        BEK=((DK(I+1,J)+DK(I,J))/4.0)*(BE/0.5)
        BWK=((DK(I-1,J)+DK(I,J))/4.0)*(BW/0.5)
        FK=BNK+BSK+BEK+BWK
        DUX(I,J)=CX3*(U(I+1,J)-U(I,J))+CX4*(U(I,J)-U(I-1,J))
        DVY(I,J)=CY3*(V(I,J+1)-V(I,J))+CY4*(V(I,J)-V(I,J-1))
        DUY(I,J)=CY3*(U(I,J+1)-U(I,J))+CY4*(U(I,J)-U(I,J-1))
        DVX(I,J)=CX3*(V(I+1,J)-V(I,J))+CX4*(V(I,J)-V(I-1,J))
        CNK=(AN+BNK)/(G+FK)
        CSK=(AS+BSK)/(G+FK)
        CEK=(AN+BEK)/(G+FK)
        CWK=(AW+BWK)/(G+FK)
        QS(I,J)=2*((DUX(I,J)**2+DVY(I,J)**2)+(DUY(I,J)+DVX(I,J))**2)
```

```
      QK(I,J)=KT(I,J)*QS(I,J)
      SK(I,J)=(1.5*QK(I,J)+(CK2-1.)*1.2*E(I,J))*DV/(G+FK)
      SKP(I,J)=-(CK2*1.2*F(I,J)*0.5*QK(I,J))*DV/((K(I,J)+1.E-40)*(G+FK))
      K(I,J)=CNK*K(I,J+1)+CSK*K(I,J-1)+CEK*K(I+1,J)+CWK*K(I-1,J)+SK(I,J)
      K(I,J)=K(I,J)/(1.-SKP(I,J))
      DO 800 LL1=2,M
      K(NN,LL1)=K(N,LL1)
  800 CONTINUE
C     ENERGY DISIPATION
      BNE=((DE(I,J+1)+DE(I,J))/4.0)*(BN/0.5)
      BSE=((DE(I,J-1)+DE(I,J))/4.0)*(BS/0.5)
      BEE=((DE(I+1,J)+DE(I,J))/4.0)*(BE/0.5)
      BWE=((DE(I-1,J)+DE(I,J))/4.0)*(BW/0.5)
      FE=BNE+BSE+BEE+BWE
      EK(I,J)=E(I,J)/(K(I,J)+1.E-40)
      SE(I,J)=(CK1*QK(I,J)+(CK2-1.)*1.2*E(I,J))*EK(I,J)*DV/(G+FE)
      SEP(I,J)=-(1.2*(2*CK2-1.)*EK(I,J)*DV/(G+FE))
      CNE=(AN+BNE)/(G+FE)
      CSE=(AS+BSE)/(G+FE)
      CEE=(AE+BEE)/(G+FE)
      CWE=(AW+BWE)/(G+FE)
      E(I,J)=CNE*E(I,J+1)+CSE*E(I,J-1)+CEE*E(I+1,J)+CWE*E(I-1,J)+SE(I,J)
      E(I,J)=E(I,J)/(1.0-SEP(I,J))
      DO 900 LL2=2,M
      E(NN,LL2)=E(N,LL2)
  900 CONTINUE
      KT(I,J)=CM*1.2*(K(I,J))**2/(E(I,J)+1.E-40)
      KE(I,J)=KT(I,J)+1.53E-5
      DK(I,J)=KE(I,J)/D1+1.53E-5
      DE(I,J)=KE(I,J)/D2+1.53E-5
      GO TO 307
  589 KT(I,J)=1.53E-5
      KE(I,J)=KT(I,J)
      DK(I,J)=KE(I,J)
      DE(I,J)=KE(I,J)
      GOTO 307
C******SOLUTION ABOVE THE RIDGE
C*********************************
  117 DO 109 L=11,M
      DV=0.25*(X(I+1)-X(I-1))*(Y(L+1)-Y(L-1))
      AN1=S(I+1,L+1)+S(I+1,L)-S(I-1,L+1)-S(I-1,L)
      AS1=S(I-1,L-1)+S(I-1,L)-S(I+1,L-1)-S(I+1,L)
      AE1=S(I+1,L-1)+S(I,L-1)-S(I+1,L+1)-S(I,L+1)
      AW1=S(I-1,L+1)+S(I,L+1)-S(I-1,L-1)-S(I,L-1)
      AN=0.125*(AN1+ABS(AN1))
      AS=0.125*(AS1+ABS(AS1))
      AE=0.125*(AE1+ABS(AE1))
      AW=0.125*(AW1+ABS(AW1))
      G=AN+AS+AE+AW
      BN=0.5*((X(I+1)-X(I-1))/(Y(L+1)-Y(L)))
```

```
      BS=0.5*((X(I+1)-X(I-1))/(Y(L)-Y(L-1)))
      BE=0.5*((Y(L+1)-Y(L-1))/(X(I+1)-X(I)))
      BW=0.5*((Y(L+1)-Y(L-1))/(X(I)-X(I-1)))
      F=BN+BS+BE+BW
      CN=(AN+BN*KE(I,L+1))/(G+F*KE(I,L))
      CS=(AS+BS*KE(I,L-1))/(G+F*KE(I,L))
      CE=(AE+BE*KE(I+1,L))/(G+F*KE(I,L))
      CW=(AW+BW*KE(I-1,L))/(G+F*KE(I,L))
      IF(L.EQ.11)GO TO 201
      W(I,L)=CE*W(I+1,L)+CW*W(I-1,L)+CN*W(I,L+1)+CS*W(I,L-1)
      GO TO 202
  201 VD=3.0*C7*(S(I,L)-S(I,L-1))/(Y(L)-Y(L-1))**2
      W(I,L)=CE*W(I+1,L)+CW*V(I-1,L)+CN*V(I,L+1)-VD
      W(I,L)=W(I,L)/(1.0+0.5*CS)
  202 W(17,11)=-((CNS*S(17,12)+CES*S(18,11)+CWS*S(16,11))*(F/DV))
      IF(I.EQ.17)GOTO 320
      GOTO 350
  320 DO 410 J1=2,9
      W(17,J1)=-((2.0/(X(16)-X(17))**2)*(S(16,J1)-S(17,J1)))
  410 CONTINUE
  350 IF(I.EQ.28)GOTO 322
      GOTO 55
  322 DO 420 J2=2,9
      W(28,J2)=-((2.0/(X(29)-X(28))**2)*(S(29,J2)-S(28,J2)))
  420 CONTINUE
   55 DO 54 I6=1,N
      W(I6,M)=W(I6,MM)
   54 CONTINUE
C     STREAM FUNCTION
      CNS=BN/F
      CSS=BS/F
      CES=BE/F
      CWS=BW/F
      Q(I,L)=W(I,L)*DV/F
      S(I,L)=CNS*S(I,L+1)+CSS*S(I,L-1)+CES*S(I+1,L)+CWS*S(I-1,L)+Q(I,L)
      S(17,11)=S(17,10)
C     VELOCITIES
      CY1=(Y(L)-Y(L-1))/(Y(L+1)-Y(L))
      CY2=1.0/CY1
      CY3=CY1/(Y(L+1)-Y(L-1))
      CY4=CY2/(Y(L+1)-Y(L-1))
      U(I,L)=CY3*(S(I,L+1)-S(I,L))+CY4*(S(I,L)-S(I,L-1))
      CX1=(X(I)-X(I-1))/(X(I+1)-X(I))
      CX2=1.0/CX1
      CX3=CX1/(X(I+1)-X(I-1))
      CX4=CX2/(X(I+1)-X(I-1))

      V(I,L)=(CX3*(S(I+1,L)-S(I,L))+CX4*(S(I,L)-S(I-1,L)))
      DO 42 II2=17,28
      U(II2,M)=U(II2,MM)
```

```
      V(II2,M)=V(II2,MM)
   42 CONTINUE
C     KINETIC ENERGY
      IF(L.GE.18)GOTO 585
      IF(L.LE.11)GOTO 585
      BNK=((DK(I,L+1)+DK(I,L))/4.0)*(2*BN)
      BSK=((DK(I,L-1)+DK(I,L))/4.0)*(2*BS)
      BEK=((DK(I+1,L)+DK(I,L))/4.0)*(2*BE)
      BWK=((DK(I-1,L)+DK(I,L))/4.0)*(2*BW)
      FK=BNK+BSK+BEK+BWK
      DUX(I,L)=CX3*(U(I+1,L)-U(I,L))+CX4*(U(I,L)-U(I-1,L))
      DVY(I,L)=CY3*(V(I,L+1)-V(I,L))+CY4*(V(I,L)-V(I,L-1))
      DUY(I,L)=CY3*(U(I,L+1)-U(I,L))+CY4*(U(I,L)-U(I,L-1))
      DVX(I,L)=CX3*(V(I+1,L)-V(I,L))+CX4*(V(I,L)-V(I-1,L))
      QS(I,L)=2.*((DUX(I,L)**2+DVY(I,L)**2)+(DUY(I,L)+DVX(I,L))**2)
      QK(I,L)=KT(I,L)*QS(I,L)
      SK(I,L)=(1.5*QK(I,L)+(CK2-1.)*1.2*E(I,L))*DV/(G+FK)
      SKP(I,L)=-(1.2*CK2*E(I,L)+0.5*QK(I,L))*DV/((K(I,L)+1.E-40)*(G+FK))
      CNK=(AN+BNK)/(G+FK)
      CSK=(AS+BSK)/(G+FK)
      CEK=(AE+BEK)/(G+FK)
      CWK=(AW+BWK)/(G+FK)
      K(I,L)=CNK*K(I,L+1)+CSK*K(I,L-1)+CEK*K(I+1,L)+CWK*K(I-1,L)+SK(I,L)
      K(I,L)=K(I,L)/(1.0-SKP(I,L))
C     ENERGY DISIPATION
      BNE=((DE(I,L+1)+DE(I,L))/4.0)*(BN/0.5)
      BSE=((DE(I,L-1)+DE(I,L))/4.0)*(BS/0.5)
      BEE=((DE(I+1,L)+DE(I,L))/4.0)*(BE/0.5)
      BWE=((DE(I-1,I)+DE(I,L))/4.0)*(BW/0.5)
      FE=BNE+BSE+BEE+BWE
      EK(I,L)=E(I,L)/(K(I,L)+1.E-40)
      SE(I,L)=(CK1*QK(I,L)+(CK2-1.)*1.2*E(I,L))*EK(I,L)*DV/(G+FE)
      SEP(I,L)=-(1.2*(2*CK2-1.)*EK(I,L))*DV/(G+FE)
      CNE=(AN+BNE)/(G+FE)
      CSE=(AS+BSE)/(G+FE)
      CEE=(AE+BEE)/(G+FE)
      CWE=(AW+BWE)/(G+FE)
      E(I,L)=CNE*E(I,L+1)+CSE*E(I,L-1)+CEE*E(I+1,L)+CWE*E(I-1,L)+SE(I,L)
      E(I,L)=E(I,L)/(1.0-SEP(I,L))
      KT(I,L)=CM*1.2*(K(I,L))**2/(E(I,L)+1.E-40)
      KE(I,L)=KT(I,L)+1.53E-5
      DK(I,L)=KE(I,L)/D1+1.53E-5
      DE(I,L)=KE(I,L)/D2+1.53E-5
      GOTO 109
  585 KT(I,L)=1.53E-5
      KE(I,L)=KT(I,L)
      DK(I,L)=KE(I,L)
      DE(I,L)=KE(I,L)
  109 CONTINUE
      GOTO 306
  307 CONTINUE
  306 CONTINUE
      H=H+1
      IF(H.LE.KKK) GOTO 105
      DO 339 I=1,NN
      DO 338 J=1,MM
      WRITE(6,400)I,J,S(I,J),E(I,J),U(I,J),K(I,J),KT(I,J)
  338 CONTINUE
  339 CONTINUE
      STOP
  400 FORMAT(1H ,2I10,5E20.8)
```

APPENDIX D

A COMPUTER PROGRAM FOR THE BOUNDARY LAYER FLOW

This Appendix presents a computer program for the calculation of turbulent boundary layer flow downstream of the recirculating flow region. The Fortran symbols used in the program are the same as the ones used in Appendix C.

Program Listing

(i) A computer program used for the smooth surface with the wall function in the near wall region.

(ii) A computer program used for the rough surface without the wall function.

(I)

```
JOB EM28SD,,RMJAP,CP76(TD1000,P2000,SP)
ATTACH(MYLIB,LIBNAGFTNSCM,ID=LIBAPPL)
LIBRARY(MYLIB)
FTN(R=3)
LDSET (MAP=B/ZZZZMP,PRESET=NGINF)
LGO(PL=10000)
####S
      PROGRAM ABFF(INPUT,OUTPUT,TAPE5=INPUT,TAPE6=OUTPUT)
      DIMENSION K(51,18),E(51,18),X(51),Y(18),U(51,18)
      DIMENSION S(51,18),W(51,18),KE(51,18),DK(51,18)
      DIMENSION DE(51,18),KT(51,18),QS(51,18),QK(51,18),SE(51,18
      DIMENSION Q(51,18),DUY(51,18),TW(51,18)
      DIMENSION SK(51,18),SKP(51,18),SEP(51,18),EK(51,18)
      INTEGER H
      REAL K,KE,KT
      KKK=6000
      N=50
      M=17
      NN=N+1
      MM=M+1
      H=0
C**********************
C     NULL VARIABLES *
C**********************
      DO 12 I=1,NN
      DO 14 J=1,MM
      W(I,J)=0.0
      S(I,J)=0.0
      K(I,J)=0.0
      E(I,J)=0.0
      U(I,J)=0.0
      DUY(I,J)=0.0
   14 CONTINUE
   12 CONTINUE
C***************************
C     BOUNDARY CONDITIONS *
C***************************
      READ (5,1)(K(1,J),U(1,J),E(1,J),J=1,MM)
    1 FORMAT(3F10.4)
      X(1)=0.0
      Y(1)=0.0
      DO 4 J=2,7
    4 Y(J)=Y(J-1)+0.001
      Y(8)=Y(7)+0.002
      Y(9)=Y(8)+0.002
      DO 3 J=10,14
    3 Y(J)=Y(J-1)+0.004
      Y(15)=Y(14)+0.008
      Y(16)=Y(15)+0.008
      Y(17)=Y(16)+0.006
```

```
      Y(18)=Y(17)+0.008
      DO 13 I=2,11
   13 X(I)=X(I-1)+0.005
      DO 80 I=12,16
   80 X(I)=X(I-1)+0.01
      DO 81 I=17,51
   81 X(I)=X(I-1)+0.02
      DO 82 J=2,MM
   82 KT(1,J)=0.09*K(1,J)*K(1,J)/E(1,J)
      S(1,1)=0.0
      DO 83 J=2,MM
      O1=(Y(J)-Y(J-1))/(Y(J+1)-Y(J))
      O2=1./O1
      O3=O1/(Y(J+1)-Y(J-1))
      O4=O2/(Y(J+1)-Y(J-1))
      W(1,J)=-(O3*(U(1,J+1)-U(1,J))+O4*(U(1,J)-U(1,J-1)))
   83 S(1,J)=S(1,J-1)+U(1,J)*(Y(J)-Y(J-1))
      WRITE(6,77)(I,K(1,I),E(1,I),S(1,I),U(1,I),W(1,I),I=1,MM
   77 FORMAT(1H ,I5,5F10.5)
      DO 8 I=1,NN
      U(I,MM)=U1
      W(I,MM)=0.0
      S(I,MM)=S(1,MM)
      K(I,MM)=K(1,MM)
      E(I,MM)=E(1,MM)
    8 CONTINUE
      DO 10 I=1,NN
      U(I,1)=0.0
      S(I,1)=0.0
      K(I,1)=0.0
      E(I,1)=0.0
   10 CONTINUE
      DO 20 I=1,NN
      DO 22 J=1,MM
      KE(I,J)=1.53E-5
      DK(I,J)=KE(I,J)
      DE(I,J)=1.18E-5
      KT(I,J)=1.53E-5
   22 CONTINUE
   20 CONTINUE
      DO 72 I=2,NN
      DO 72 J=2,MM
   72 K(I,J)=1.0
      DO 51 I5=2,N
      K(I5,15)=K(1,15)
      K(I5,16)=K(1,16)
      K(I5,17)=K(1,17)
   51 CONTINUE
      DO 53 I4=2,N
      E(I4,15)=E(1,15)
```

```
      E(I4,16)=E(1,16)
      E(I4,17)=E(1,17)
   53 CONTINUE
      DO 98 I8=2,NN
      K(I8,2)=K(1,2)
   98 E(I8,2)=E(1,2)
C*********************************************
C     SOLUTION OF FINIT-DIFFERANCE EQUATIONS *
C*********************************************
C     CALCULATION OF THE B"S AND A"S
C*************************************
  105 DO 306 I=2,N
      DO 307 J=2,M
      DV=0.25*(X(I+1)-X(I-1))*(Y(J+1)-Y(J-1))
      AN1=S(I+1,J+1)+S(I+1,J)-S(I-1,J+1)-S(I-1,J)
      AS1=S(I-1,J-1)+S(I-1,J)-S(I+1,J-1)-S(I+1,J)
      AE1=S(I+1,J-1)+S(I,J-1)-S(I+1,J+1)-S(I,J+1)
      AW1=S(I-1,J+1)+S(I,J+1)-S(I-1,J-1)-S(I,J-1)
      BN=0.5*((X(I+1)-X(I-1))/(Y(J+1)-Y(J)))
      BS=0.5*((X(I+1)-X(I-1))/(Y(J)-Y(J-1)))
C     BE=0.5*((Y(J+1)-Y(J-1))/(X(I+1)-X(I)))
C     BW=0.5*((Y(J+1)-Y(J-1))/(X(I)-X(I-1)))
      BE=0.0
      BW=0.0
      F=BN+BS+BE+BW
      AN=0.125*(AN1+ABS(AN1))
      AS=0.125*(AS1+ABS(AS1))
      AE=0.125*(AE1+ABS(AE1))
      AW=0.125*(AW1+ABS(AW1))
      G=AN+AS+AE+AW
C***************
C     VELOCITY *
C***************
      CY1=(Y(J)-Y(J-1))/(Y(J+1)-Y(J))
      CY2=1.0/C36
      CY3=CY1/(Y(J+1)-Y(J-1))
      CY4=CY2/(Y(J+1)-Y(J-1))
      U(I,J)=CY3*(S(I,J+1)-S(I,J))+CY4*(S(I,J)-S(I,J-1))
      DO 41 II1=2,N
      U(II1,M)=U(II1,MM)
   41 CONTINUE
      DO 710 L1=2,M
      U(NN,L1)=U(N,L1)
  710 CONTINUE
C**********************
C     KINETIC ENERGY *
C**********************
      IF(J.GE.16)GOTO 589
      BNK=((DK(I,J+1)+DK(I,J))/4.0)*(2*BN)
      BSK=((DK(I,J-1)+DK(I,J))/4.0)*(2*BS)
```

```
      BEK=((DK(I+1,J)+DK(I,J))/4.0)*(2*BE)
      BWK=((DK(I-1,J)+DK(I,J))/4.0)*(2*BW)
      FK=BNK+BSK+BEK+BWK
      DUY(I,J)=CY3*(U(I,J+1)-U(I,J))+CY4*(U(I,J)-U(I,J-1))
      CNK=(AN+BNK)/(G+FK)
      CSK=(AS+BSK)/(G+FK)
      CEK=(AE+BEK)/(G+FK)
      CWK=(AW+BWK)/(G+FK)
      IF(J.GT.2)GO TO 99
      K(I,J)=CNK*K(I,J+1)+CSK*K(I,J-1)+CEK*K(I+1,J)+CWK*K(I-1,J)
      RSK=1.2*SQRT(ABS(K(I,J)))
      CYPTW=0.547*(Y(J)-Y(J-1))/1.53E-5
      YPUSTW=RSK*CYPTW
      TW(I,J)=0.224*U(I,J)*RSK/ALOG(9.0*YPUSTW)
      ATW=ABS(TW(I,J))
      VOLGF=DV/(G+FK)
      SK(I,J)=ATW*U(I,J)*VOLGF
      SKP(I,J)=-0.128*K(I,J)*U(I,J)*VOLGF/((Y(J)-Y(J-1))*(ATW+1.E-30
      GO TO 801
   99 QS(I,J)=DUY(I,J)**2
      QK(I,J)=KT(I,J)*QS(I,J)
      SK(I,J)=(1.5*QK(I,J)+1.08*E(I,J))*DV/(G+FK)
      SKP(I,J)=-(2.48*E(I,J)+0.5*QK(I,J))*DV/((K(I,J)+1.E-40)*(G+FK)
  801 K(I,J)=CNK*K(I,J+1)+CSK*K(I,J-1)+CEK*K(I+1,J)+CWK*K(I-1,J)+SK(
      K(I,J)=K(I,J)/(1.-SKP(I,J))
      DO 800 LL1=2,M
      K(NN,LL1)=K(N,LL1)
  800 CONTINUE
C*************************
C     ENERGY DISIPATION *
C*************************
      BNE=((DE(I,J+1)+DE(I,J))/4.0)*(2*BN)
      BSE=((DE(I,J-1)+DE(I,J))/4.0)*(2*BS)
      BEE=((DE(I+1,J)+DE(I,J))/4.0)*(2*BE)
      BWE=((DE(I-1,J)+DE(I,J))/4.0)*(2*BW)
      FE=BNE+BSE+BEE+BWE
      IF(J.GT.2)GO TO 100
      CDK=0.3*K(I,J)
      VOLGF4=DV/(G+FE)
      E(I,J)=CDK*((ABS(CDK)**0.5))/(0.41*(Y(J)-Y(J-1)))
      GO TO 101
  100 EK(I,J)=E(I,J)/(K(I,J)+1.E-40)
      SE(I,J)=(1.44*QK(I,J)+1.08*E(I,J))*EK(I,J)*DV/(G+FE)
      SEP(I,J)=-(3.36*EK(I,J)*DV/(G+FE))
      CNE=(AN+BNE)/(G+FE)
      CSE=(AS+BSE)/(G+FE)
      CEE=(AE+BEE)/(G+FE)
      CWE=(AW+BWE)/(G+FE)
      E(I,J)=CNE*E(I,J+1)+CSE*E(I,J-1)+CEE*E(I+1,J)+CWE*E(I-1,J)+SE(
      E(I,J)=E(I,J)/(1.0-SEP(I,J))
```

```
      DO 900 LL2=2,M
      E(NN,LL2)=E(N,LL2)
  900 CONTINUE
  101 KT(I,J)=0.108*(K(I,J))**2/(E(I,J)*1.E-40)
      KE(I,J)=KT(I,J)+1.53E-5
      DK(I,J)=KE(I,J)
      DE(I,J)=KE(I,J)/1.3
      GO TO 300
  589 KT(I,J)=1.53E-5
      KE(I,J)=KT(I,J)
      DK(I,J)=KE(I,J)
      DE(I,J)=KE(I,J)
C**********************
C     VORTICITY        *
C**********************
  300 CN=(AN+BN*KE(I,J+1))/(G+F*KE(I,J))
      CS=(AS+BS*KE(I,J-1))/(G+F*KE(I,J))
      CE=(AE+BE*KE(I+1,J))/(G+F*KE(I,J))
      CW=(AW+BW*KE(I-1,J))/(G+F*KE(I,J))
      W(I,J)=CE*W(I+1,J)+CW*W(I-1,J)+CN*W(I,J+1)+CS*W(I,J-1)
      DO 405 I1=2,N
  405 W(I1,1)=-((2.0/Y(2)**2)*(S(I1,2)-S(I1,1)))
      DO 220 L=2,M
      W(NN,L)=W(N,L)
  220 CONTINUE
      DO 50 I3=1,N
      W(I3,M)=W(I3,MM)
   50 CONTINUE
C***************
C     STREAM   *
C***************
      CNS=BN/F
      CSS=BS/F
      CES=0.0
      CWS=0.0
      Q(I,J)=W(I,J)*DV/F
      S(I,J)=CNS*S(I,J+1)+CSS*S(I,J-1)+CES*S(I+1,J)+CWS*S(I-1,J)+Q(I,J)
      DO 260 LL=2,M
      S(NN,LL)=S(N,LL)
  260 CONTINUE
  307 CONTINUE
  306 CONTINUE
      H=H+1
      IF(H.LE.KKK) GOTO 105
      DO 339 I=1,NN
      DO 338 J=1,MM
      WRITE(6,400)I,J,S(I,J),TW(I,J),U(I,J),K(I,J),KT(I,J)
  338 CONTINUE
  339 CONTINUE
      STOP
  400 FORMAT(1H ,2I10,5E20.8)
      END
####S
```

(II) .

```
JOB E128RD,,RUJAP,CP76(TD1000,P2000,SP)
ATTACH(MYLIB,LIBRAGETUSCH,ID=LIBAPPL)
LIBRARY(MYLIB)
FTN(R=3)
LDSET (MAP=B/ZZZZUP,PRESET=NGINF)
LGO(PL=10000)
####S
      PROGRAM ABUN(INPUT,OUTPUT,TAPE5=INPUT,TAPE6=OUTPUT)
      DIMENSION K(51,22),E(51,22),X(51),Y(22),U(51,22)
      DIMENSION S(51,22),V(51,22),KE(51,22),DK(51,22)
      DIMENSION DE(51,22),KT(51,22),QS(51,22),QK(51,22),SE(51,22)
      DIMENSION Q(51,22),DUY(51,22)
      DIMENSION SK(51,22),SKP(51,22),SEP(51,22),EK(51,22)
      INTEGER H
      REAL K,KE,KT
      KKK=6000
      N=50
      M=21
      NN=N+1
      MM=M+1
      H=0
C**********************
C     NULL VARIABLES *
C**********************
      DO 12 I=1,NN
      DO 14 J=1,MM
      U(I,J)=0.0
      S(I,J)=0.0
      K(I,J)=0.0
      E(I,J)=0.0
      U(I,J)=0.0
      DUY(I,J)=0.0
   14 CONTINUE
   12 CONTINUE
C*****************************************
C     BOUNDARY CONDITIONS AND GRID POINTS *
C*****************************************
      READ (5,1)(K(1,J),U(1,J),J=1,MM)
    1 FORMAT(2F10.4)
      X(1)=0.0
      Y(1)=0.0
      DO 4 J=2,7
    4 Y(J)=Y(J-1)+0.001
      DO 3 J=8,9
    3 Y(J)=Y(J-1)+0.002
      DO 15 J=10,11
   15 Y(J)=Y(J-1)+0.004
      DO 16 J=12,13
   16 Y(J)=Y(J-1)+0.006
      DO 17 J=14,16
```

```
17 Y(J)=Y(J-1)+0.008
   Y(17)=Y(16)+0.01
   Y(18)=Y(17)+0.01
   DO 18 J=19,20
18 Y(J)=Y(J-1)+0.008
   Y(21)=Y(20)+0.006
   Y(22)=Y(21)+0.004
   DO 19 I=2,11
19 X(I)=X(I-1)+0.005
   DO 21 I=12,16
21 X(I)=X(I-1)+0.01
   DO 81 I=17,51
81 X(I)=X(I-1)+0.02
   DO 24 J=2,MM
24 E(1,J)=0.4*K(1,J)**1.5/Y(J)
   DO 82 J=2,MM
82 KT(1,J)=0.09*K(1,J)*K(1,J)/E(1,J)
   S(1,1)=0.0
   DO 83 J=2,MM
   01=(Y(J)-Y(J-1))/(Y(J+1)-Y(J))
   02=1./01
   03=01/(Y(J+1)-Y(J-1))
   04=02/(Y(J+1)-Y(J-1))
   W(1,J)=-(03*(U(1,J+1)-U(1,J))+04*(U(1,J)-U(1,J-1)))
83 S(1,J)=S(1,J-1)+U(1,J)*(Y(J)-Y(J-1))
   WRITE(6,77)(I,K(1,I),E(1,I),S(1,I),U(1,I),W(1,I),I=1,MM
77 FORMAT(1H ,I5,5E20.5)
   DO 8 I=1,NN
   U(I,MM)=U1
   W(I,MM)=0.0
   S(I,MM)=S(1,MM)
   K(I,MM)=K(1,MM)
   E(I,MM)=E(1,MM)
 8 CONTINUE
   DO 10 I=1,NN
   U(I,1)=0.0
   S(I,1)=0.0
   K(I,1)=0.0
   E(I,1)=0.0
10 CONTINUE
   DO 20 I=1,NN
   DO 22 J=1,MM
   KE(I,J)=1.55E-5
   DK(I,J)=KE(1,J)
   DE(I,J)=1.13E-5
   KT(I,J)=1.55E-5
22 CONTINUE
20 CONTINUE
   DO 51 I5=2,8
   K(I5,20)=K(1,20)
```

```
      K(I5,21)=K(1,21)
   51 CONTINUE
      DO 53 I4=2,N
      E(I4,20)=E(1,20)
      E(I4,21)=E(1,21)
   53 CONTINUE
C*********************************************
C     SOLUTION OF FINIT-DIFERANCE EQUASIONS*
C*********************************************
C     CALCULATION OF THE B"S AND A"S
C*************************************
  105 DO 306 I=2,N
      DO 307 J=2,M
      DV=0.25*(X(I+1)-X(I-1))*(Y(J+1)-Y(J-1))
      AN1=S(I+1,J+1)+S(I+1,J)-S(I-1,J+1)-S(I-1,J)
      AS1=S(I-1,J-1)+S(I-1,J)-S(I+1,J-1)-S(I+1,J)
      AE1=S(I+1,J-1)+S(I,J-1)-S(I+1,J+1)-S(I,J+1)
      AW1=S(I-1,J+1)+S(I,J+1)-S(I-1,J-1)-S(I,J-1)
      AN=0.125*(AN1+ABS(AN1))
      AS=0.125*(AS1+ABS(AS1))
      AE=0.125*(AE1+ABS(AE1))
      AW=0.125*(AW1+ABS(AW1))
      G=AN+AS+AE+AW
      BN=0.5*((X(I+1)-X(I-1))/(Y(J+1)-Y(J)))
      BS=0.5*((X(I+1)-X(I-1))/(Y(J)-Y(J-1)))
C     BE=0.5*((Y(J+1)-Y(J-1))/(X(I+1)-X(I)))
C     BW=0.5*((Y(J+1)-Y(J-1))/(X(I)-X(I-1)))
      BE=0.0
      BW=0.0
      F=BN+BS+BE+BW
      CN=(AN+BN*KE(I,J+1))/(G+F*KE(I,J))
      CS=(AS+BS*KE(I,J-1))/(G+F*KE(I,J))
      CE=(AE+BE*KE(I+1,J))/(G+F*KE(I,J))
      CW=(AW+BW*KE(I-1,J))/(G+F*KE(I,J))
      W(I,J)=CE*W(I+1,J)+CW*W(I-1,J)+CN*W(I,J+1)+CS*W(I,J-1
      DO 405 I1=2,N
  405 W(I1,1)=-((2.0/Y(2)**2)*(S(I1,2)-S(I1,1)))
      DO 220 L=2,M
      W(NN,L)=W(N,L)
  220 CONTINUE
      DO 50 I3=1,N
      W(I3,M)=W(I3,MM)
   50 CONTINUE
C***********************
C     STREAM FUNCTION *
C***********************
      CNS=BN/F
      CSS=BS/F
      CES=0.0
      CWS=0.0
```

```
      Q(I,J)=W(I,J)*DV/F
      S(I,J)=CNS*S(I,J+1)+CSS*S(I,J-1)+CES*S(I+1,J)+CWS*S(I-1,J)+Q(I,J)
      DO 260 LL=2,M
      S(NN,LL)=S(N,LL)
  260 CONTINUE
C***************
C     VELOCITY *
C***************
      CY1=(Y(J)-Y(J-1))/(Y(J+1)-Y(J))
      CY2=1.0/CY1
      CY3=CY1/(Y(J+1)-Y(J-1))
      CY4=CY2/(Y(J+1)-Y(J-1))
      U(I,J)=CY3*(S(I,J+1)-S(I,J))+CY4*(S(I,J)-S(I,J-1))
      DO 41 II1=2,N
      U(II1,1)=U(II1,NN)
   41 CONTINUE
      DO 710 L1=2,M
      U(NN,L1)=U(N,L1)
  710 CONTINUE
C************************
C     KINETIC ENERGY    *
C************************
      IF(J.GE.20)GOTO 589
      IF(J.LE.2)GOTO 589
      BNK=((DK(I,J+1)+DK(I,J))/4.0)*(2+BN)
      BSK=((DK(I,J-1)+DK(I,J))/4.0)*(2+BS)
      BEK=((DK(I+1,J)+DK(I,J))/4.0)*(2+BE)
      BWK=((DK(I-1,J)+DK(I,J))/4.0)*(2+BW)
      FK=BNK+BSK+BEK+BWK
      DUY(I,J)=CY3*(U(I,J+1)-U(I,J))+CY4*(U(I,J)-U(I,J-1))
      CNK=(AN+BNK)/(G+FK)
      CSK=(AS+BSK)/(G+FK)
      CEK=(AE+BEK)/(G+FK)
      CWK=(AW+BWK)/(G+FK)
      QS(I,J)=DUY(I,J)**2
      QK(I,J)=KT(I,J)*QS(I,J)
      SK(I,J)=(1.5*QK(I,J)+1.08*E(I,J))*DV/(G+FK)
      SKP(I,J)=-(2.48*E(I,J)+0.5*QK(I,J))*DV/((K(I,J)+1.E-40)*(G+FK))
      K(I,J)=CNK*K(I,J+1)+CSK*K(I,J-1)+CEK*K(I+1,J)+CWK*K(I-1,J)+SK(I,J)
      K(I,J)=K(I,J)/(1.-SKP(I,J))
      DO 800 LL1=2,M
      K(NN,LL1)=K(N,LL1)
  800 CONTINUE
C************************
C     ENERGY DISIPATION  *
C************************
      BNE=((DE(I,J+1)+DE(I,J))/4.0)*(2+BN)
      BSE=((DE(I,J-1)+DE(I,J))/4.0)*(2+BS)
      BEE=((DE(I+1,J)+DE(I,J))/4.0)*(2+BE)
      BWE=((DE(I-1,J)+DE(I,J))/4.0)*(2+BW)
```

```
      FE=BNE+BSE+BEE+BWE
      EK(I,J)=E(I,J)/(K(I,J)+1.E-40)
      SE(I,J)=(1.44*QK(I,J)+1.08*E(I,J))*EK(I,J)*DV/(G+FE)
      SEP(I,J)=-(3.36*EK(I,J)*DV/(G+FE))
      CNE=(AN+BNE)/(G+FE)
      CSE=(AS+BSE)/(G+FE)
      CEE=(AE+BEE)/(G+FE)
      CWE=(AW+BWE)/(G+FE)
      E(I,J)=CNE*E(I,J+1)+CSE*E(I,J-1)+CEE*E(I+1,J)+CWE*E(I-1,J)+SE(I,J)
      E(I,J)=E(I,J)/(1.0-SEP(I,J))
      DO 900 LL2=2,11
      E(NN,LL2)=E(N,LL2)
  900 CONTINUE
      KT(I,J)=0.198*(K(I,J))**2/(E(I,J)+1.E-40)
      KE(I,J)=KT(I,J)+1.53E-5
      DK(I,J)=KE(I,J)
      DE(I,J)=KE(I,J)/1.3
      GO TO 307
  589 KT(I,J)=1.53E-5
      KE(I,J)=KT(I,J)
      DK(I,J)=KE(I,J)
      DE(I,J)=KE(I,J)
  307 CONTINUE
  306 CONTINUE
      N=N+1
      IF(N.LE.KKK) GOTO 105
      DO 339 I=1,NN
      DO 338 J=1,MM
      WRITE(6,400)I,J,S(I,J),E(I,J),U(I,J),K(I,J),KT(I,J)
  338 CONTINUE
  339 CONTINUE
      STOP
  400 FORMAT(1H ,2I10,5E20.8)
      END
****S
```

REFERENCES

ABBOTT, D.E. and KLINE, S.J. (1962). Experimental Investigation of Subsonic Turbulent Flow Over Single and Double Backward Facing Steps, J. Bsic Engng. Trans. ASME, Sept. (1962), pp.317.

ANTONIA, R.A. and LUXTON, R.E. (1971) The Response of a Turbulent Boundary-Layer to an Upstanding Step Change in Surafce Roughness, J. Basic Engng. Trans. ASME, March (1971), pp.23.

ANTONIA, R.A. and LUXTON, R.E. (1971) The Response of a Turbulent Boundary-Layer to a Step Change in Surface Roughness, (Part 1 - Smooth to Rough), J. Fluid Mech. (1971), Vol.48, Part 4, pp.721-761.

ARIE, M. and ROUSE, H. (1956) Experiments on Two-Dimensional Flow Over a Normal Wall. J. Fluid Mech. (1956), Vol.1, Part 1, pp.129-141.

ARIE, M., KIYA, M., TAMURA, H. and KANAYAMA, Y. (1975) Flow Over Rectangular Cylinders Immersed in a Turbulent Boundary-Layer. (Part 1 - Correlation Between Pressure Drag and Boundary-Layer Characteristics). Bulletin of the JSME, Vol.18, No.125, Nov. 1975.

ARIE, M., KIYA, M., TAMURA, H., KOSUGI, M. and TAKAOKA, K. (1975) Flow Over Rectangular Cylinders Immersed in a Turbulent Boundary-Layer. (Part 2 - Flow Patterns and Pressure Distributions). Bulletin of the JSME, Vol.18, No.125, Nov. 1975.

BRADSHAW, P. and GALEA, P.V. (1967) Step Induced Separation of a Turbulent Boundary-Layer in Incompressible Flow. J. luid Mech. (1967), Vol.27, Part 1, pp.111-130.

BRADSHAW, P., FERRISS, D.H. and ATWELL, N.P. (1967) Calculation of Boundary-Layer Development Using the Turbulent Energy Equation. J. Fluid Mech. (1967), Vol.28, Part 3, pp.593-616.

BRADSHAW, P. and WONG, F.Y.F. (1972) The Reattachment and Relaxation of a Turbulent Shear Layer. J. Fluid Mech. (1972), Vol.52, Part 1, pp.113-135.

CASTRO, I.P. (1977) Numerical Difficulties in the Calculation of Complex Turbulent Flows. Turbulent Shear Flows, Vol.1, Selected Paper from the First International Symposium on Turbulent Shear Flows, The Pennsylvania State University, USA, April 1977.

CASTRO, I.P. and ROBINS, A.G. (1977) The Flow Around a Surface - Mounted Cube in Uniform and Turbulent Streams. J. Fluid Mech. (1977), Vol.79, Part 2, pp.307-335.

CASTRO, I.P. (1979) Relaxing Wakes Behind Surface - Mounted Obstacles in Rough Wall Boundary-Layers. J. Fluid Mech. (1979), Vol.93, Part 4, pp.631-659.

CLAUSER, F.H. (1956) The Turbulent Boundary-Layer. Advances in Applied Mechanics, Vol.IV, New York: Academic Press.

COLES, D.E. (1956) The Law of the Wake in the Turbulent Boundary-Layer. J. Fluid Mech. (1956), Vol.1, Part 2, pp.191.

COUNIHAN, J., HUNT, J.C.R. and JACKSON, P.S. (1974) Wakes Behind Two-Dimensional Surface Obstacles in Turbulent Boundary-Layers. J. Fluid Mech. (1974), Vol.64, Part 3, pp.529-563.

DEBENHAM, W.M. and DUGGINS, R.K. (1971) The Numerical Solution of a Turbulent Recirculating Flow. Paper 17, University of Nottingham, a symposium of Internal Flows, University of Salford, 1971.

DISA EQUIPMENT and B & K. Frequency Analyzer and Recording Unit Manual Books.

DISA MANUAL (1970) DISA Type 55M01 Anemometer Unit, DISA Type 55D35 Voltmeter, DISA Type 55M25 Lineariser, DIS Type Turbulence Processor, DISA Type 55D70 Analog Correlation, Herlev, Denmark.

DURST, F. and RASTOGI, A.K. (1977) Theretical and Experimental Investigations of Turbulent Flows with Separation. Turbulent Shear Flows, Vol.1, Selected Papers from the First International Symposium on Turbulent Shear Flows, the Pennsylvania State, University, USA. April 1977.

EL-SAMANOUDY, M.A. (1974) Turbulent Boundary-Layers on an Irregularly Rough Surface. Ph.D. Thesis, University of Liverpool, 1974.

FINLY, P.J., PHOE, K.C. and POH, C.J. (1966) Velocity Measurements in a Thin Turbulent Water Layer. La Houille Blanche, Vol.21, 1966, pp.713.

FRIEDMAN, M. (1972) Laminar Flow in Channel with a Step. J. Engng. Mathematics, Vol.6, No.3, July 1972, pp.285-290.

FURUYA, Y., NAKAMURA, I. MIYATA, M. and YAMA, Y. (1972) Turbulent Boundary-Layer Along Streamwise Bar of a Rectangular Cross-Section Placed on a Flat Plate. Bulletin of the JSME, Vol.20, No.141, March 1977.

GOOD, M.C. and JOUBERT, P.N. (1968) (The Form Drag of Two-Dimensional Bluff-Plates Immersed in Turbulent Boundary-Layer. J. Fluid Mech. (1968), Vol.31, Part 3, pp.547-582.

GOSMAN, A.D., PUN, W.M., RUNCHAL, A.K., SPALDING, D.B. and WOLFSHTEIN, M. (1969) Heat and Mass Transfer in Recirculating Flows. Academic Press, London and New York, 1979.

GREENSPAN, D. (1969) Numerical Studies of Steady Viscous, Incompressible Flow in a Channel with a Step. J. Engng. Mathematics, Vol.3, No.1, Jan (1969), pp.21-28.

HANJALIC, K. and LAUNDER, B.E. (1972) A Reynolds Stress Model of Turbulence and its Application to Thin Shear Flows. J. Fluid Mech. (1972), Vol.52, Part 4, pp.609-638.

HESENBERG, W. (1948) Zur Statistischen Theorie Der Turbulenz. Zs.f. Phs., Bd. 124, Heft 7/12, 1948.

HINZE, J.O. (1975) Turbulence. McGraw Hill, Second Edition, (1975).

HUNT, J.C.P. (1971) A Theory for the Laminar Wake of a Two-Dimensional Body in a Boundary-Layer. J. Fluid Mech. (1971), Vol49, Part 1, pp.159-178.

KIYA, M. and ARIE, M. (1972) A Free Streamline Theory for Bluff Bodies Attached to a Plane Wall. J. Fluid Mech. (1972), Vol.56, Part 2, pp.201-219.

KIYA, M. and ARIE, M. (1973) A Perturbation Analysis of the Laminer Far Wake Behind a Symmetrical Two-Dimensional Body in a Uniform Shear Flow. J. Fluid Mech. (1973), Vol.61, Part 2, pp.305-321.

KLEBANOFF, P.S. (1954) Characteristics of Turbulence in a Boundary-Layer with Zero Pressure Gradient. NACA. TN3178, (1954).

KOLMOGROFF, A. (1941) The Local Structure of Turbulence in Incompressible Viscous Fluids for Very Large Reynolds Numbers. Comp. Rend. Acad. Sci., URSS, Vol.30, No.4, Feb(1941), pp.301.

KUO, Y. and BADWIN, L.Y. (1966) Diffusion and Decay of Turbulent Elliptic Wakes. A.I.A.A. Journal, Vol.4, (1966), No.9, pp.1566-1572.

LACKENBY, H. (1962) The Resistance of Ships, with Special Reference to Skin Friction and Hull Surface Condition. The Thirty-Fourth Thomas Lowe Gray Lecture. Institution of Mechanical Engineers, L 4/62, London.

LAUFER, J. (155) The Structure of Turbulence in Fully Developed Pipe Flow. NACA, Report 1174, (1955).

LAUNDER, B.E. and SPALDING, D.B. (1972) Mathematical Models of Turbulence. Academic Press 1972, London and New York.

LAUNDER, B.E. adn SPALDING, D.B. (1974) The Numerical Computation of Turbulent Flows. Computer Methods in Applied Mechanics and Engineering 3 (1974), pp.269-289.

LAUNDER, B.E., REECE, G.J. and RODI, W. (1975) Progress in the Development of a Reynolds-Stress Turublence Closure. J. Fluid Mech. (1975), Vol.68, Part 3, pp.537-566.

LEWKOWICZ, A.K., HORLOCK, J.H., HOADIY, D. and PERKINS, H.J. (1970) A Family of Integral Methods for Predicting Turbulent Boundary-Layers. A.I.A.A. Journal, Vol.8, (1970), pp.44.

MINH, H. and CHASSING, P. (1978) Some numerical Predictions of Incompressible Turbulent Flows. Numerical Method in Laminer and Turublent Flow. July 1978, Pentech Press, London: Plymouth.

MOSES, H.L. (1964) The Behaviour of Turbulent Boundary-Layers in Adverse Pressure Gradient. Gas Turbine Laboratory, Massachusettes Inst. of Technology, Report 73, 1964.

MUSKER, A.J. (1977) Turbulent Shear-Flows Near Irregularly Rough Surface With Particular Reference to Ships' Hulls. Ph.D. Thesis, University of Liverpool (1977).

MUELLER, T.J. and REBERTSON, H.M. (1963) A Study of the Mean Motion and Turbulence Downstream of a Roughness Element. Development in Theoretical and Applied Mechanics, Vol.1, 1963, pp.326-340.

MUELLER, T.J., KORST, H.H. and CHOW, W.L. (1964) On the Separation, Reattachment, and Redevelopment of Incompressible Turbulent Shear Flow. Trans. of the ASME. J. Basic Engng., June (1964), pp.221-226.

NEE, V.W. and KOVASZNAY, S.G. (1969) Simple Phenomenological Theory of Turbulent Shear Flows. J. Physics of Fluid, Vol.12, No.3, March (1969), pp.473-484.

NKURADSE, J. (1933) Laws of Flow in Rough Pipes. Trns. NACA TM 1292 (1933).

OTTA, T. and ITOSAKA, M. (1976) A Separated and Reattached Flow on a Blunt Flat Plate. Trans. of the ASME, J. Fluid Engng., March (1976), pp.79-86.

PATANKAR, S.V. and SPALDING, D.B. (1967) A Finite-Difference Procedure for Solving the Equations of the Two-Dimensional Boundary-Layer. Int. J. Heat Mass Transfer, Vol.10, (1967), pp.1389-1411.

PATANKAR, S.V. and SPALDING, D.B. (1970) Heat and Mass Transfer in Boundary-Layers. Intertext Books, London (1970).

PATANKAR, S.V. and SPALDING, D.B. (1972) A Calculation Procedure for Heat, Mass and Momentum Transfer in Three-Dimensional Parabolic Flows. Int. J. Heat M ss Tranfer, Vol.15, (1972), pp.1787-1806.

PERRY, A.E. and JOUBERT, P.N. (1963) Rough Wall Boundary-Layers in Adverse Pressure Gradients. J. Fluid Mech. (1963), Vol.17, pp.993-111.

PERRY, A.E., SCHOFIELD, W.H. and JOUBERT, P.N. (1969) Rough Wall Turbulent Boundary-Layers. J. Fluid Mech. (1969), Vol.37, Part 2, pp.383-413.

PLATE, E.J. and LIN, C.Y. (1965) The Velocity Field Downstream from a Two-Dimensional Model Hill. Colorado State University Rep. CER 65 EJP 14.

PLATE, E.G. (1967) Diffusion From a Ground Level Line Source Into the Disturbed Boundary-Layer Far Downstream From a Fence. Int. J. Heat Mass Tranfer, (1967), Vol.10, pp.195-205.

POPE, S.B. and WHITELAW, J.H. (1976) The Calculation of Near-Wak Flows. J. Fluid Mech. (1976), Vol.73, Part 1, pp.9-32.

PRESTON, J.H. and LEWKOWICZ, A.K. (1973) Proposals for the Extension of the Investigation of the Effect of Waviness and Roughness on Ship Resistance. University of Liverpool, Mech. Engng. Dept., FM/A1/1973.

PUN, W.M. and SPALDING, D.B. (1977) A General Computer Program for Two-Dimensional Elliptic Flows. Imperial College, London Mechanical Engng. Dept., Report No. HTS/76/2.

RANGARAJU, K.G., LOESER, J. and PLATE, E.J. (1976) Velocity Profiles and Fence Drag for a Turbulent Boundary-Layer along Smooth and Rough Flat Plates. J. Fluid Mech. (1976), Vol.76, Part 2, pp.401-413.

ROBERTSTON, J.M. (1965) Hydrodynamics in Theory and Application. Prentice-Hall, Englewood Cliffs, N.J., 1965, pp.141-143.

SAKAMOTO, H., MORIYA, M. and ARIE, M. (1975) A Study on the Flow Around Bluff Bodies Immersed in Turbulent Boundary-Layers. (Part 1 - on the Form Drage of a Normal Plate), Bulletin of the JSME, Vol.18, No.124, Oct. 1975).

SAKAMOTO, H., MORIYA, M. and ARIE, M. (1977) A Study on the Flow Around Bluff Bodies Immersed in Turublent Boundary-Layers. (Part 2 - the Pressure Forces Acting on Inclined Plates), Bulletin of the JSME, Vol.20, No.139, Jan. (1977).

SHCLICHTING, H. (1960) Boundary-Layer Theory. McGraw-Hill Book Co. Inc., New York.

SFORZA, P.M. and MONS, R. (1970) Wall-Wake: Flow Behind a Leading Edge Obstacle. A.I.A.A. Journal, Dec. (1970), Vol.8, No.12, pp.2162-2167.

SMITH, F.T. (1973) Laminer Flow Over a Small Hump on a Flat Plate. J. Fluid Mech. (1973), Vol.57, Part 4, pp.803-824.

STEIGER, M.H. and BLOOM, M.H. (1963) Three-Dimensional Effects in Viscous Wakes. A.I.A.A. Journal, Vol.1, 1963, pp.776.

STRATFORD, B.S. (1959) The Prediction of Separation of the Turbulent Boundary-Layer. J. Fluid Mech., (1959), Vol.5, Part 1, pp.1-16.

TANY, I. and IUCHI, M. (1961) Experimental Investigation of Flow Separation Associated with a Step or a Grove. Aeronautical Research Institute, University of Tokyo, (1961), Report No.364.

TAYLOR, G.I. (1938) The Spectrum of Turbulence. Proc. Royal Society, A, Vol.164, pp.476-490.

TAULBEE, D.B. and ROBERTSON, J.M. (1972) Turbulent Separation Analysis Ahead of a Step. Trans. of the ASME, Journal of Basic Engng., Sept.(1972), pp.544-550.

TCHEN, C.M. (1953) On the Spectrum of Energy in Turbulent Shear Flow. Research Paper RP 2388, Jn.1, Research, National Bureau of Standards, Vol.50, No.1, June (1953), pp.51.

TILLMAN, W. (1945) Investigations of Turbulent Boundary-Layer on Plates. British Rep. and Transl. CGD - 497, MAP - VG 34 - T, (1945).

TOWNES, H.W., GOW, J.L., POWE, R.E. and WEBER, N. (1972) Turbulent Flow in Smooth and Rough Pipes. Trnas. of the ASME, J. Basic Engng., June (1972), pp.353-362.

TOWNSEND, A.A. (1947) The Measurement of Double and Triple Correlation Derivative in Isotropic Turbulence. Proc. Cambridge Phil. Soc., Vol.43, (1947), Part 4, pp.560-570.

TOWNSEND, A.A. (1960) The Development of Turbulent Boundary-Layers with Negligible Wall Stress. J. Fluid Mech. (1960), Vol.8, Part 1, pp.143-155.

TOWNSEND, A.A. (1962) The Behaviour of a Turbulent Boundary-Layer Near Separation. J. Fluid Mech. (1962), Vol.12, pp.536-554.

TOWNSEND, A.A. (1976) The Structure of Turbulence Shear Flow. Cambridge University Press, Second Edition, 1976.

UEDA, H. and HINZE, J.O. (1975) Fine-Structure Turbulence in the Wall Region of a Turbulent Boundary-Layer. J. Fluid Mech. (1975), Vol.67, Part 1, pp.125-143.

VASLIC'-MELLING (1976) Three-Dimensional Turbulent Flow Past Rectangular Bluff Bodies. Imperial College, London, Ph.D. Thesis, April (1977), HTS/77/10.

WOLFSHTINE, M. (1967) Convection Processes in Turbulent Impinging Jets. Imperial College Mech. Eng. Dept., Ph.D. Thesis, Rep. SF/R/2.

FIG.(2.1)

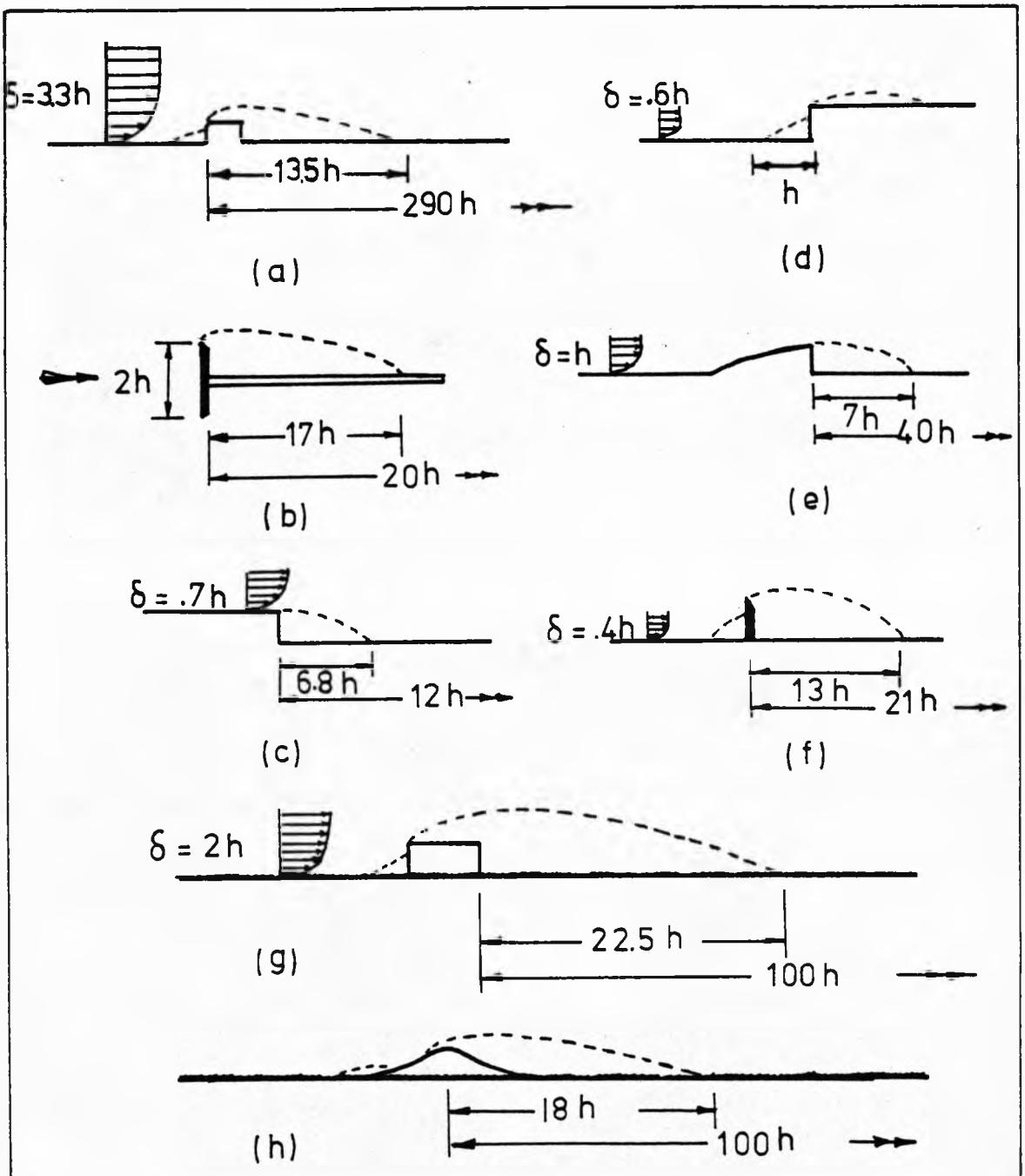

(a) Tillman (1945). (b) Arie & Rouse (1956). (c) Tani et al (1961). (d) Bradshaw & Galea (1967). (e) Muler & Robertson (1963), Bradshaw & Wong (1972). (f) Good & Joubert (1968). (g) and (h) Present experiment.

FIG.(2.2)

FLOW PATTERNS AROUND A NORMAL PLATE IMMERSED IN TURBULENT BOUNDARY-LAYER

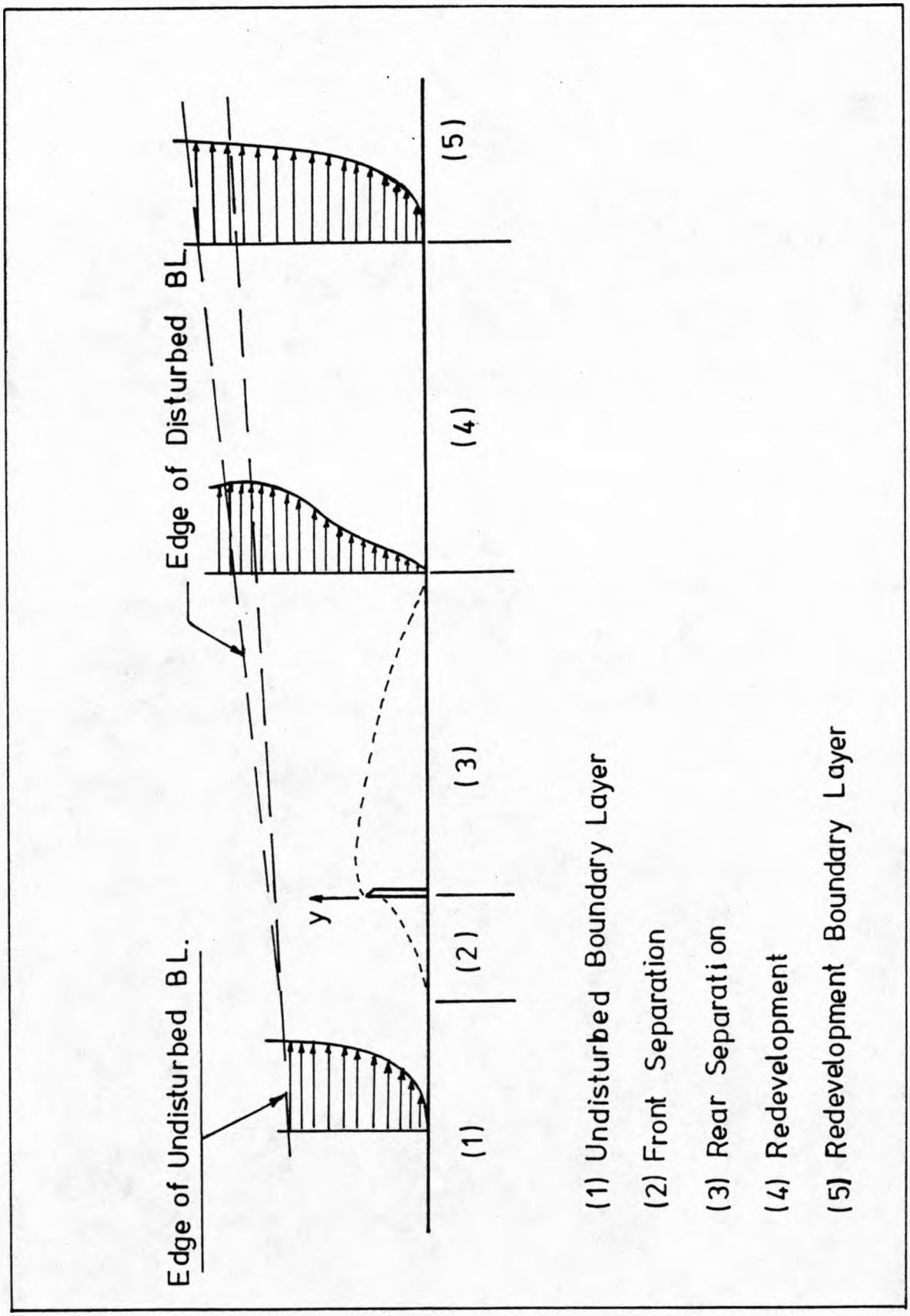

1- Working section.

2- 9:1 Contraction streamline diffuser.

3- 2 × 20 Mesh screens & Honeycomb.

4- 14 Mesh diffuser screen (curved).

5 - 5 Npl straightener vanes.

6 - 4 Bladed fan.

7 - Dynamatic coupling.

8 - 50 H.P. Motor.

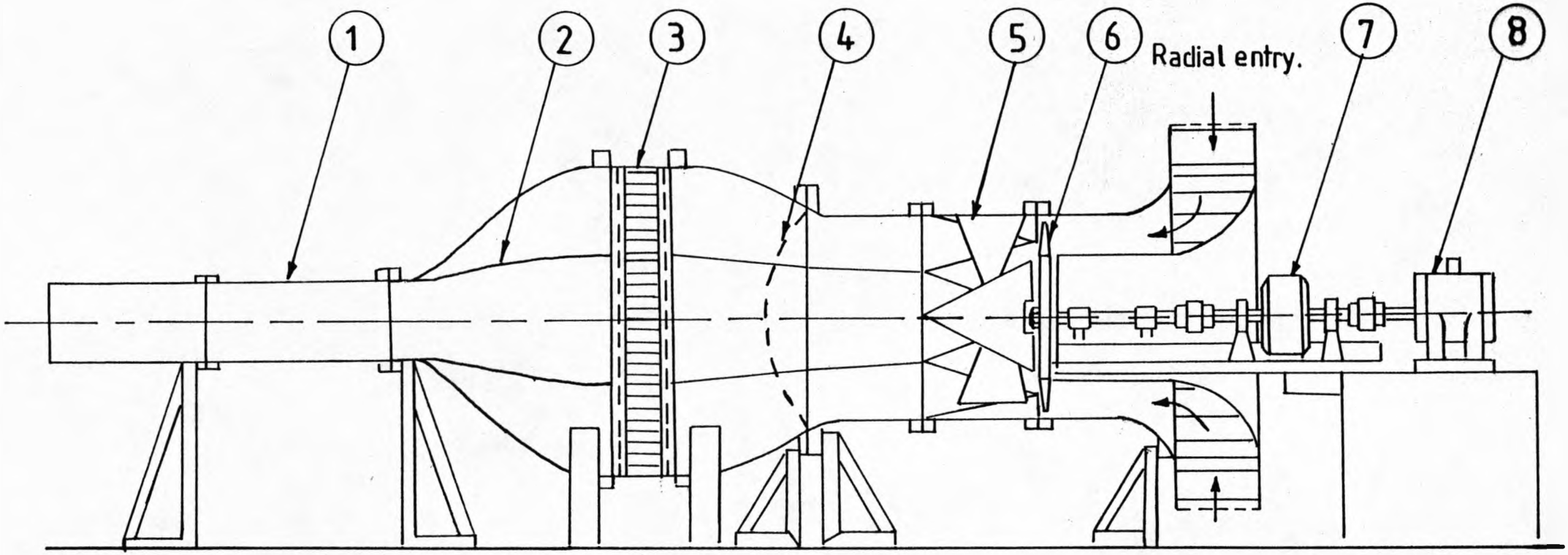

BLOWER WIND TUNNEL

FIG(3.1)

FIG(3.2)

a) TWO DIMENSIONAL OBSTACLE (BOUNDARY-LAYER FLOW)

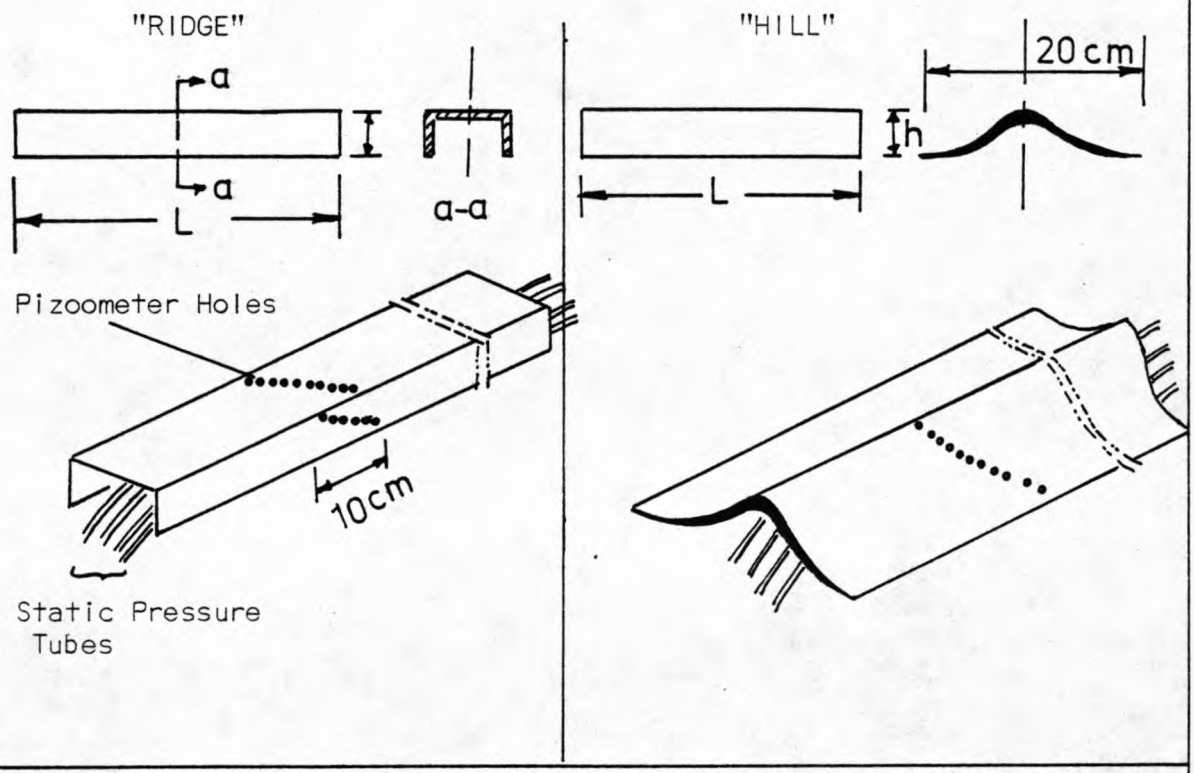

b) TWO DIMENSIONAL OBSTACLE (PIPE FLOW) "RING"

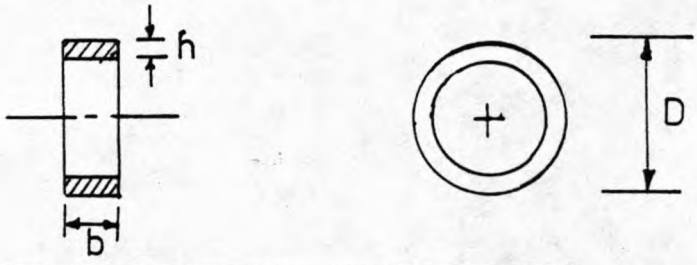

PIPE	h	b	D
ROUGH	0.6	0.7	4.9 (5.08 (2in))
SMOOTH	0.47	0.55	3.84 (1½in)

$\frac{R = 2.45}{h = 0.6} = \frac{4}{1}$

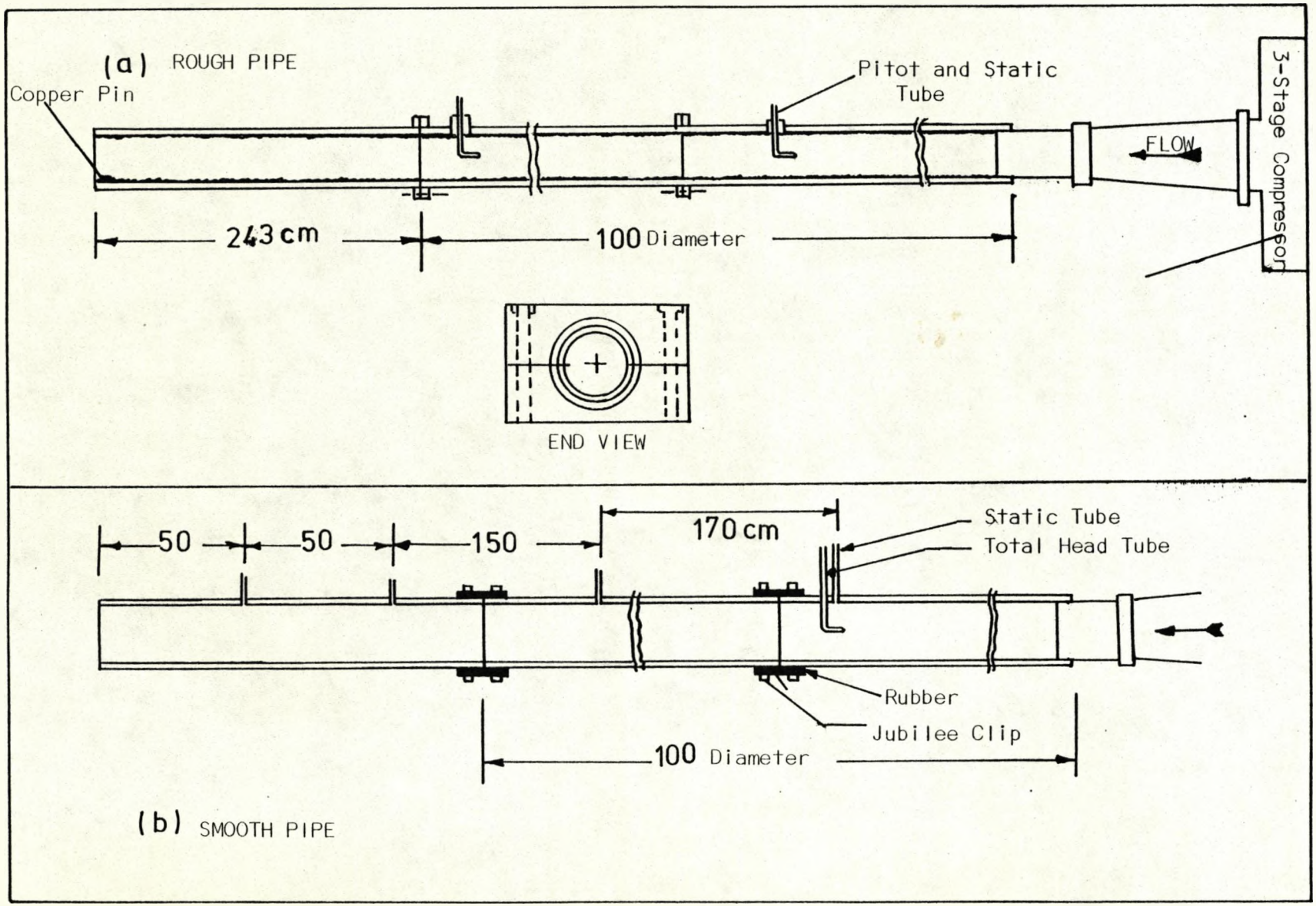
(a) ROUGH PIPE
Copper Pin
Pitot and Static Tube
FLOW
3-Stage Compressor
243 cm
100 Diameter
END VIEW
50
50
150
170 cm
Static Tube
Total Head Tube
Rubber
Jubilee Clip
100 Diameter
(b) SMOOTH PIPE

FIG. (3.3)

FIG.(3.4)

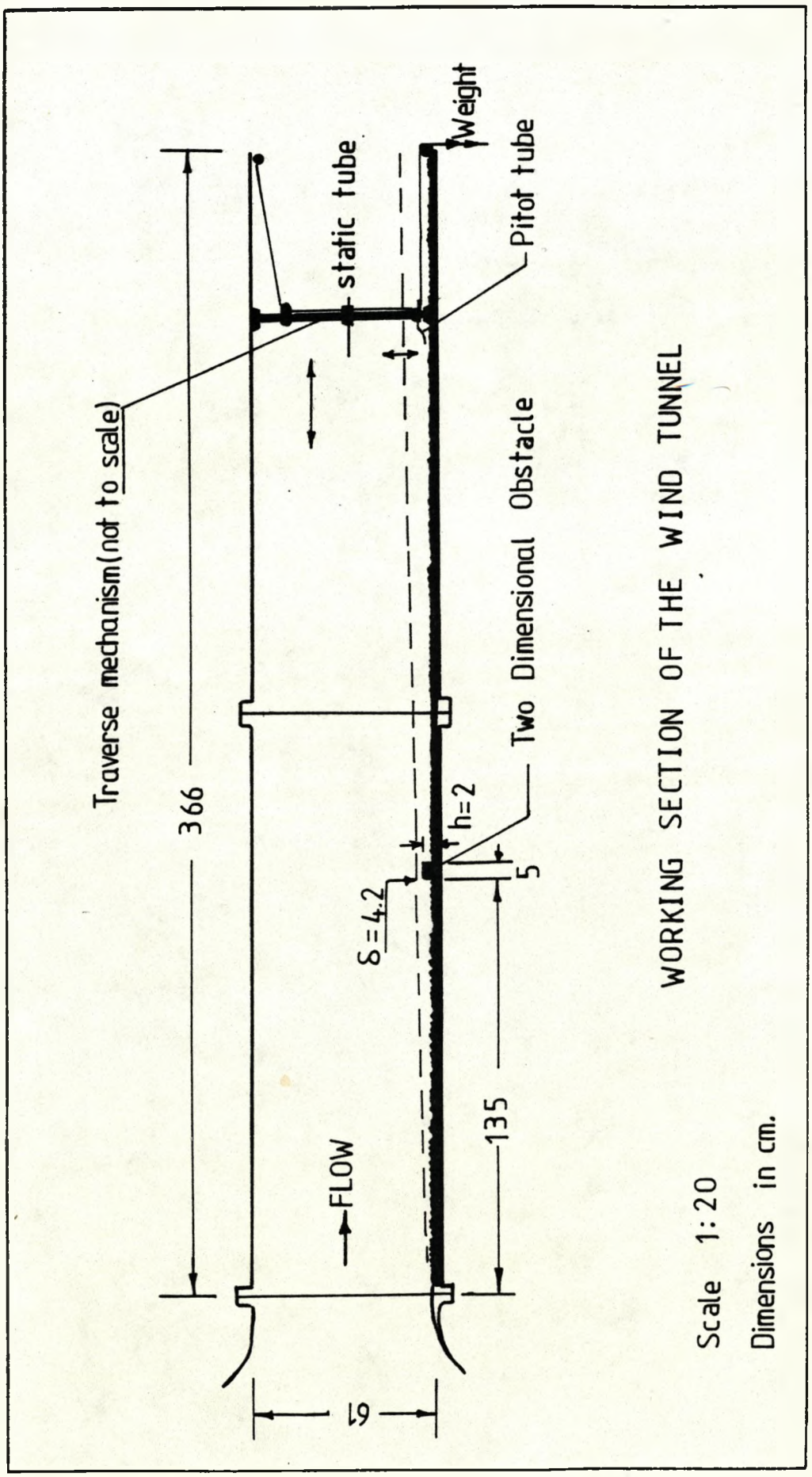

WORKING SECTION OF THE WIND TUNNEL

Scale 1:20

Dimensions in cm.

FIG.(3.5)

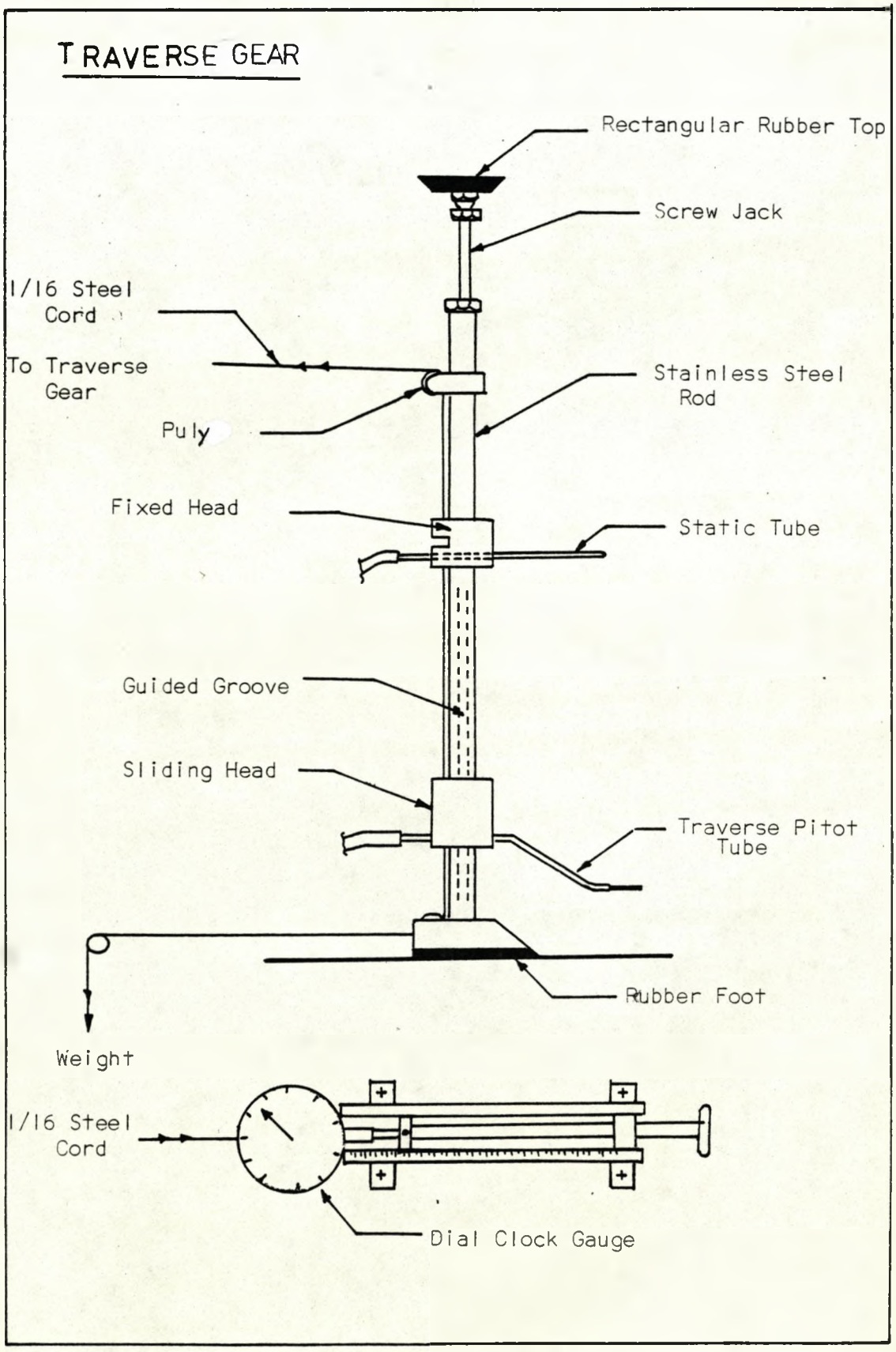
TRAVERSE GEAR
Rectangular Rubber Top
Screw Jack
1/16 Steel Cord
To Traverse Gear
Stainless Steel Rod
Puly
Fixed Head
Static Tube
Guided Groove
Sliding Head
Traverse Pitot Tube
Rubber Foot
Weight
1/16 Steel Cord
Dial Clock Gauge

FIG.(3.6)

(a) INTER CONNECTIONS FOR TURBULENCE MEASURING EQUIPMENT

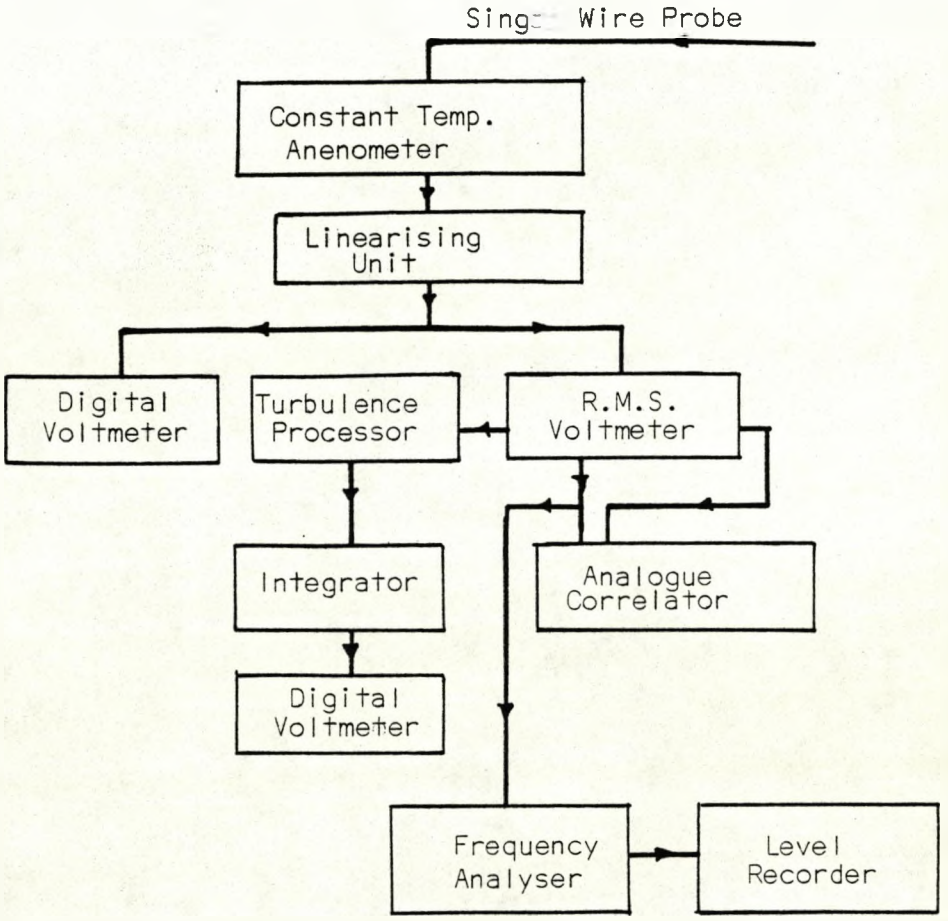

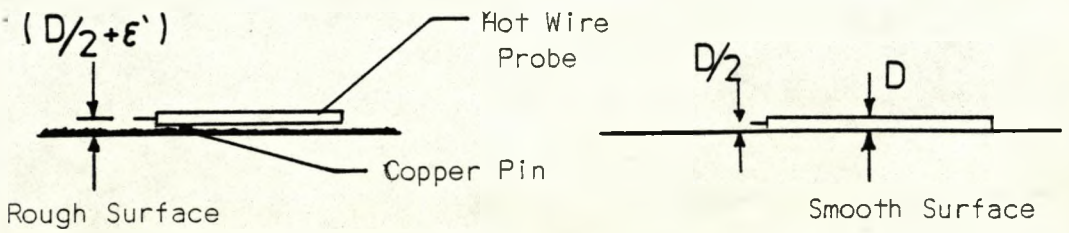

(b) MEASUREMENT OF THE WALL DISTANCE IN THE WIND TUNNEL EXPERIMENTS

MEAN VELOCITY AND STATIC PRESSURE DISTRIBUTIONS IN SPANWISE DIRECTION ABOVE THE RIDGE

FIG.(3.7)

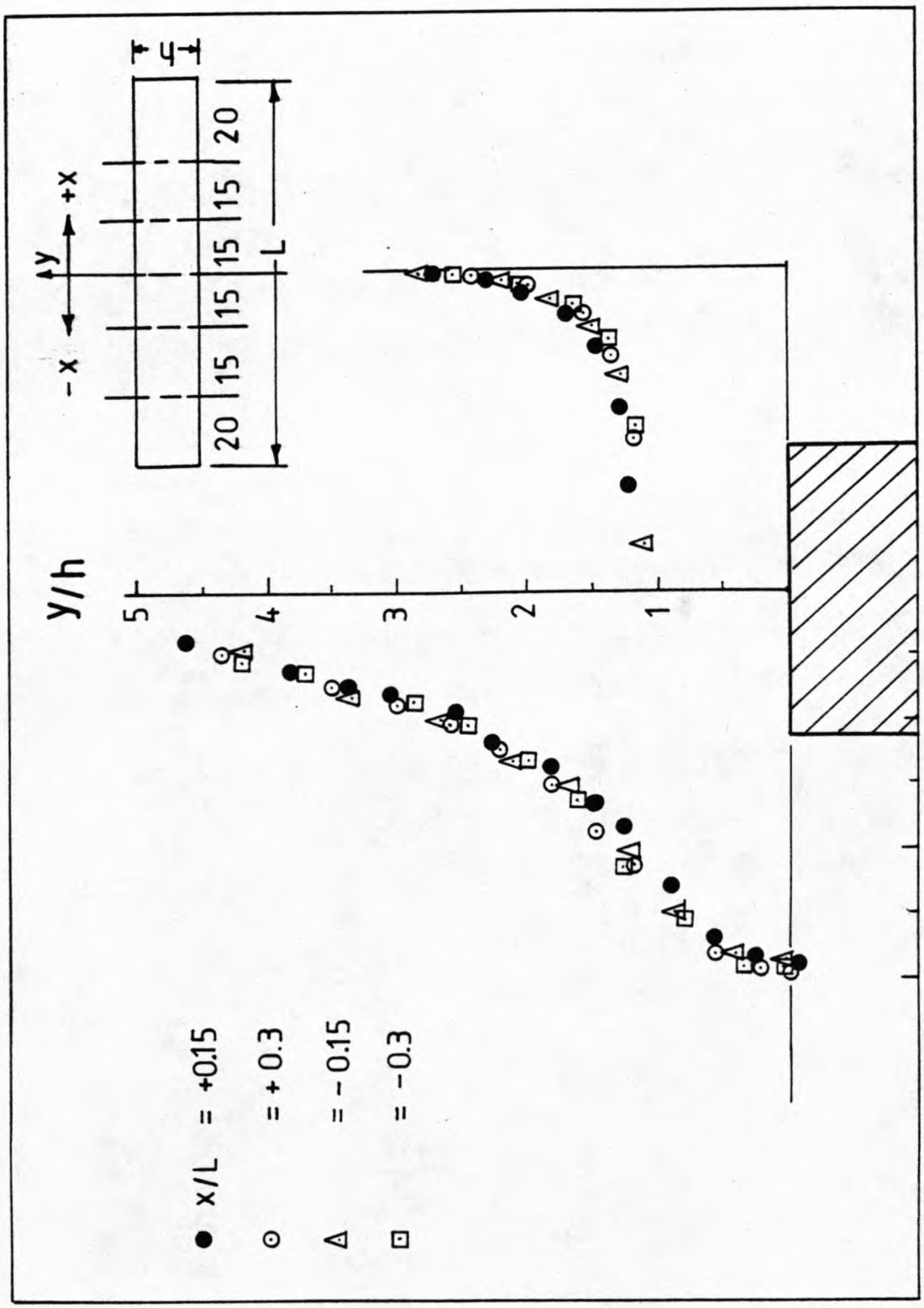

STATIC PRESSURE DISTRIBUTION ON FRONT AND REAR SURFACES OF RECTANGULAR CROSS-SECTION OBSTACLE (RIDGE) ATTACHED TO ROUGH AND SMOOTH SURFACES

FIG.(4.1)

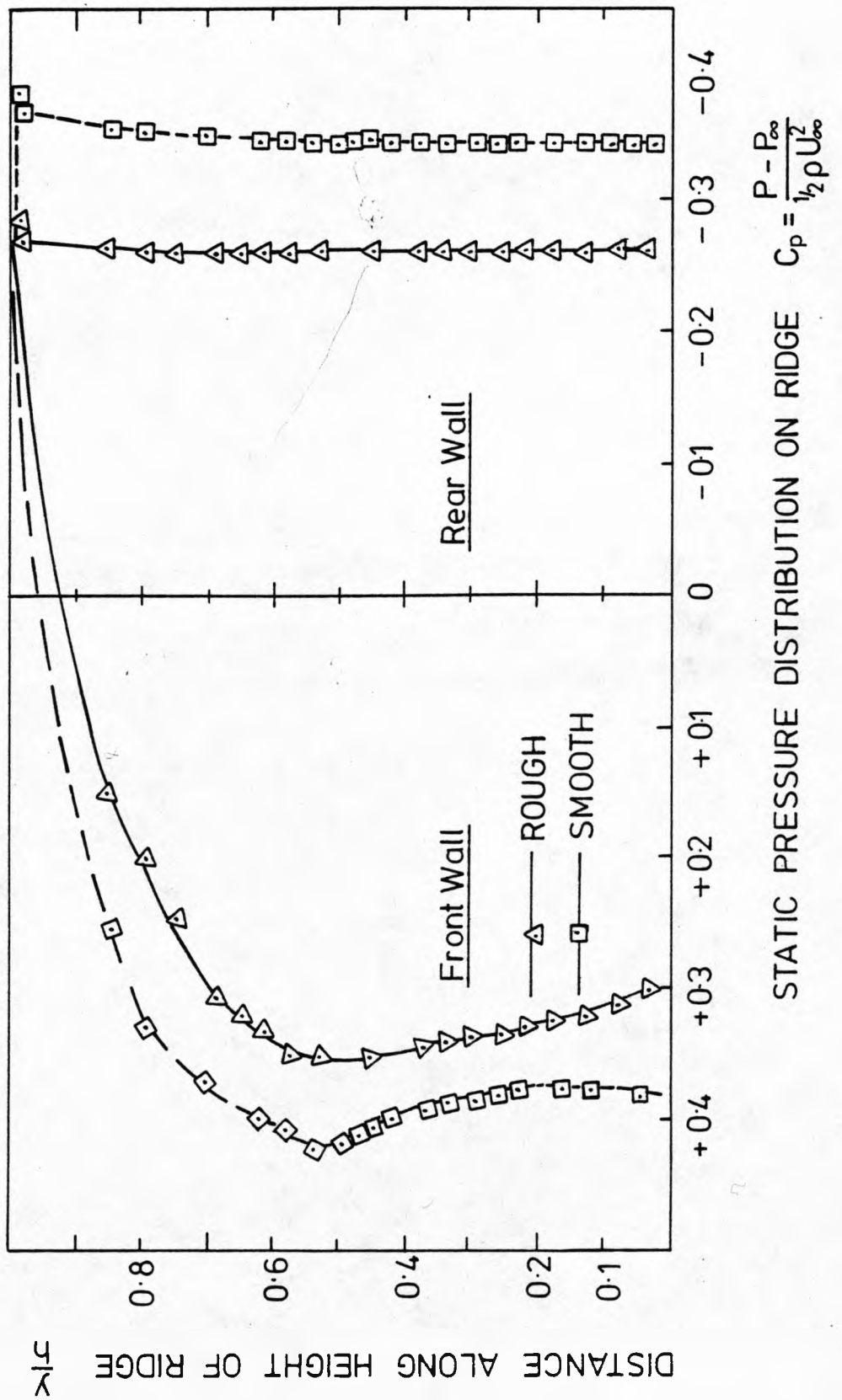

FIG.(4.2a)

STATIC PRESSURE DISTRIBUTION ON FRONT AND REAR SURFACES OF HILL SHAPED OBSTACLE ATTACHED TO ROUGH SURFACE

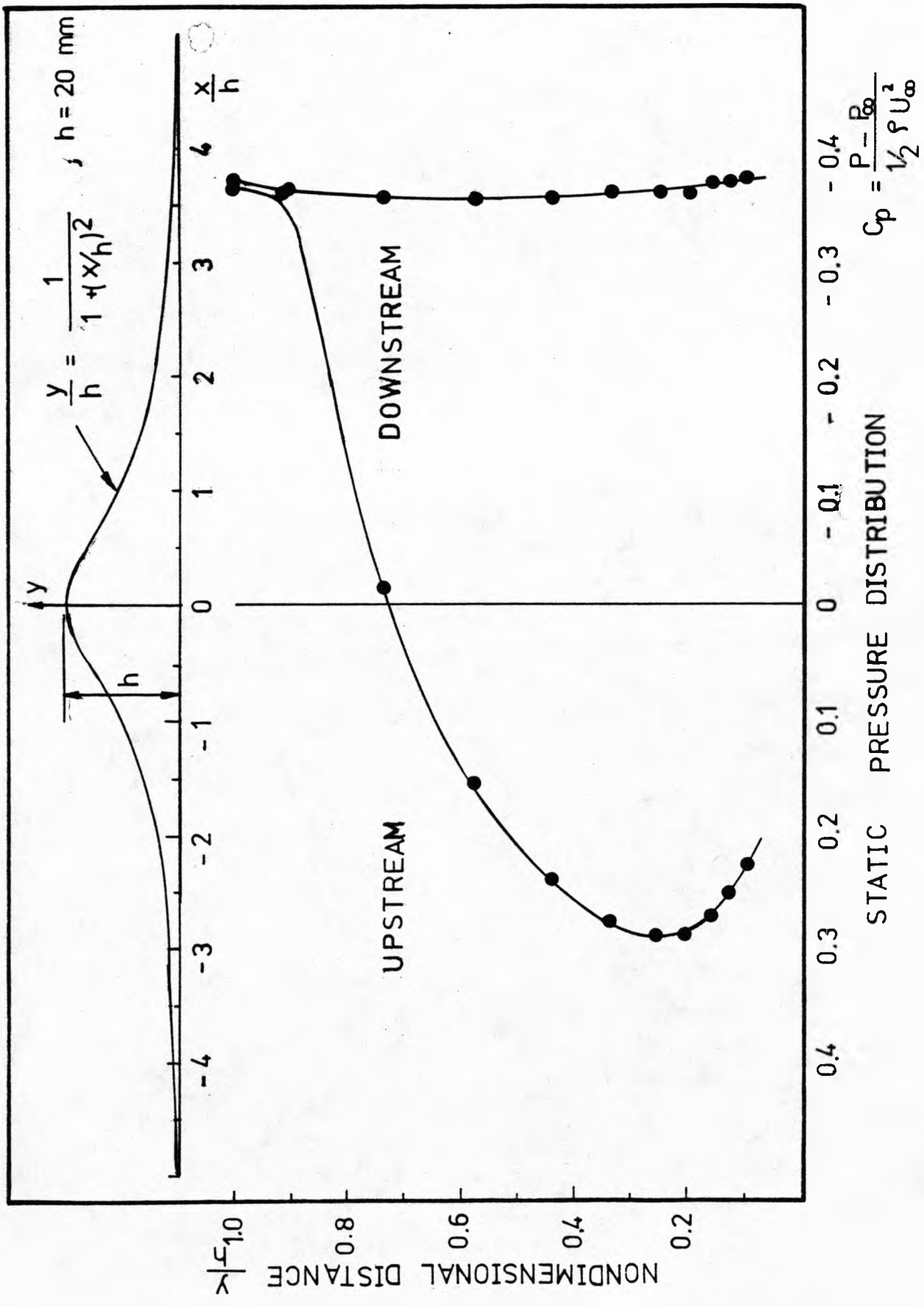

FIG.(4.2b)

STATIC PRESSUR DISTRTIBUTION ON FRONT AND REAR SURFACES OF HILL SHAPED OBSTACLE ATTACHED TO ROUGH SURFACE

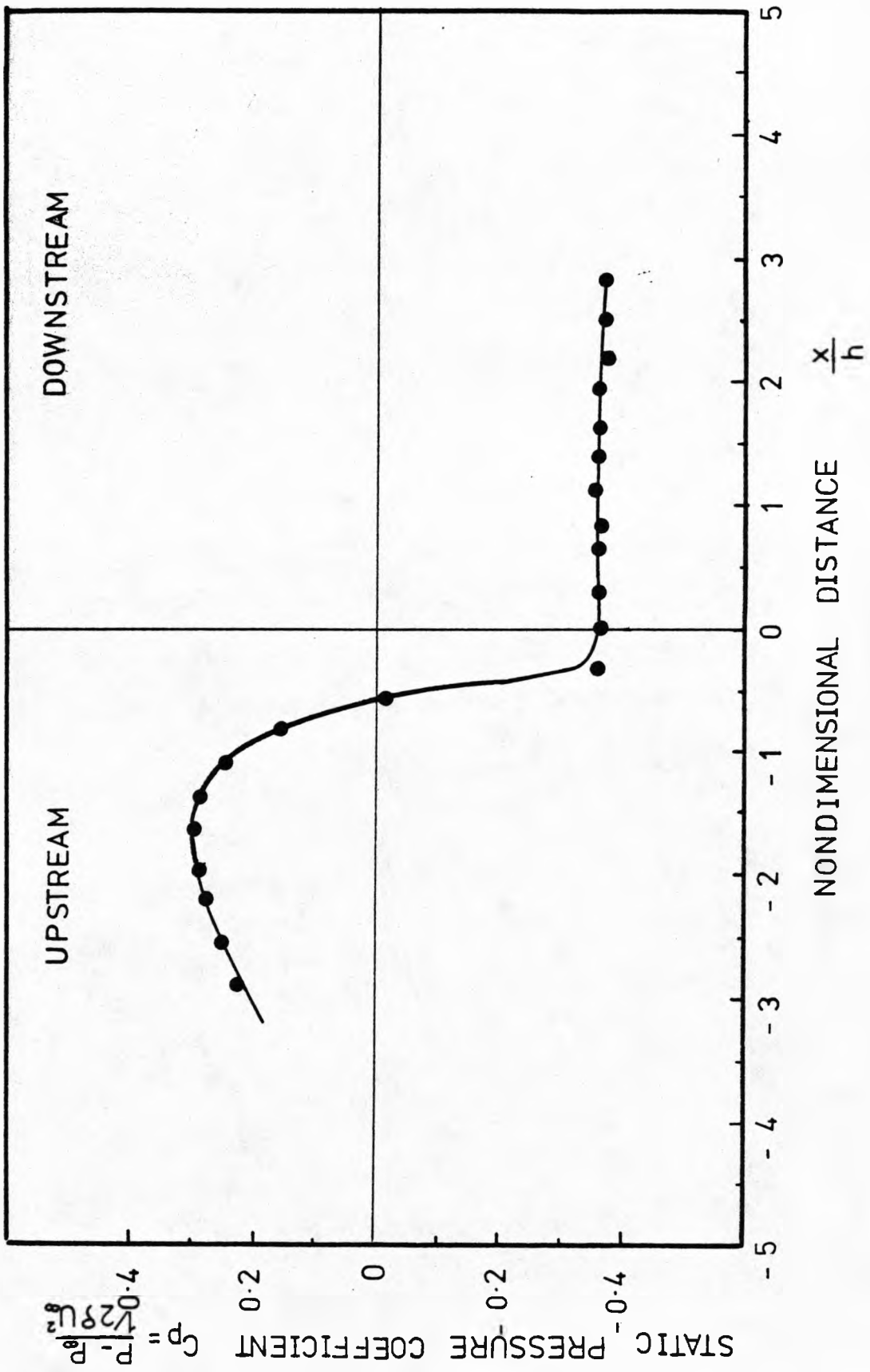

FIG.(4.3)

STATIC PRESSURE DISTRIBUTION ON UPPER SURFACE OF
RECTANGULAR CROSS-SECTION OBSTACLE (RIDGE)
ATTACHED TO ROUGH AND SMOOTH SURFACES

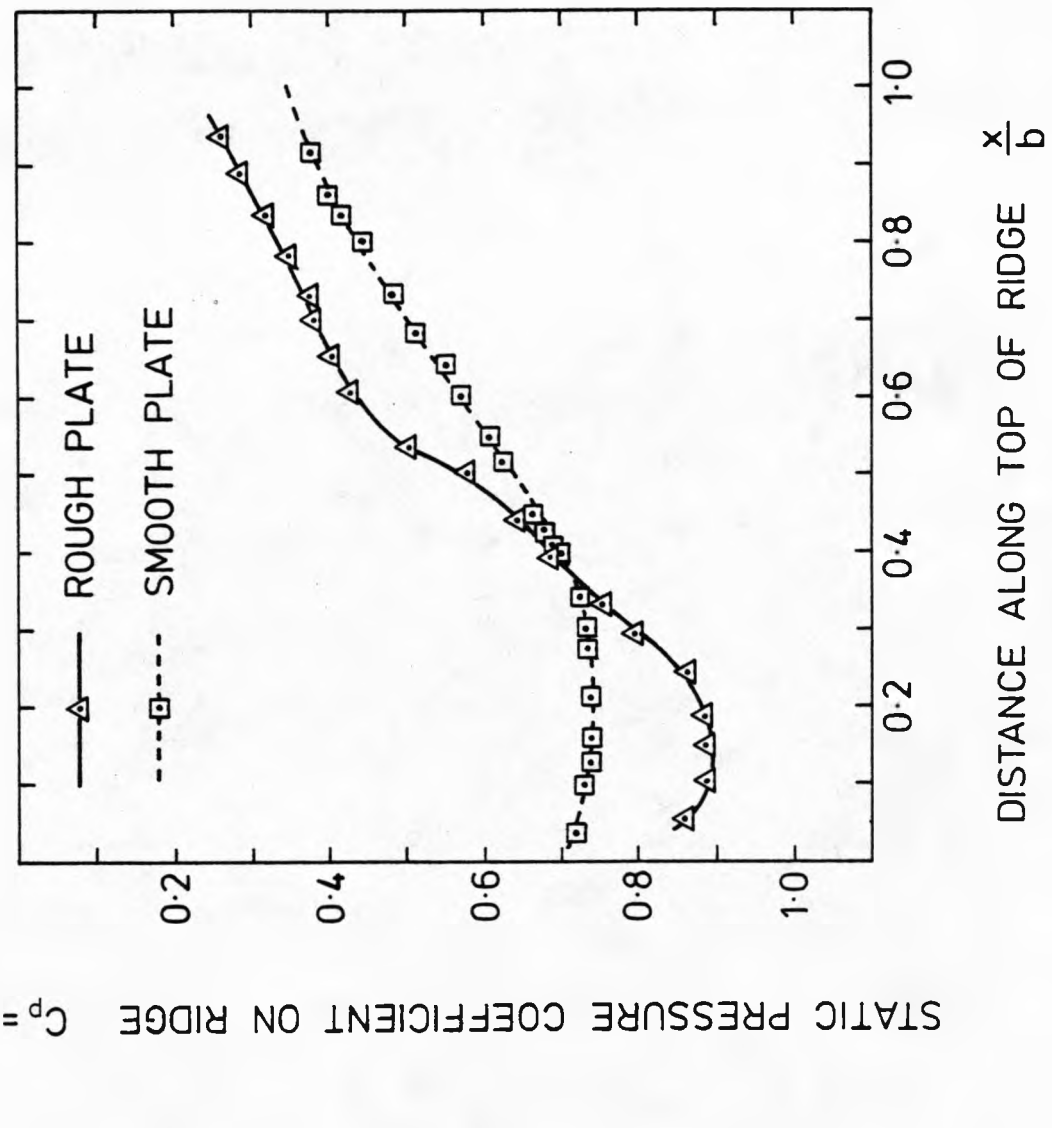

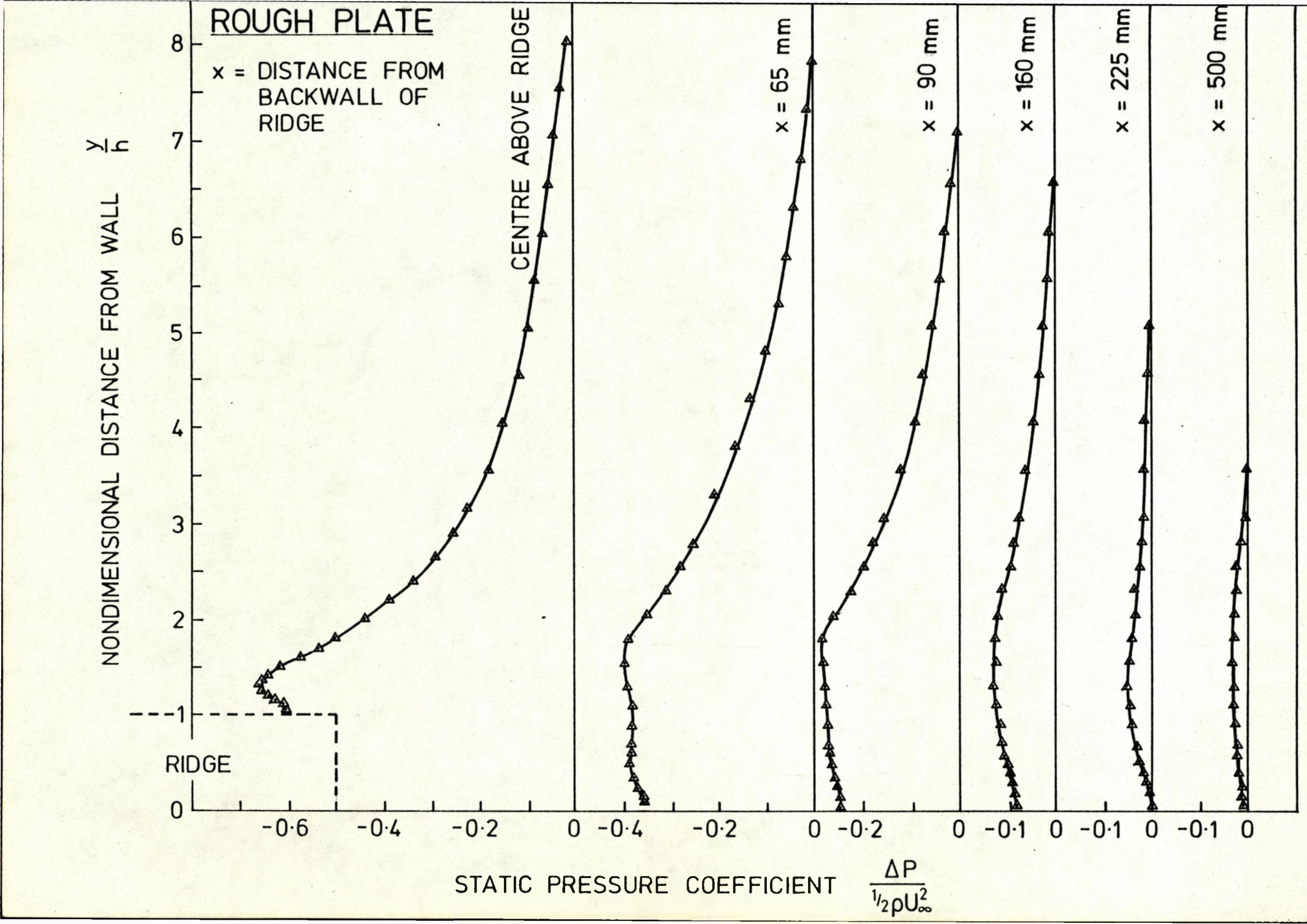

STATIC PRESSURE DISTRIBUTION ON SEPARATION ZONE DOWNSTREAM OF RIDGE ATTACHED TO ROUGH SURFACE

FIG. (4.4a)

FIG.(4.4b)

STATIC PRESSURE DISTRIBUTION ON SEPARATION ZONE
DOWNSTREAM OF HILL ATTACHED TO ROUGH SURFACE

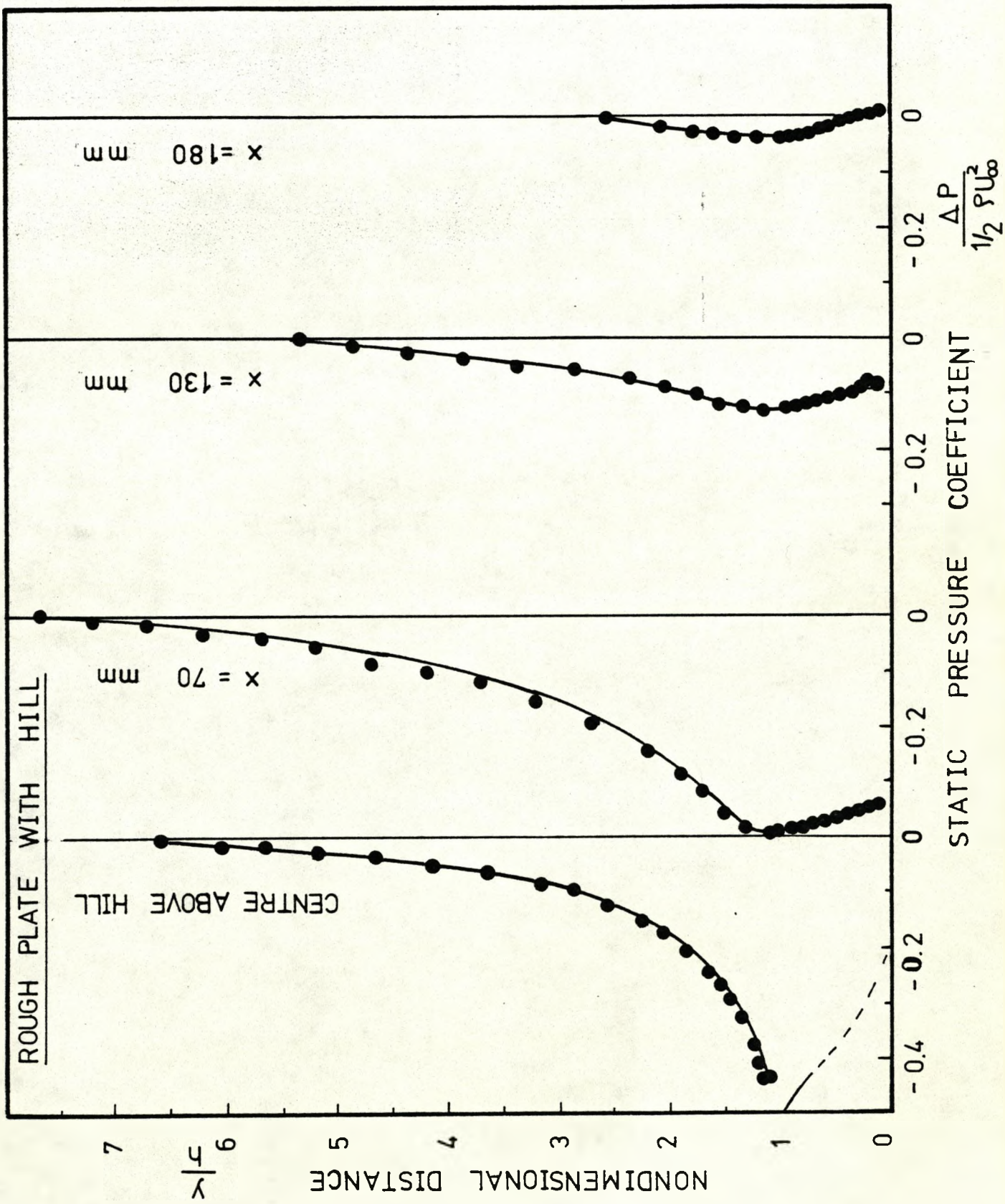

STATIC PRESSURE DISTRIBUTION ON SEPARATION ZONE DOWNSTREAM OF RIDGE ATTACHED TO SMOOTH SURFACE

FIG.(4.4c)

MEAN VELOCITY DISTRIBUTIONS ON ROUGH PLATE
WITHOUT RIDGE

FIG.(4.5 a)

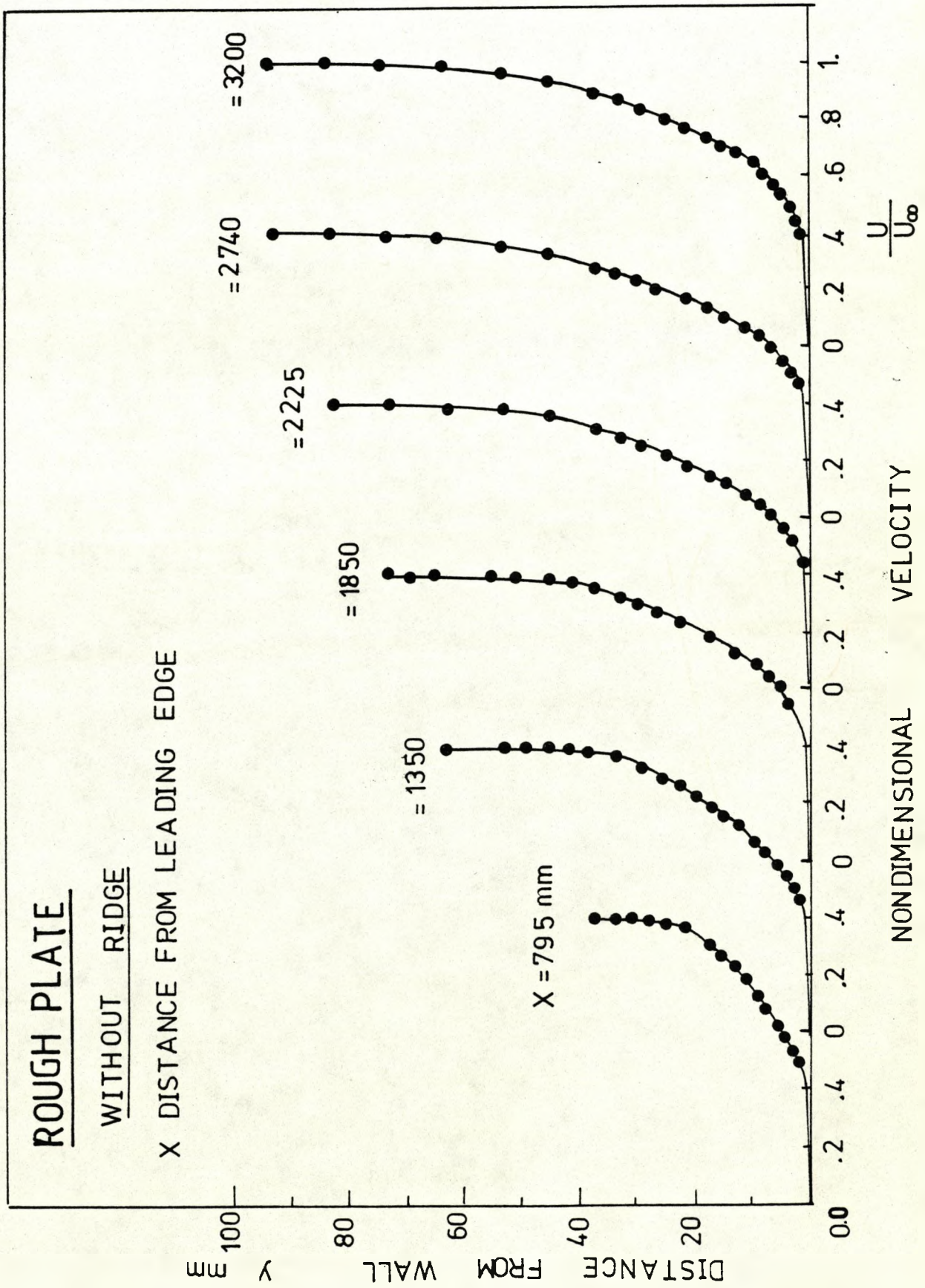

MEAN VELOCITY DISTRIBUTIONS ON SMOOTH PLATE
WITHOUT RIDGE

FIG.(4.5b)

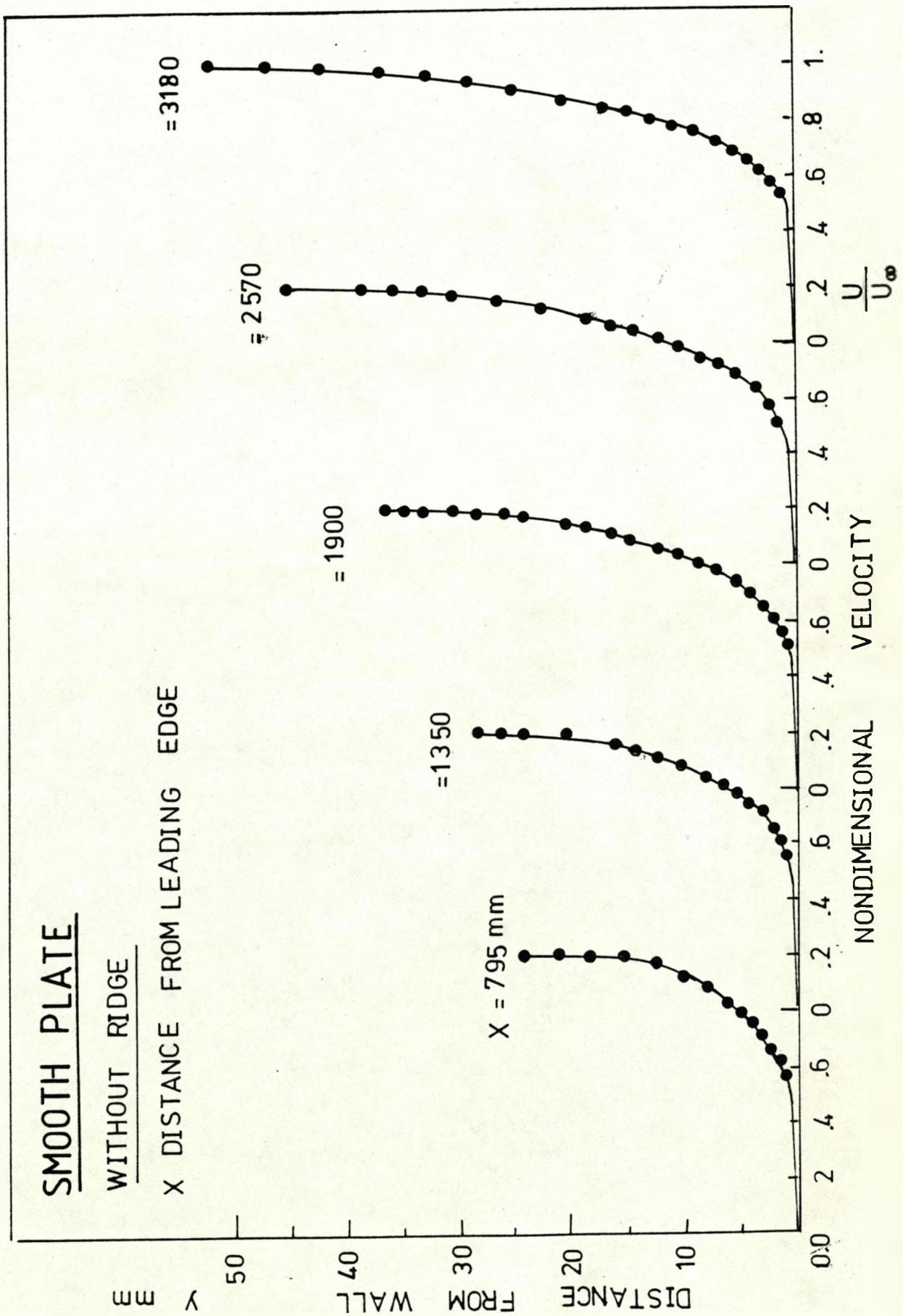

MEAN VELOCITY DISTRIBUTION DOWNSTREAM OF RIDGE ATTACHED TO ROUGH SURFACE

FIG. 4.6a

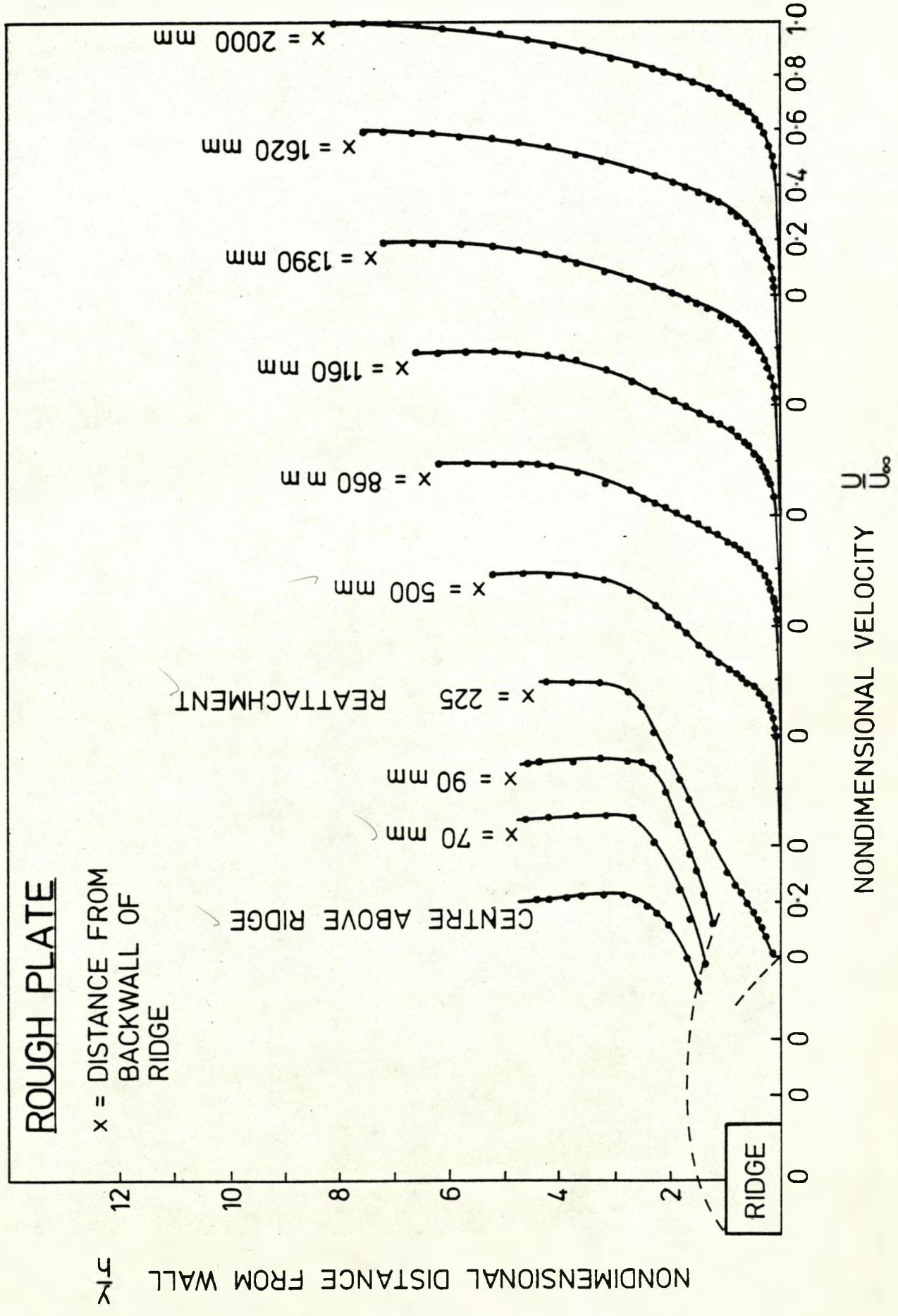

FIG.(4.6b)

MEAN VELOCITY DISTRIBUTION DOWNSTREAM OF HILL ATTACHED TO ROUGH SURFACE

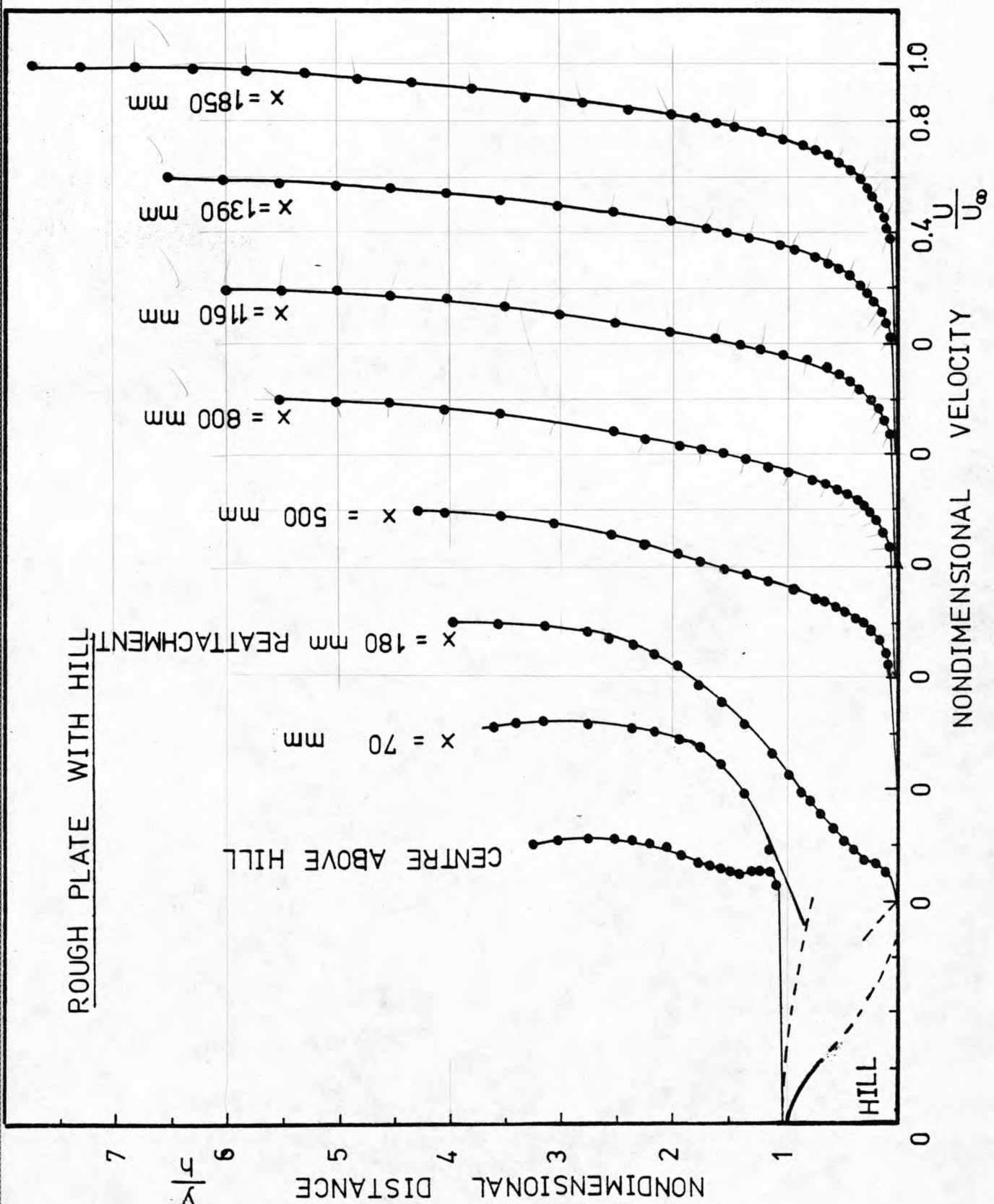

MEAN VELOCITY DISTRIBUTION DOWNSTREAM OF RIDGE ATTACHED TO SMOOTH SURFACE

FIG.(4.6c)

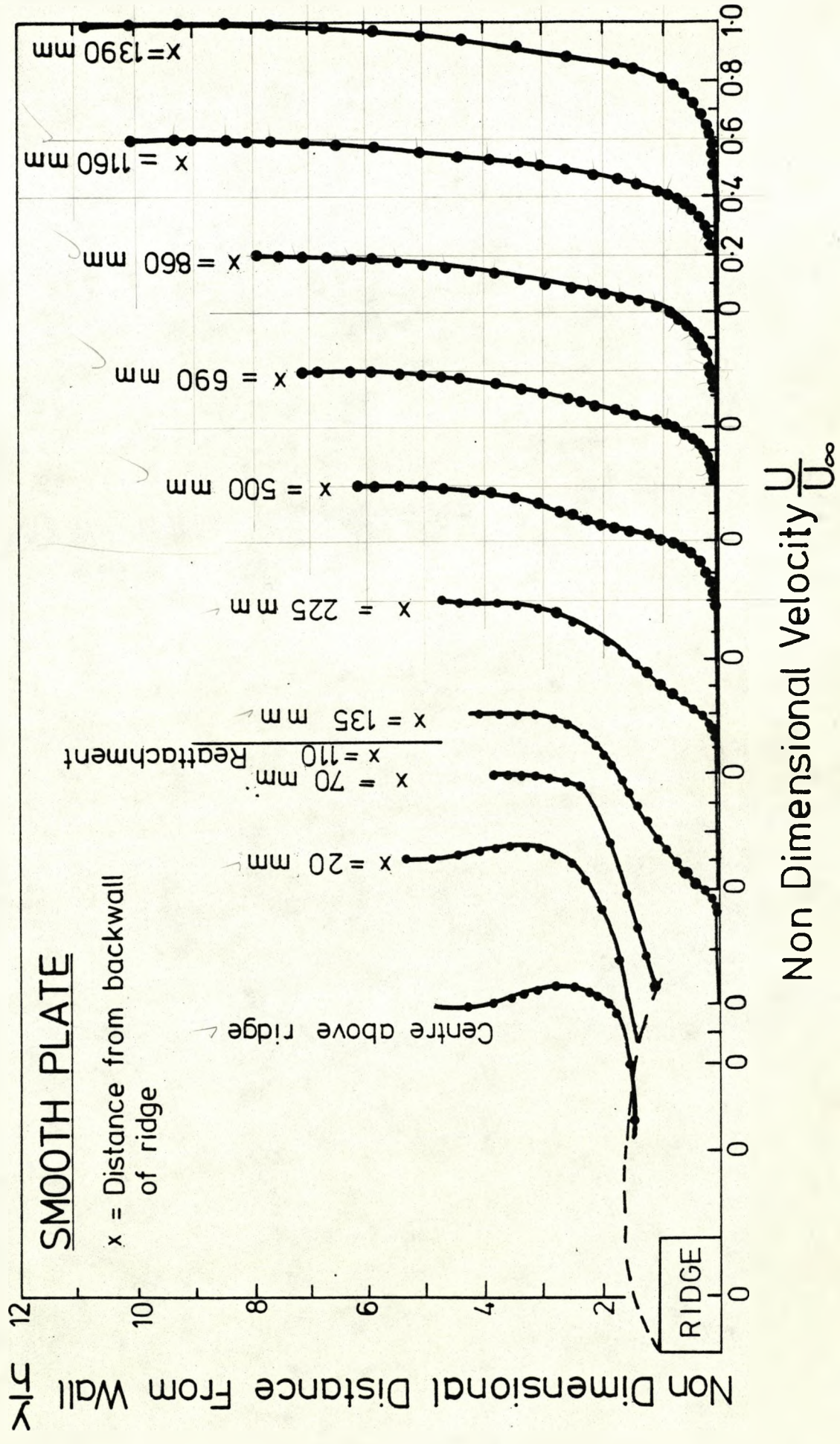

MEAN VELOCITY DISTRIBUTION DOWNSTREAM OF RIDGE ATTACHED TO ROUGH SURFACE IN "LAW-OF-THE-WALL" CO-ORDINATES

FIG.(4.7a)

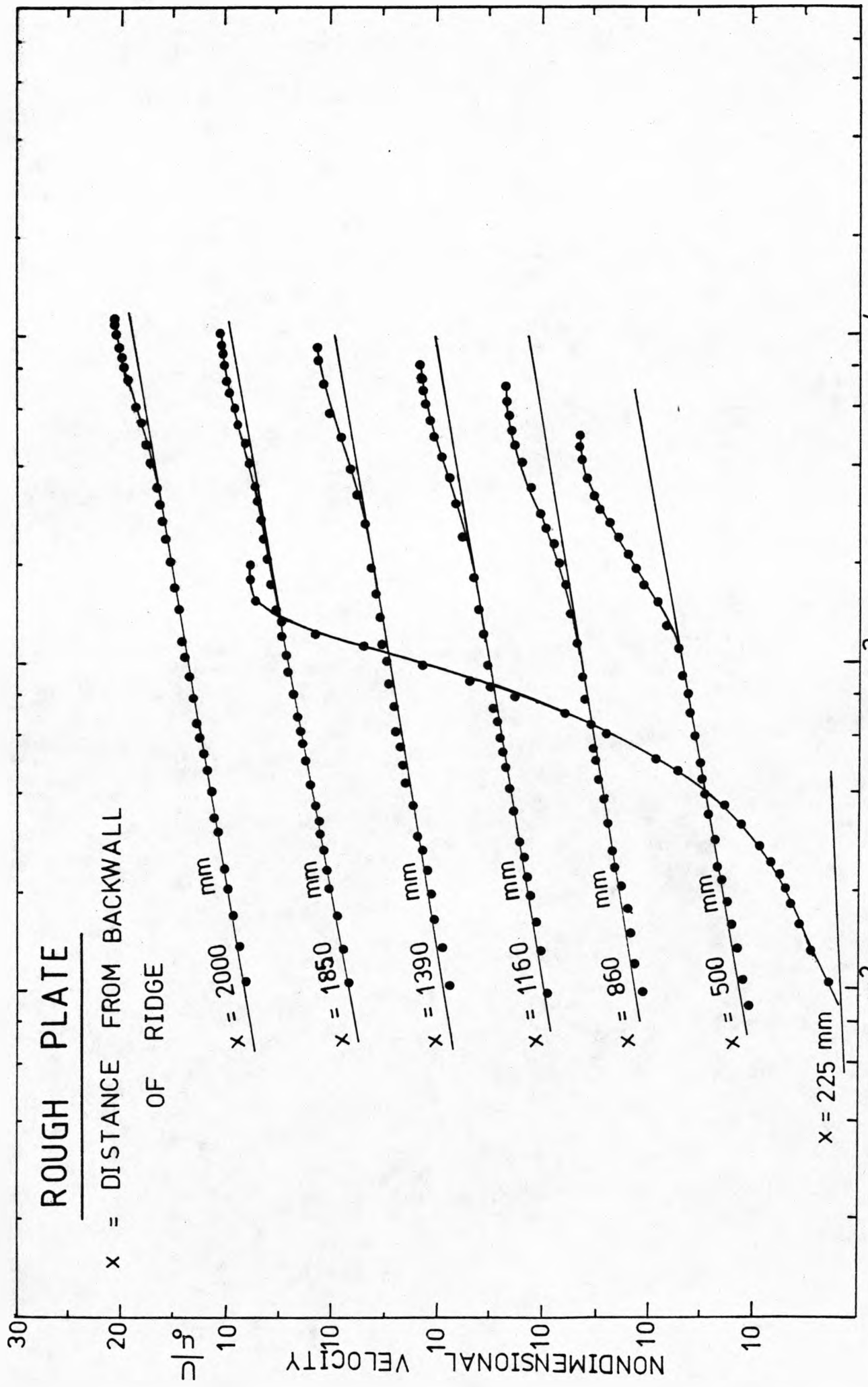

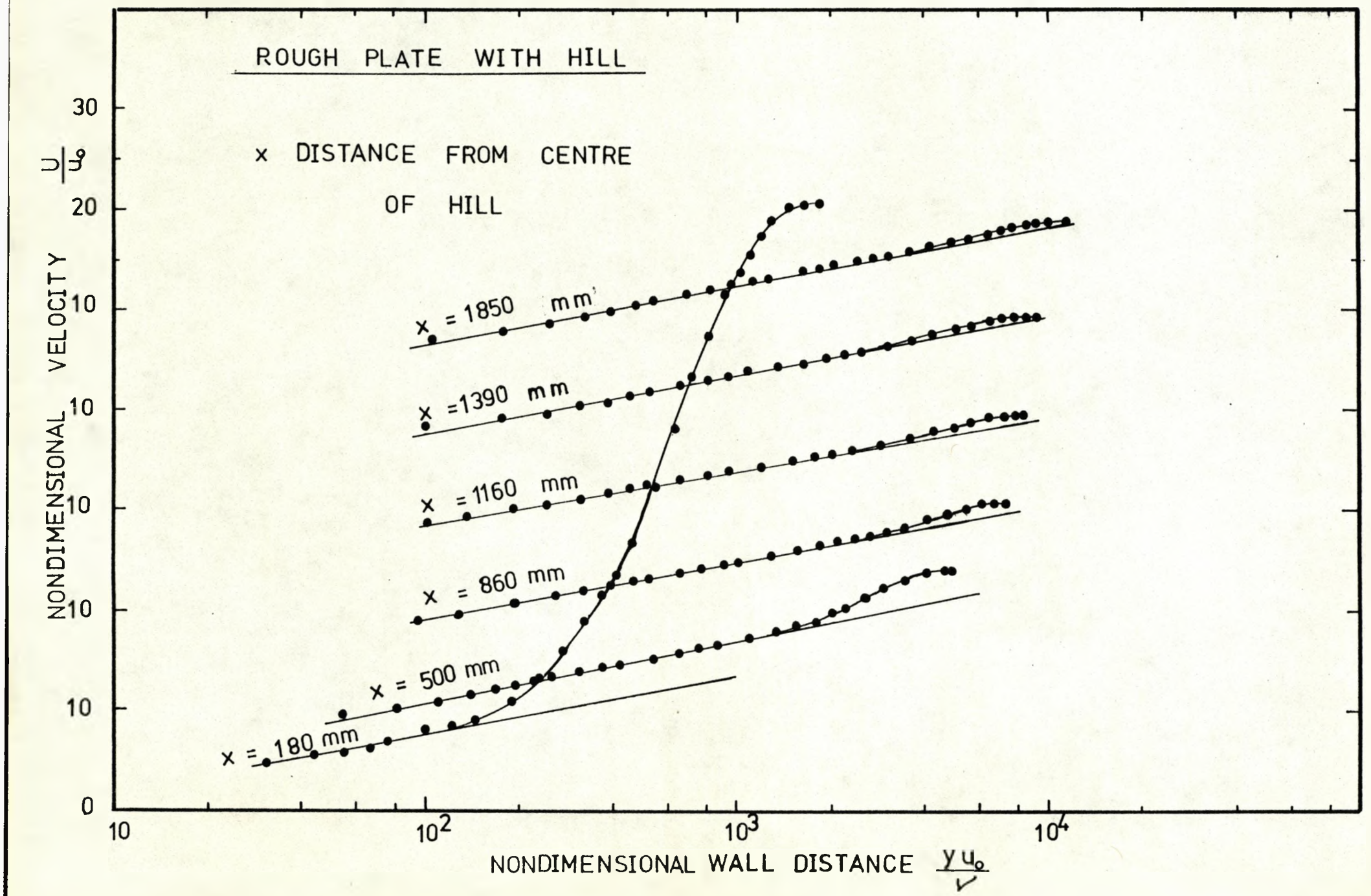

MEAN VELOCITY DISTRIBUTION DOWNSTREAM OF HILL ATTACHED TO ROUGH SURFACE IN "LAW-OF-THE-WALL" CO-ORDINATES

FIG.(4.7b)

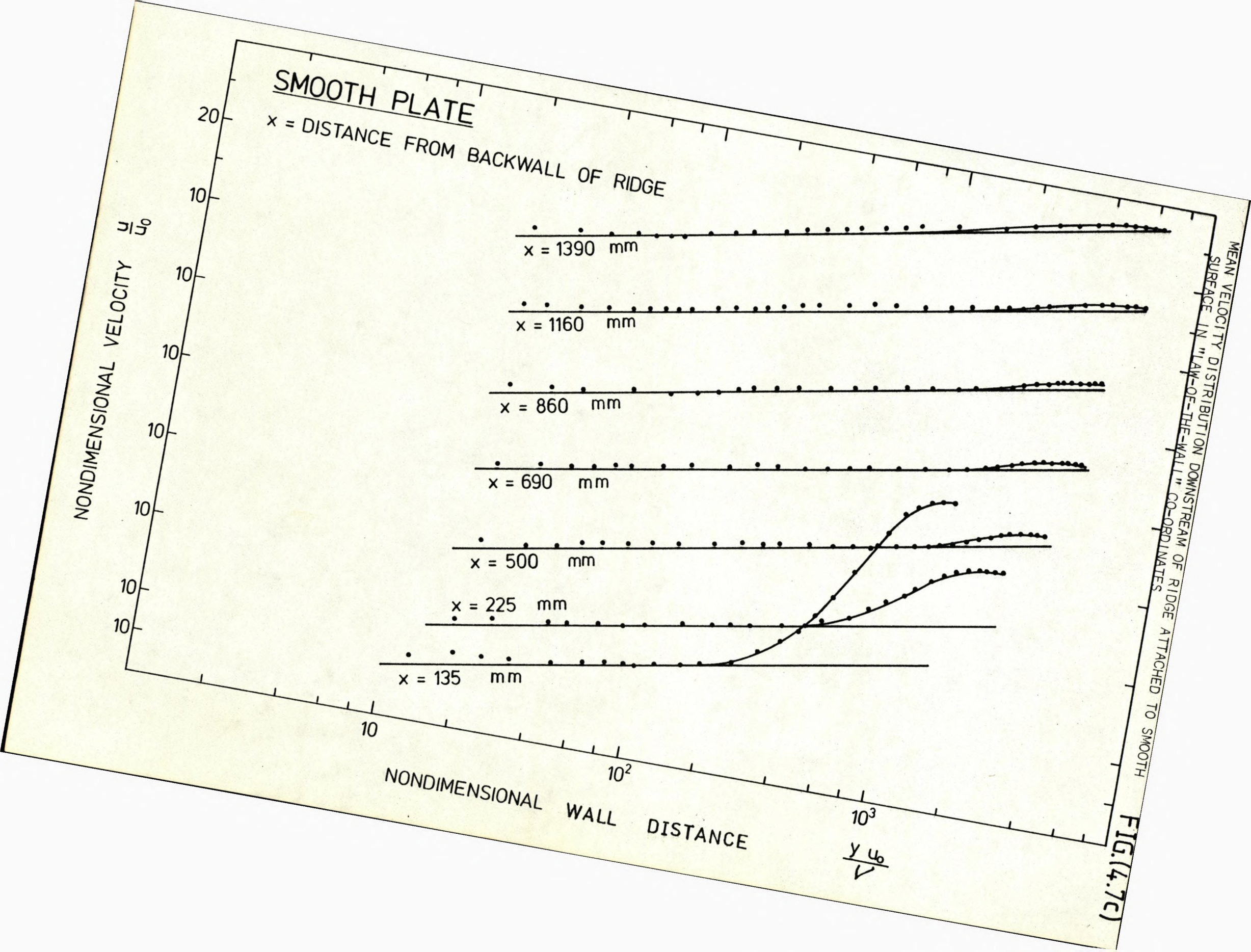

MEAN VELOCITY DISTRIBUTION DOWNSTREAM OF RIDGE ATTACHED TO SMOOTH SURFACE IN "LAW-OF-THE-WALL" CO-ORDINATES

FIG.(4.7c)

DISTRIBUTION OF THE ROUGHNESS FUNCTION $\frac{\Delta u}{u_o}$ DOWNSTREAM OF RIDGE AND HILL ATTACHED TO ROUGH SURFACE

FIG.(4.8)

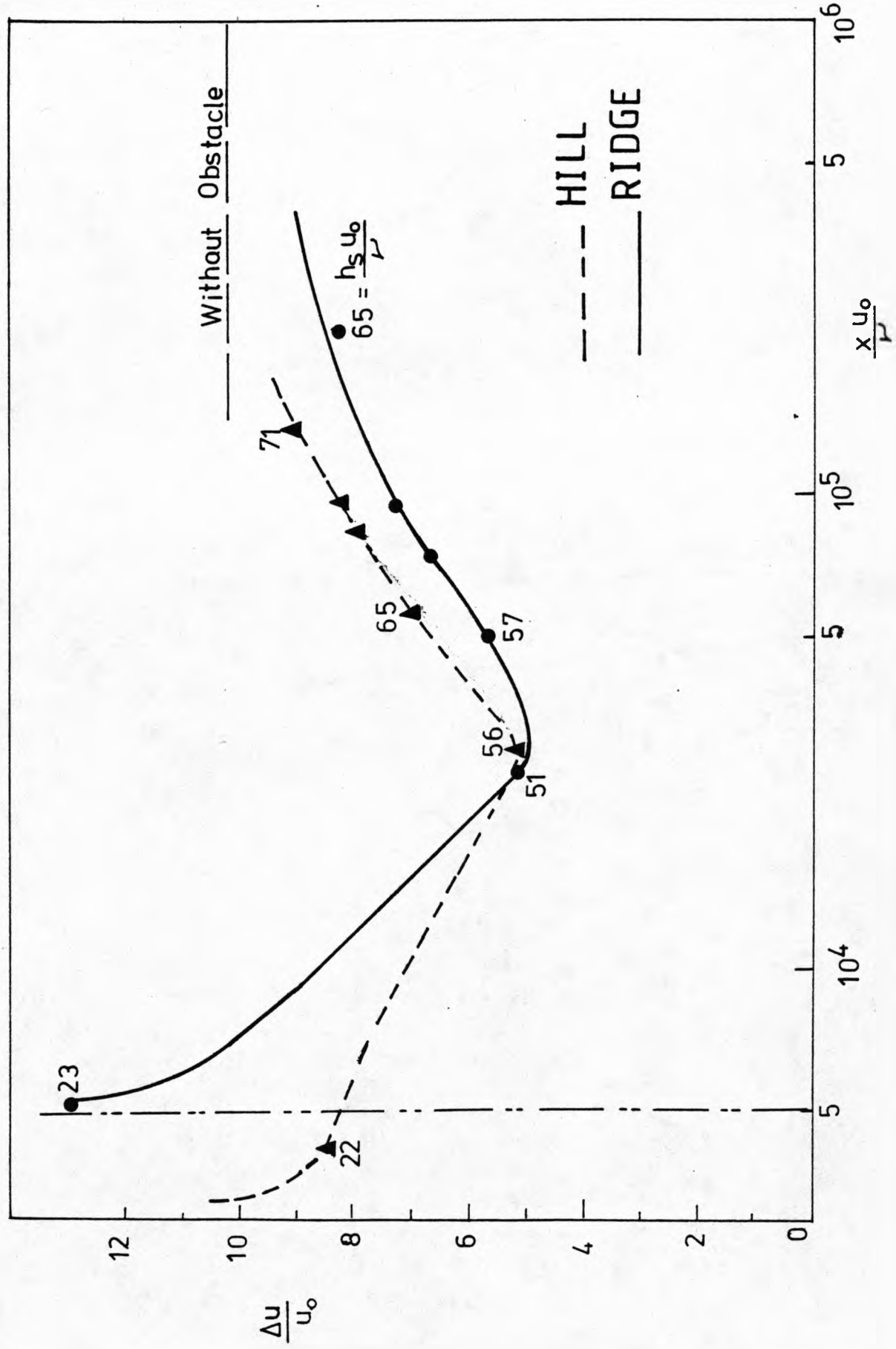

FIG.(4.9a)

WALL FRICTION COEFFICIENT DOWNSTREAM OF RIDGE AND HILL ATTACHED TO ROUGH SURFACE

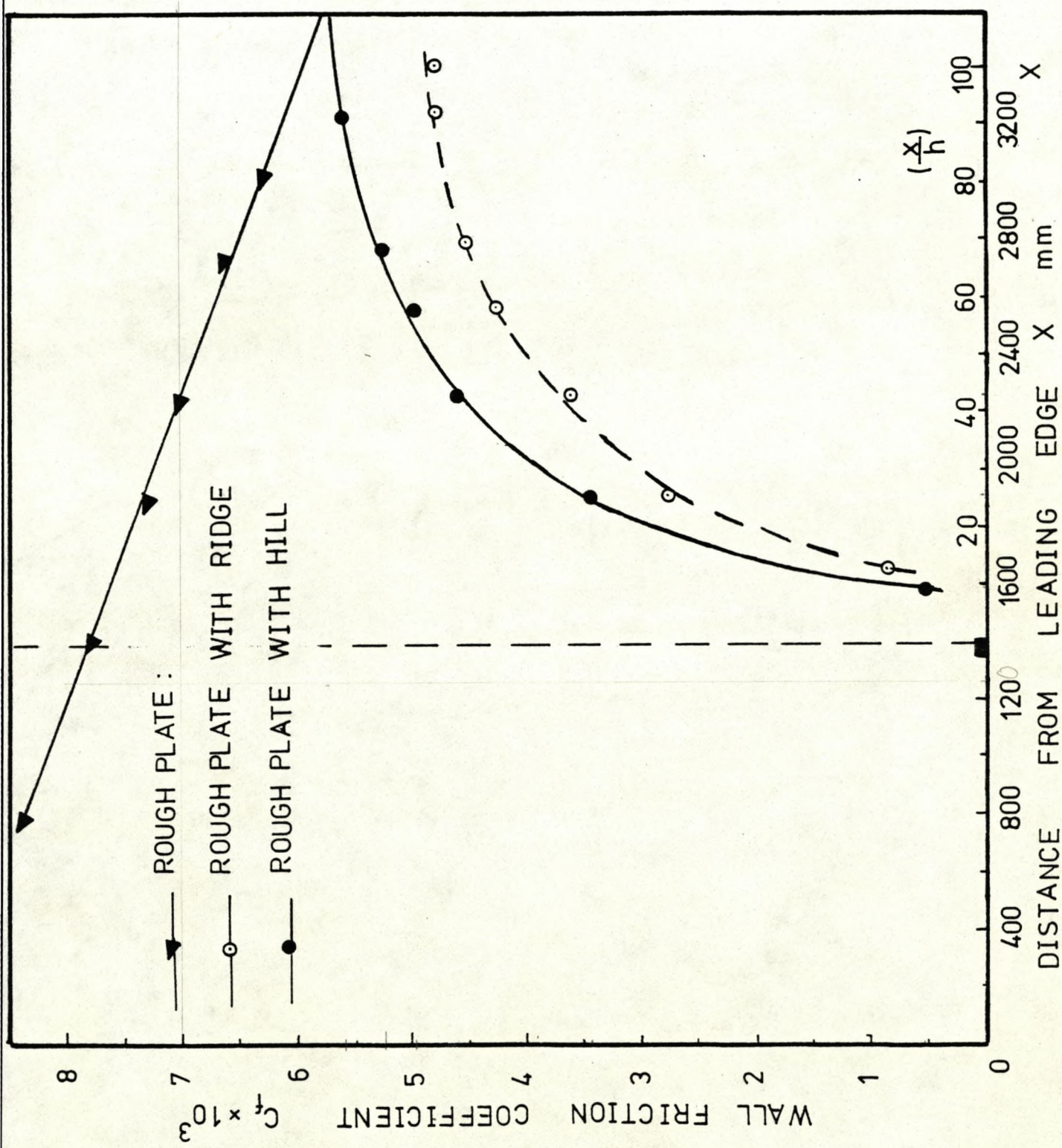

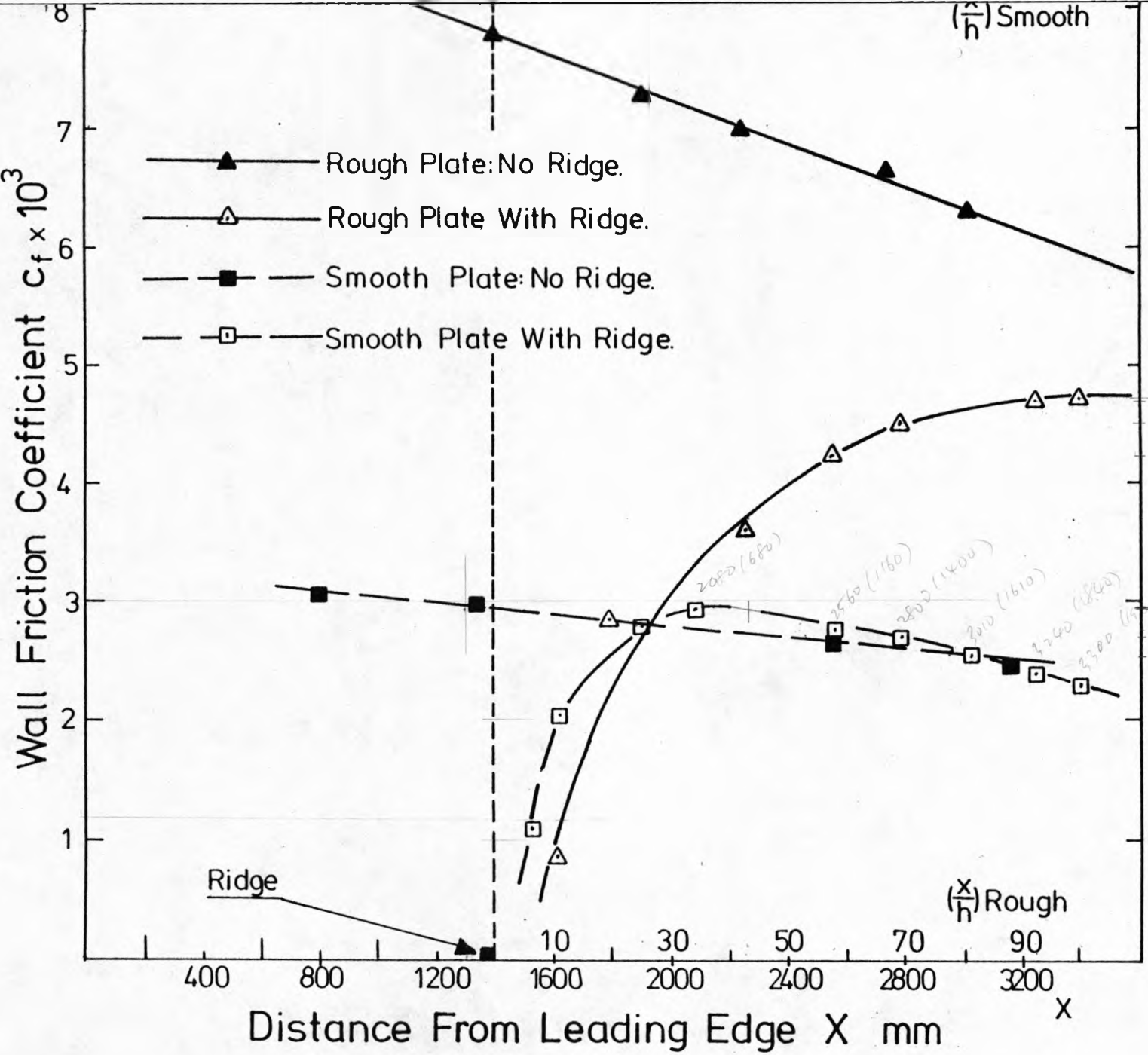

WALL FRICTION COEFFICIENT DOWNSTREAM OF RIDGE ATTACHED TO ROUGH AND SMOOTH SURFACES

FIG.(4.9b)

FIG.(4.10a)

1- BOUNDARY-LAYER SHAPE PARAMETER WITHOUT OBSTACLE FOR ROUGH AND SMOOTH SURFACES

2- BOUNDARY-LAYER THICKNESS WITH AND WITHOUT OBSTACLE ON ROUGH AND SMOOTH SURFACES

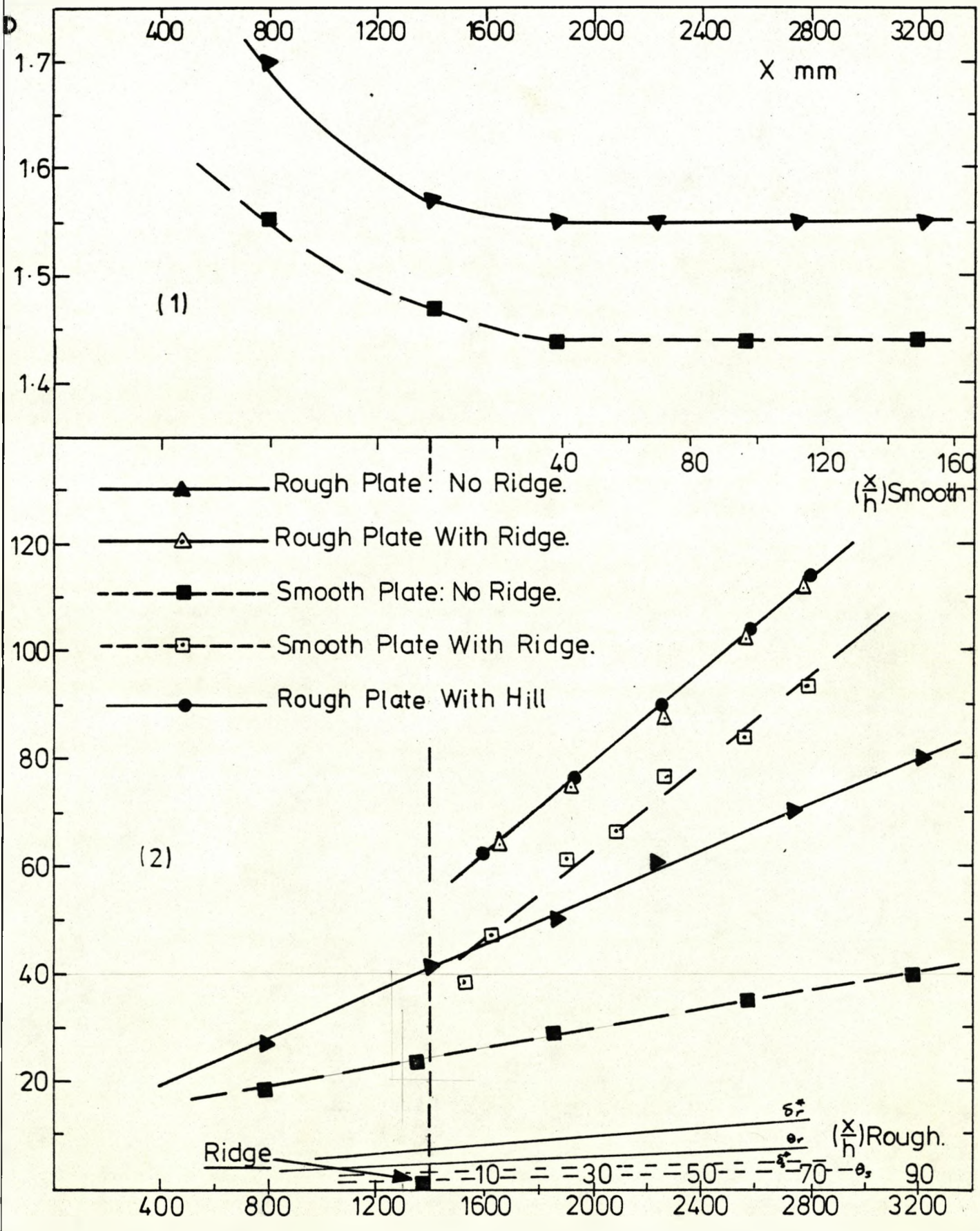

Distance From Leading Edge X mm

FIG.(4.10b)

BOUNDARY-LAYER SHAPE PARAMETER AND INTEGRAL THICKNESSES DOWNSTREAM OF RIDGE AND HILL ATTACHED TO ROUGH SURFACE

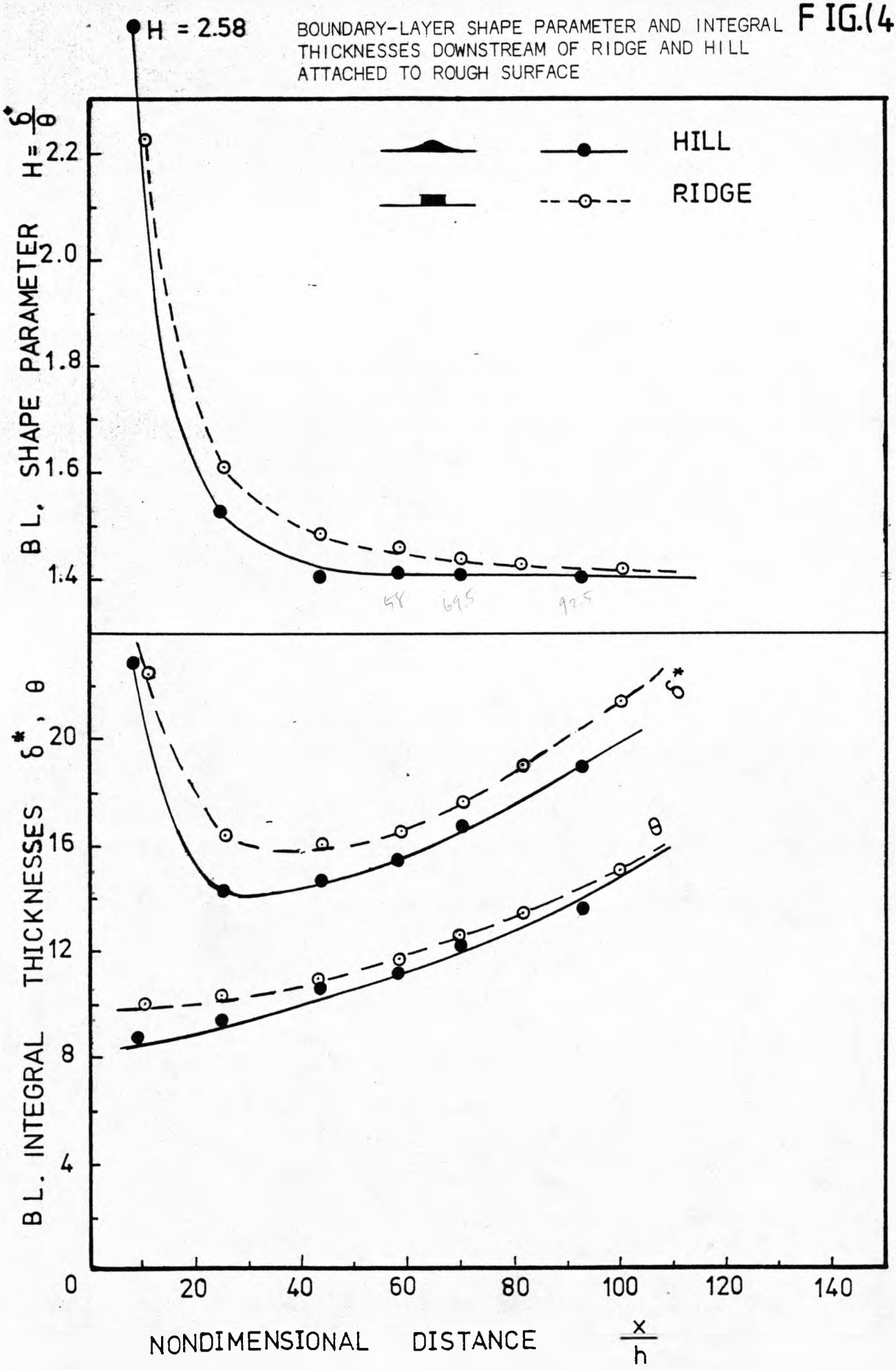

BOUNDARY-LAYER SHAPE PARAMETER AND INTEGRAL THICKNESSES DOWNSTREAM OF RIDGE ATTACHED TO ROUGH AND SMOOTH SURFACE

FIG.(4.10c)

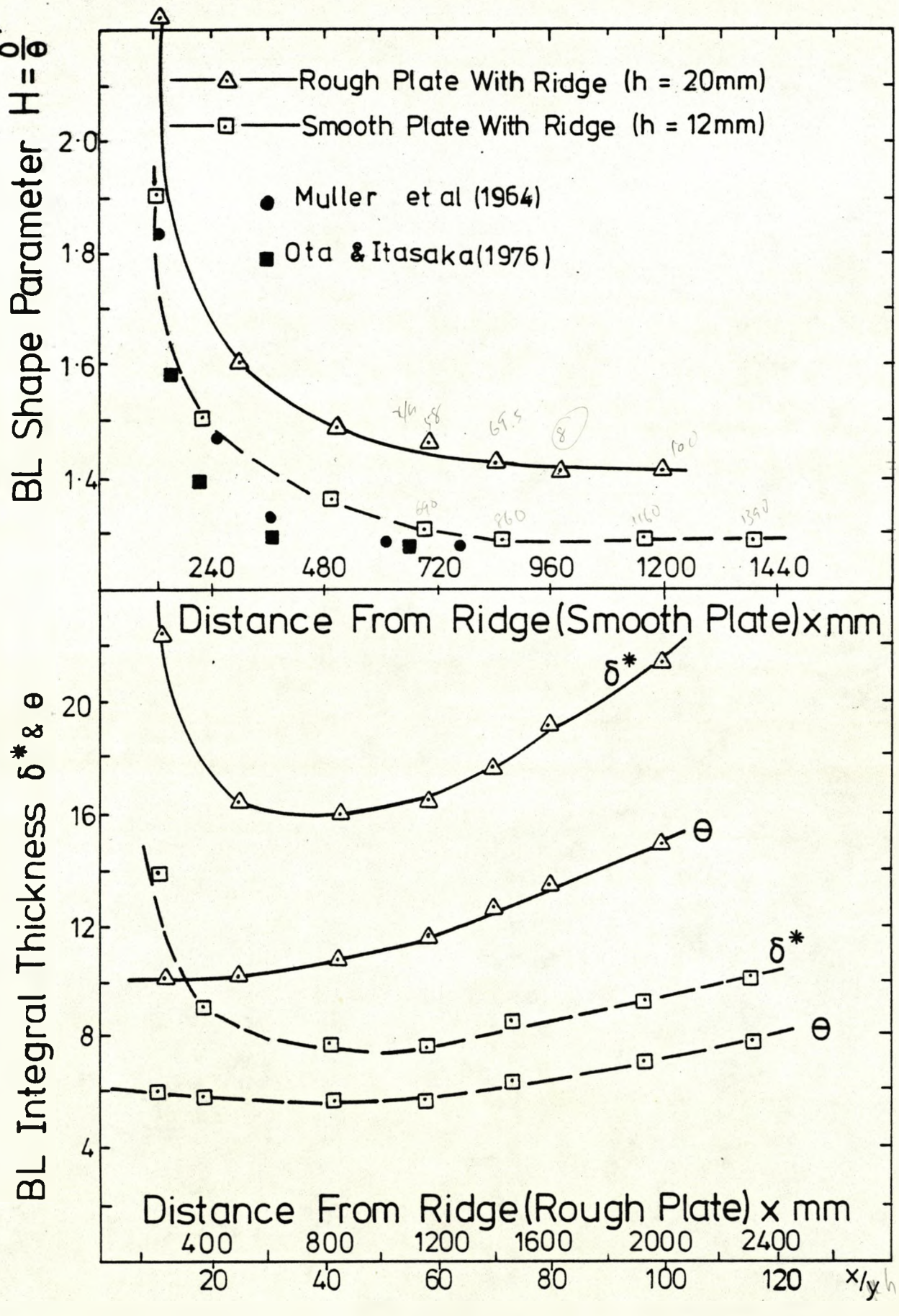

FIG.(4.11)

VALUES OF CLAUSER PARAMETER G DOWNSTREAM OF RIDGE AND HILL ON SMOOTH AND ROUGH SURFACES

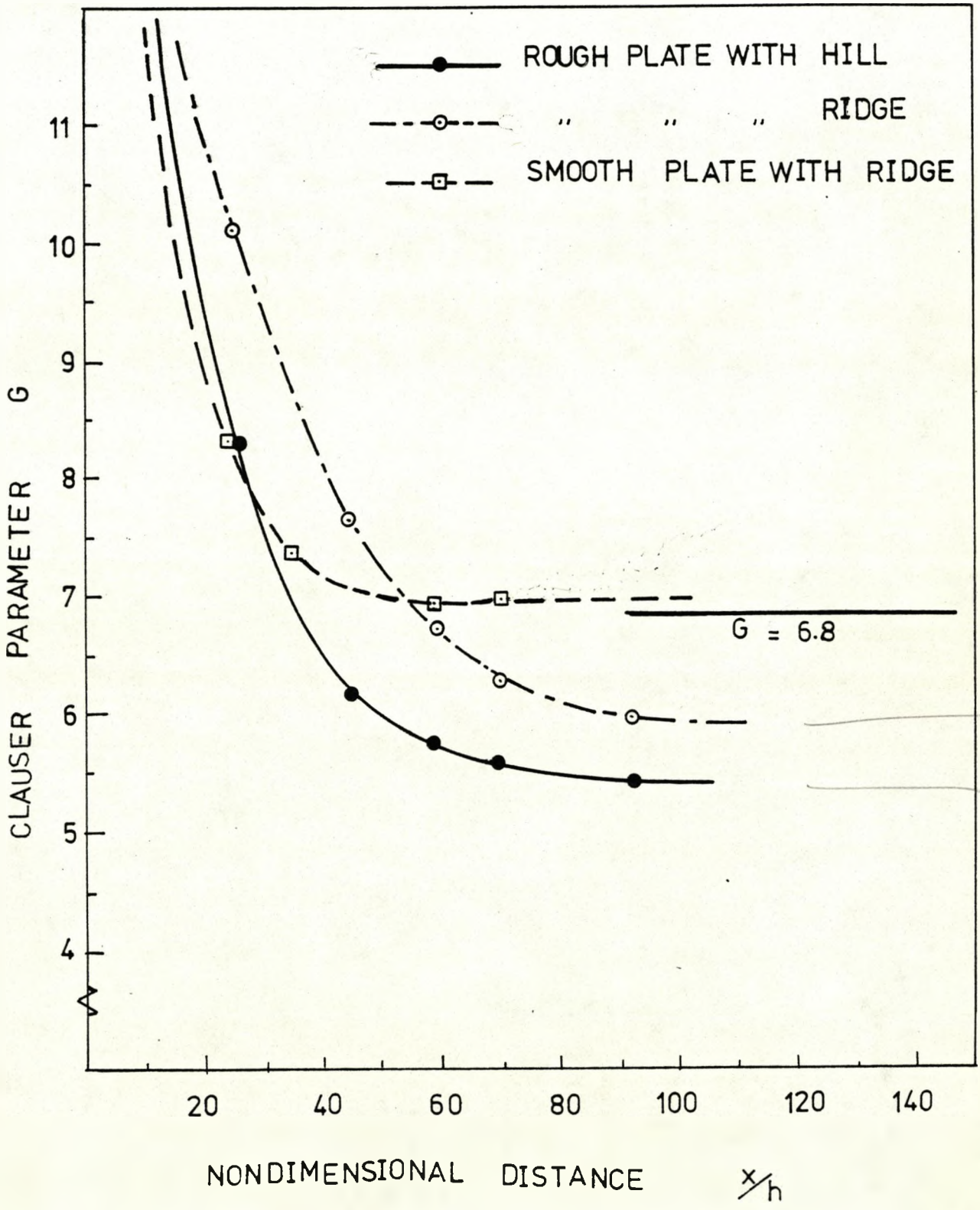

FIG.(4.12a)

LONGITUDINAL TURBULENT NORMAL STRESS DOWNSTREAM
OF RIDGE AND HILL ATTACHED TO ROUGH SURFACE

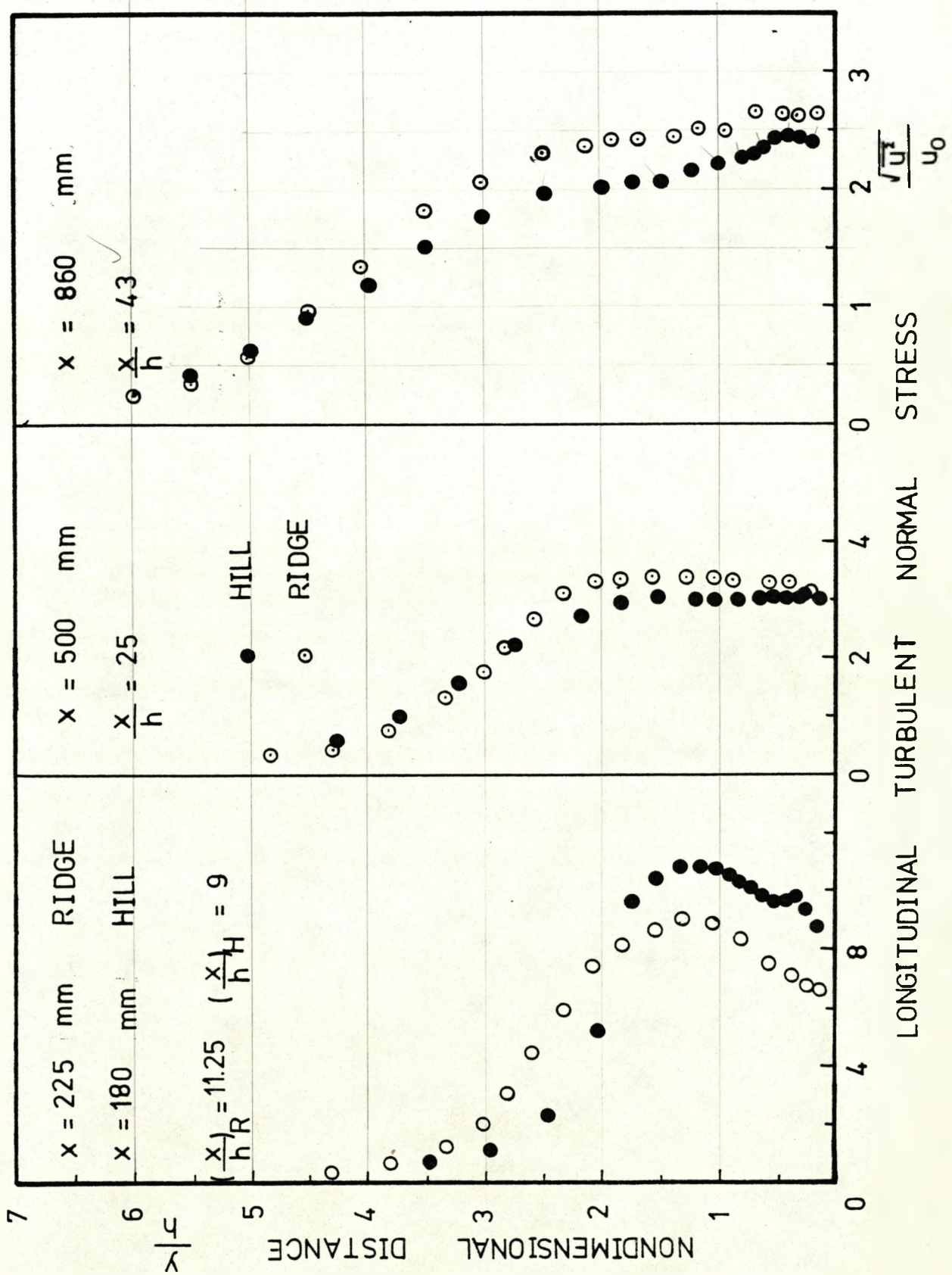

FIG.(4.12 b)

LONGITUDINAL TURBULENT NORMAL STRESS DOWNSTREAM
OF RIDGE AND HILL ATTACHED TO ROUGH SURFACE

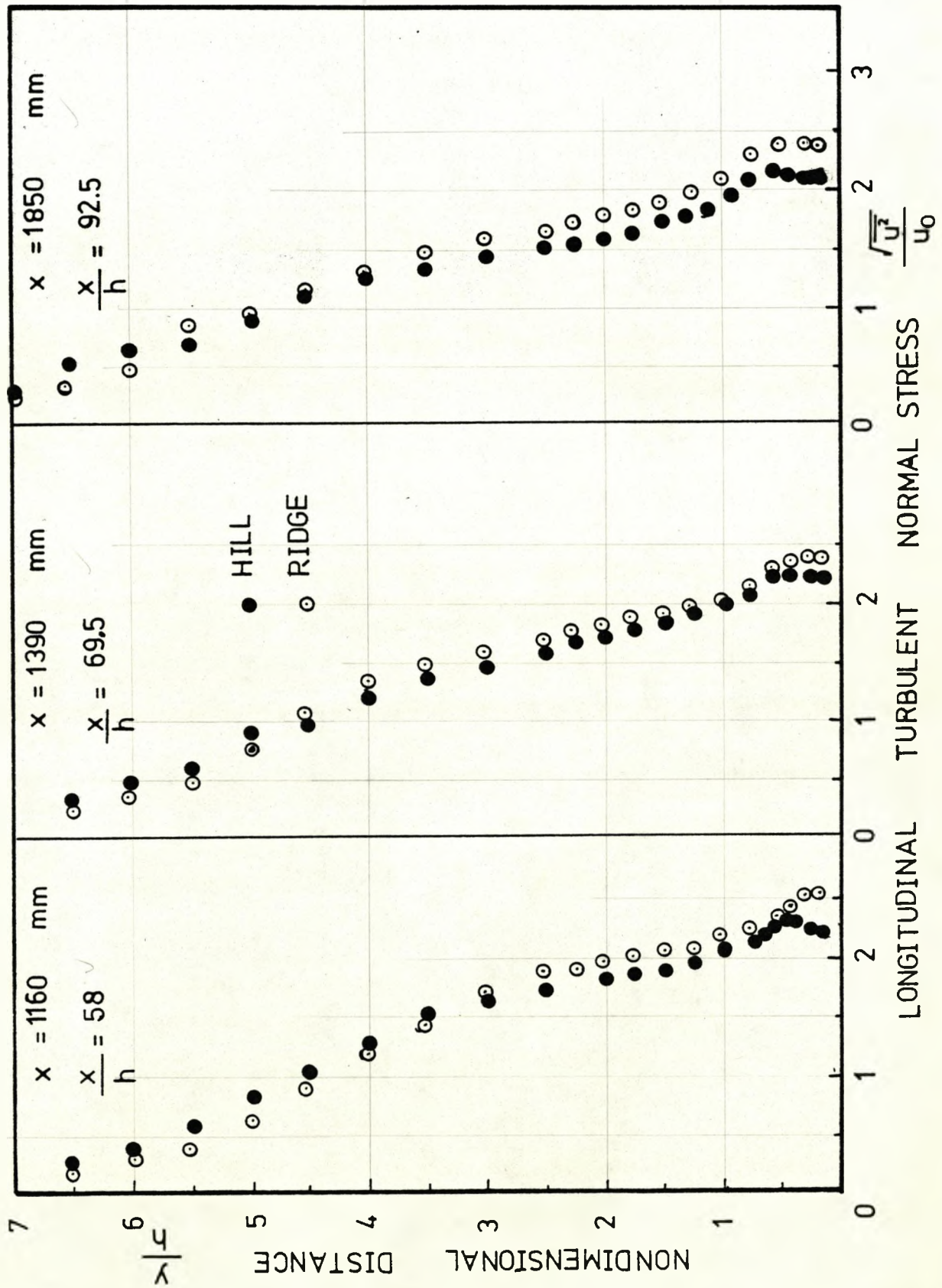

FIG.(4.13a)

TRANSVERSE TURBULENT NORMAL STRESS DOWNSTREAM OF
RIDGE AND HILL ATTACHED TO ROUGH SURFACE

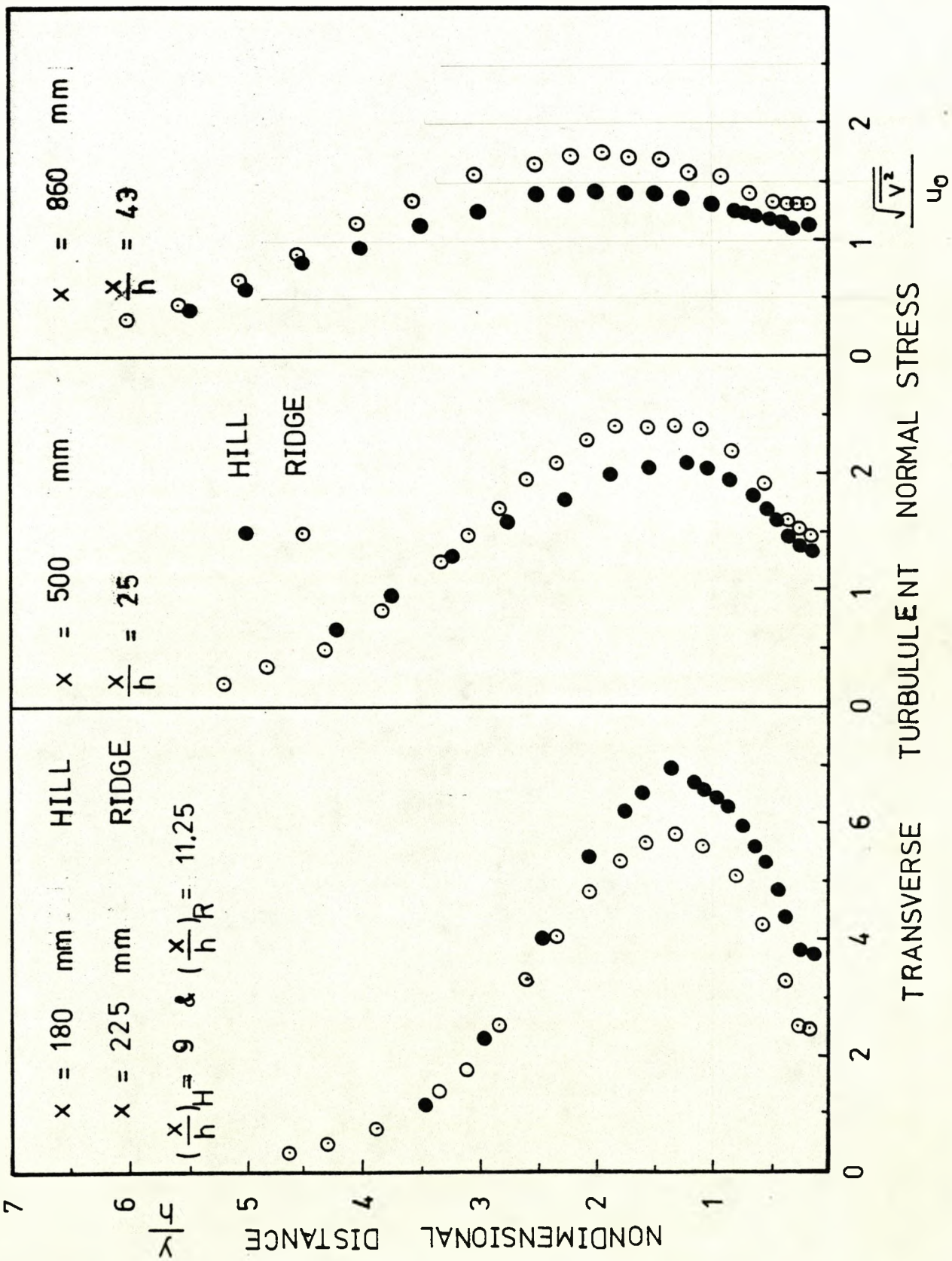

FIG. (4.13 b)

TRANSVERSE TURBULENT NORMAL STRESS DOWNSTREAM
OF RIDGE AND HILL ATTACHED TO ROUGH SURFACE

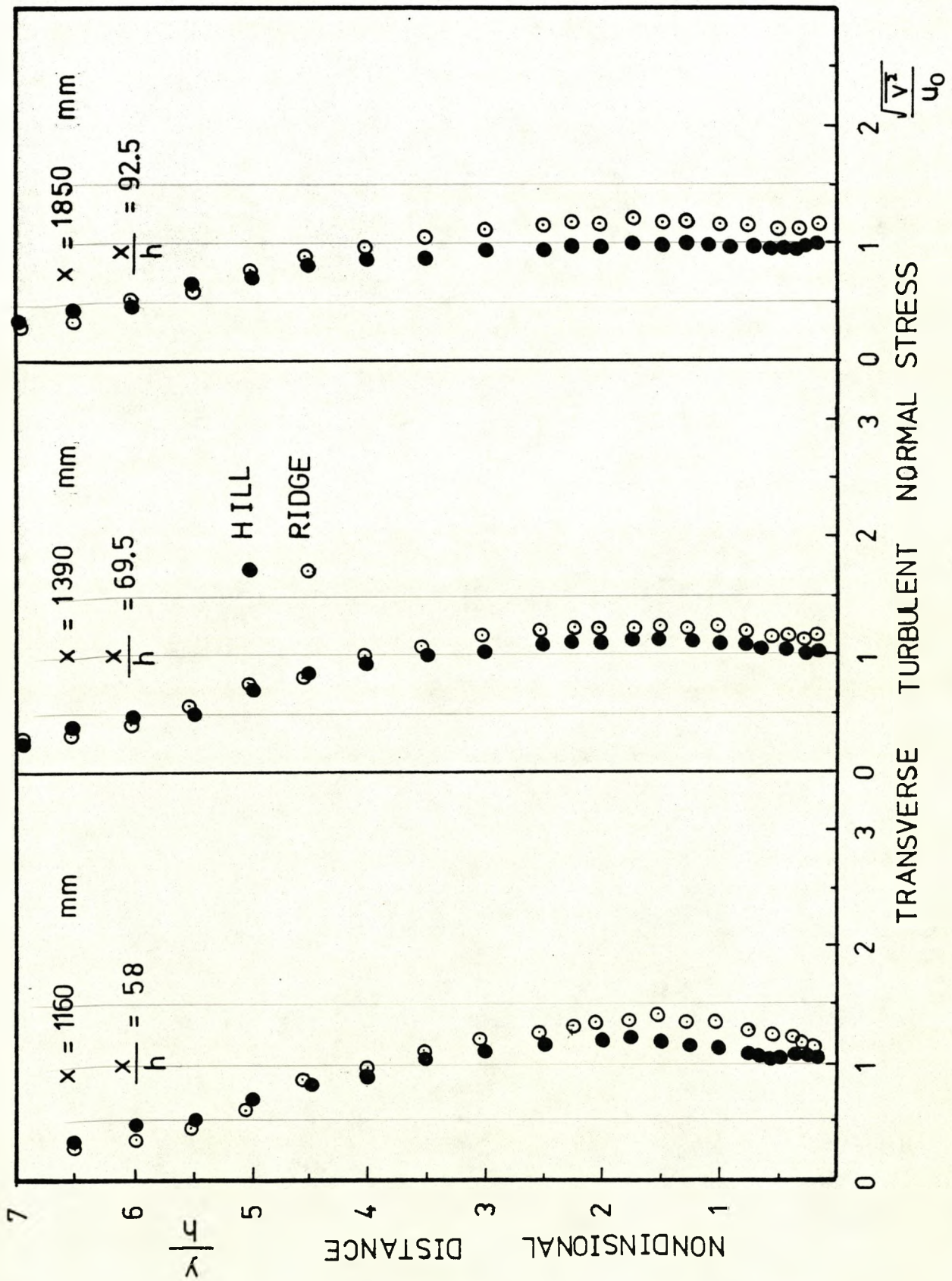

LONGITUDINAL TURBULENT NORMAL STRESS DOWNSTREAM OF RIDGE ATTACHED TO ROUGH AND SMOOTH SURFACES

FIG.(4.14a)

LONGITUDINAL TURBULENT NORMAL STRESS DOWNSTREAM OF RIDGE ATTACHED TO ROUGH AND SMOOTH SURFACES

FIG.(4.14b)

TRANSVERSE TURBULENT NORMAL STRESS DOWNSTREAM OF RIDGE ATTACHED TO ROUGH AND SMOOTH SURFACES

FIG.(4.15a)

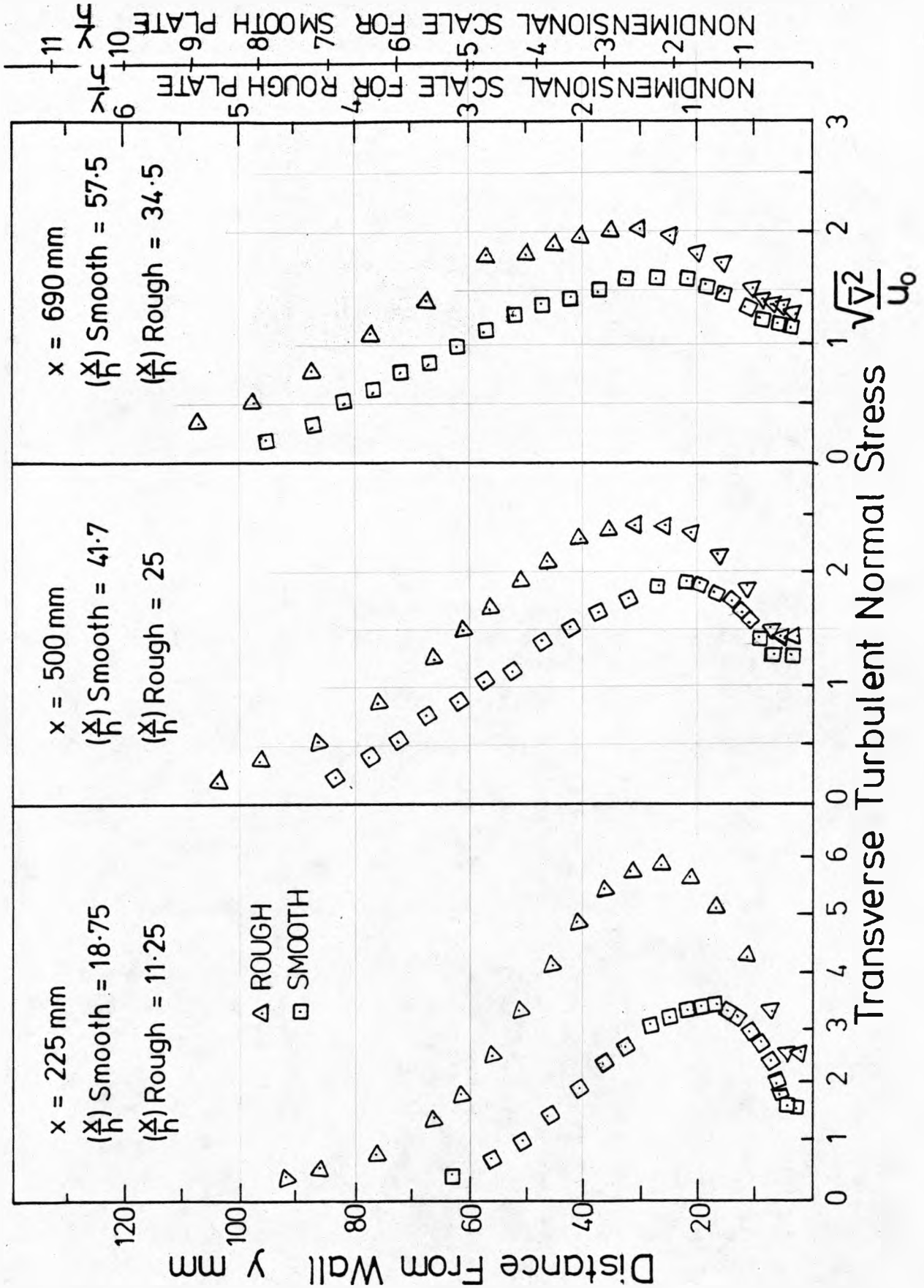

TRANSVERSE TURBULENT NORMAL STRESS DOWNSTREAM OF RIDGE ATTACHED TO ROUGH AND SMOOTH SURFACES

FIG.(4.15b)

FIG.(4.16a)

TURBULENT SHEAR STRESS DOWNSTREAM OF RIDGE AND HILL ATTACHED TO ROUGH SURFACE

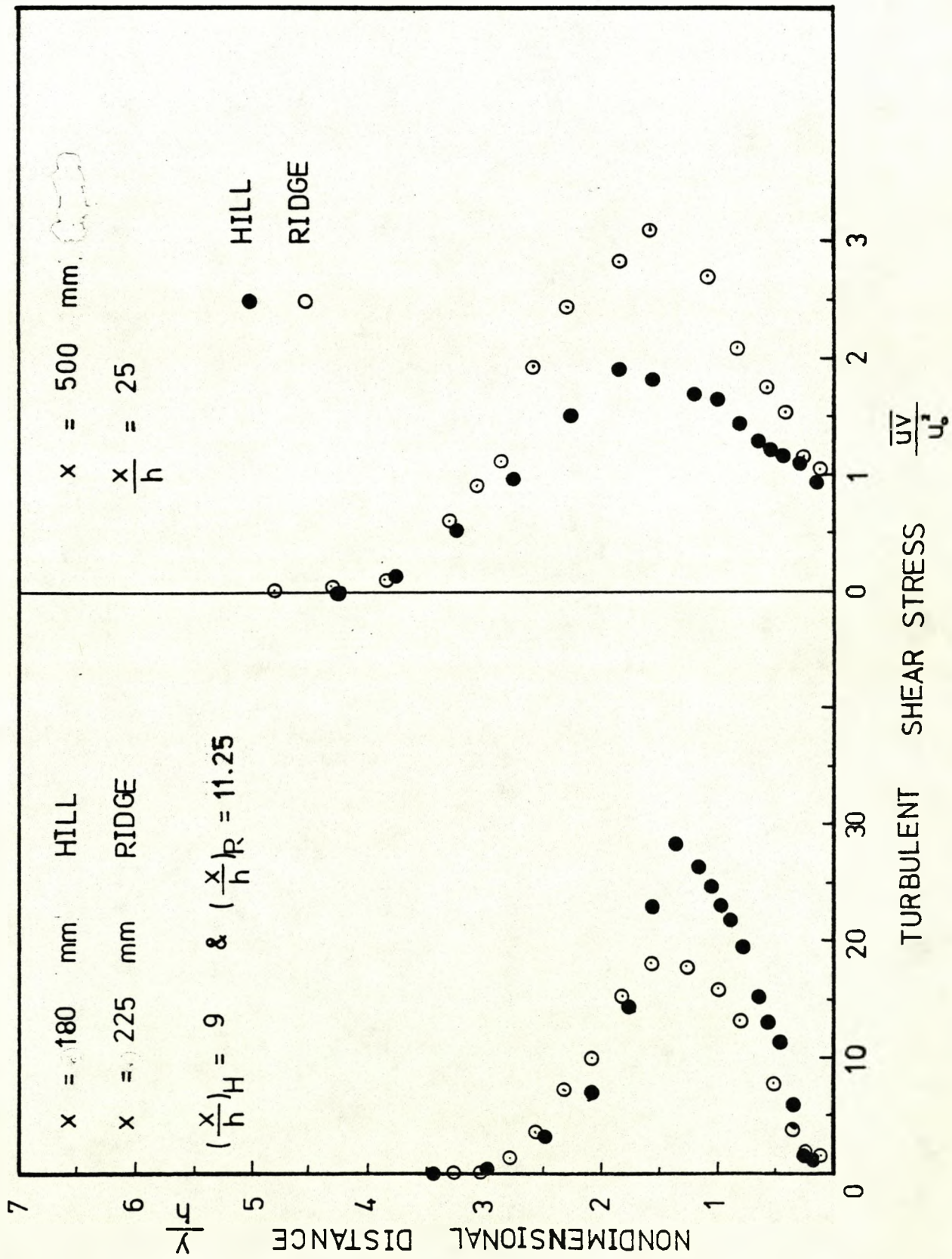

FIG.(4.16b)

TURBULENT SHEAR STRESS DOWNSTREAM OF RIDGE
AND HILL ATTACHED TO ROUGH SURFACE

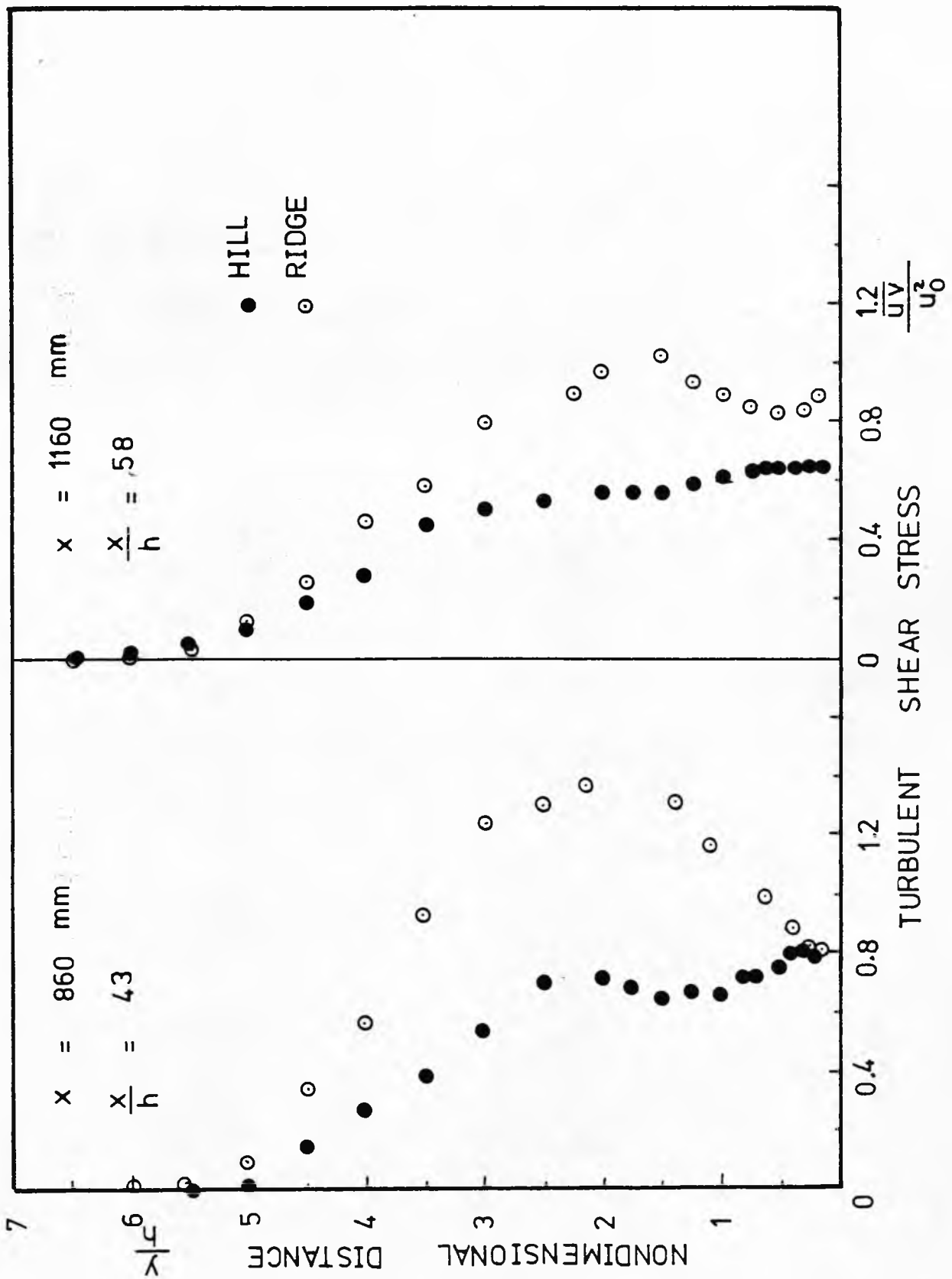

FIG.(4.16c)

TURBULENT SHEAR STRESS DOWNSTREAM OF RIDGE AND HILL ATTACHED TO ROUGH SURFACE

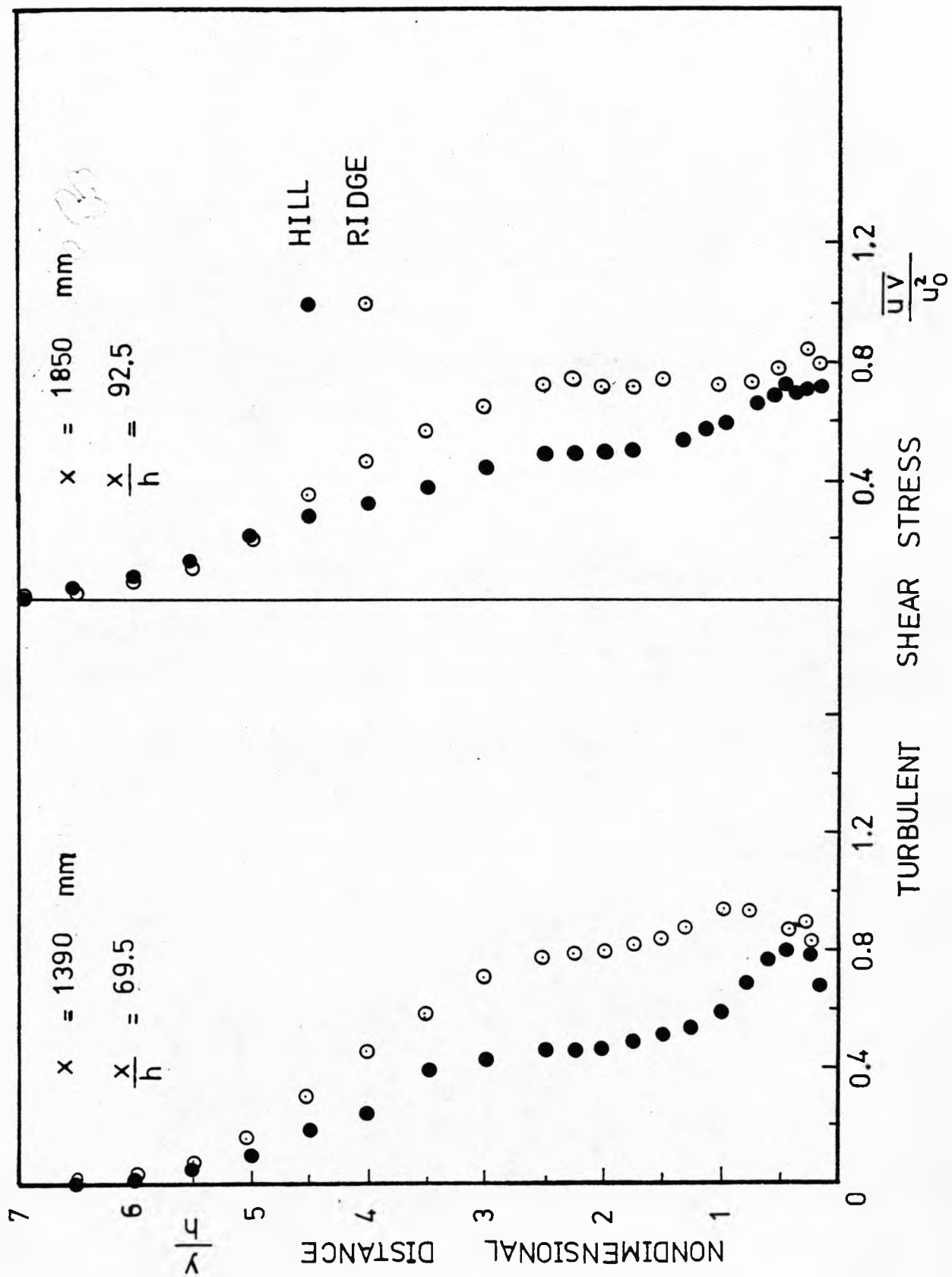

TURBULENT SHEAR STRESS DOWNSTREAM OF RIDGE
ATTACHED TO ROUGH AND SMOOTH SURFACES

FIG. (4.17a)

TURBULENT SHEAR STRESS DOWNSTREAM OF RIDGE
ATTACHED TO ROUGH AND SMOOTH SURFACES

FIG.(4.17b)

TURBULENT SHEAR STRESS DOWNSTREAM OF RIDGE
ATTACHED TO ROUGH AND SMOOTH SURFACES

FIG.(4.17c)

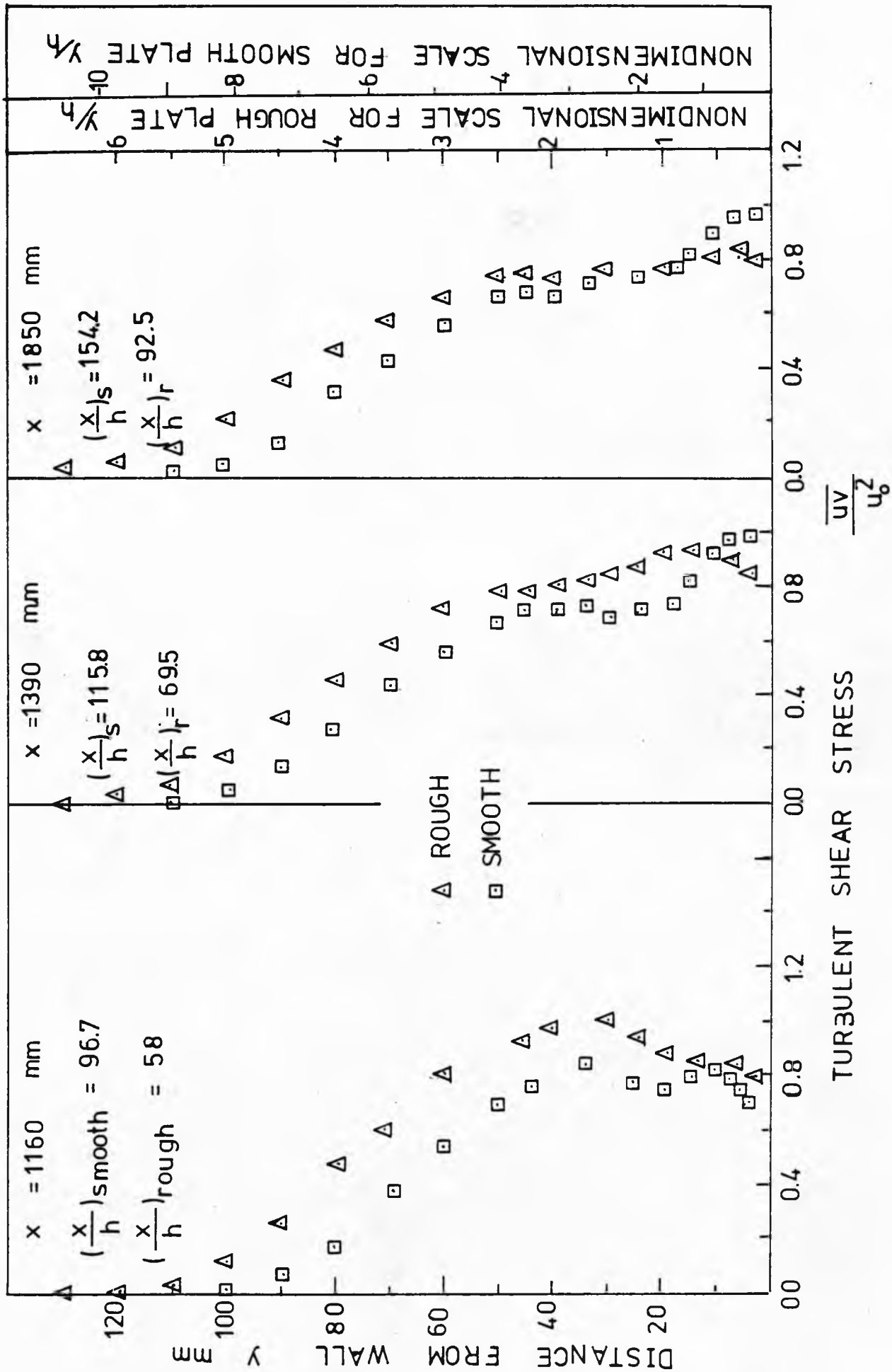

FIG. (4.18)

SKEWNESS FACTOR DOWNSTREAM OF RIDGE ATTACHED TO ROUGH AND SMOOTH SURFACES

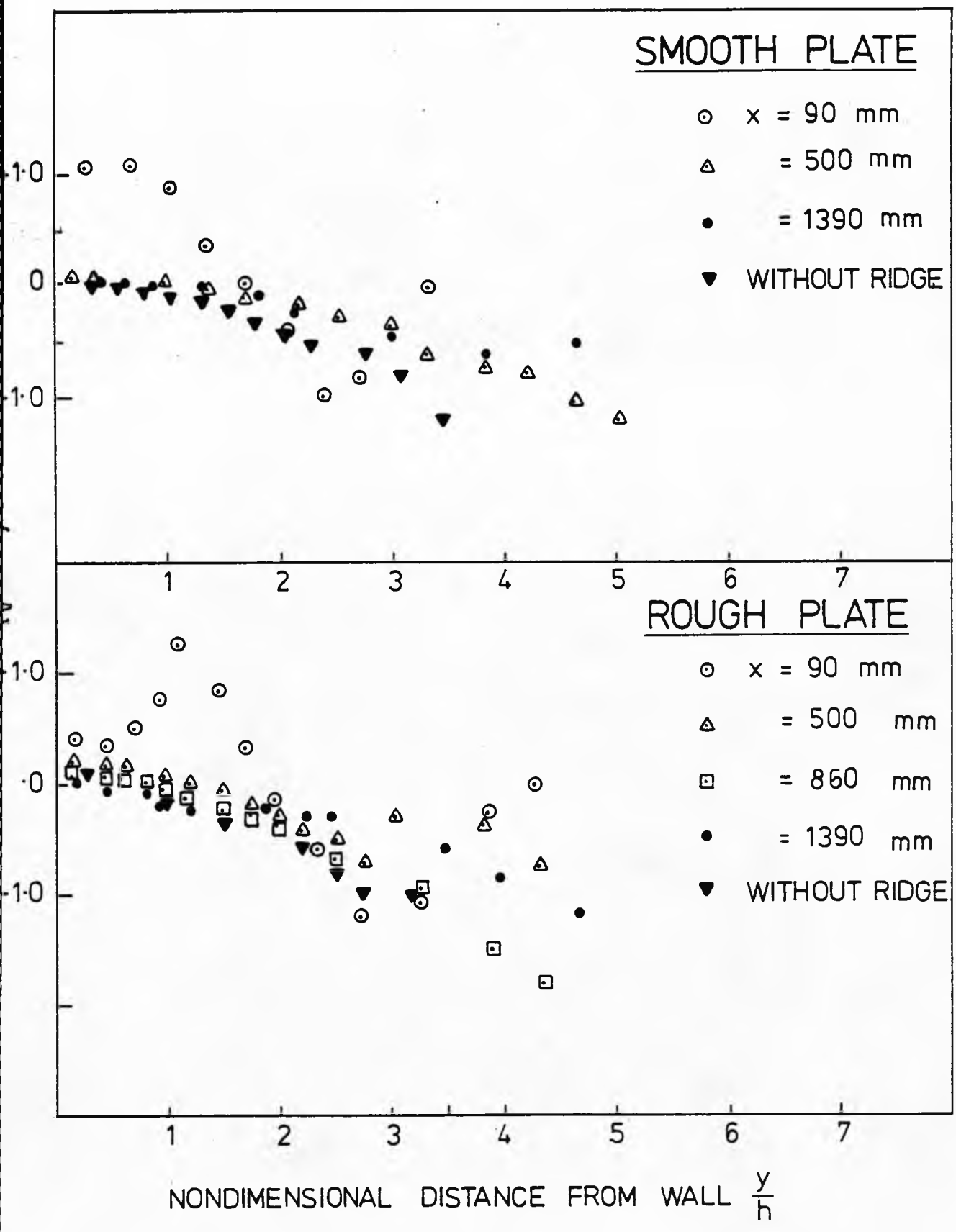

FIG.(4.19)

FLATNESS FACTOR DOWNSTREAM OF RIDGE ATTACHED TO ROUGH AND SMOOTH SURFACES

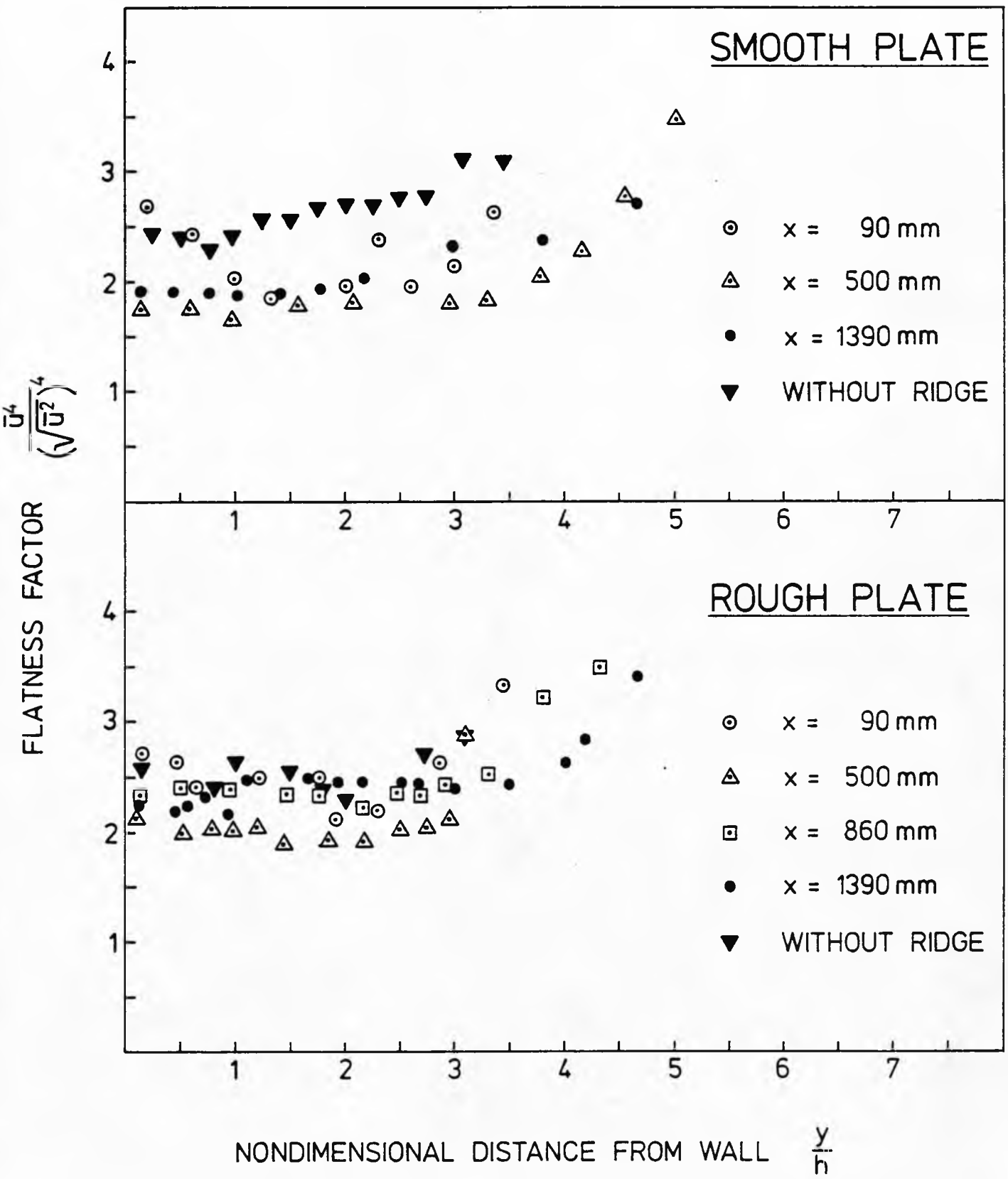

FREQUENCY SPECTRA OF $\overline{u^2}$ at x = 225 mm DOWNSTREAM OF RIDGE ATTACHED TO ROUGH SURFACE

FIG.(4.20a)

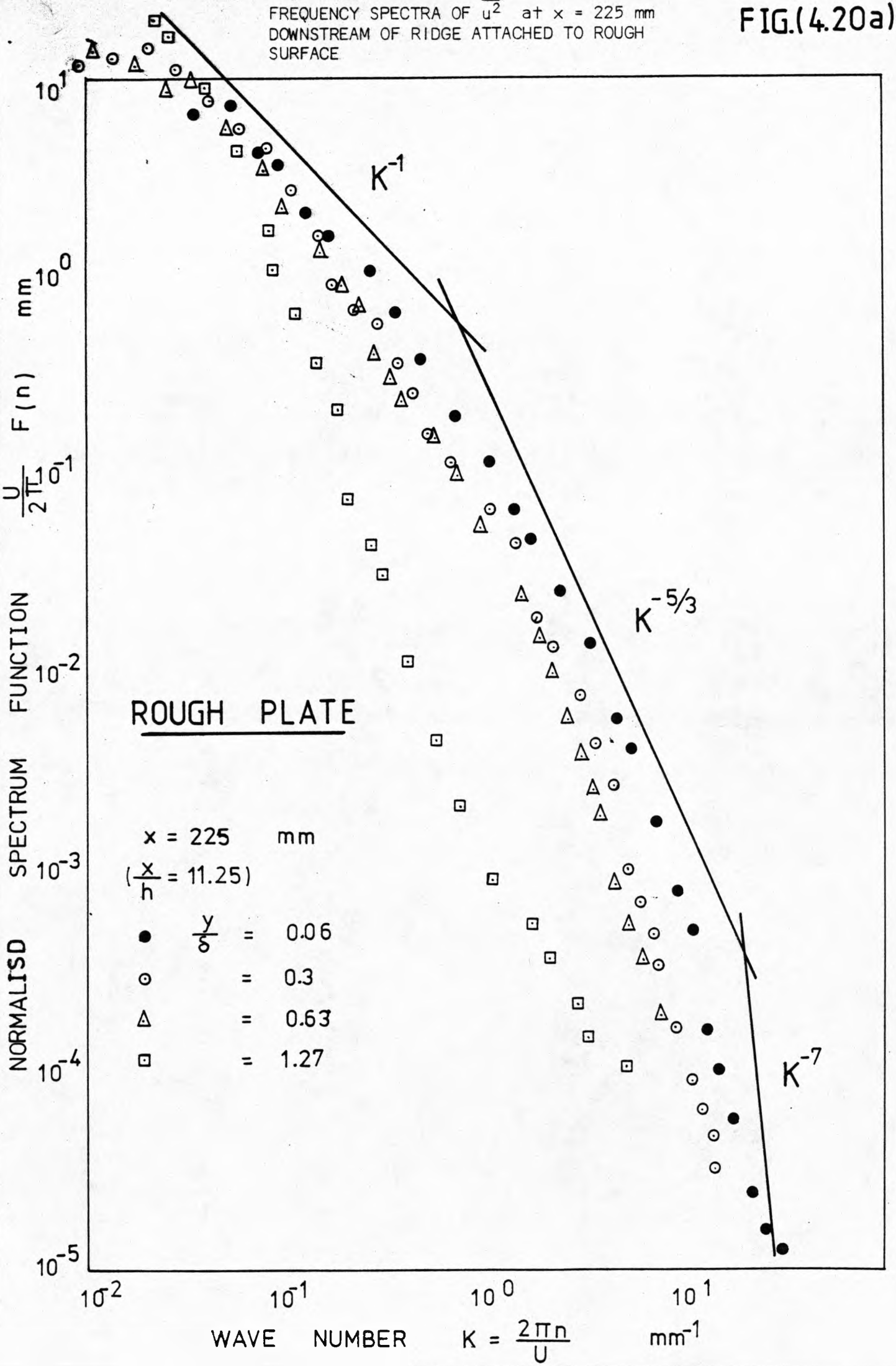

FREQUENCY SPECTRA OF $\overline{u^2}$ at x = 500 mm DOWNSTREAM OF RIDGE ATTACHED TO ROUGH SURFACE

FIG.(4.20b)

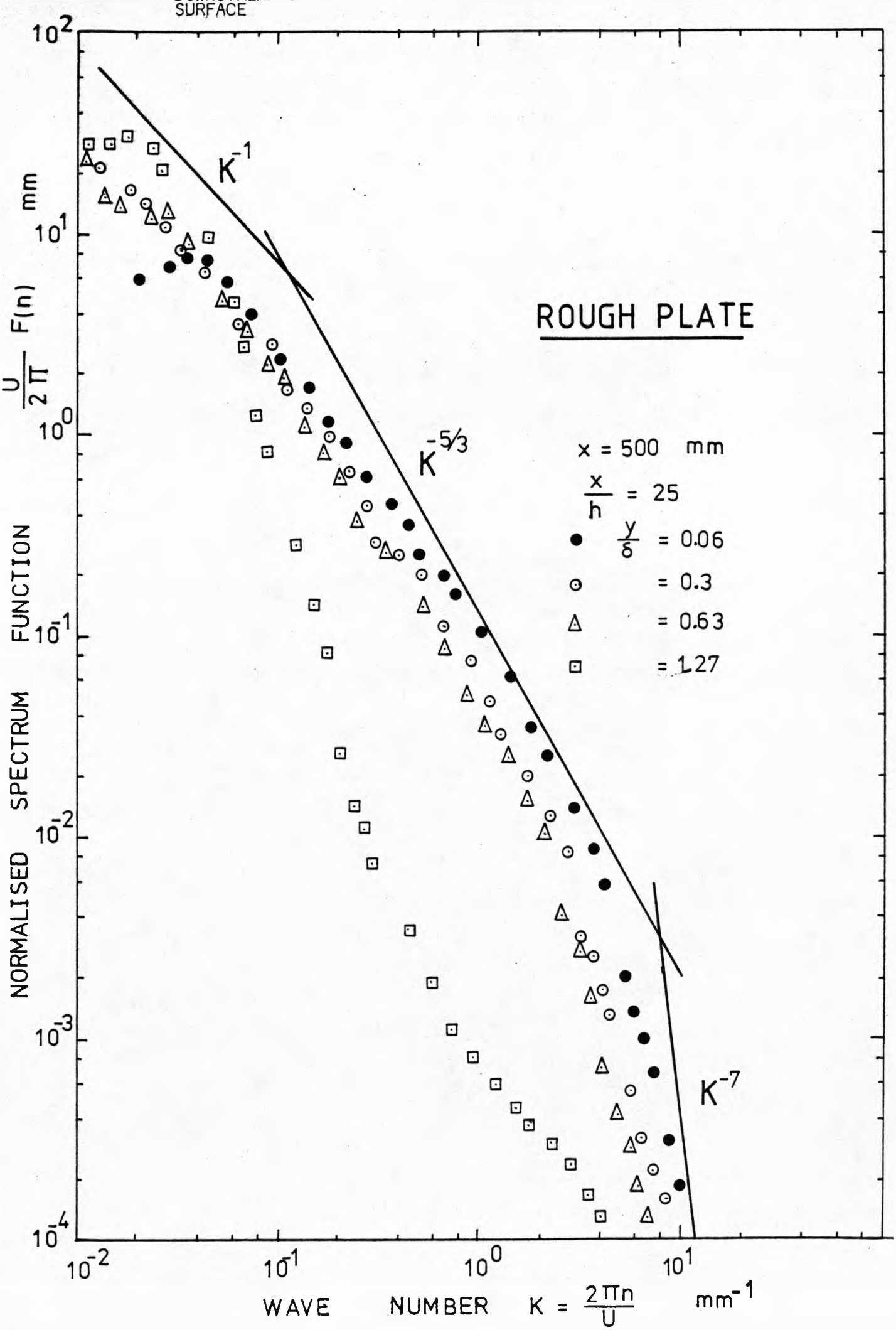

FIG.(4.20c)

FREQUENCY SPECTRA OF $\overline{u^2}$ at x = 860 mm DOWNSTREAM OF RIDGE ATTACHED TO ROUGH SURFACE

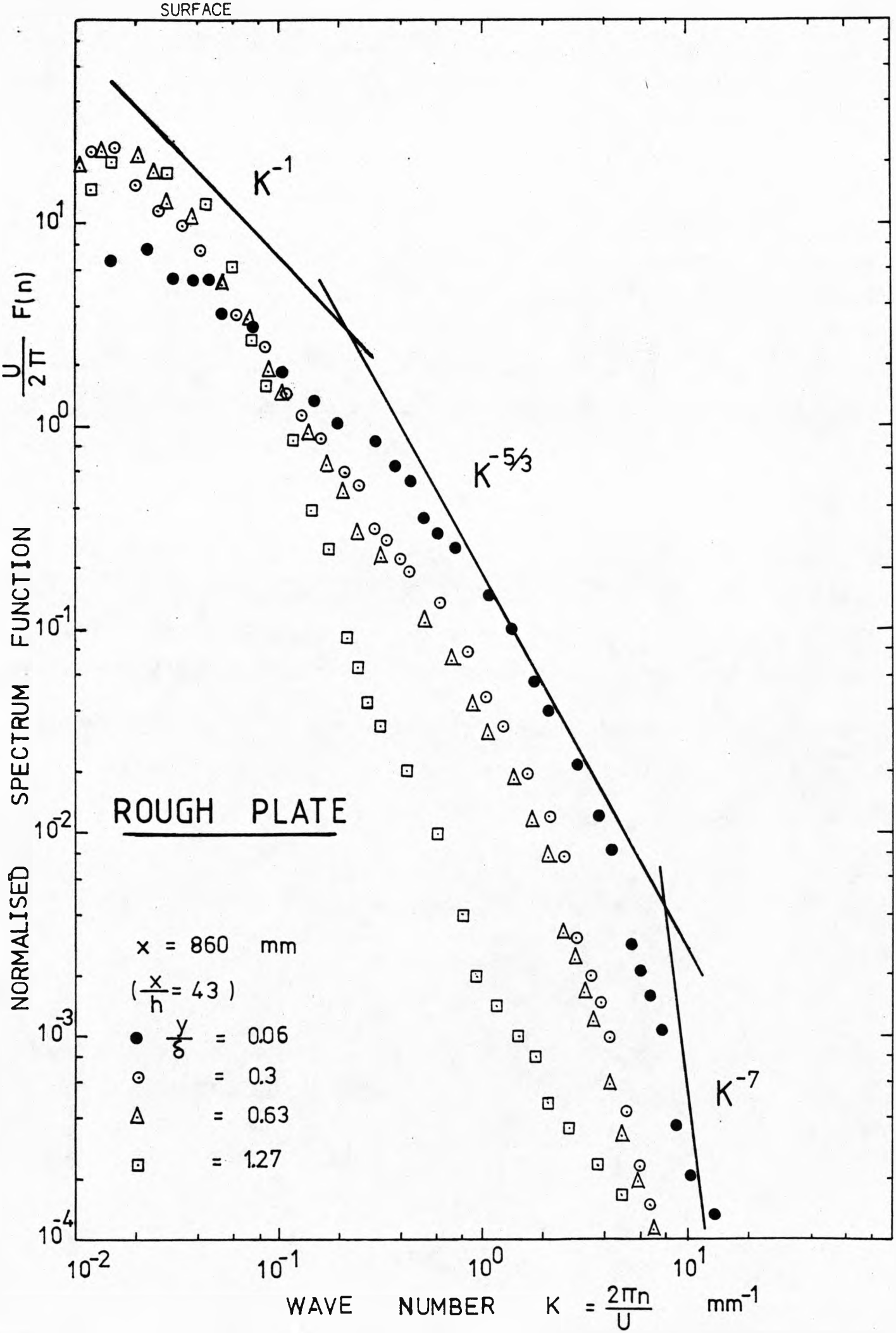

FIG.(4.20d)

FREQUENCY SPECTRA OF $\overline{u^2}$ at x = 1390 mm DOWNSTREAM OF RIDGE ATTACHED TO ROUGH SURFACE.

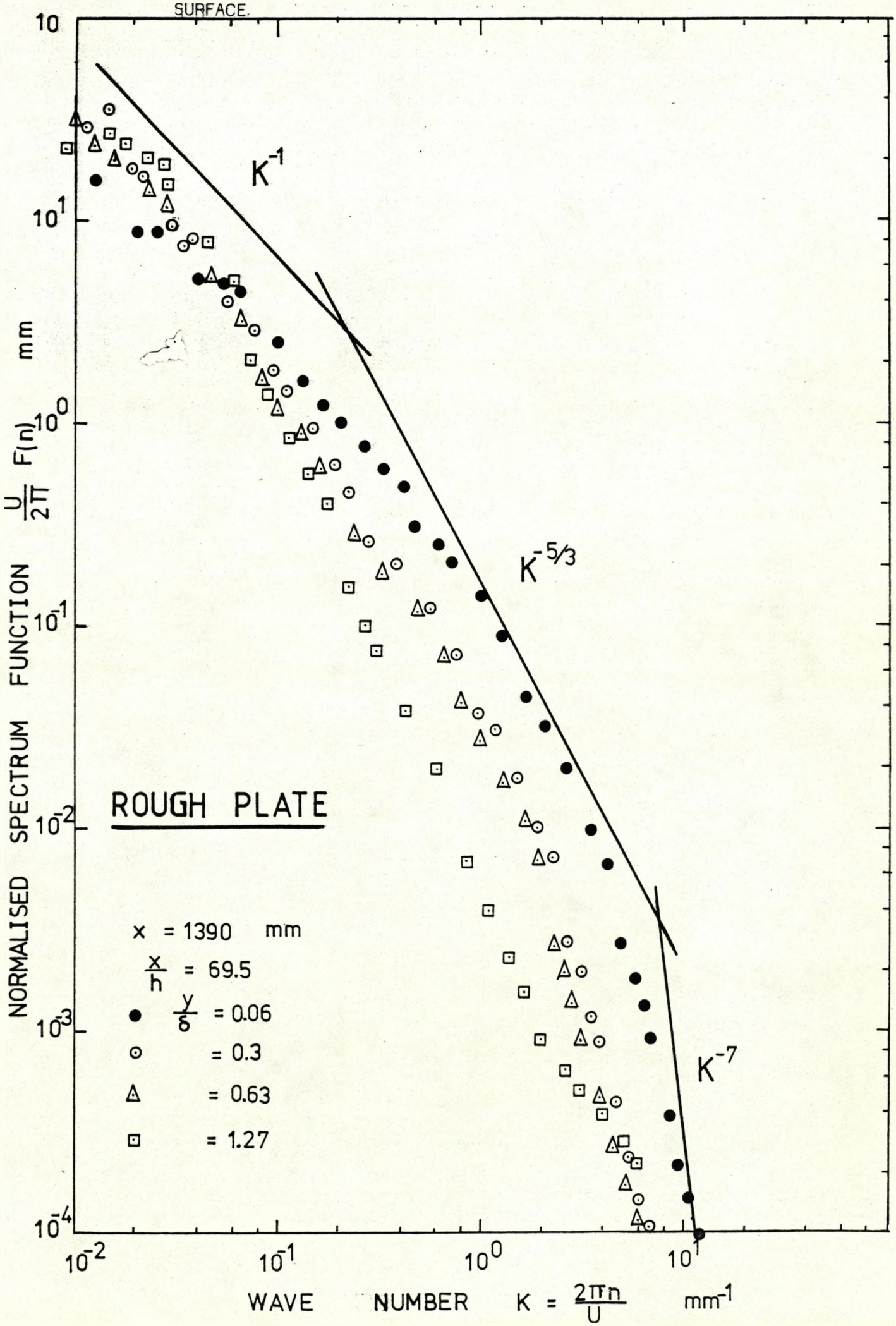

FREQUENCY SPECTRA OF $\overline{u^2}$ at x = 1860 mm DOWNSTREAM OF RIDGE ATTACHED TO ROUGH SURFACE

FIG.(4.20e)

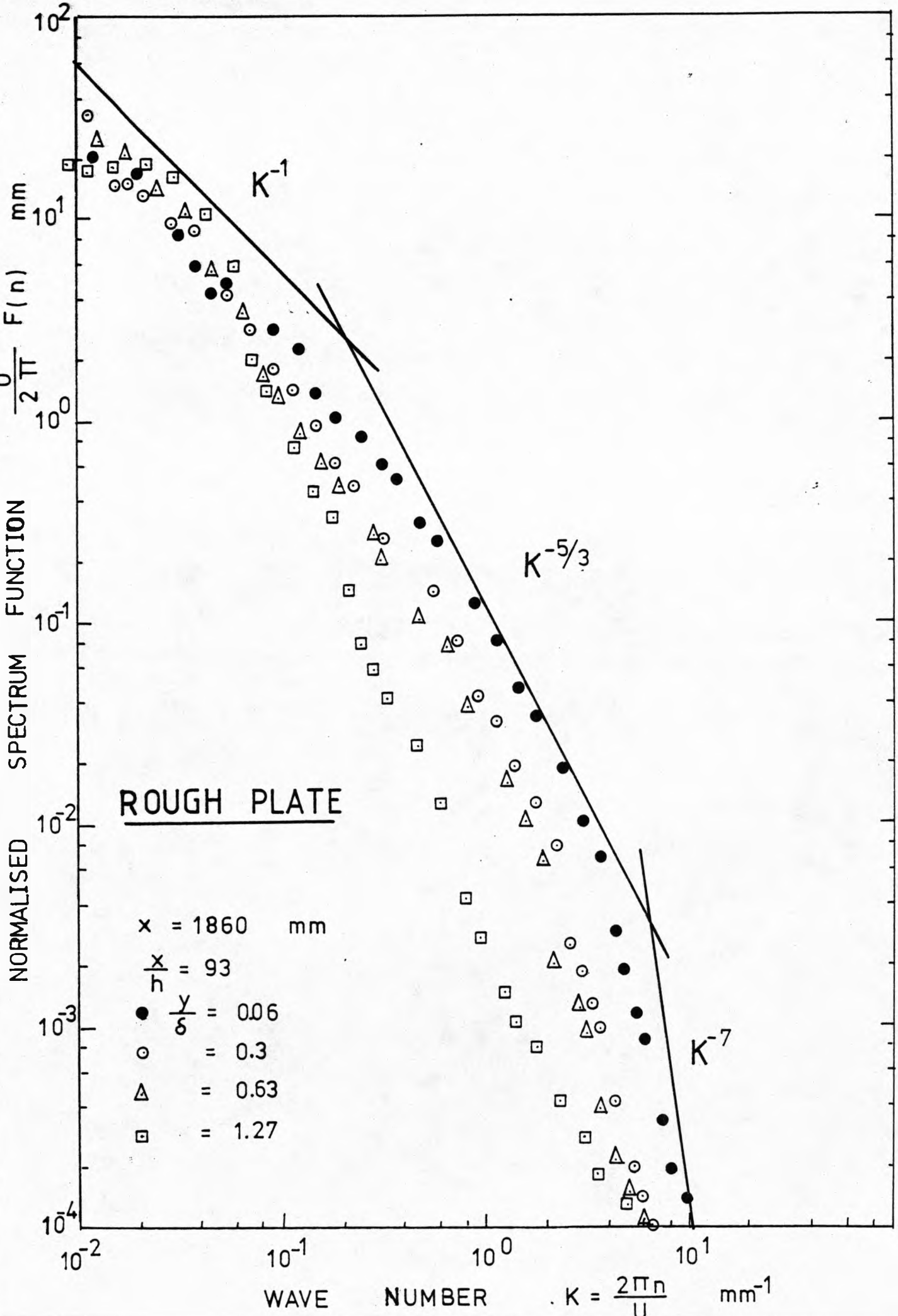

FREQUENCY SPECTRA OF $\overline{u^2}$ at x = 130 mm DOWNSTREAM OF RIDGE ATTACHED TO SMOOTH SURFACE

FIG.(4.21a)

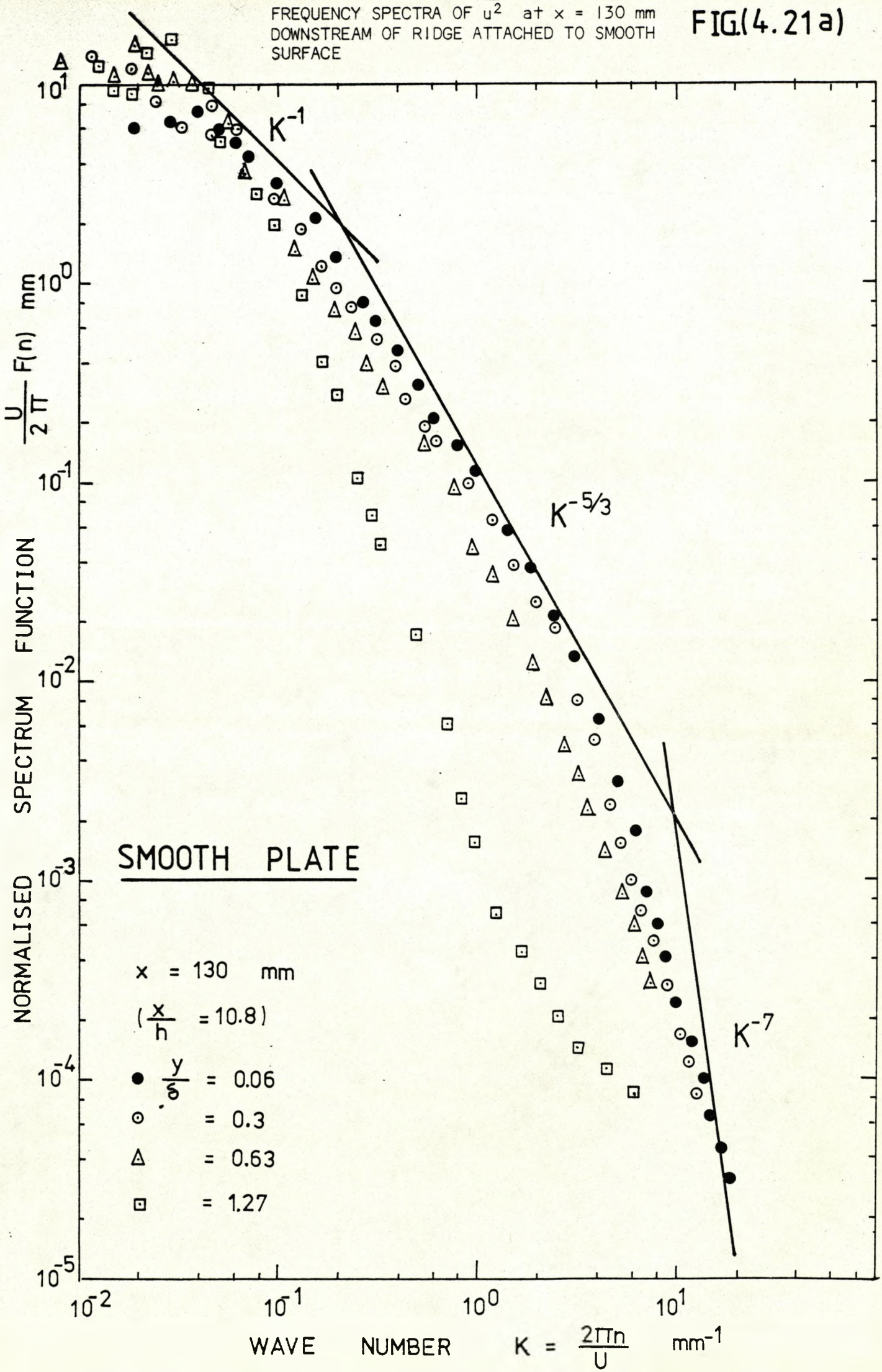

FIG. (4.21b)

FREQUENCY SPECTRA OF $\overline{u^2}$ at x = 225 mm DOWNSTREAM OF RIDGE ATTACHED TO SMOOTH SURFACE

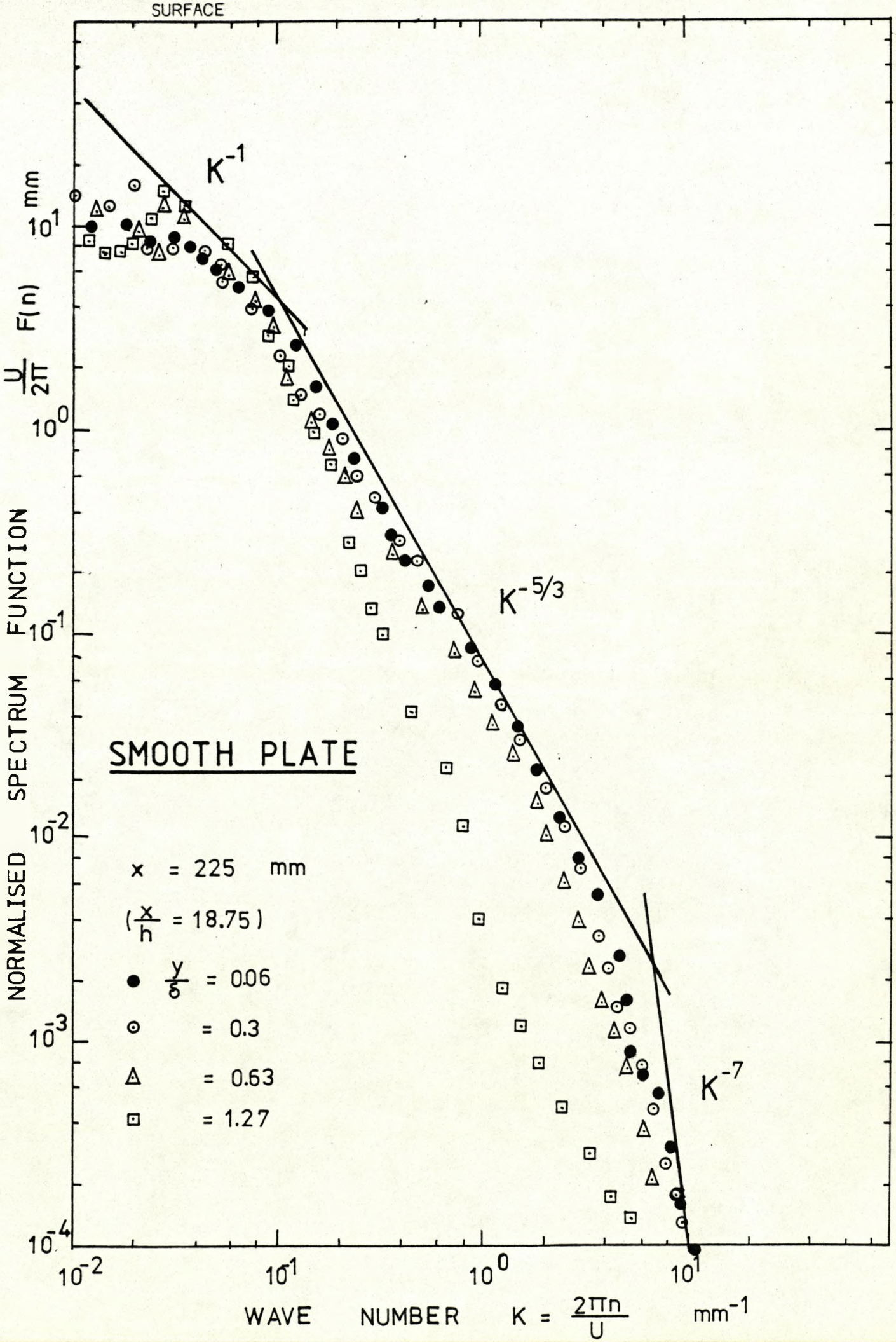

FREQUENCY SPECTRA OF $\overline{u^2}$ at x = 500 mm DOWNSTREAM OF RIDGE ATTACHED TO SMOOTH SURFACE

FIG.(4.21c)

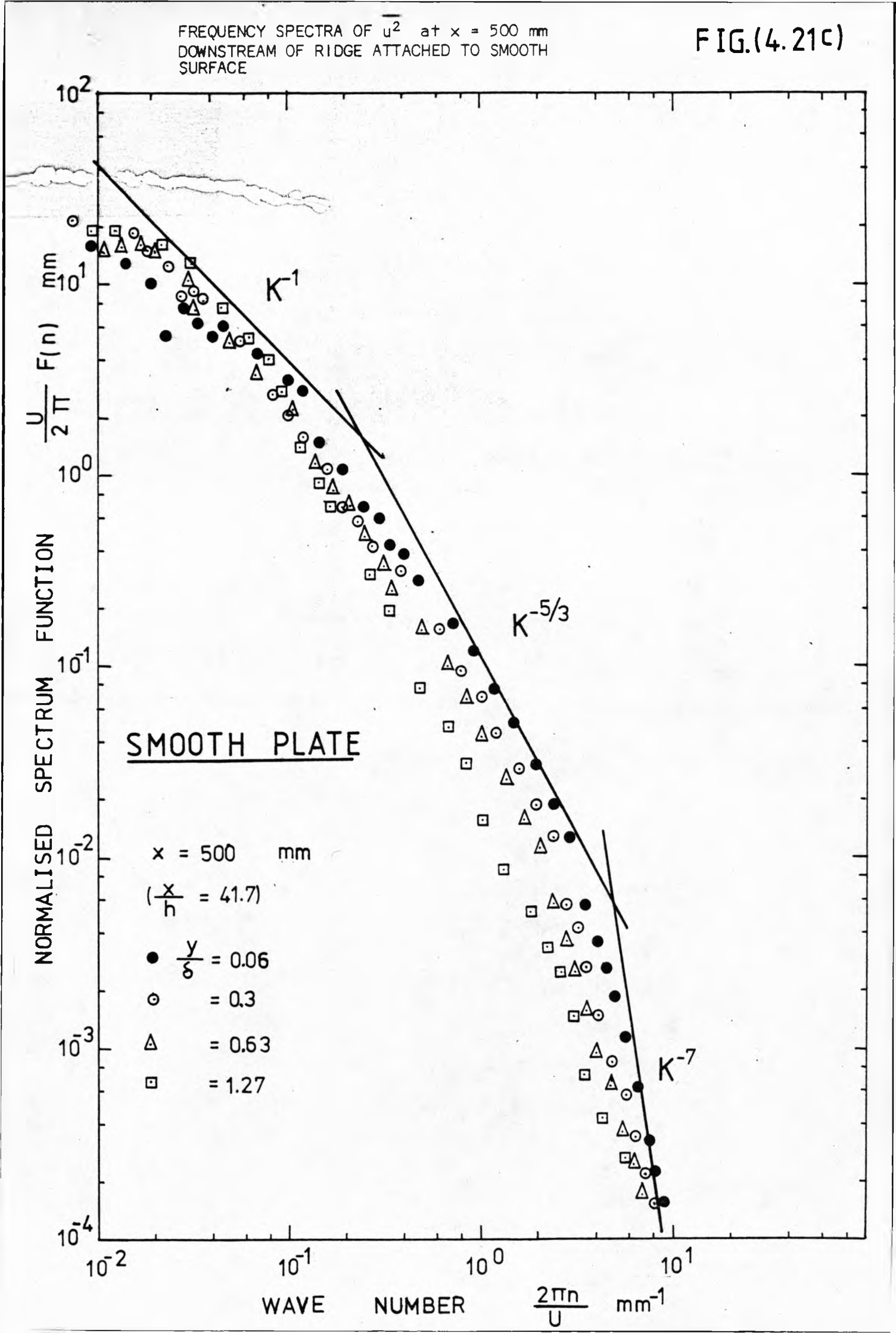

FIG.(4.21d)

FREQUENCY SPECTRA OF $\overline{u^2}$ at x = 860 mm DOWNSTREAM OF RIDGE ATTACHED TO SMOOTH SURFACE

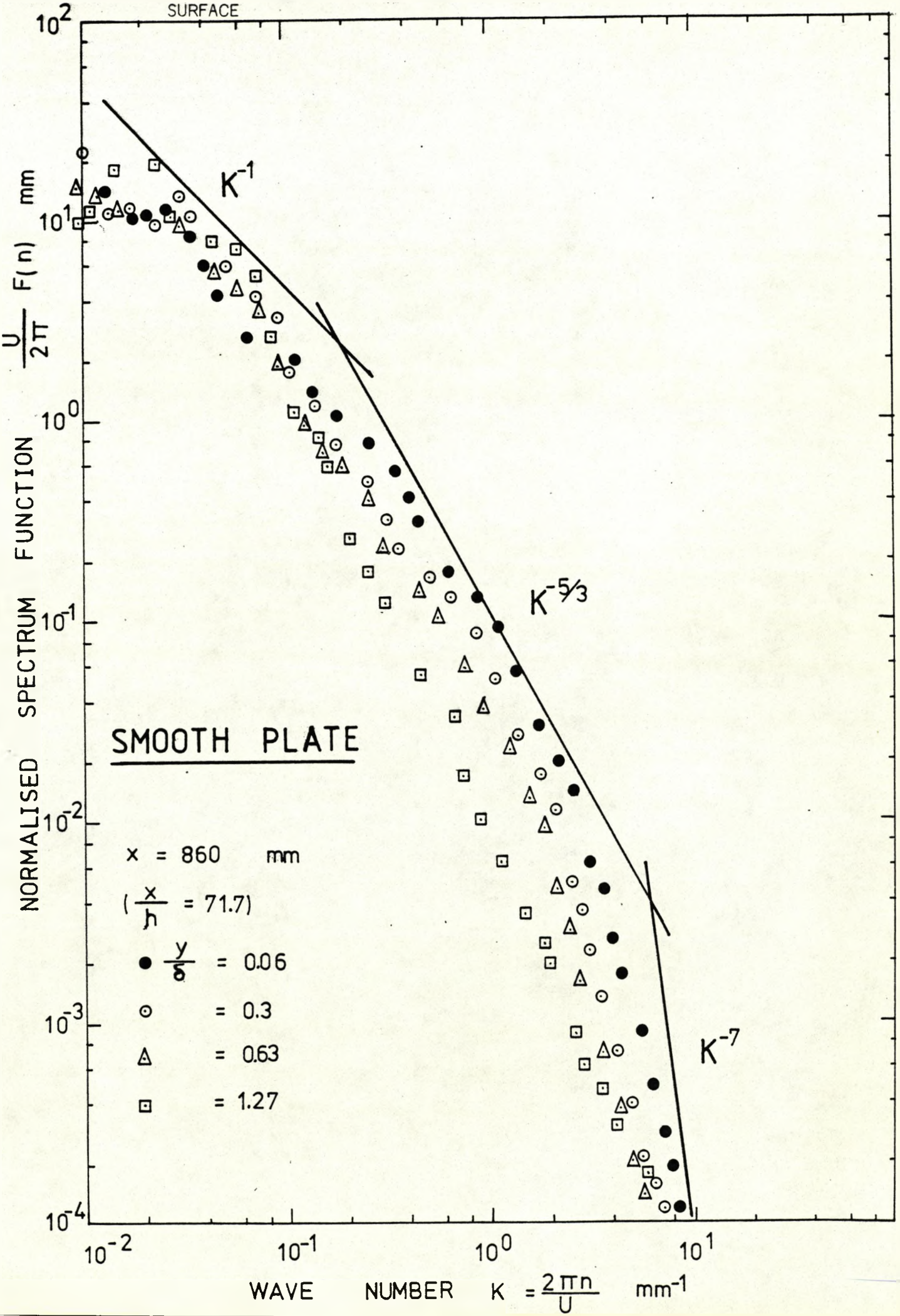

FIG. (4.21e)

FREQUENCY SPECTRA OF $\overline{u^2}$ at x = 1390 mm DOWNSTREAM OF RIDGE ATTACHED TO SMOOTH SURFACE

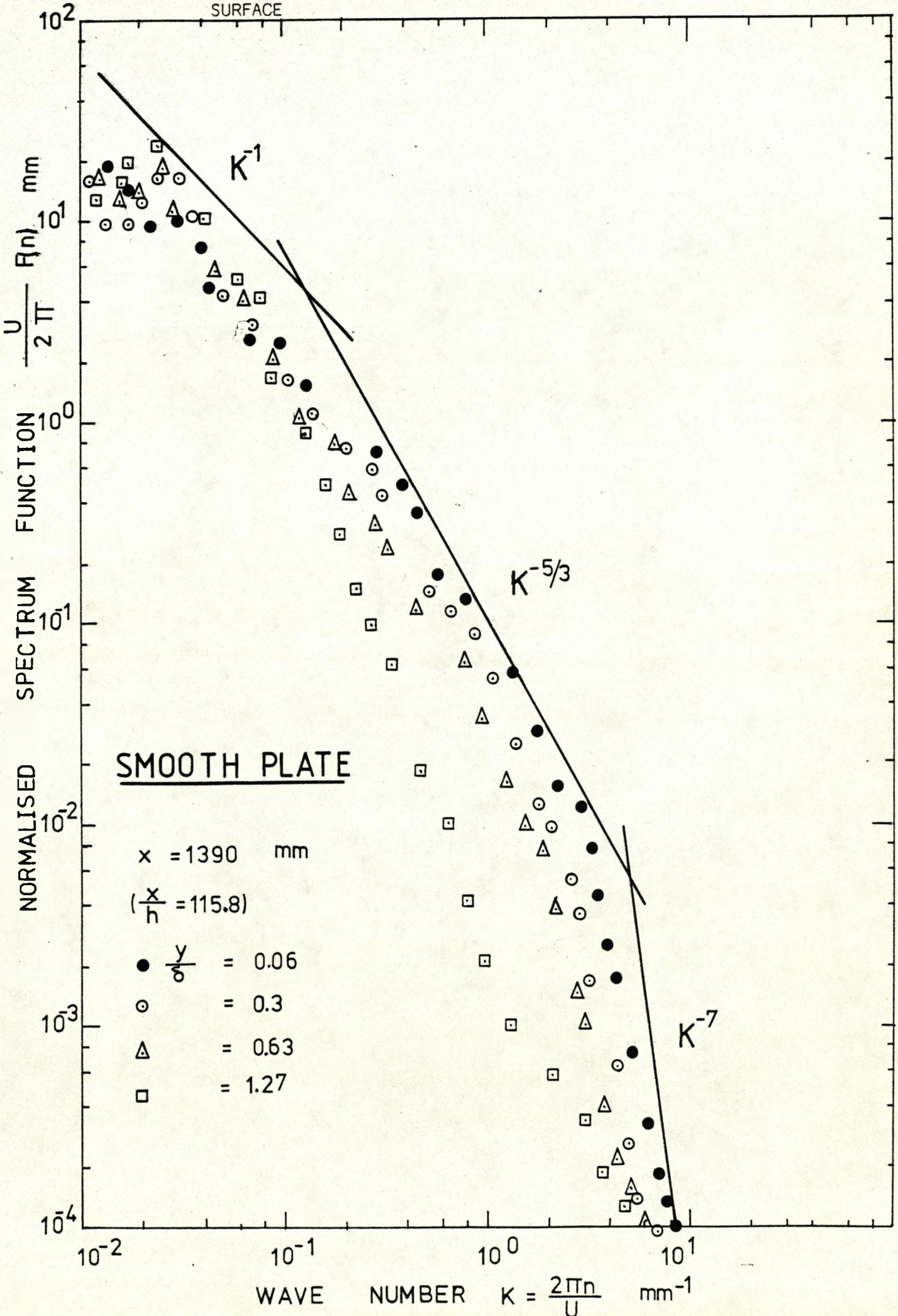

FIG.(4.22a)

LONGITUDINAL SPATIAL CORRELATION COEFFICIENT AT x = 225 mm DOWNSTREAM OF RIDGE ATTACHED TO ROUGH AND SMOOTH SURFACES

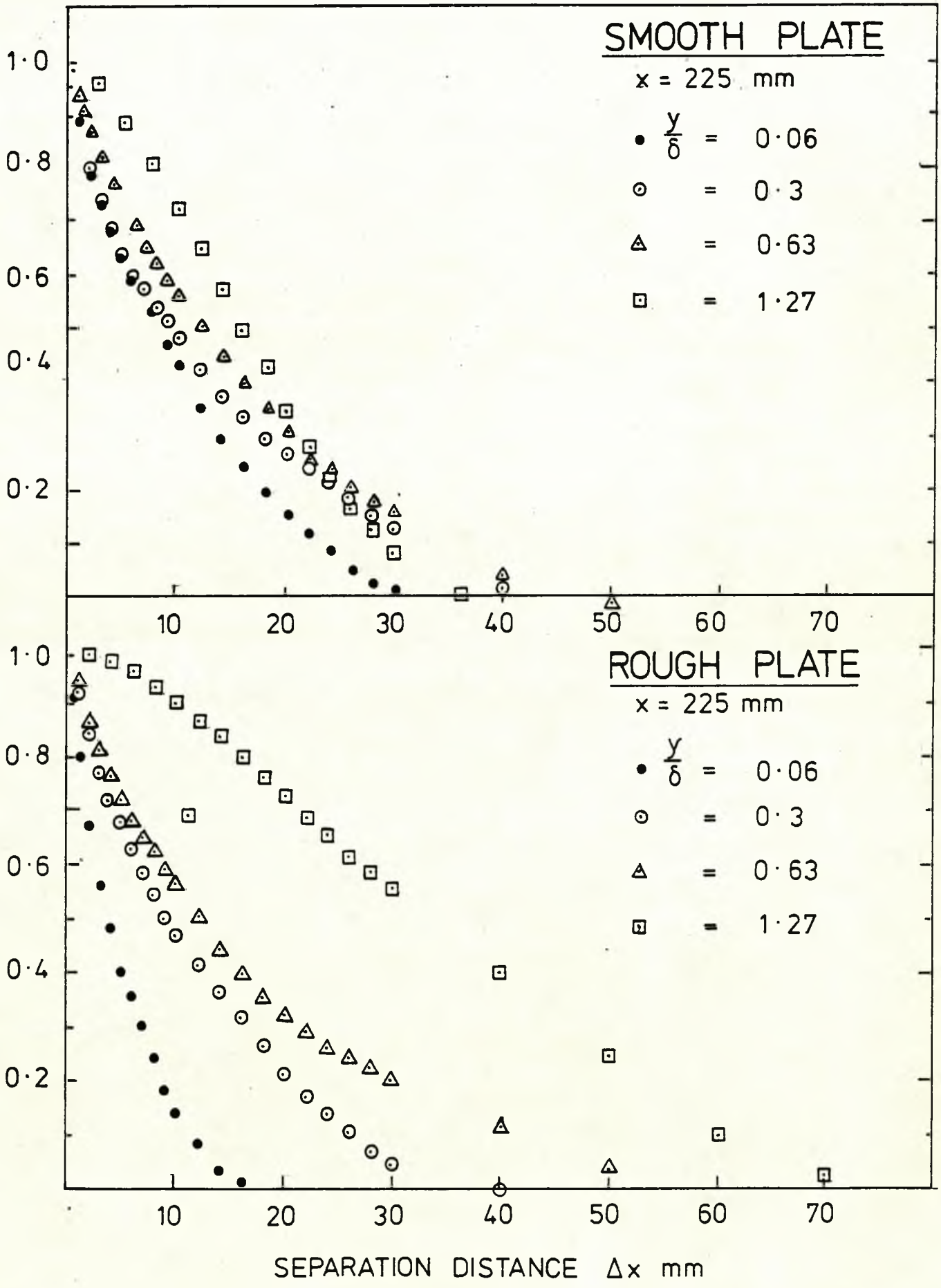

FIG.(4.22b)

LONGITUDINAL SPATIAL CORRELATION COEFFICIENT AT x = 500 mm DOWNSTREAM OF RIDGE ATTACHED TO ROUGH AND SMOOTH SURFACES

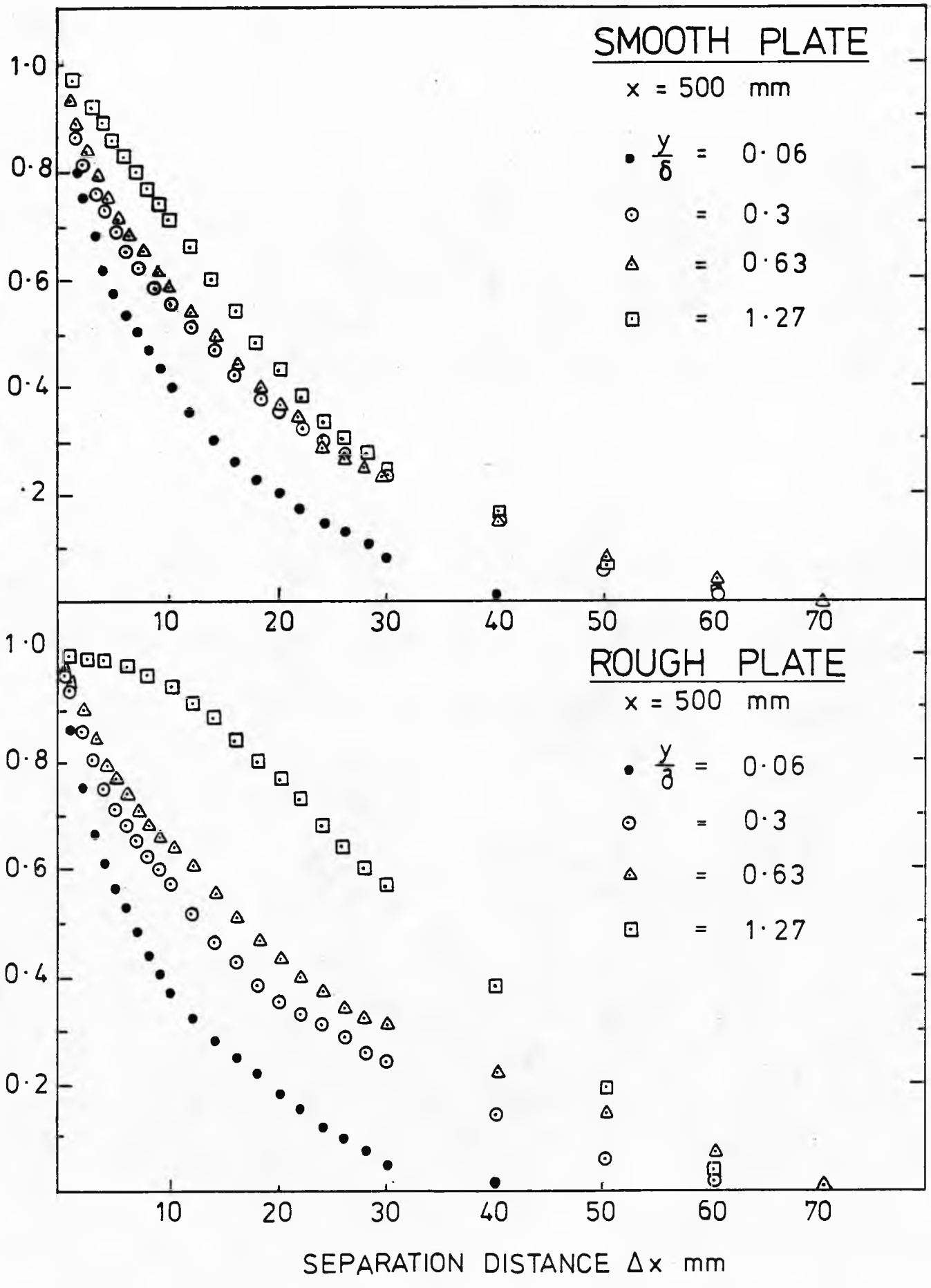

FIG.(4.22c)

LONGITUDINAL SPATIAL CORRELATION COEFFICIENT AT x = 860 mm DOWNSTREAM OF RIDGE ATTACHED TO ROUGH AND SMOOTH SURFACES

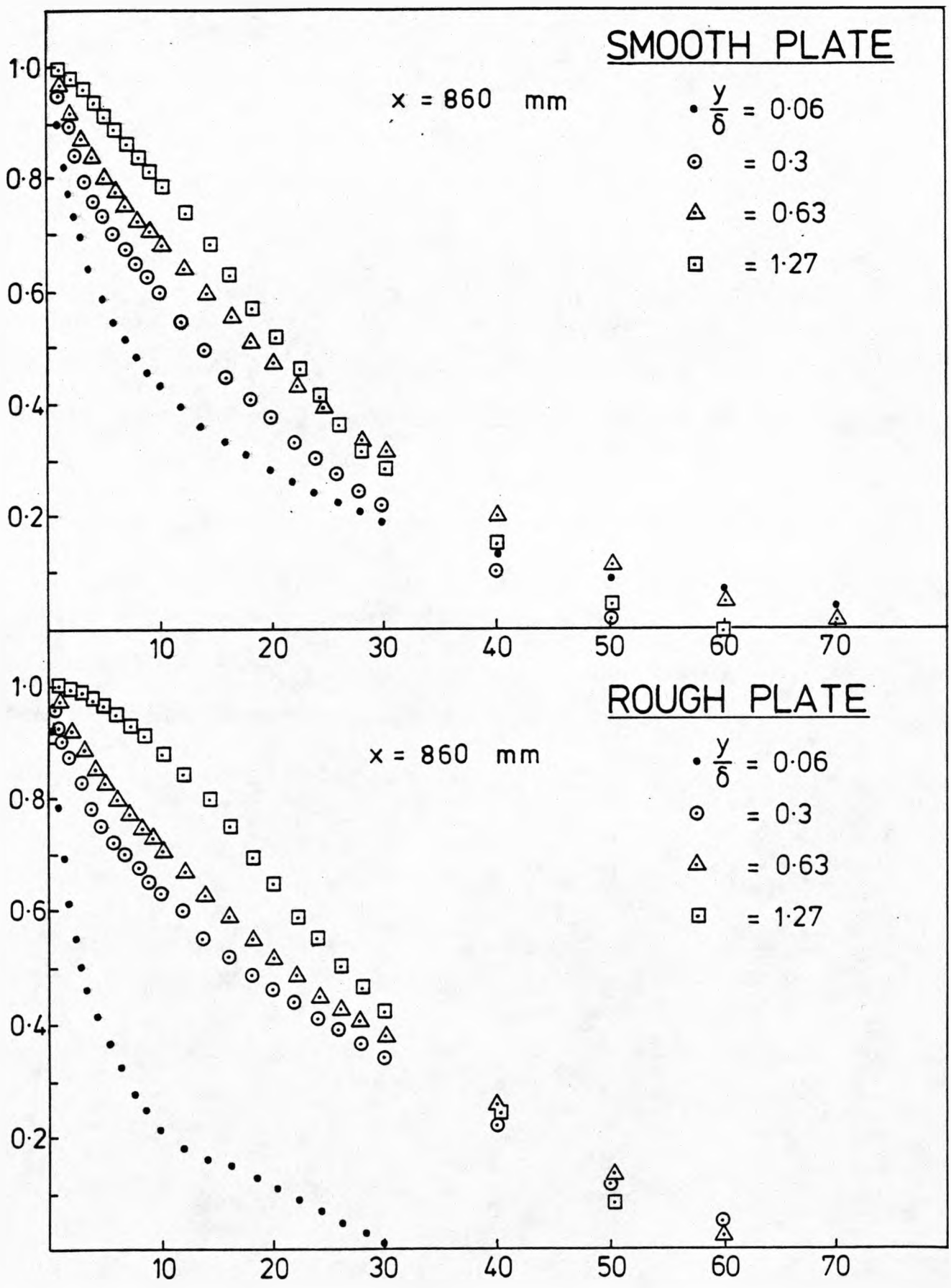

LONGITUDINAL SPACE CORRELATION COEFFICIENT R_T

SEPARATION DISTANCE Δx mm

FIG.(4.22d)

LONGITUDINAL SPATIAL CORRELATION COEFFICIENT AT x = 1390 mm DOWNSTREAM OF RIDGE ATTACHED TO ROUGH AND SMOOTH SURFACES

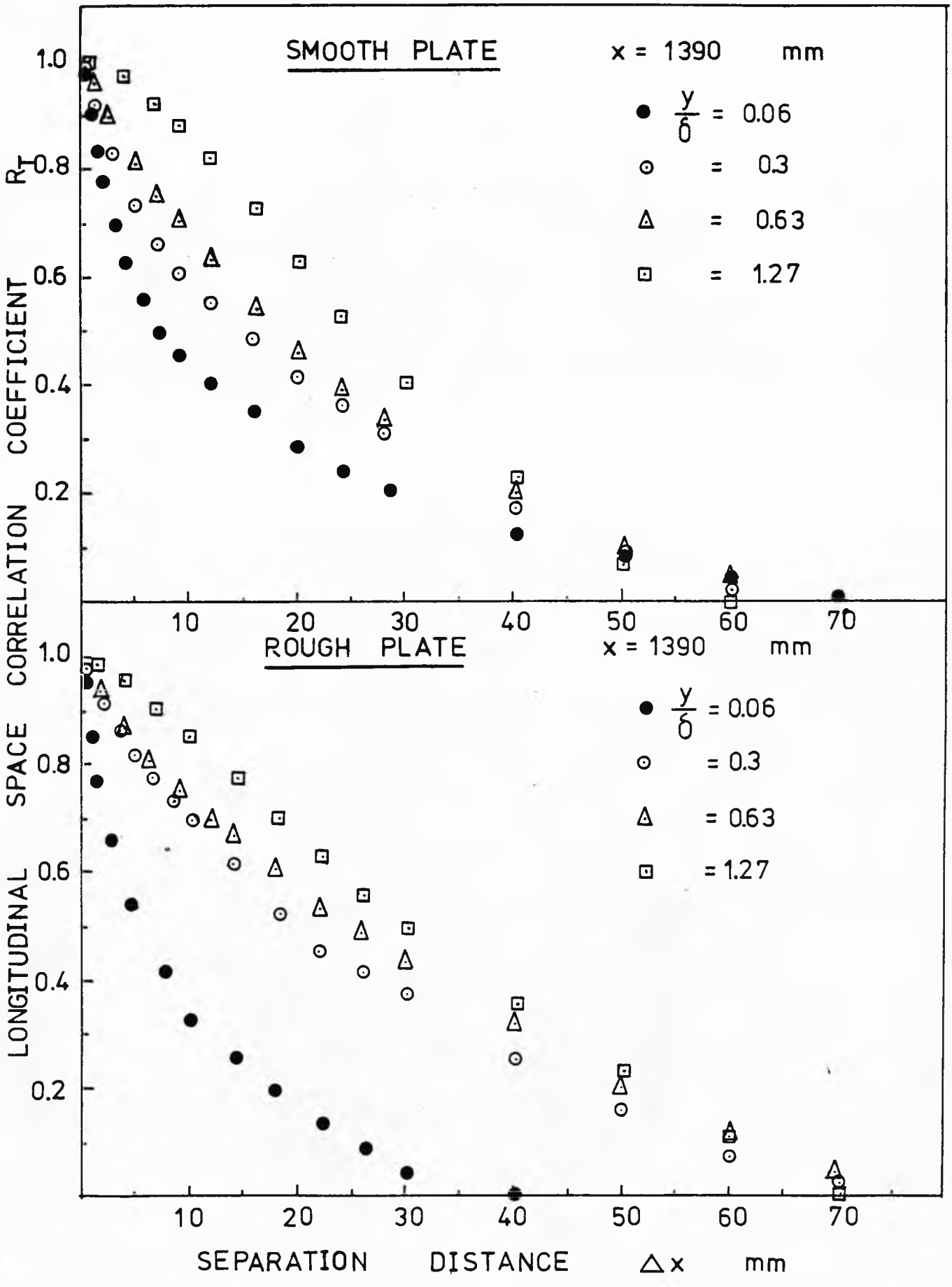

FIG.(4.23a)

SECOND MOMENTS OF FREQUENCY SPECTRA OF $\overline{u^2}$ AT x = 225 mm DOWNSTREAM OF RIDGE ATTACHED TO ROUGH AND SMOOTH SURFACES

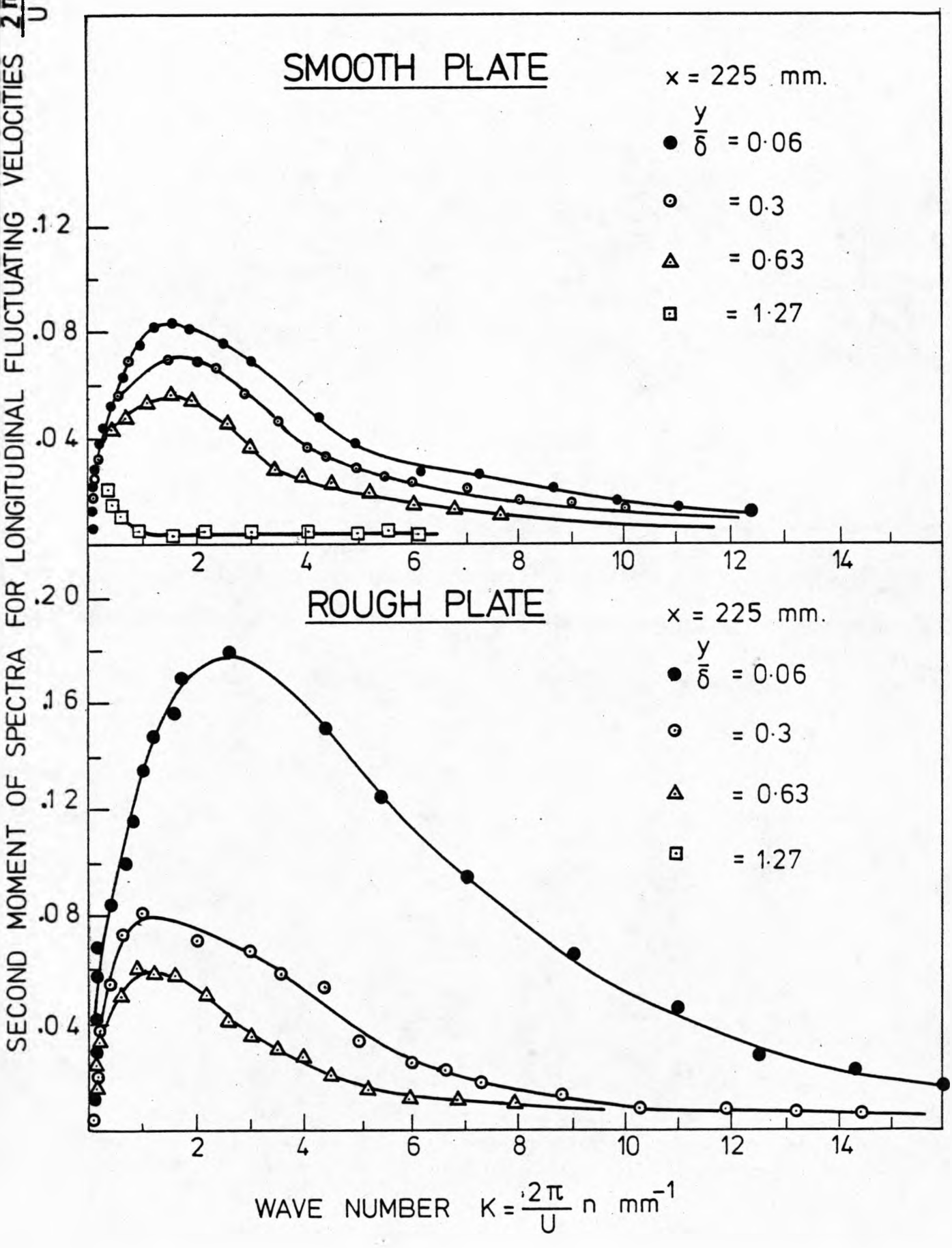

FIG. (4.23 b)

SECOND MOMENTS OF FREQUENCY SPECTRA OF $\overline{u^2}$ AT x = 500 mm DOWNSTREAM OF RIDGE ATTACHED TO ROUGH AND SMOOTH SURFACES

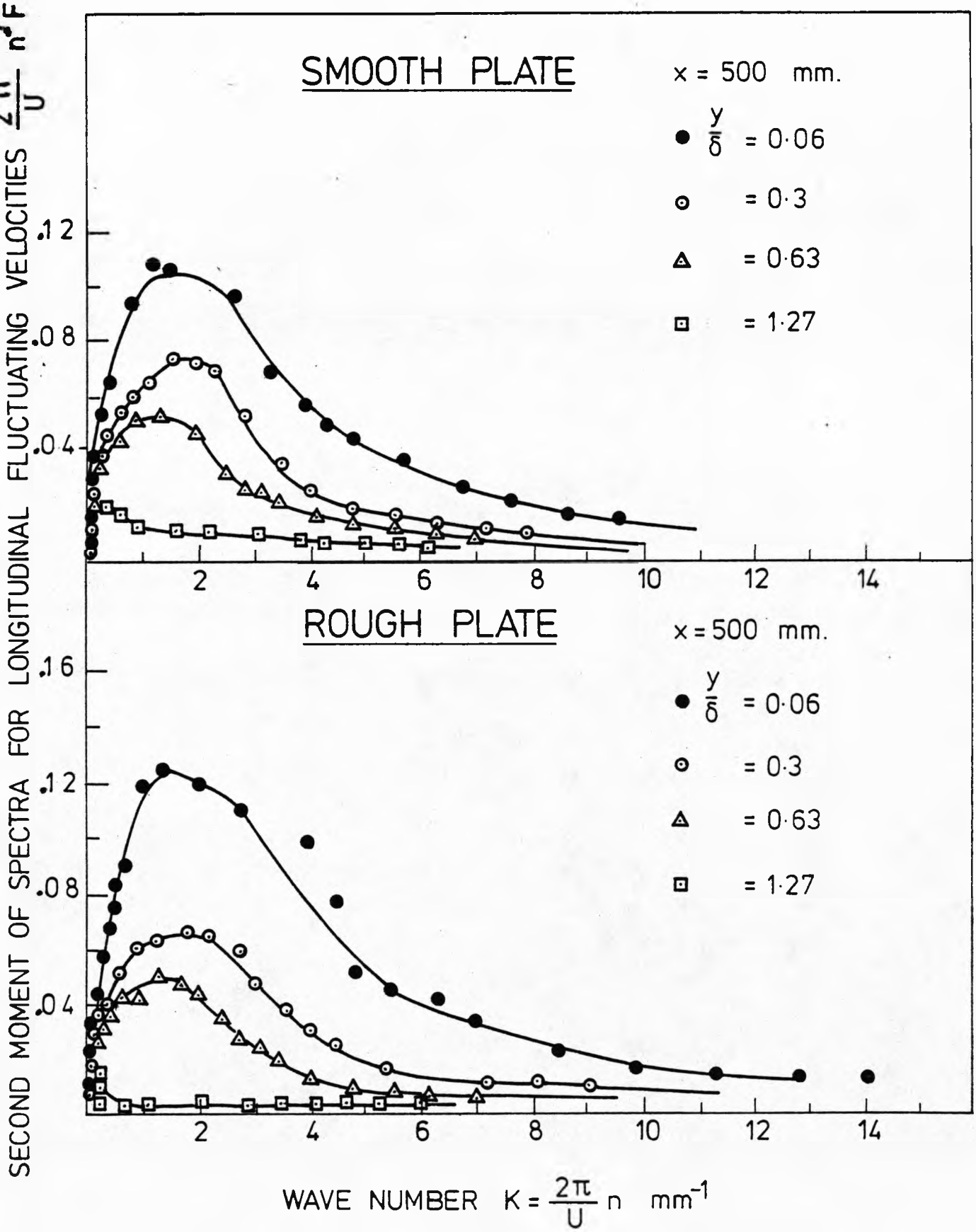

FIG. (4.23c)

SECOND MOMENTS OF FREQUENCY SPECTRA OF $\overline{u^2}$ AT x = 860 mm DOWNSTREAM OF RIDGE ATTACHED TO ROUGH AND SMOOTH SURFACES

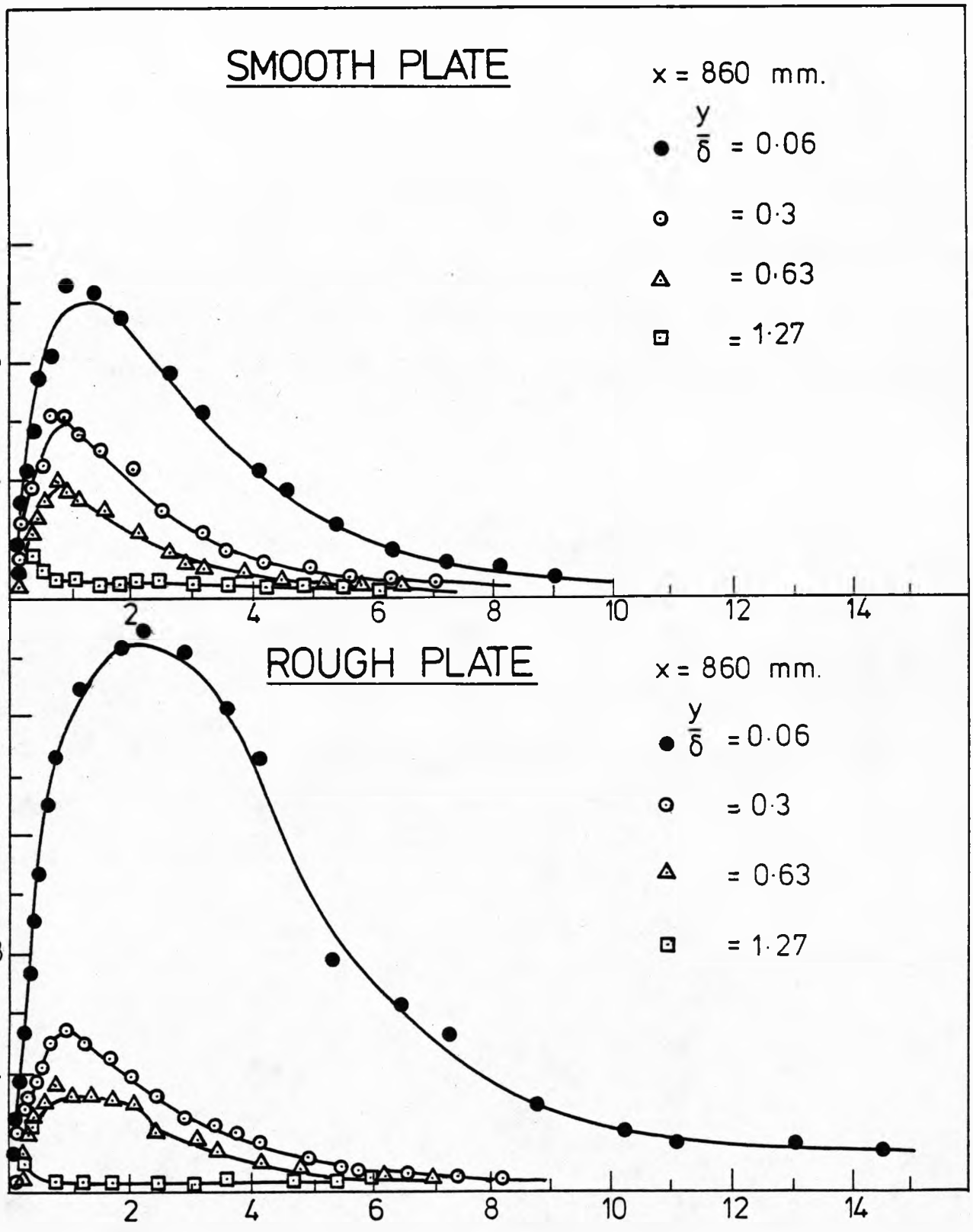

SECOND MOMENT OF SPECTRA FOR LONGITUDINAL FLUCTUATING VELOCITIES u

WAVE NUMBER $K = \frac{2\pi}{U} n \ mm^{-1}$

FIG. (4.23d)

SECOND MOMENTS OF FREQUENCY SPECTRA OF $\overline{u^2}$
AT x = 1390 mm DOWNSTREAM OF RIDGE ATTACHED
TO ROUGH AND SMOOTH SURFACES

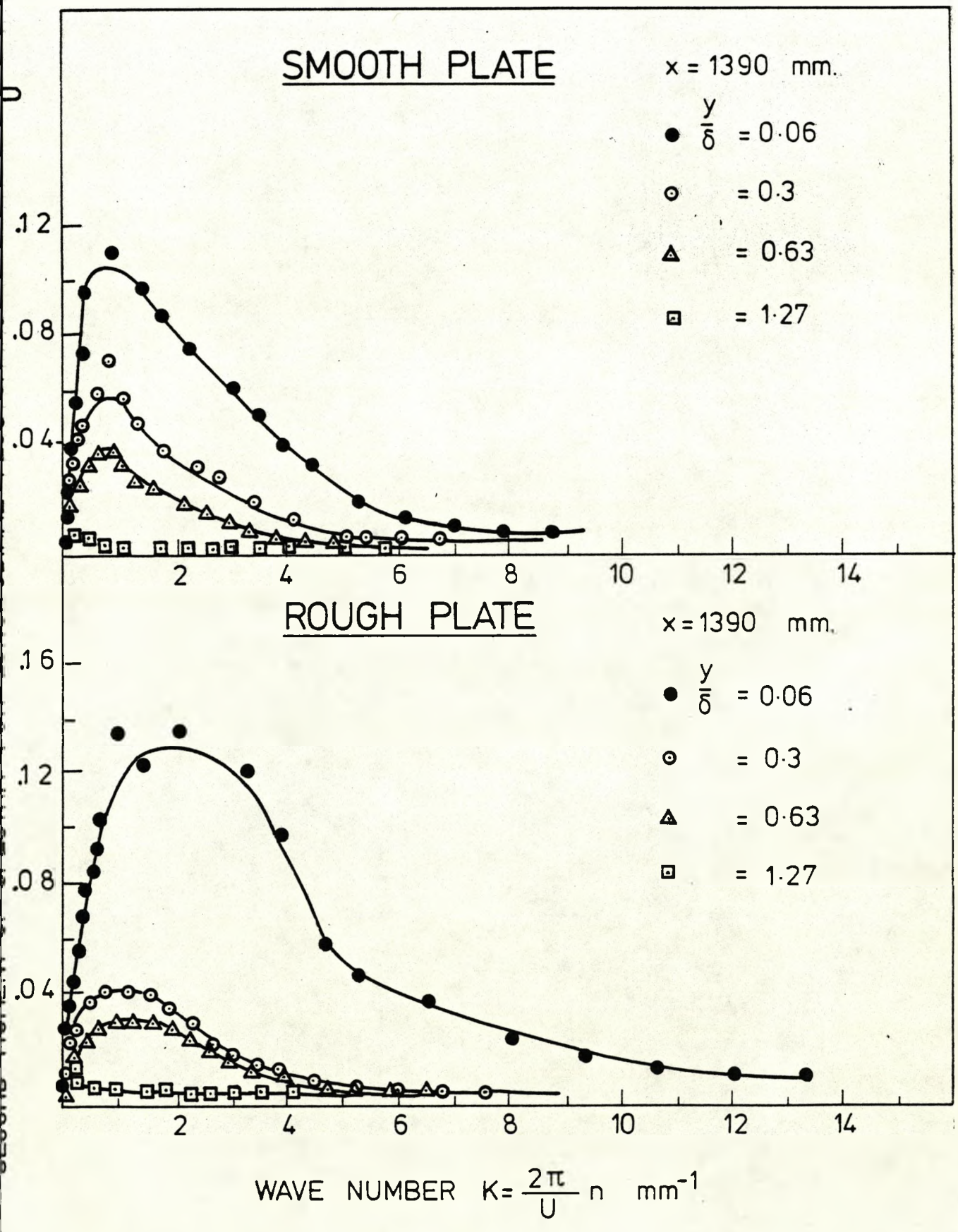

WAVE NUMBER $K = \frac{2\pi}{U} n \quad mm^{-1}$

FIG.(4.24)

MACRO-SCALE OF TURBULENCE DOWNSTREAM OF RIDGE
ATTACHED TO ROUGH AND SMOOTH SURFACES

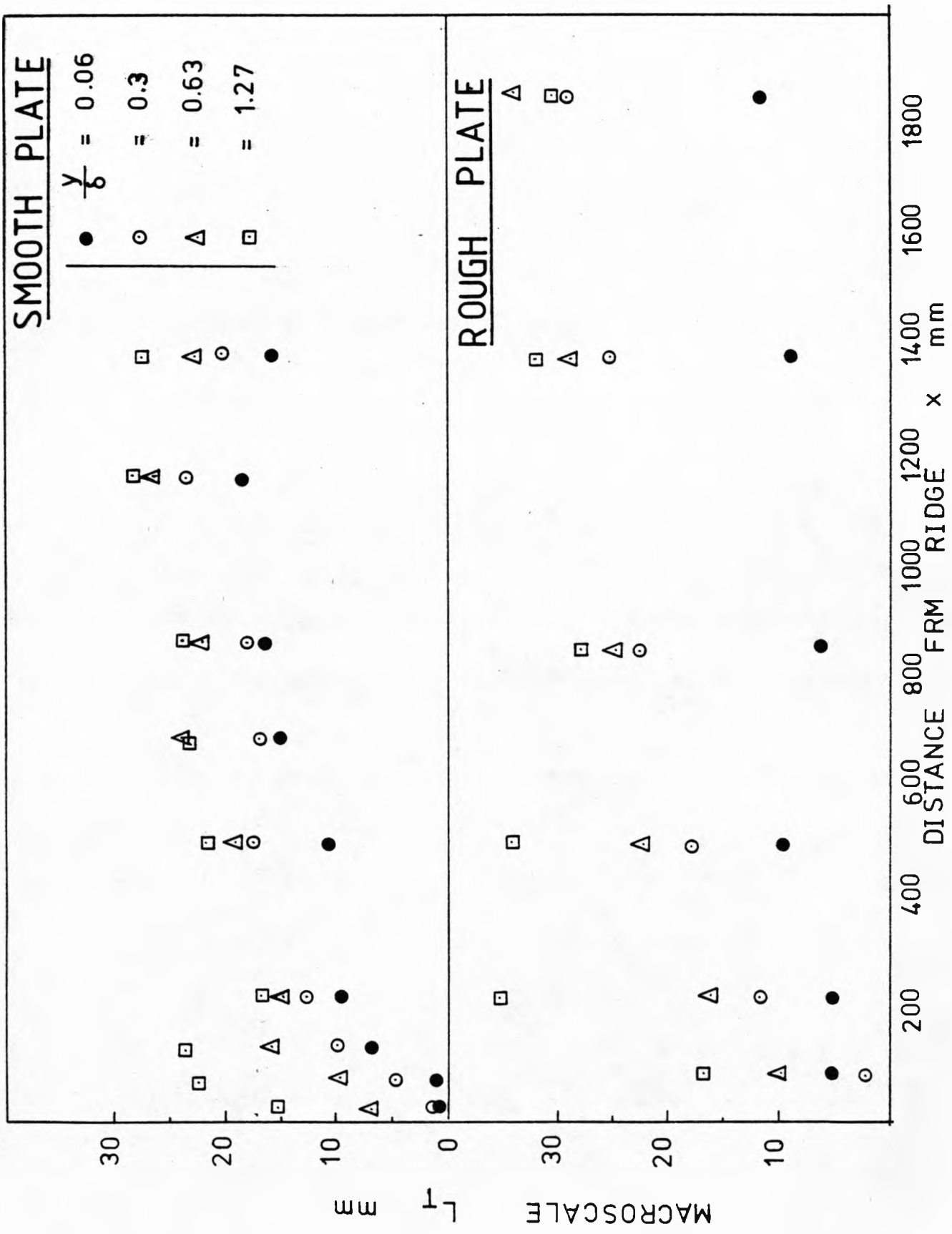

FIG.(4.25)

MICRO-SCALE OF TURBULENCE DOWNSTREAM OF
RIDGE ATTACHED TO ROUGH AND SMOOTH SURFACES

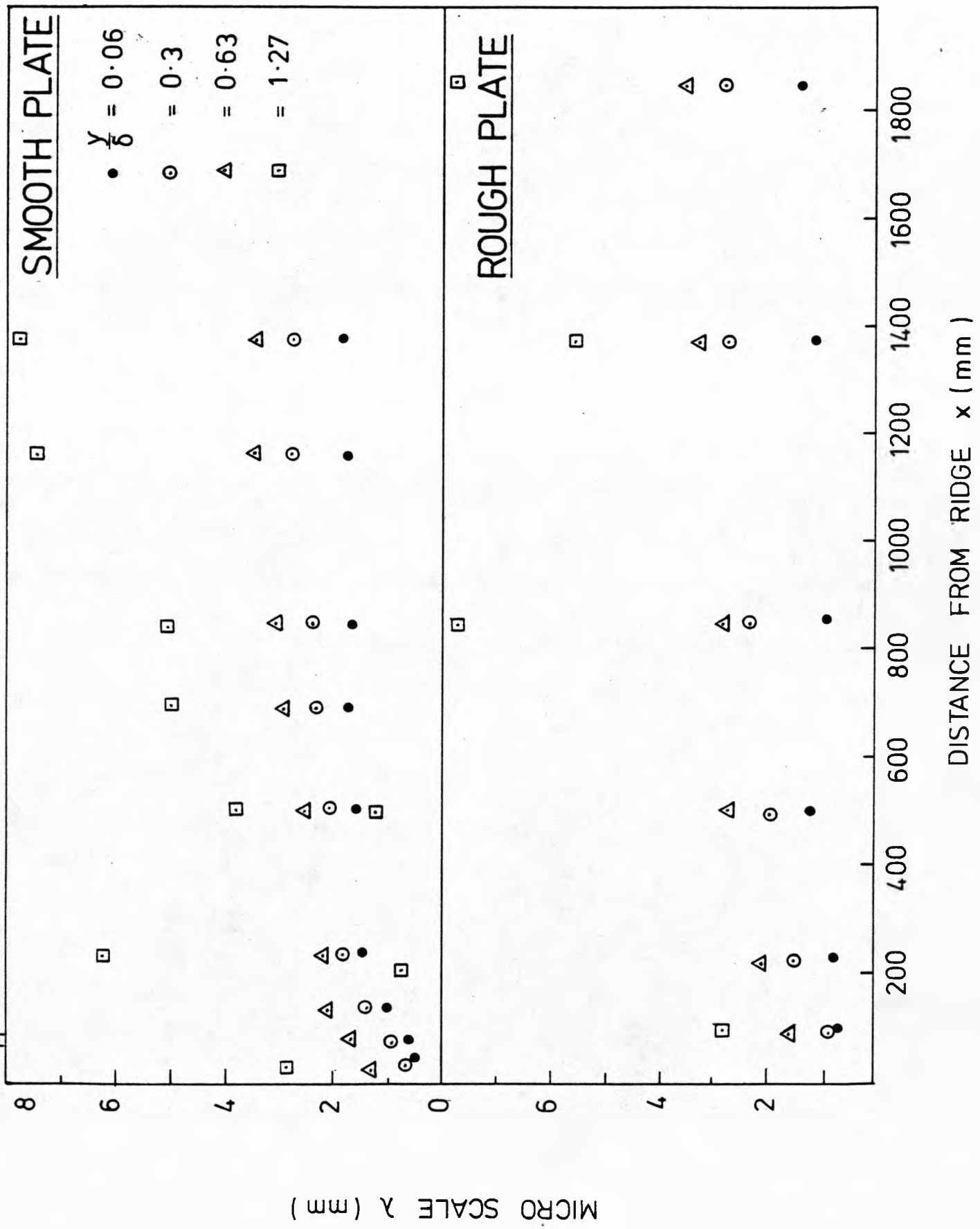

FIG.(4.26a)

TURBULENT EDDY VISCOSITY DOWNSTREAM OF RIDGE AND HILL ATTACHED TO ROUGH SURFACE

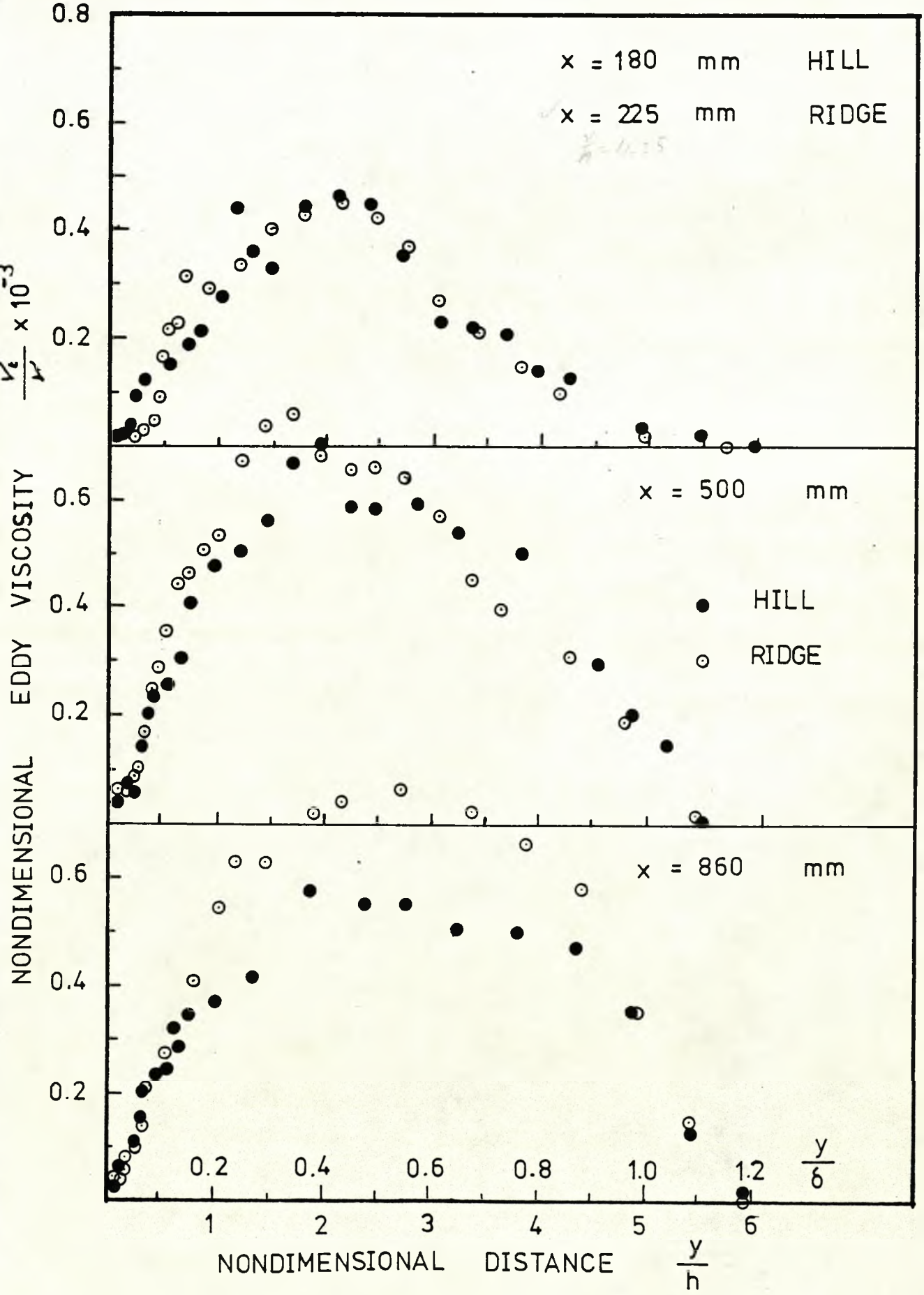

FIG.(4.26b)

TURBULENT EDDY VISCOSITY DOWNSTREAM OF
RIDGE AND HILL ATTACHED TO ROUGH SURFACE

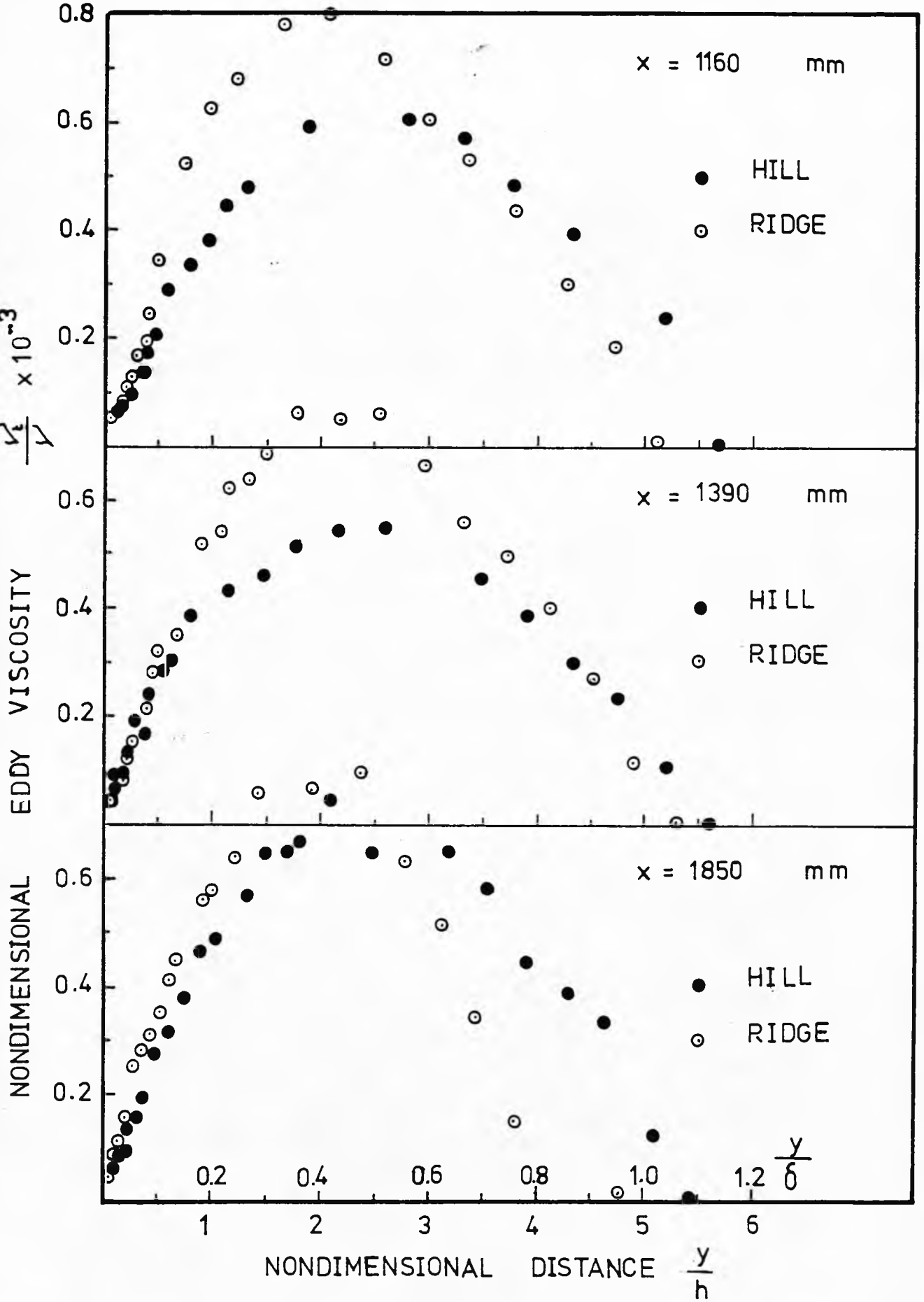

FIG.(4.27a)

TURBULENT EDDY VISCOSITY DOWNSTREAM OF
RIDGE ATTACHED TO ROUGH AND SMOOTH SURFACES

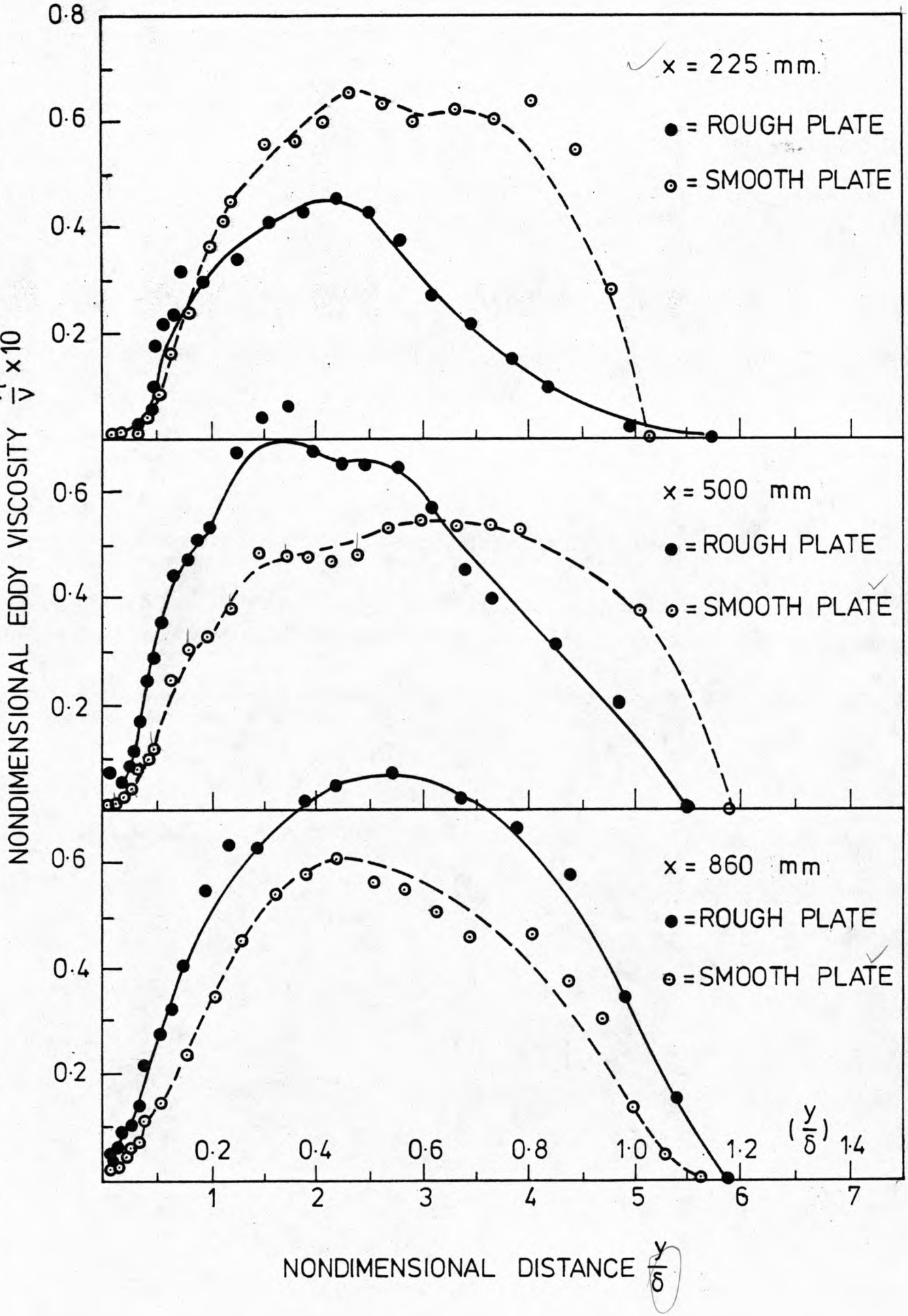

TURBULENT EDDY VISCOSITY DOWNSTREAM OF
RIDGE ATTACHED TO ROUGH AND SMOOTH SURFACES

FIG.(4.27b)

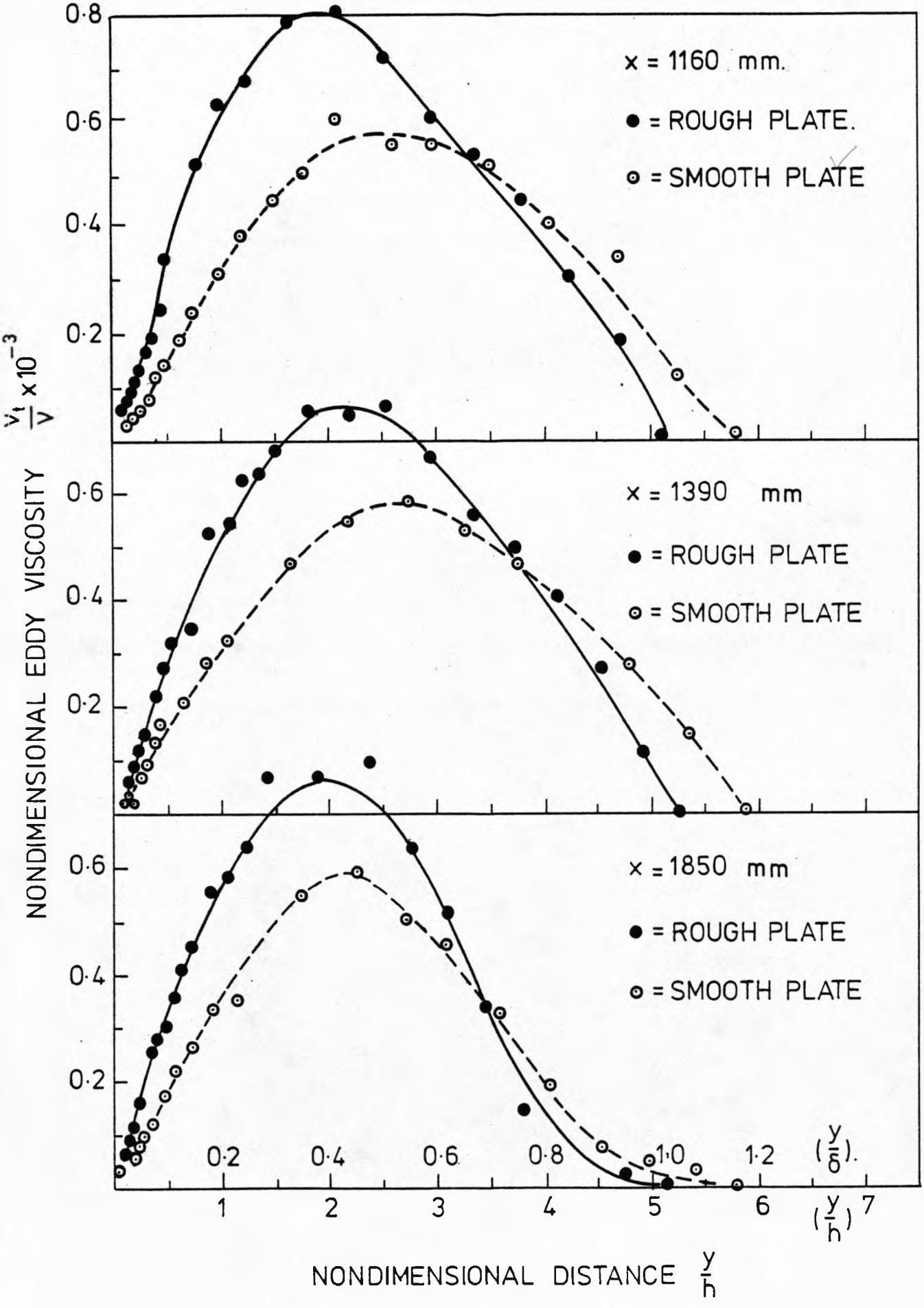

FIG.(4.29a)

MIXING LENGTH DISTRIBUTIONS DOWNSTREAM OF
RIDGE AND HILL ATTACHED TO ROUGH SURFACE

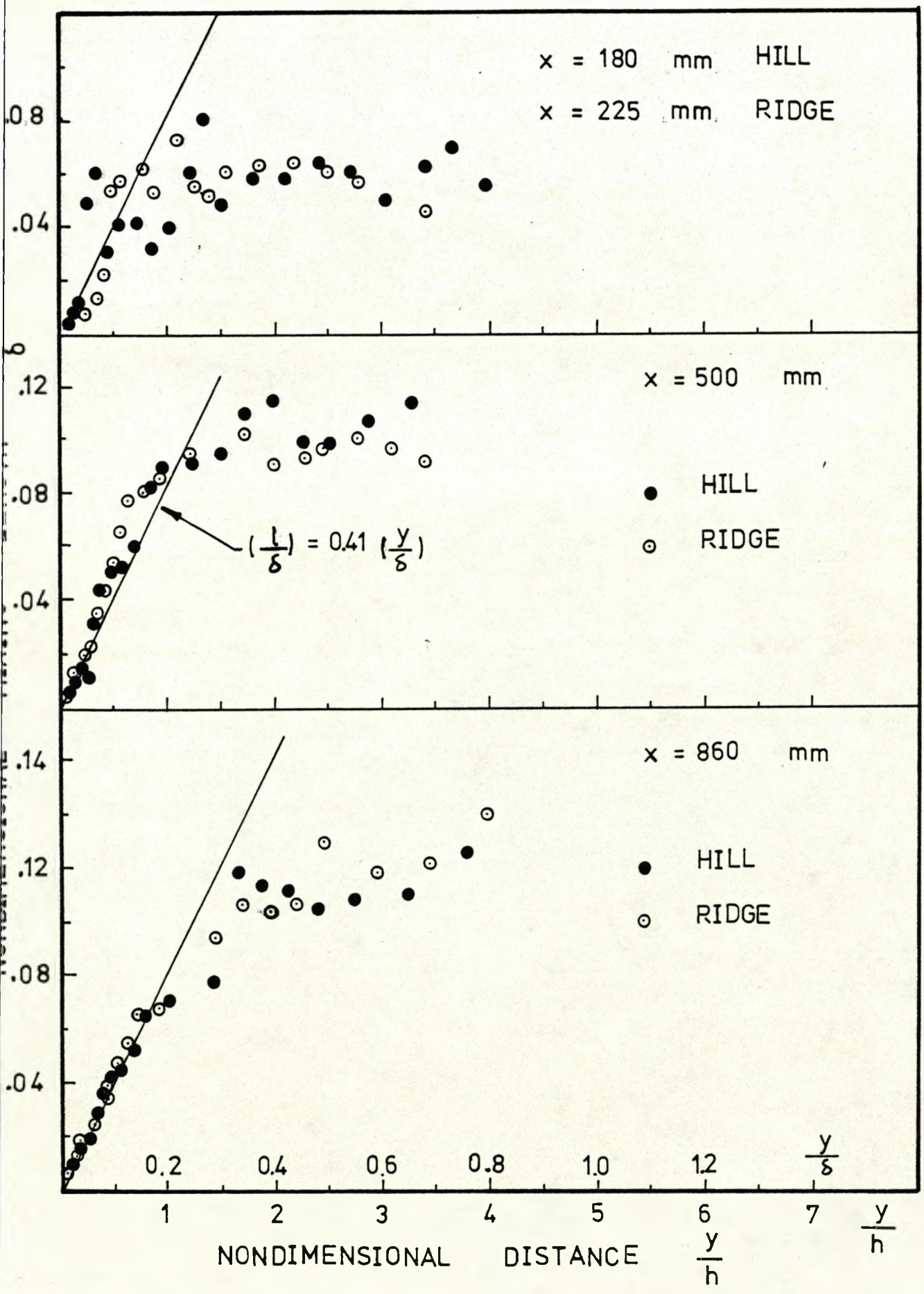

EDDY VISCOSITY PROPORTIONALITY CONSTANT α DOWNSTREAM OF RIDGE AND HILL ON SMOOTH AND ROUGH SURFACES

FIG.(4.28)

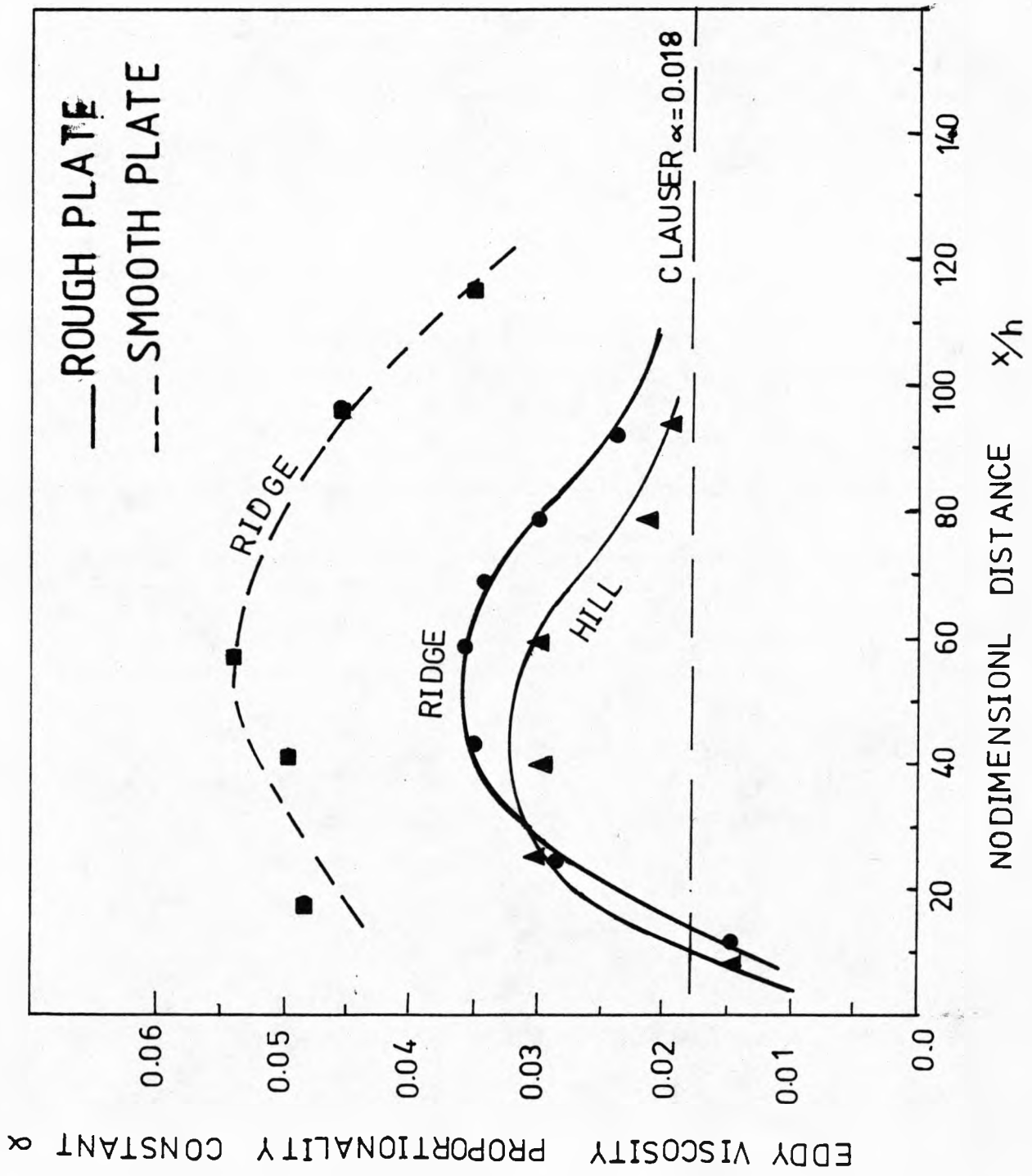

FIG. (4.29b)

MIXING LENGTH DISTRIBUTIONS DOWNSTREAM OF RIDGE AND HILL ATTACHED TO ROUGH SURFACE

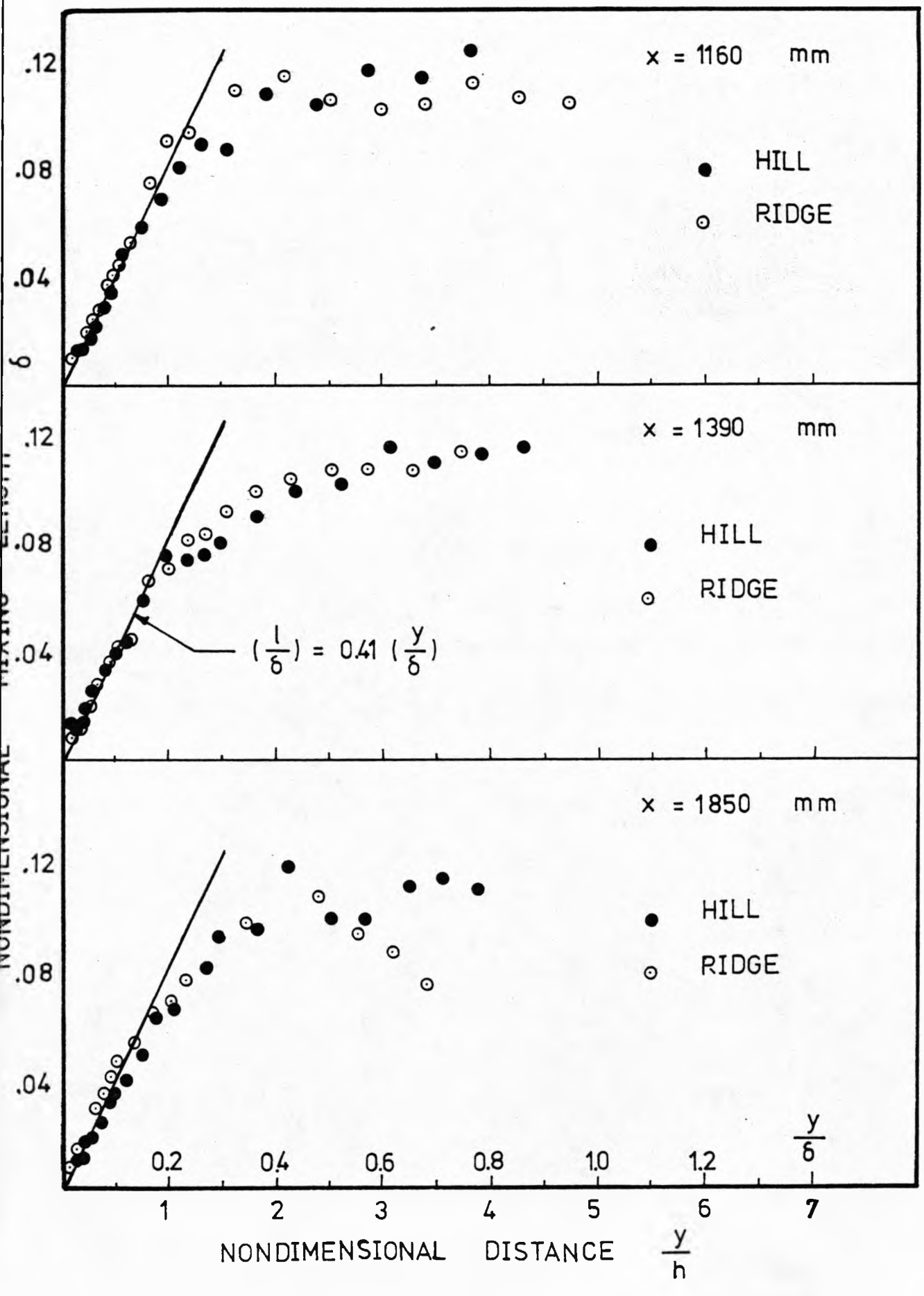

FIG.(4.30a)

MIXING LENGTH DISTRIBUTIONS DOWNSTREAM OF
RIDGE ATTACHED TO ROUGH AND SMOOTH SURFACES

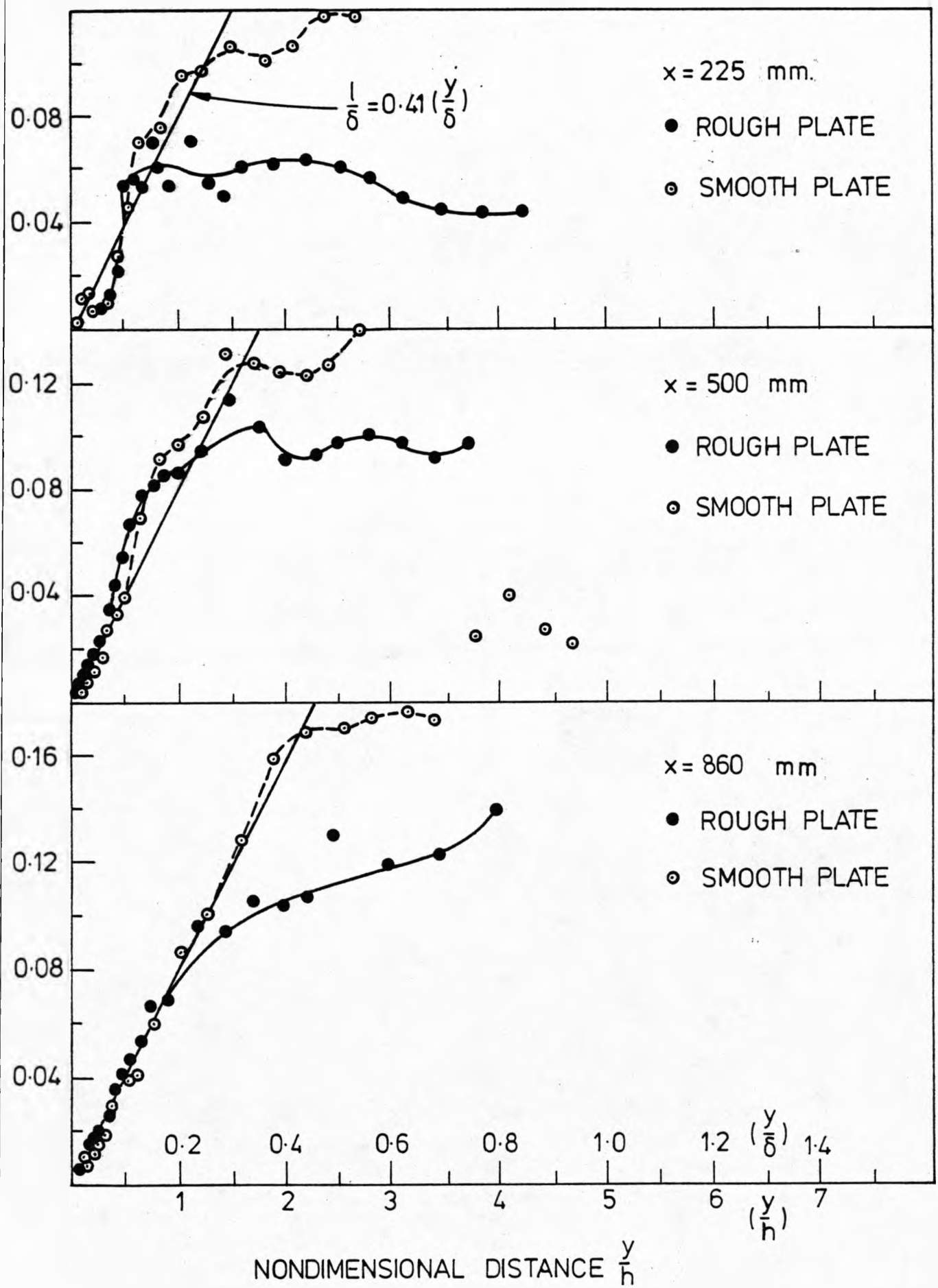

FIG.(4.30b)

MIXING LENGTH DISTRIBUTIONS DOWNSTREAM OF RIDGE ATTACHED TO ROUGH AND SMOOTH SURFACES

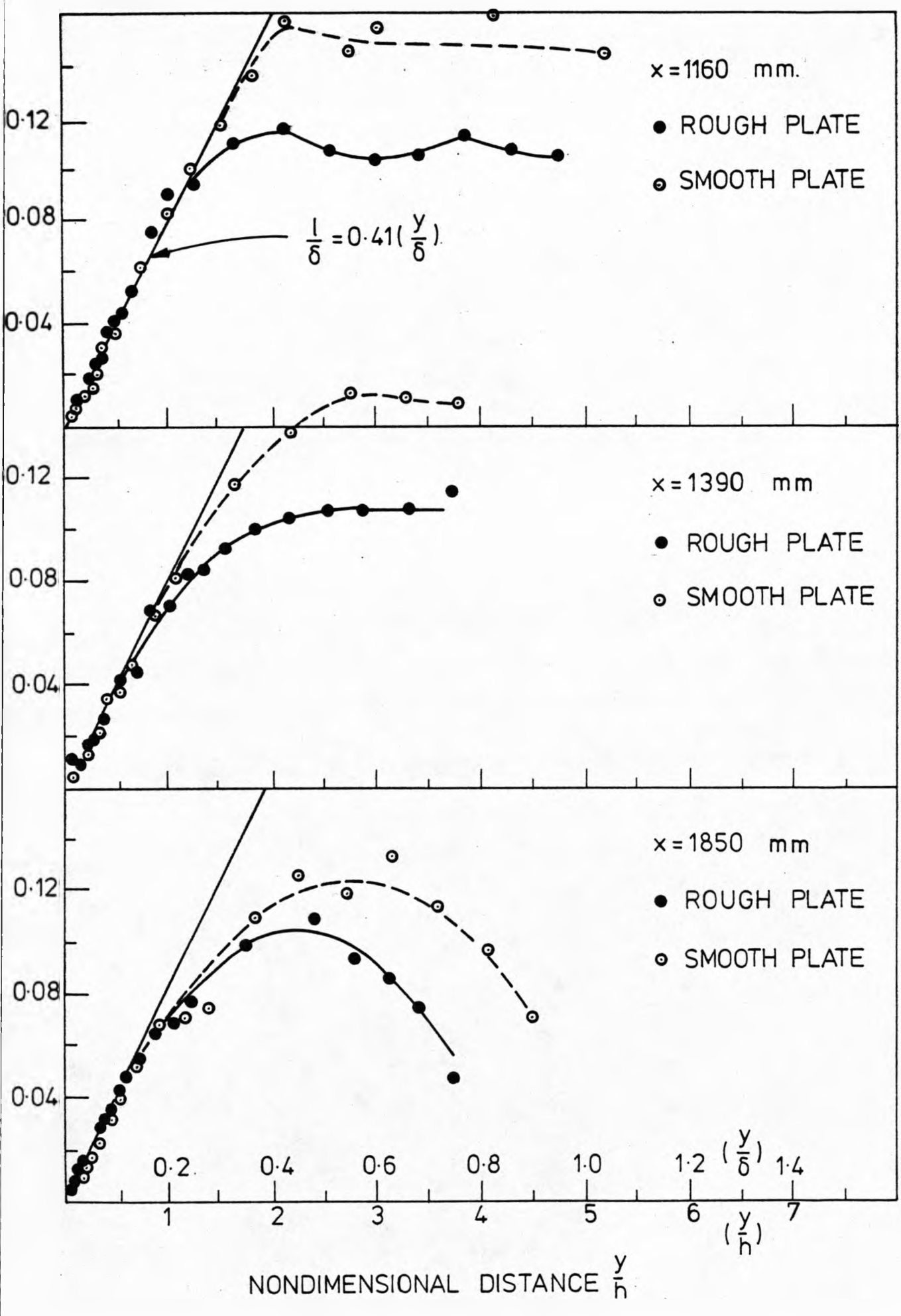

AVERAGE VELOCITY IN THE ROUGH AND SMOOTH PIPES

FIG.(5.1)

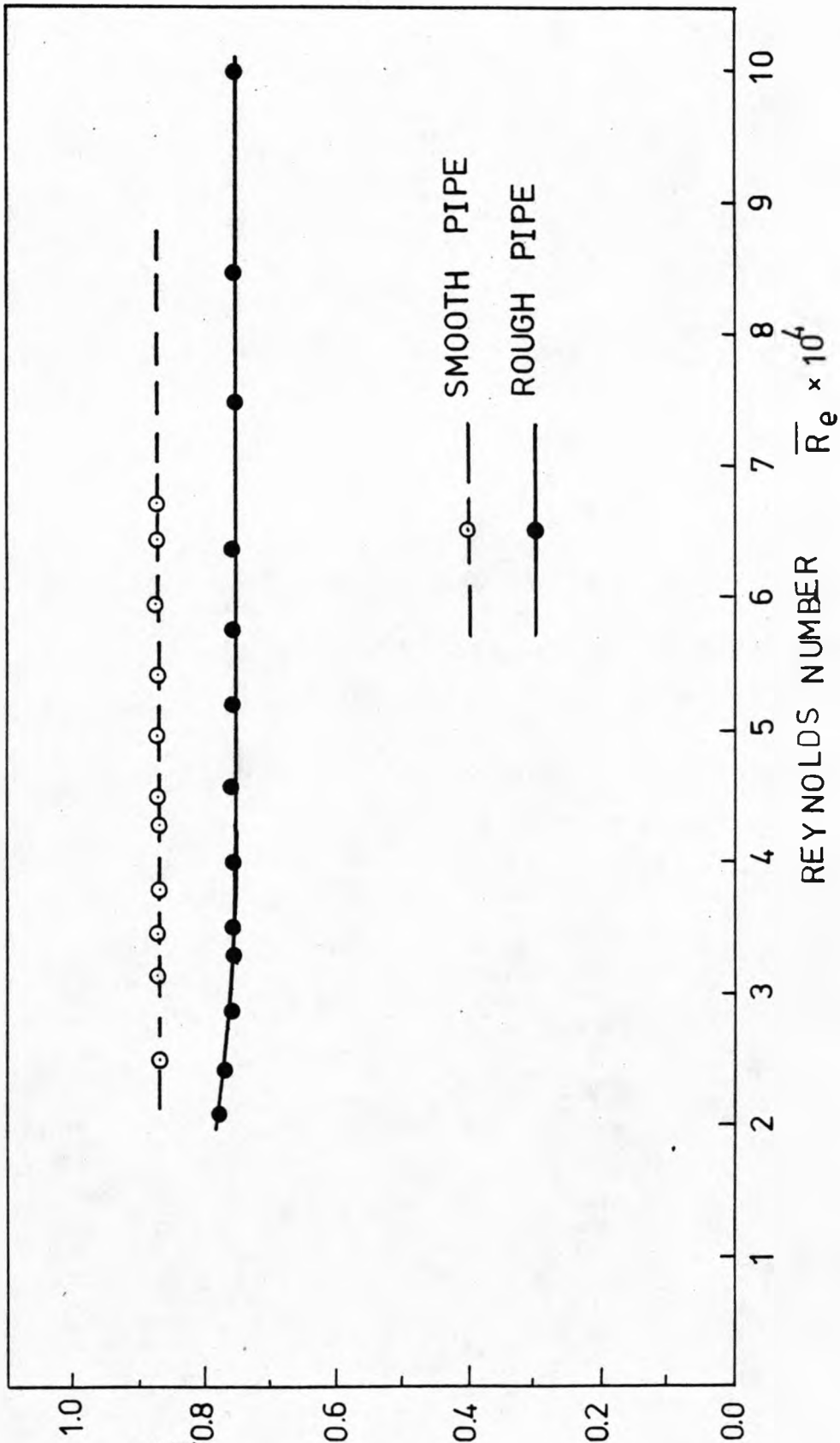

FRICTION FACTOR AND ROUGHNESS FUNCTION IN THE PIPE FLOW

FIG(5.2)

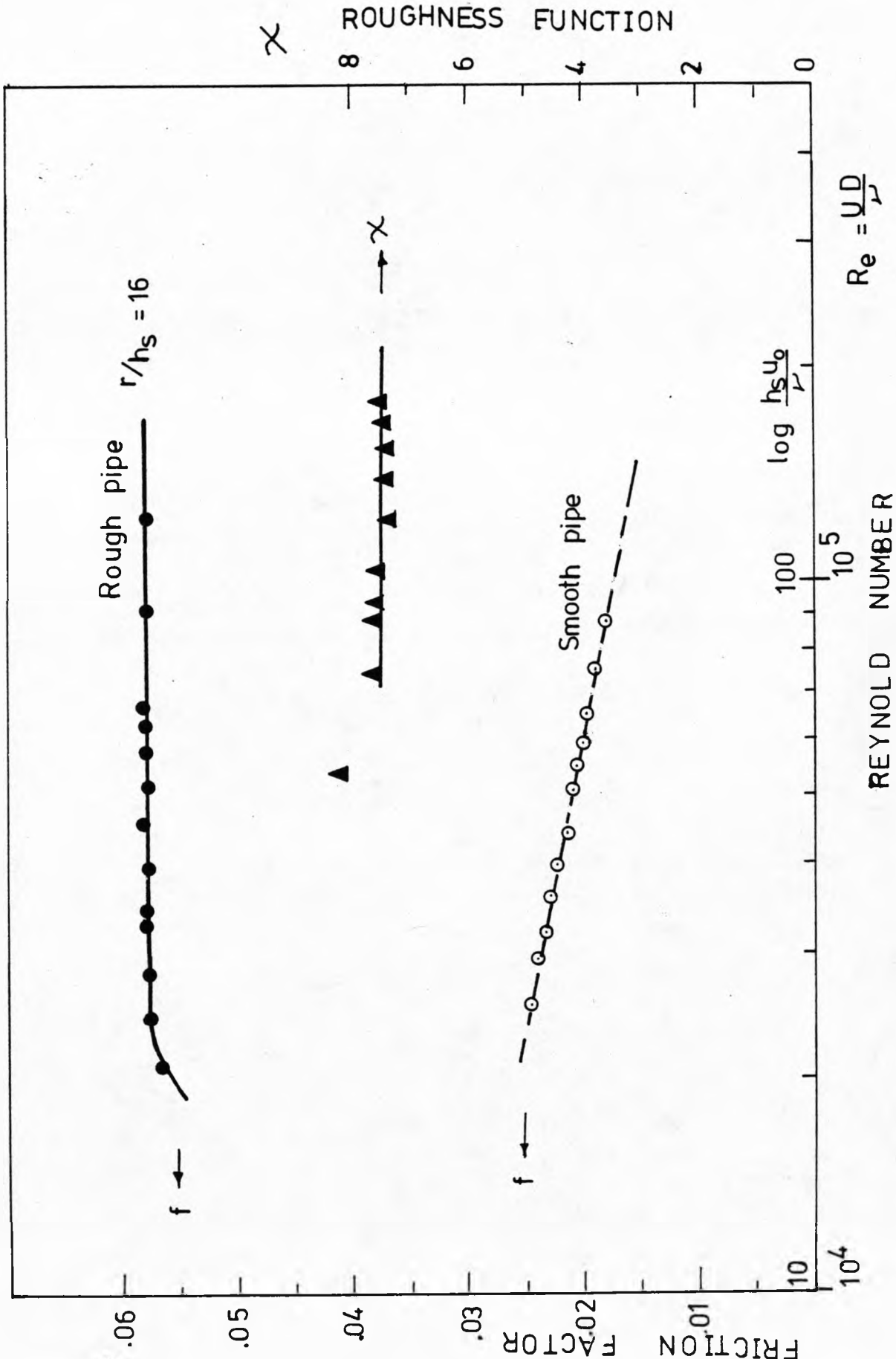

FIG.(5.3)

INNER REGION VELOCITY DISTRIBUTIONS FOR THE ROUGH PIPE

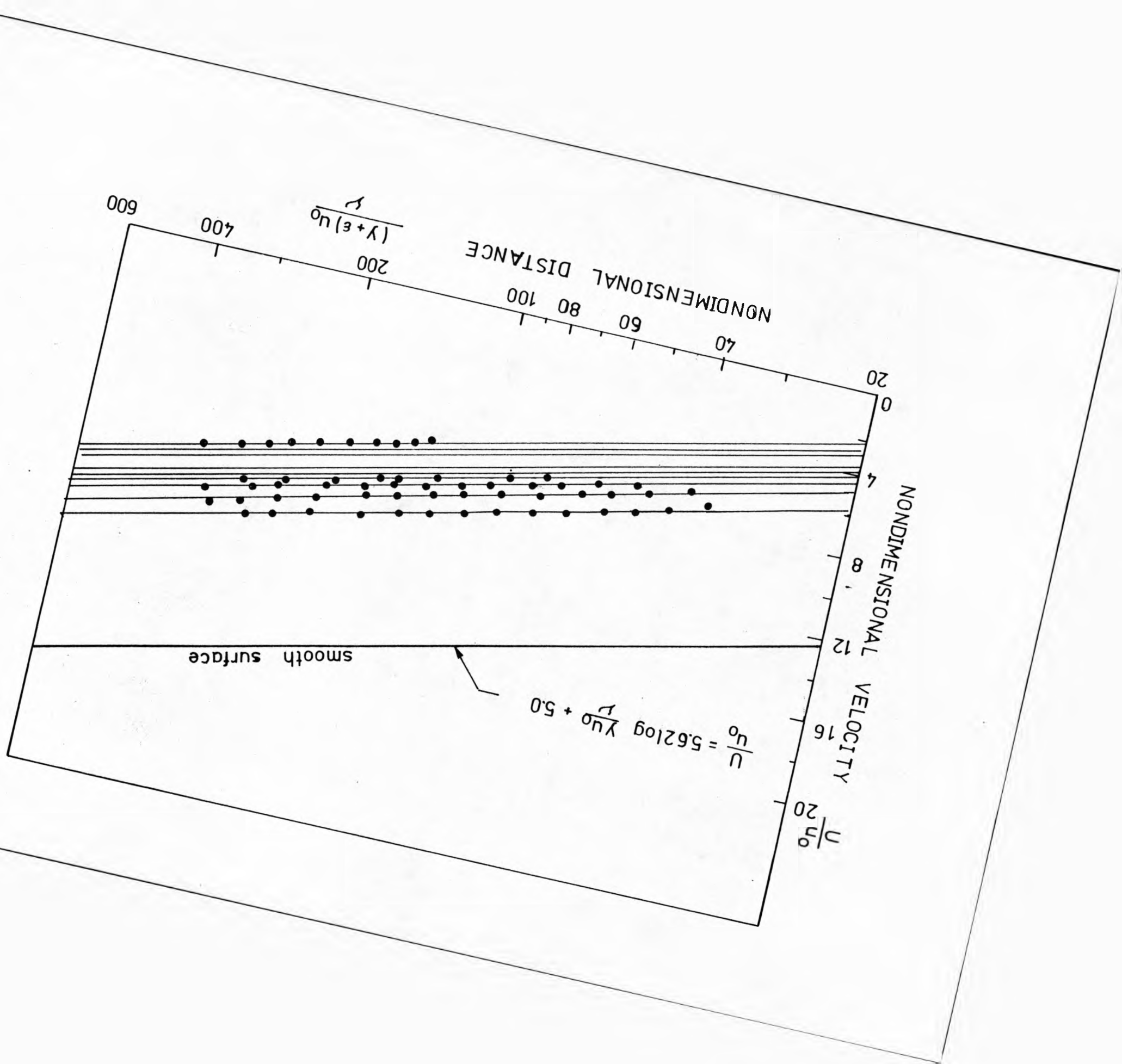

MEAN VELOCITY DISTRIBUTIONS DOWNSTREAM OF RING IN ROUGH PIPE ($R_e = 1.06 \times 10^5$)

FIG(5.4a)

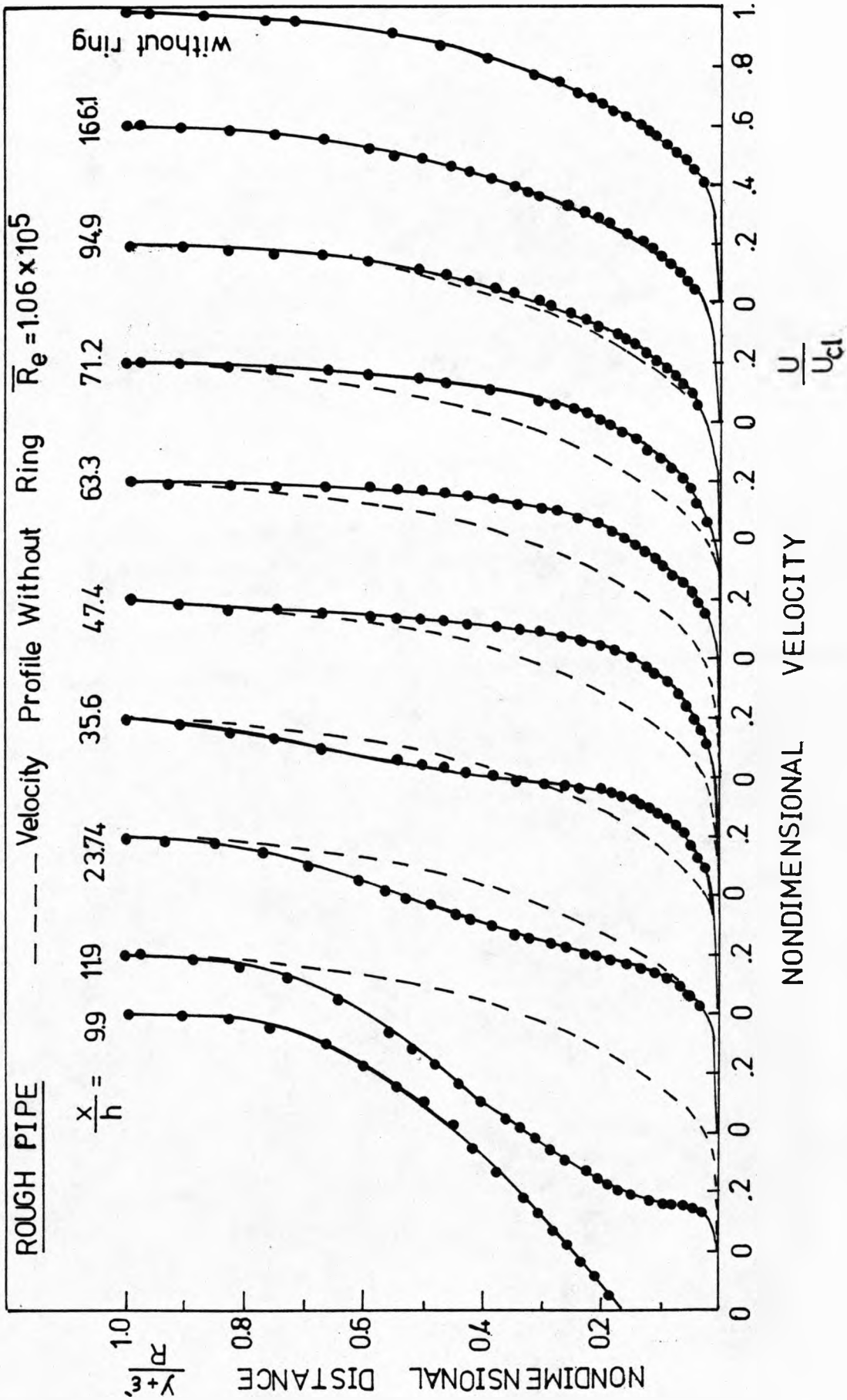

FIG.(5.4b)

MEAN VELOCITY DISTRIBUTIONS DOWNSTREAM OF RING IN ROUGH PIPE ($\bar{R}_e = 4.5 \times 10^4$)

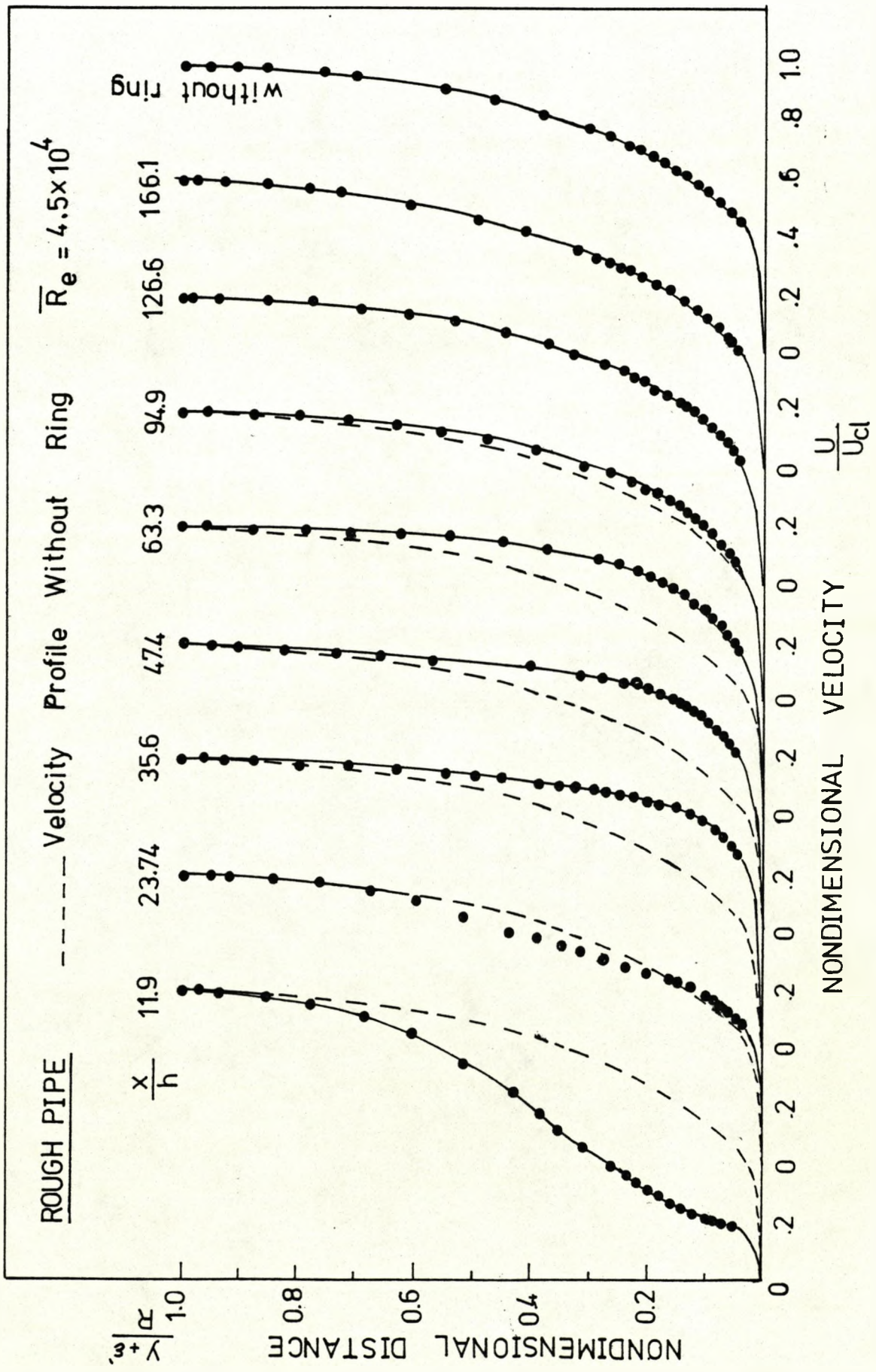

FIG.(5.4c)

MEAN VELOCITY DISTRIBUTIONS DOWNSTREAM OF RING IN SMOOTH PIPE ($\bar{R}_e$ = 4.5 x 10^4)

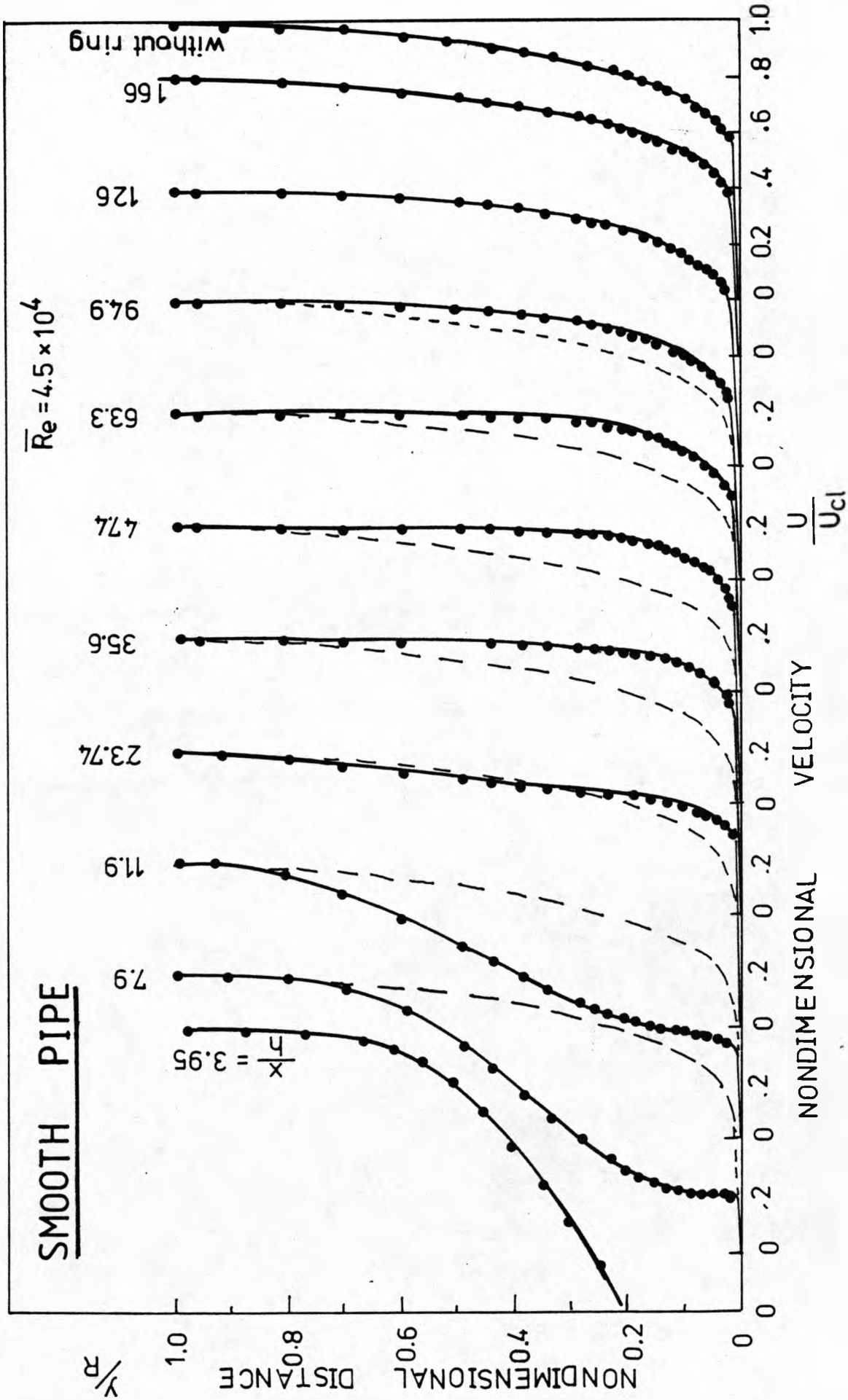

MEAN VELOCITY DISTRIBUTIONS DOWNSTREAM OF RING IN ROUGH PIPE IN 'LAW-OF-THE-WALL' CO-ORDINATES

FIG(5.5a)

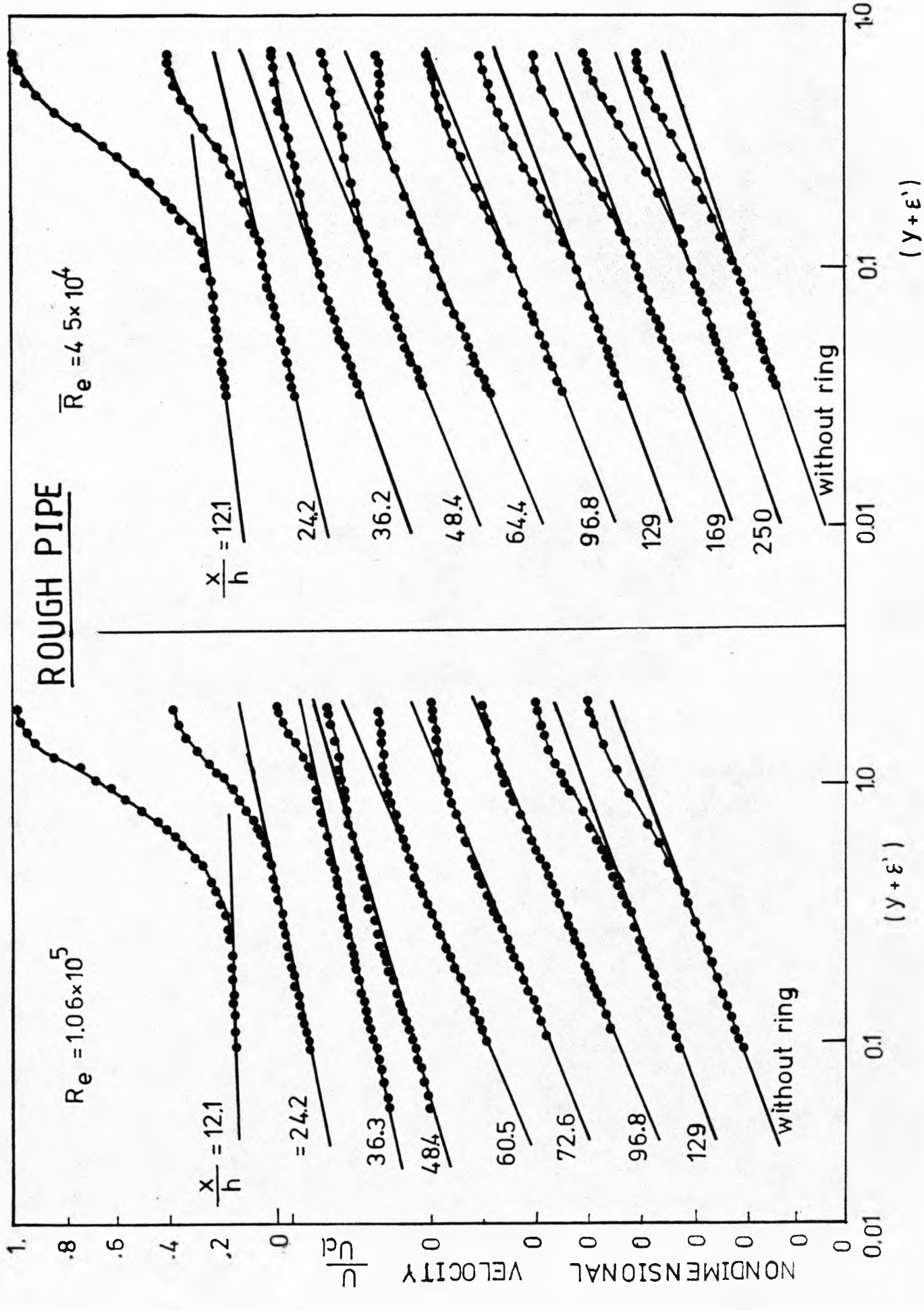

SMOOTH PIPE

x = Distance From Ring

without ring

$\frac{x}{h}$ = 166

126.6

94.9

63.3

47.4

35.6

23.74

11.9

$\frac{U}{u_o} = 5.75 \log \frac{y\, u_o}{\nu} + 5.1$

NONDIMENSIONAL VELOCITY $\frac{U}{u_o}$

30
20
10
10
10
10
10
10
10

NONDIMENSIONAL DISTANCE $\frac{y\, u_o}{\nu}$

10^1
10^2
10^3

MEAN VELOCITY DISTRIBUTIONS DOWNSTREAM OF RING IN SMOOTH PIPE IN 'LAW-OF-THE-WALL' CO-ORDINATES

FIG. (5.5b)

FIG.(5.6)

VARIATIONS OF THE WAKE PARAMETER Π DOWNSTREAM OF RING IN ROUGH AND SMOOTH PIPES

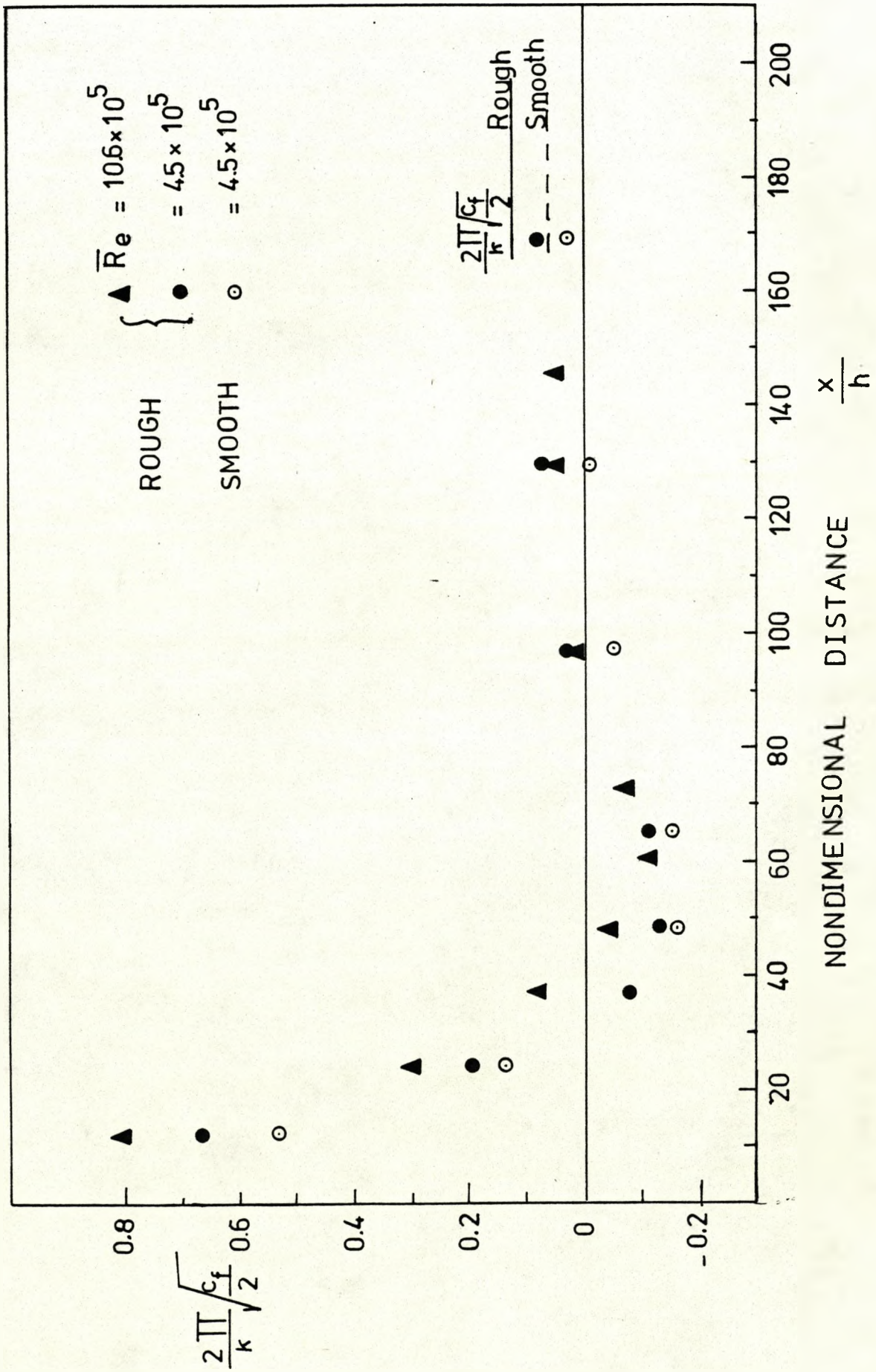

VARIATIONS OF THE CENTRE LINE VELOCITY DOWNSTREAM OF RING IN ROUGH AND SMOOTH PIPES

FIG.(5.7)

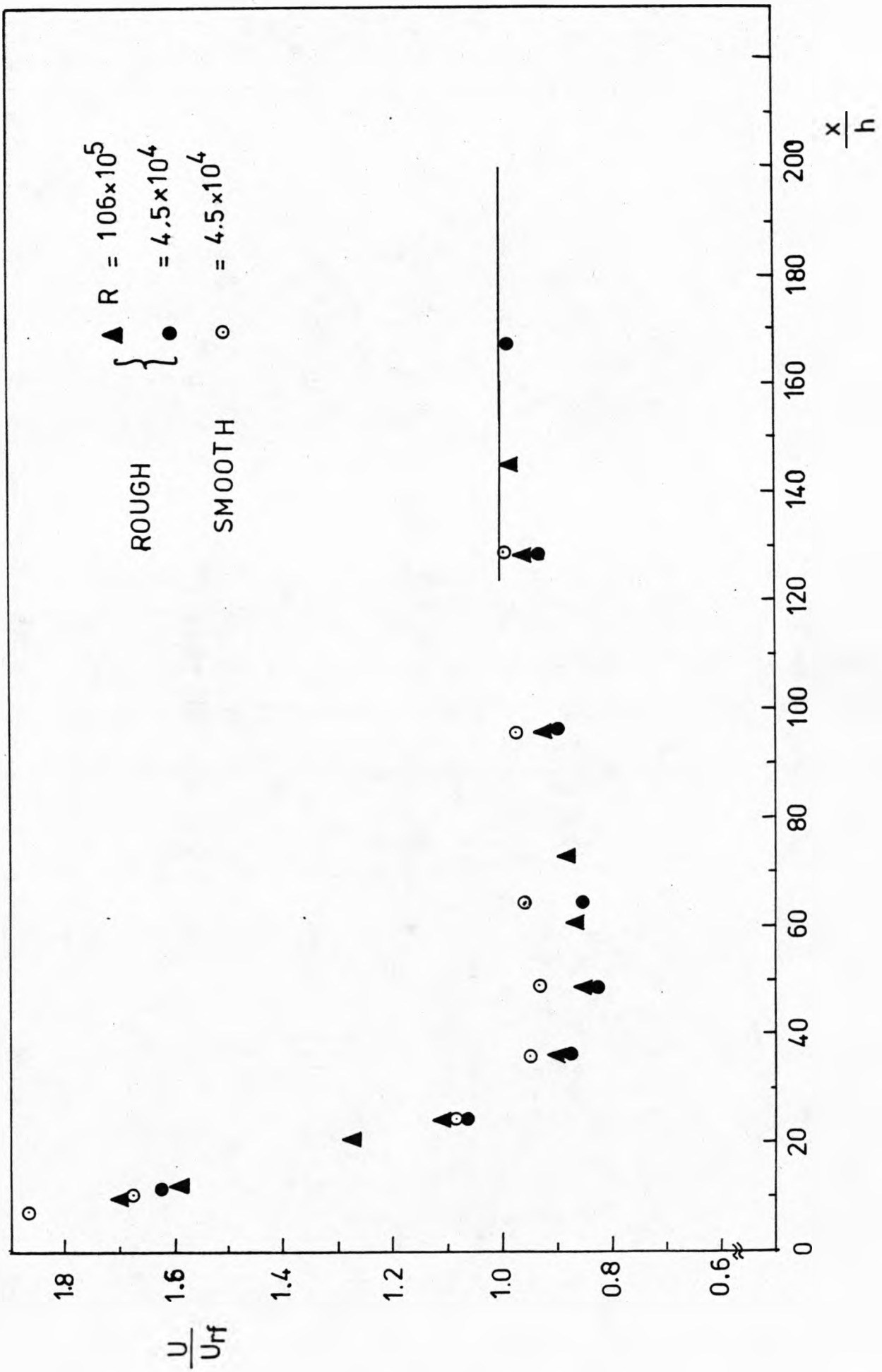

FIG.(5.8)

WALL FRICTION COEFFICIENT DOWNSTREAM OF RING IN ROUGH AND SMOOTH PIPE

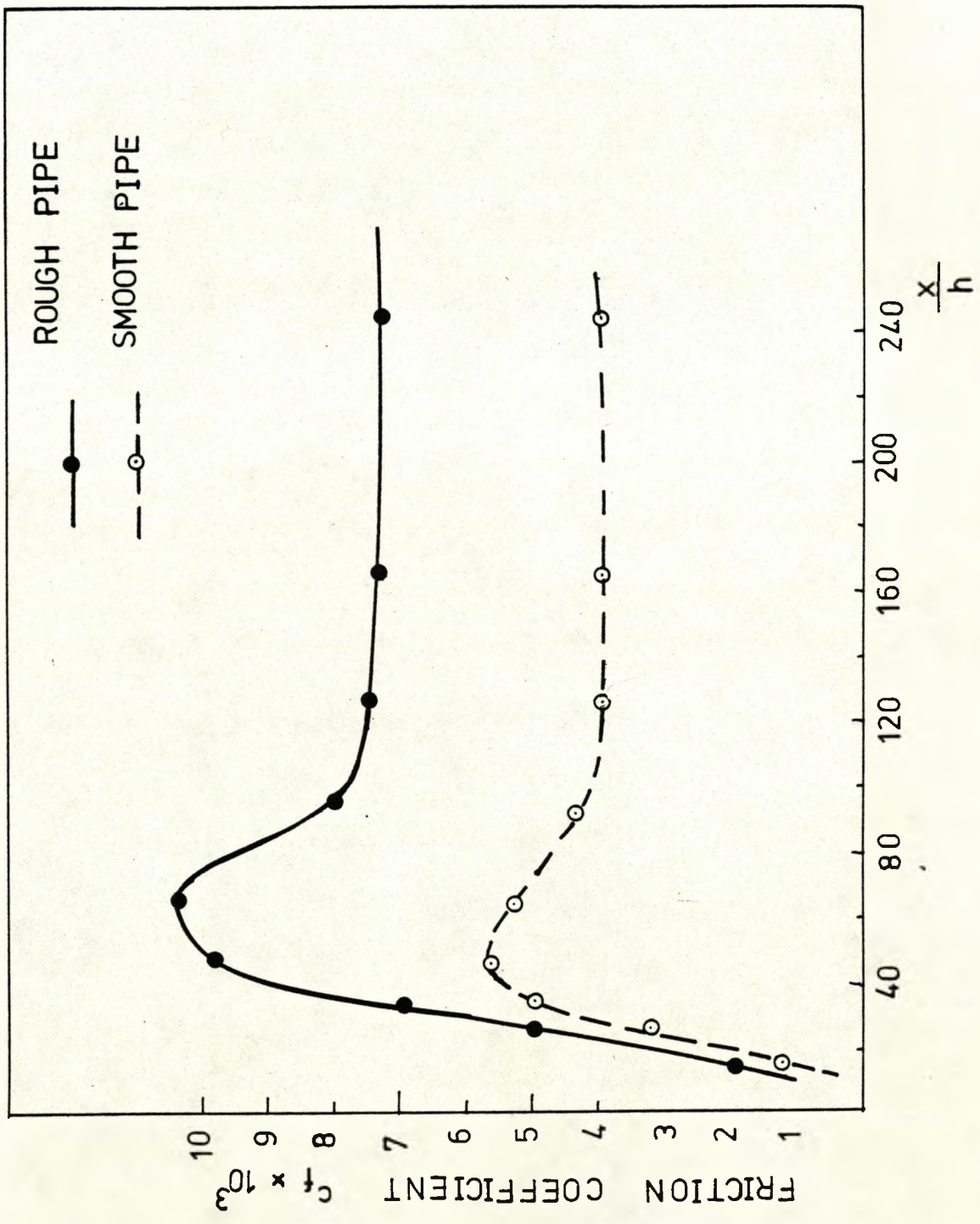

FIG.(5.9)

TURBULENT SHEAR STRESS DISTRIBUTION IN
ROUGH AND SMOOTH PIPES

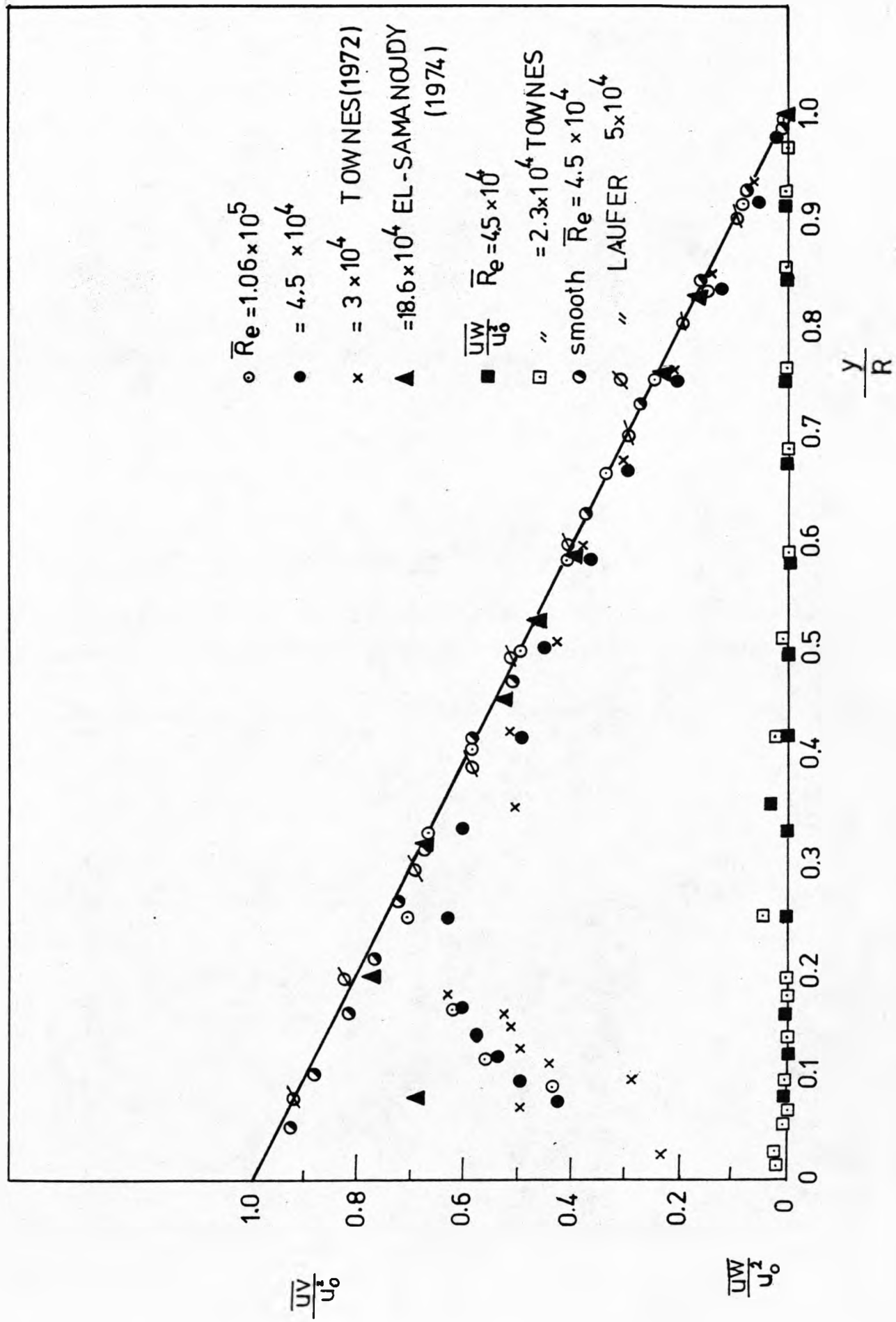

LONGITUDINAL TURBULENT NORMAL STRESS DISTRIBUTIONS
DOWNSTREAM OF RING IN ROUGH AND SMOOTH PIPES

FIG.(5.10a)

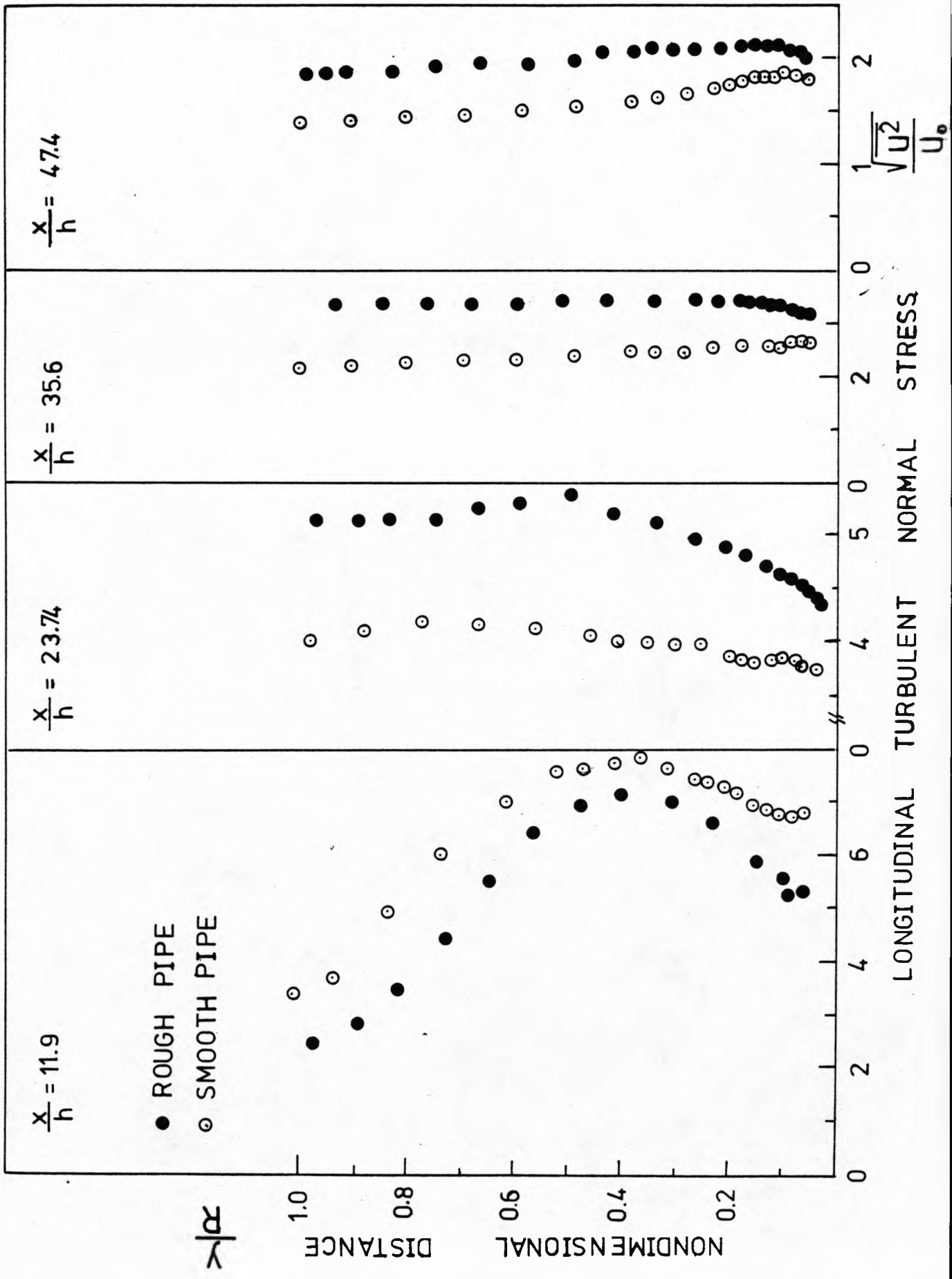

LONGITUDINAL TURBULENT NORMAL STRESS DISTRIBUTIONS
DOWNSTREAM OF RING IN ROUGH AND SMOOTH PIPES

FIG.(5.10b)

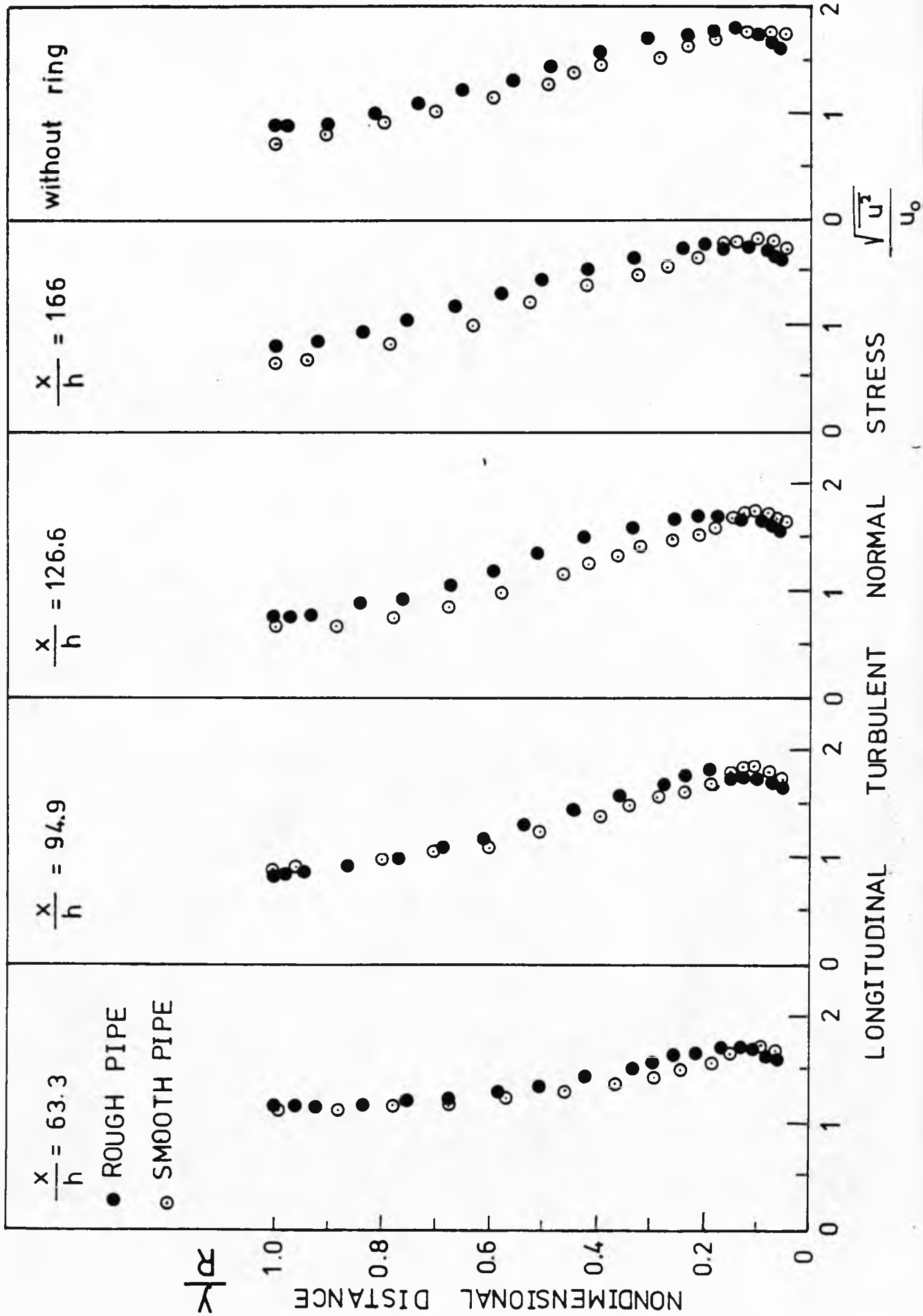

RADIAL TURBULENT NORMAL STRESS DISTRIBUTIONS
DOWNSTREAM OF RING IN ROUGH AND SMOOTH PIPES

FIG.(5.11a)

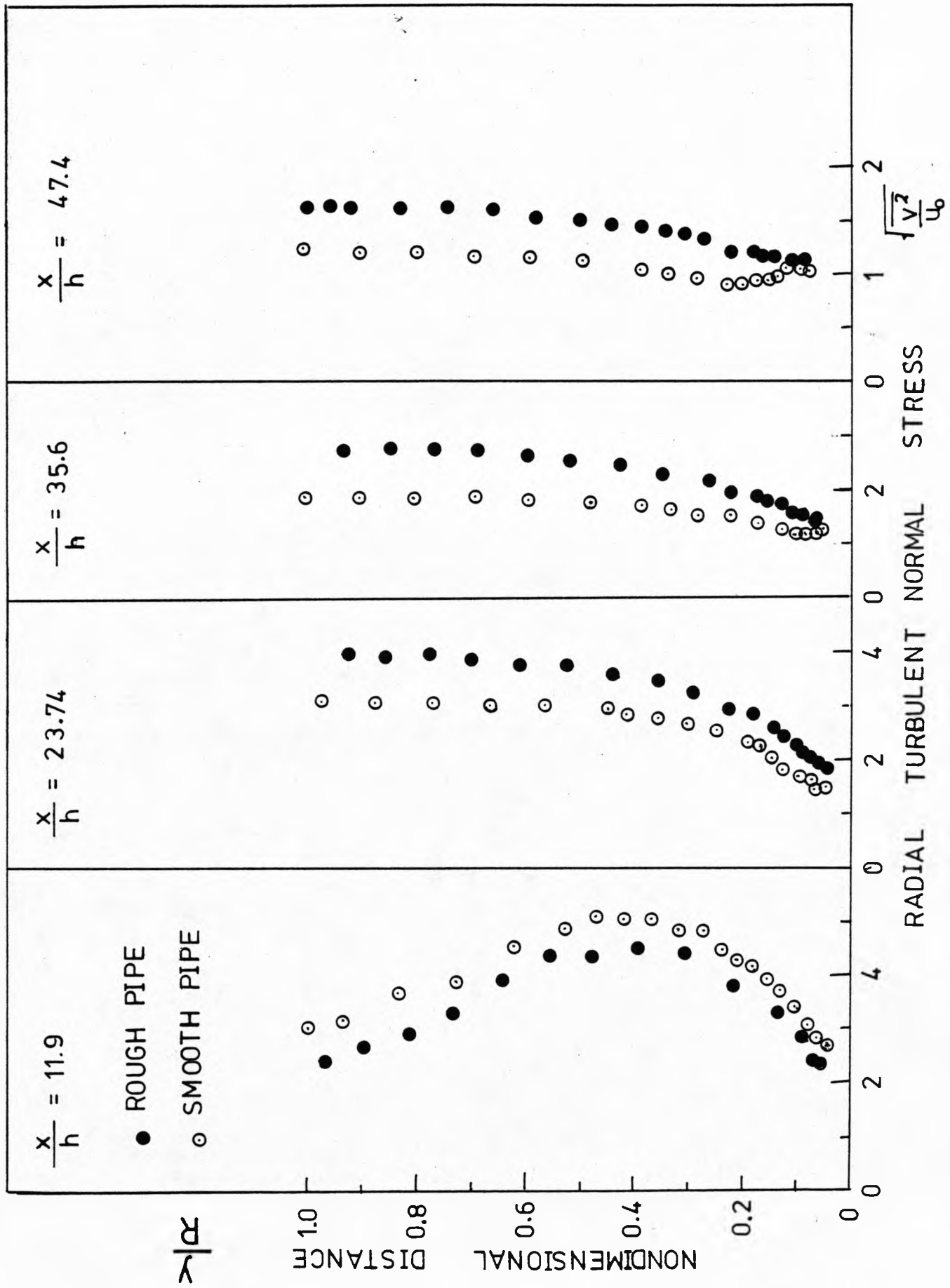

RADIAL TURBULENT NORMAL STRESS DISTRIBUTIONS
DOWNSTREAM OF RING IN ROUGH AND SMOOTH PIPES

FIG.(5.11b)

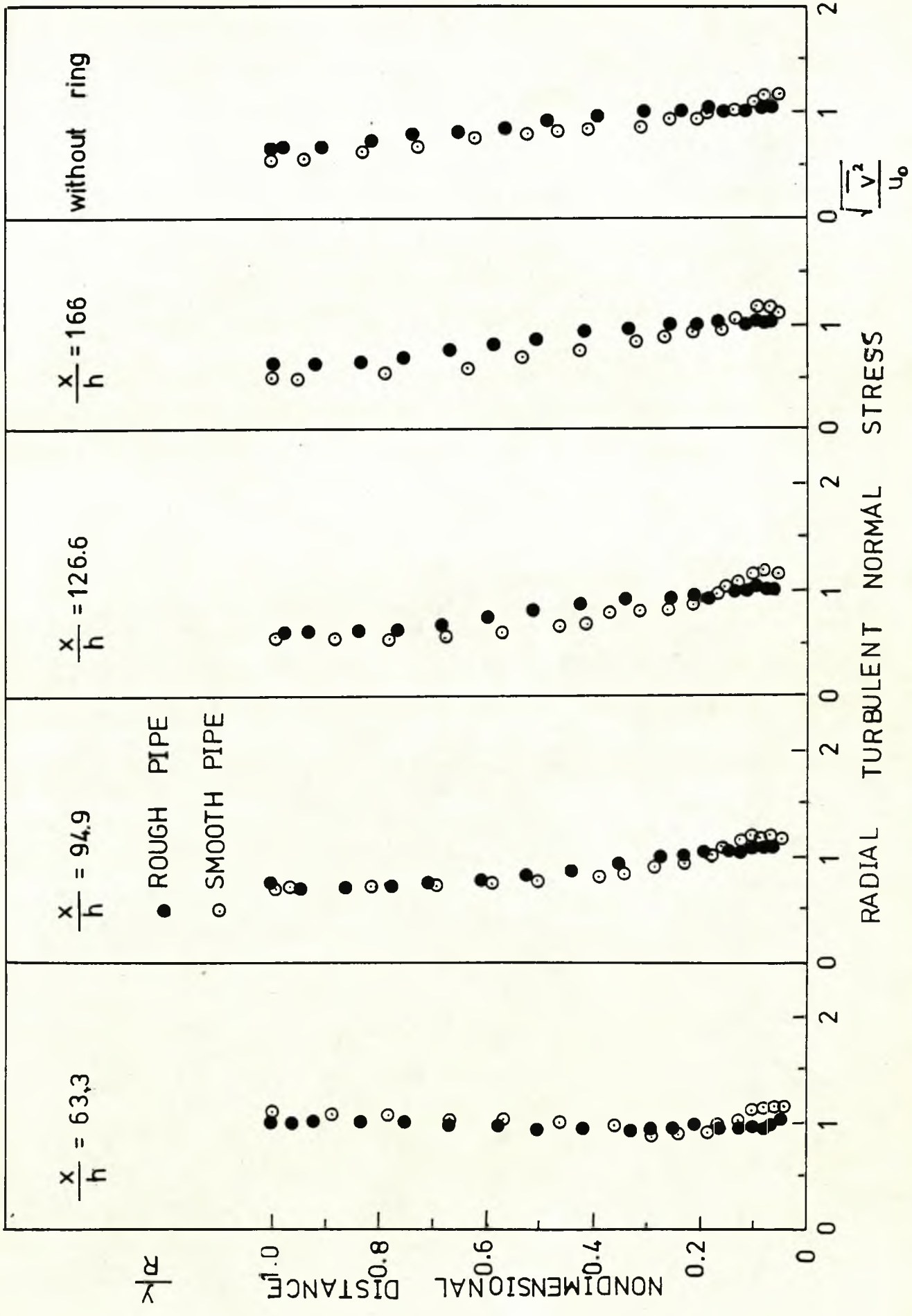

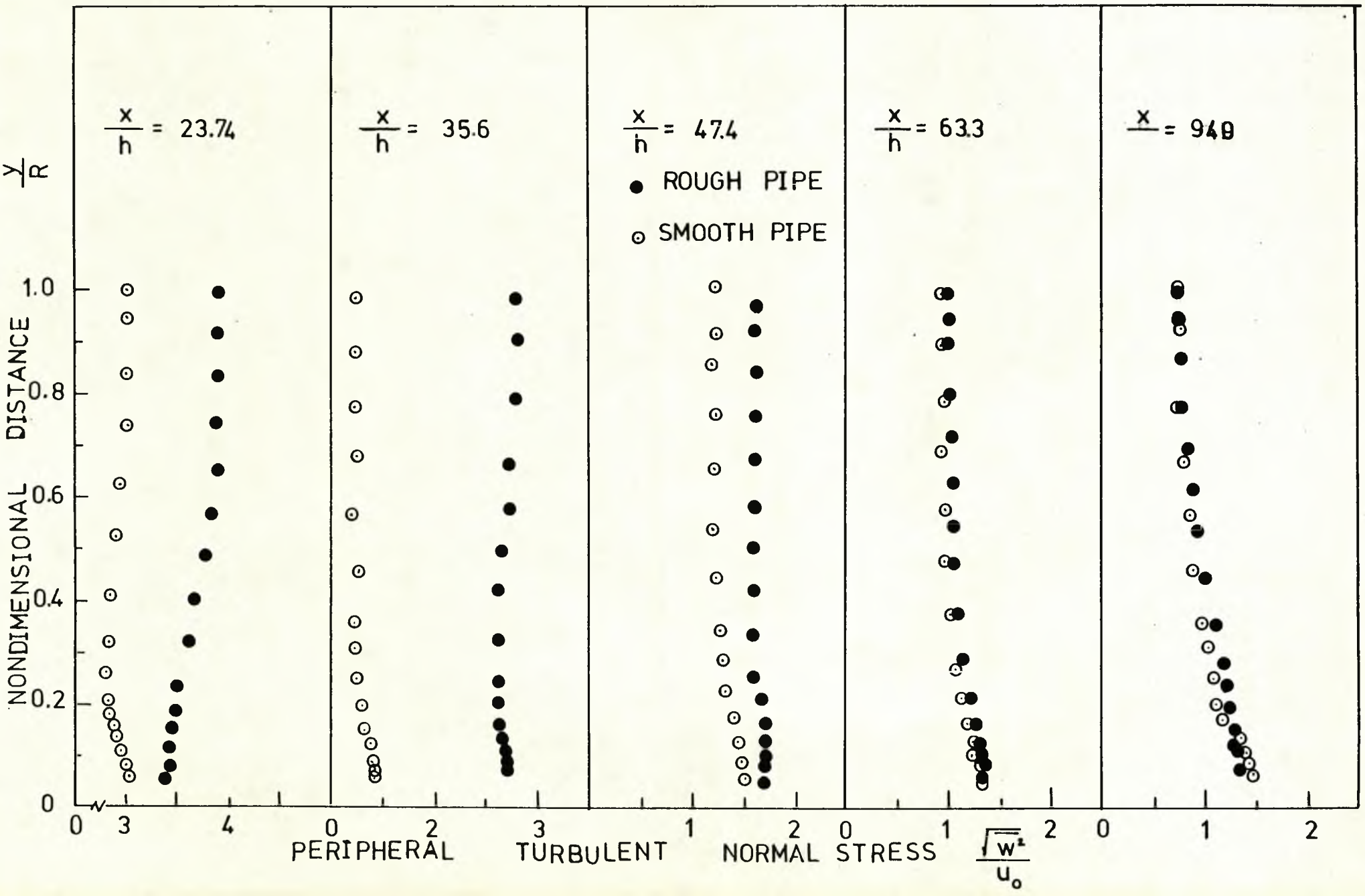

PERIPHERAL TURBULENT NORMAL STRESS DISTRIBUTIONS DOWNSTREAM OF RING IN ROUGH AND SMOOTH PIPES

FIG.(5.12a)

PERIPHERAL TURBULENT NORMAL STRESS DISTRIBUTIONS
DOWNSTREAM OF RING IN ROUGH AND SMOOTH PIPES

FIG.(5.12b)

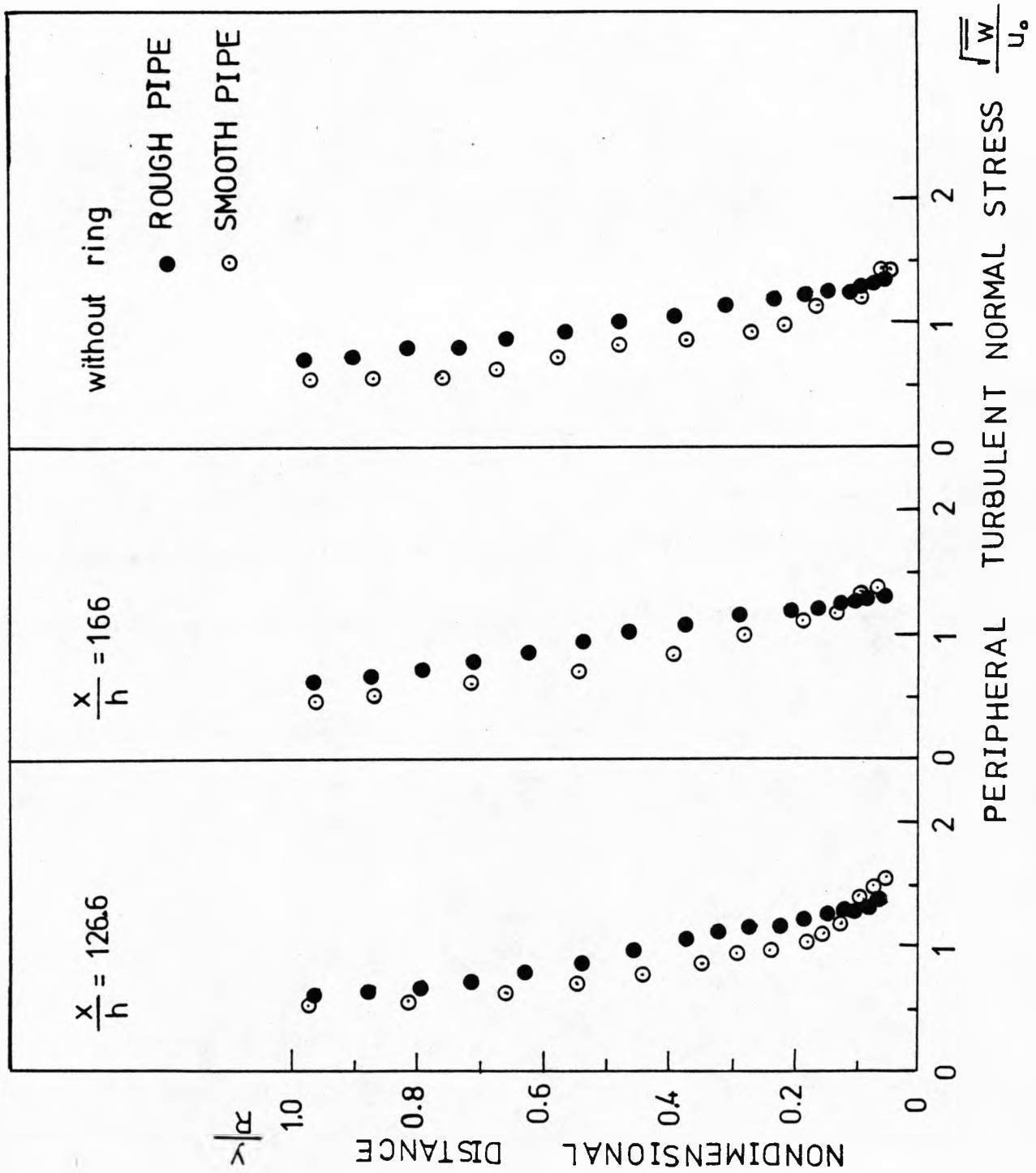

TURBULENT SHEAR STRESS DISTRIBUTIONS DOWNSTREAM OF RING
IN ROUGH AND SMOOTH PIPES

FIG.(5.13a)

TURBULENT SHEAR STRESS DISTRIBUTIONS DOWNSTREAM OF RING IN ROUGH AND SMOOTH PIPES

FIG.(5.13b)

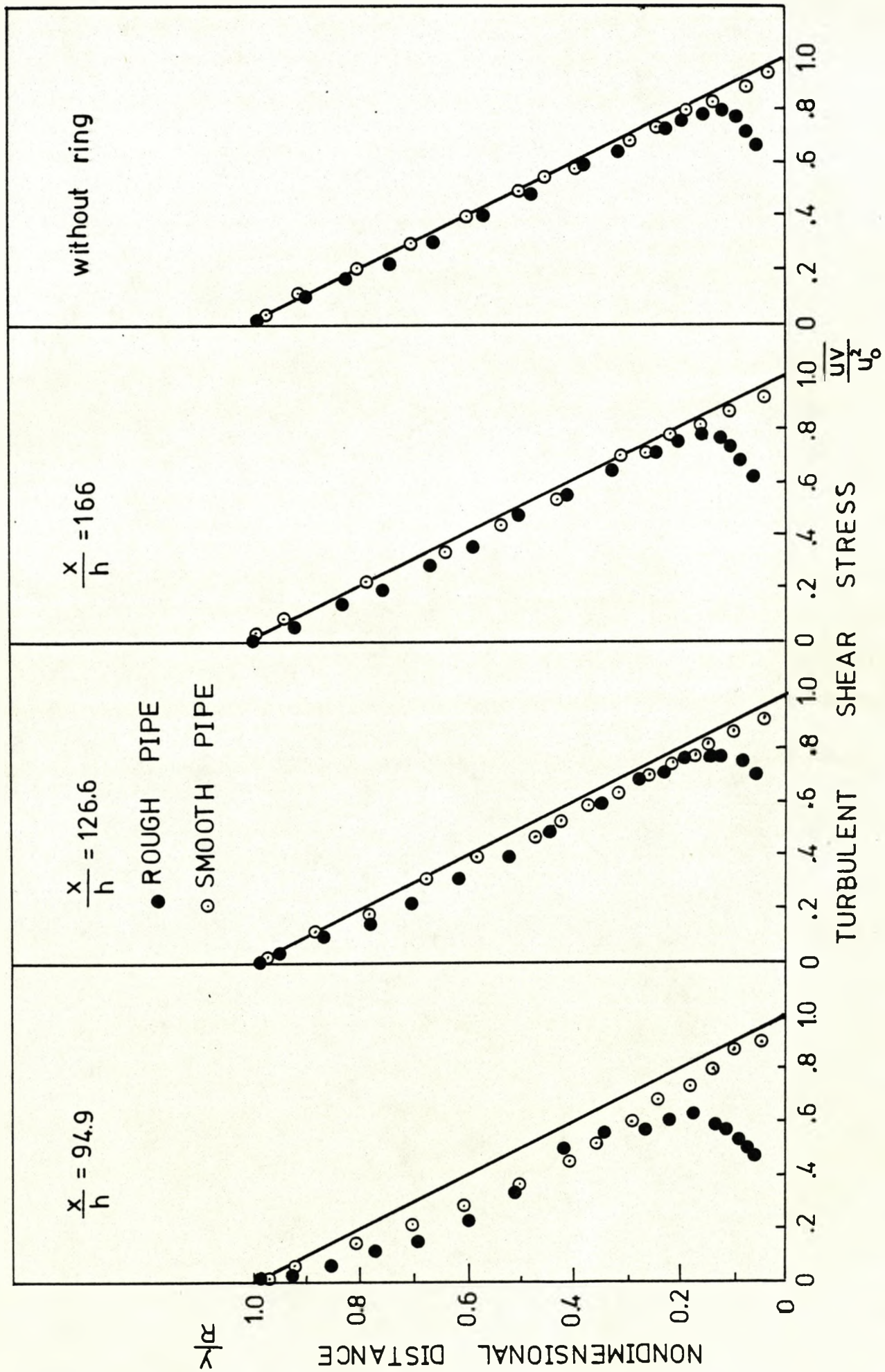

SKEWNESS FACTOR DOWNSTREAM OF RING IN ROUGH AND SMOOTH PIPES

FIG.(5.14)

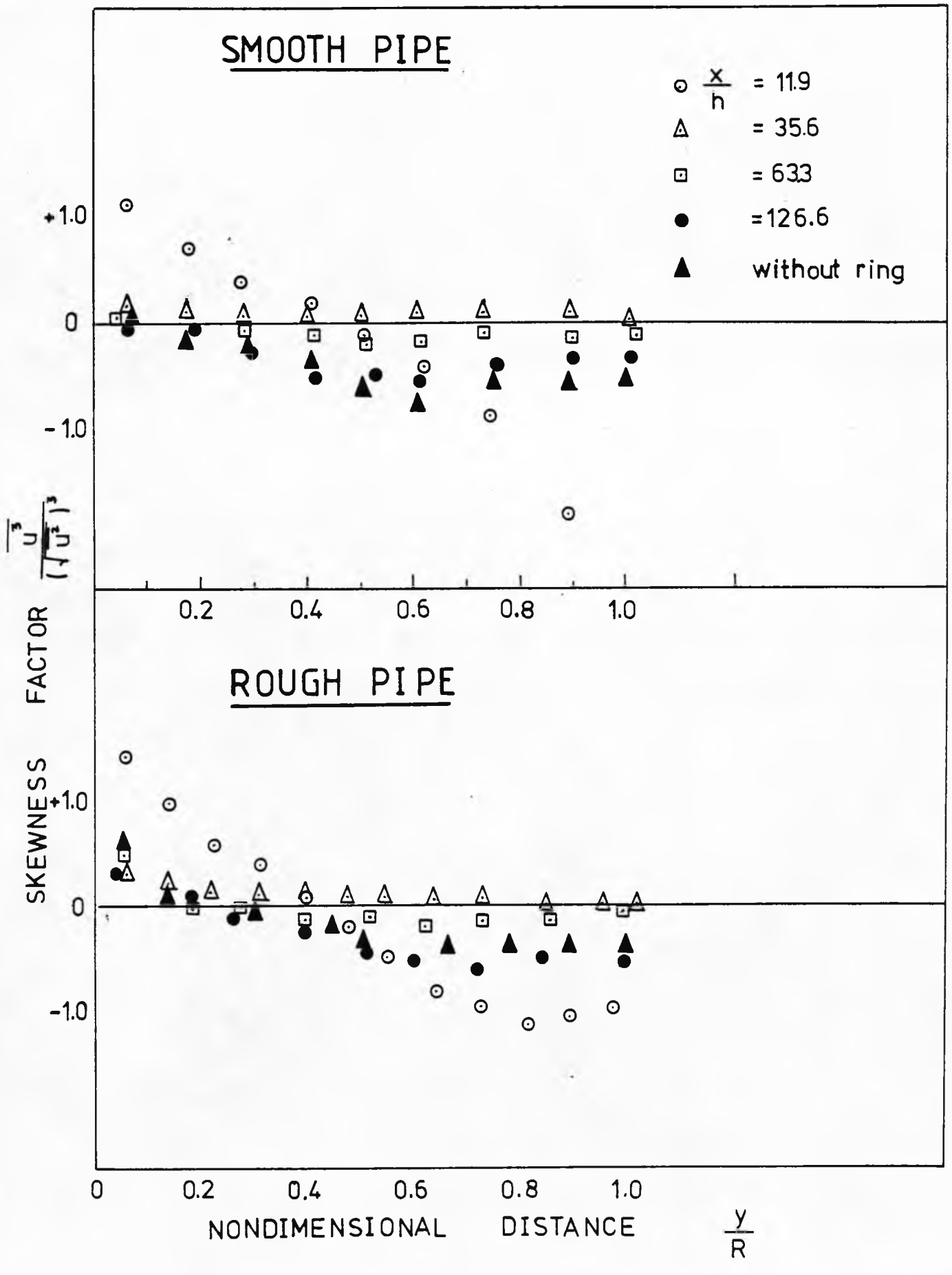

FLATNESS FACTOR DOWNSTREAM OF RING IN ROUGH AND SMOOTH PIPES

FIG.(5.15)

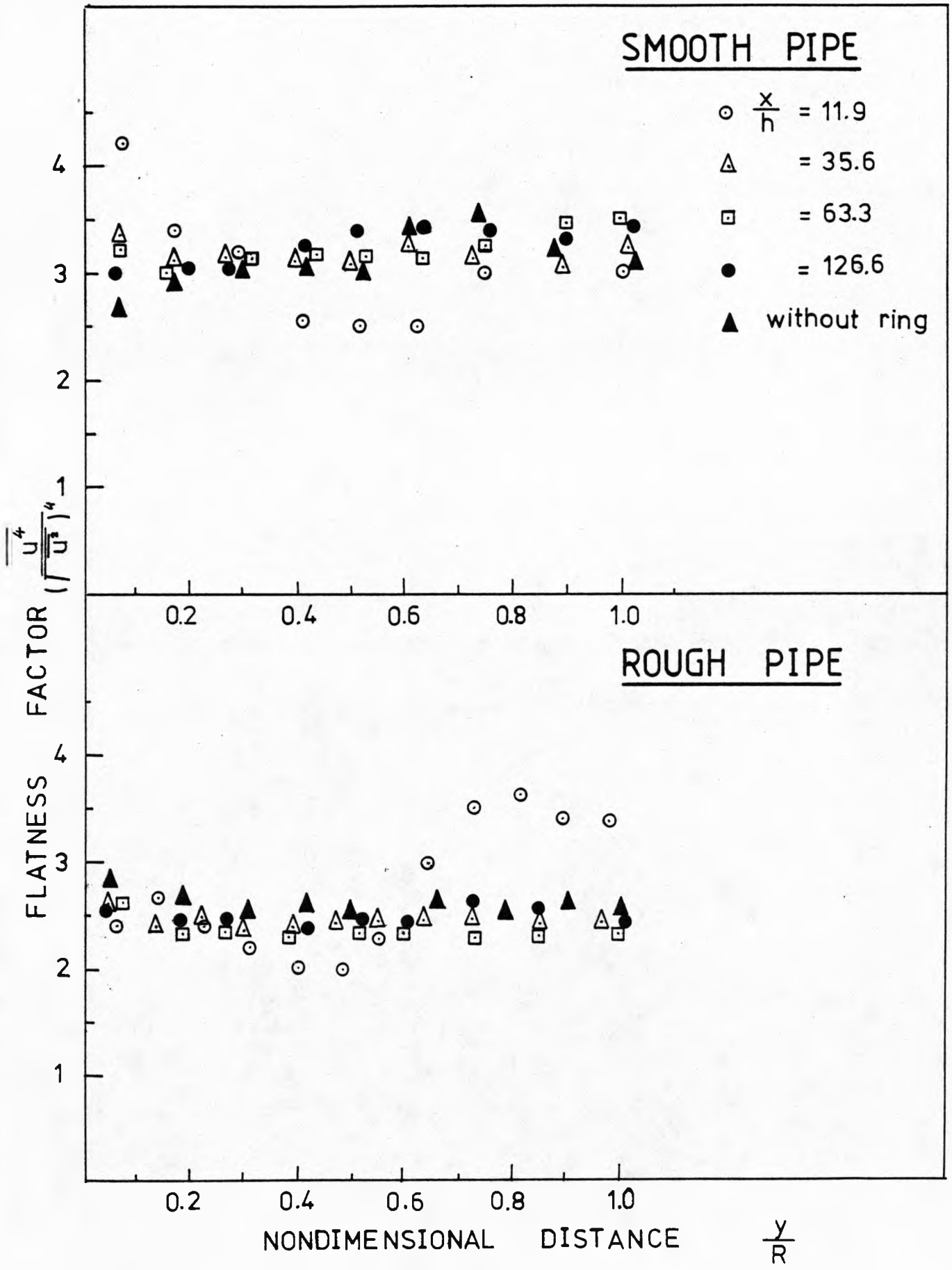

FIG. (5.16 a)

FREQUENCY SPECTRA OF $\overline{u^2}$ AT $\frac{x}{h}$ = 11.9 DOWNSTREAM OF RING IN ROUGH PIPE

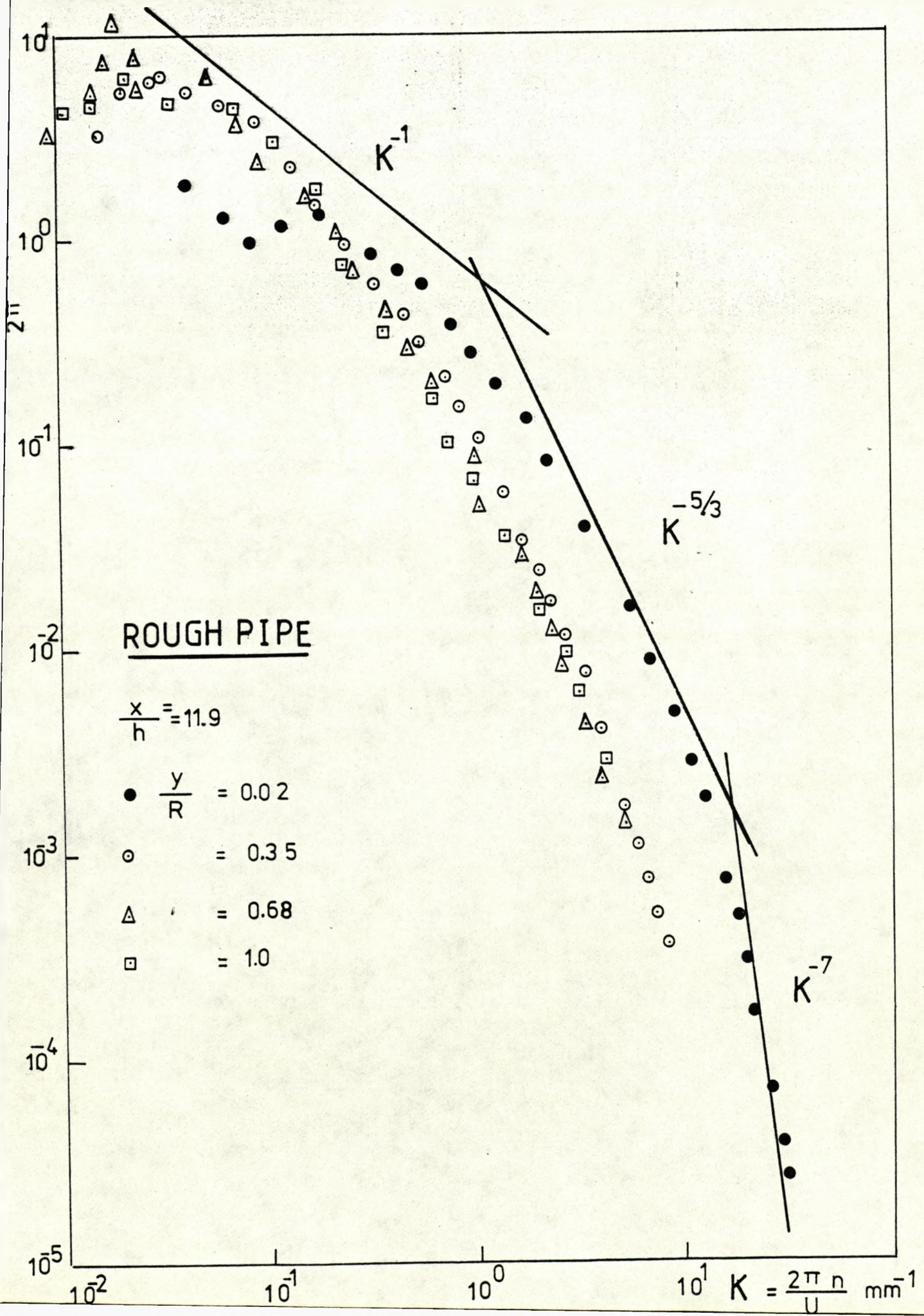

FREQUENCY SPECTRA OF $\overline{u^2}$ AT $\frac{x}{h}$ = 35.6 DOWNSTREAM OF RING IN ROUGH PIPE

FIG.(5.16b)

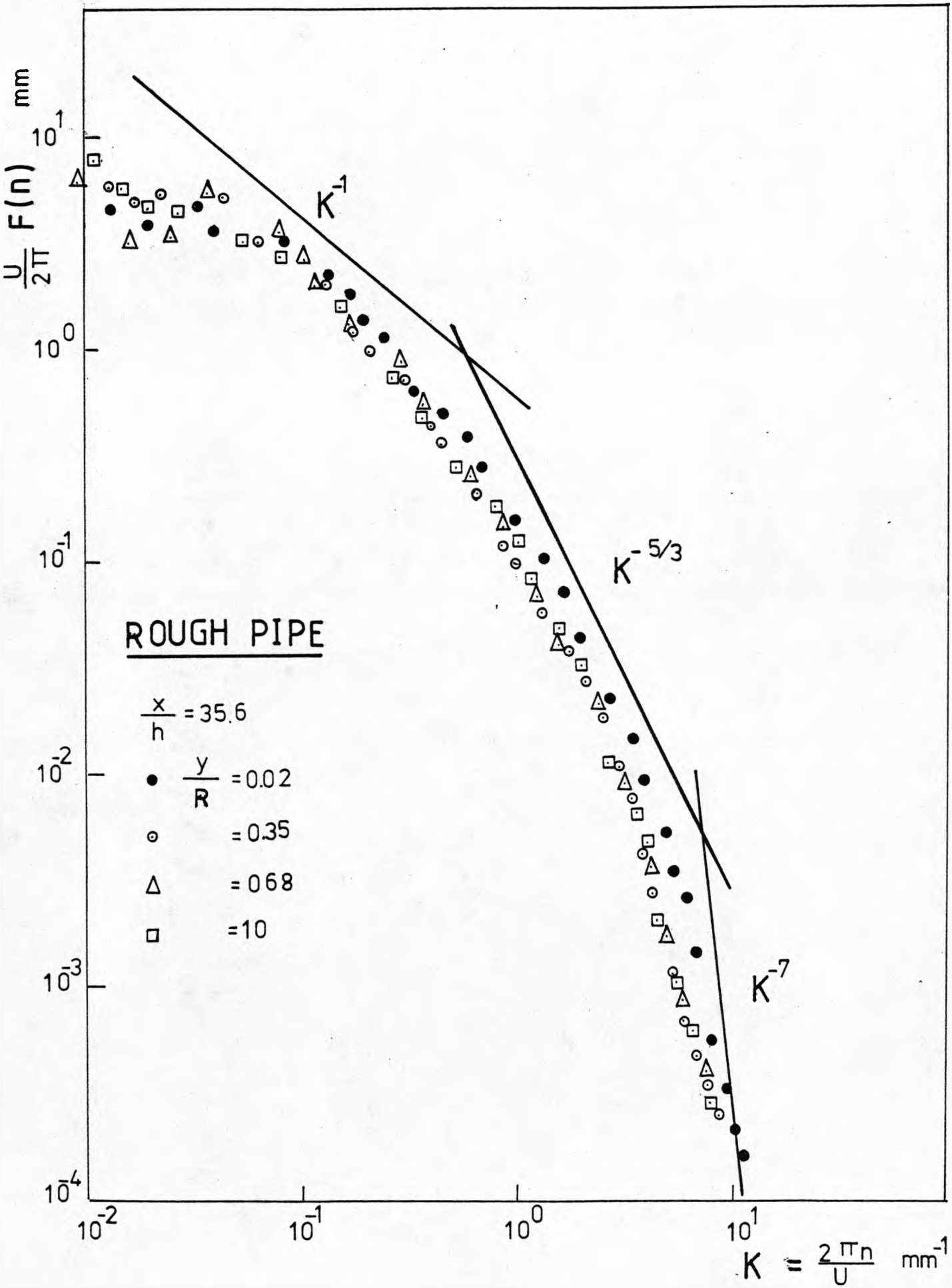

FREQUENCY SPECTRA OF $\overline{u^2}$ AT $\frac{x}{h}$ = 63.3 DOWNSTREAM OF RING IN ROUGH PIPE

FIG. (5.16c)

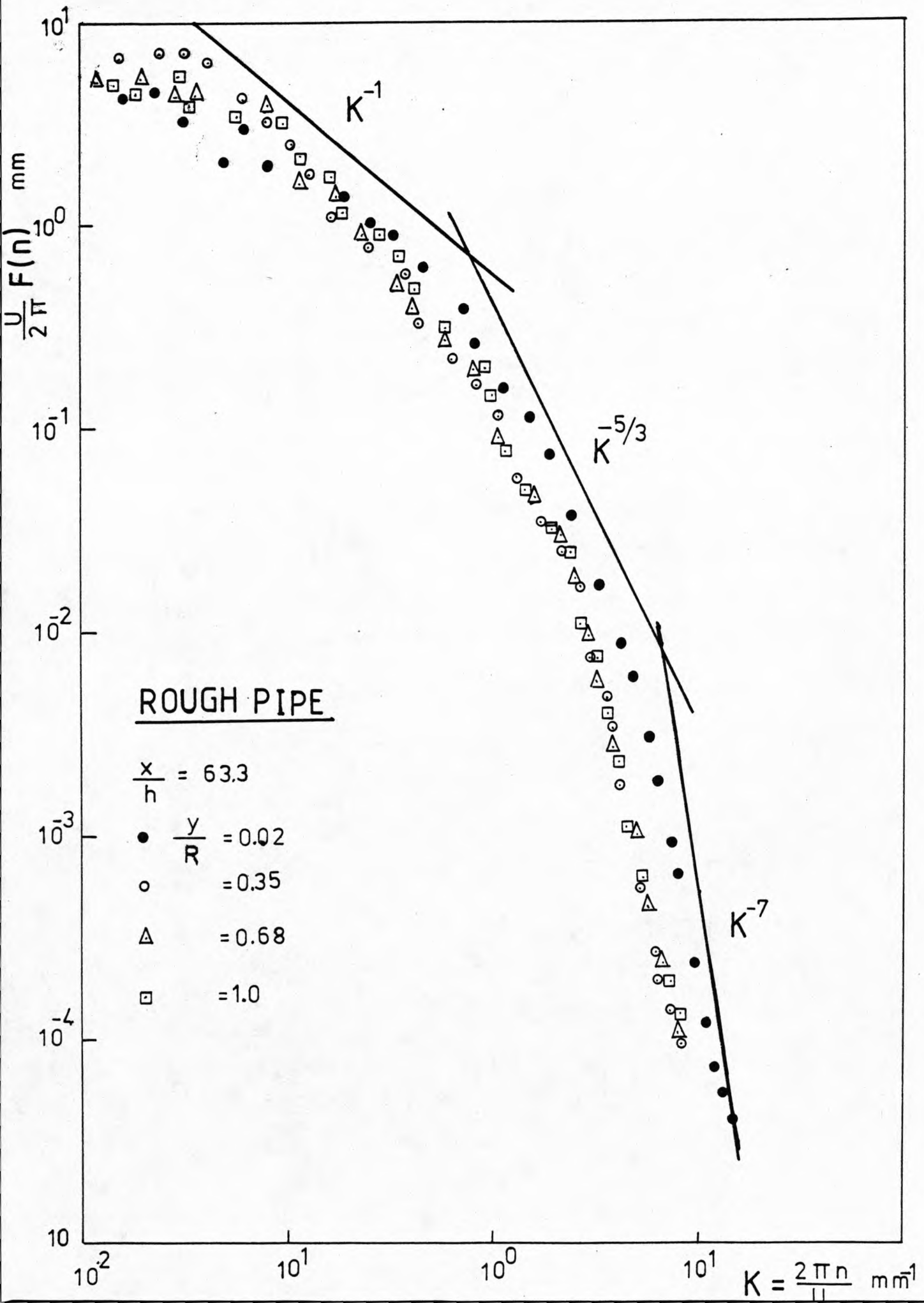

FREQUENCY SPECTRA OF $\overline{u^2}$ AT $\frac{x}{h}$ = 126.6 DOWNSTREAM OF RING IN ROUGH PIPE

FIG. (5.16d)

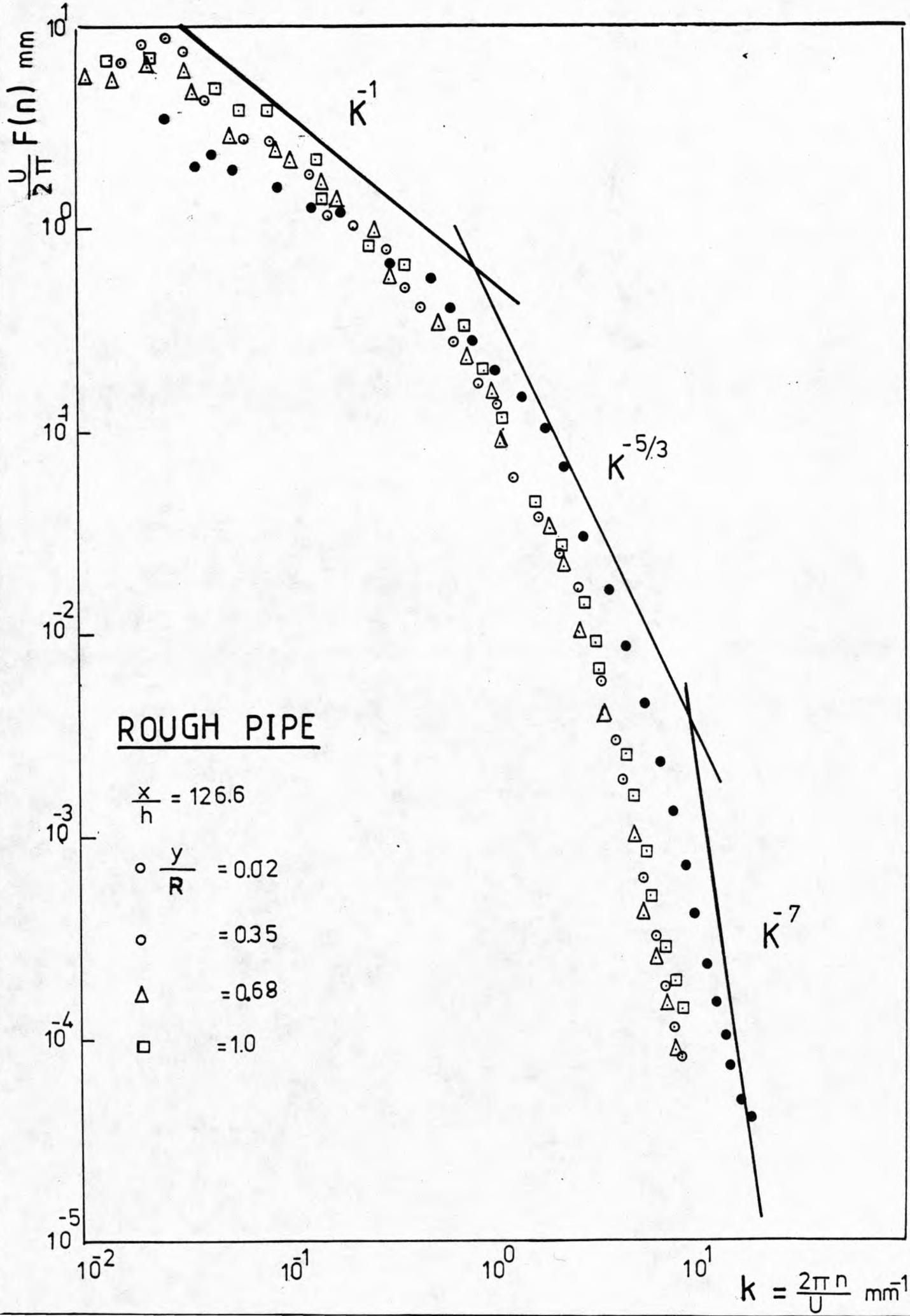

FREQUENCY SPECTRA OF $\overline{u^2}$ IN ROUGH PIPE WITHOUT RING

FIG.(5.16e)

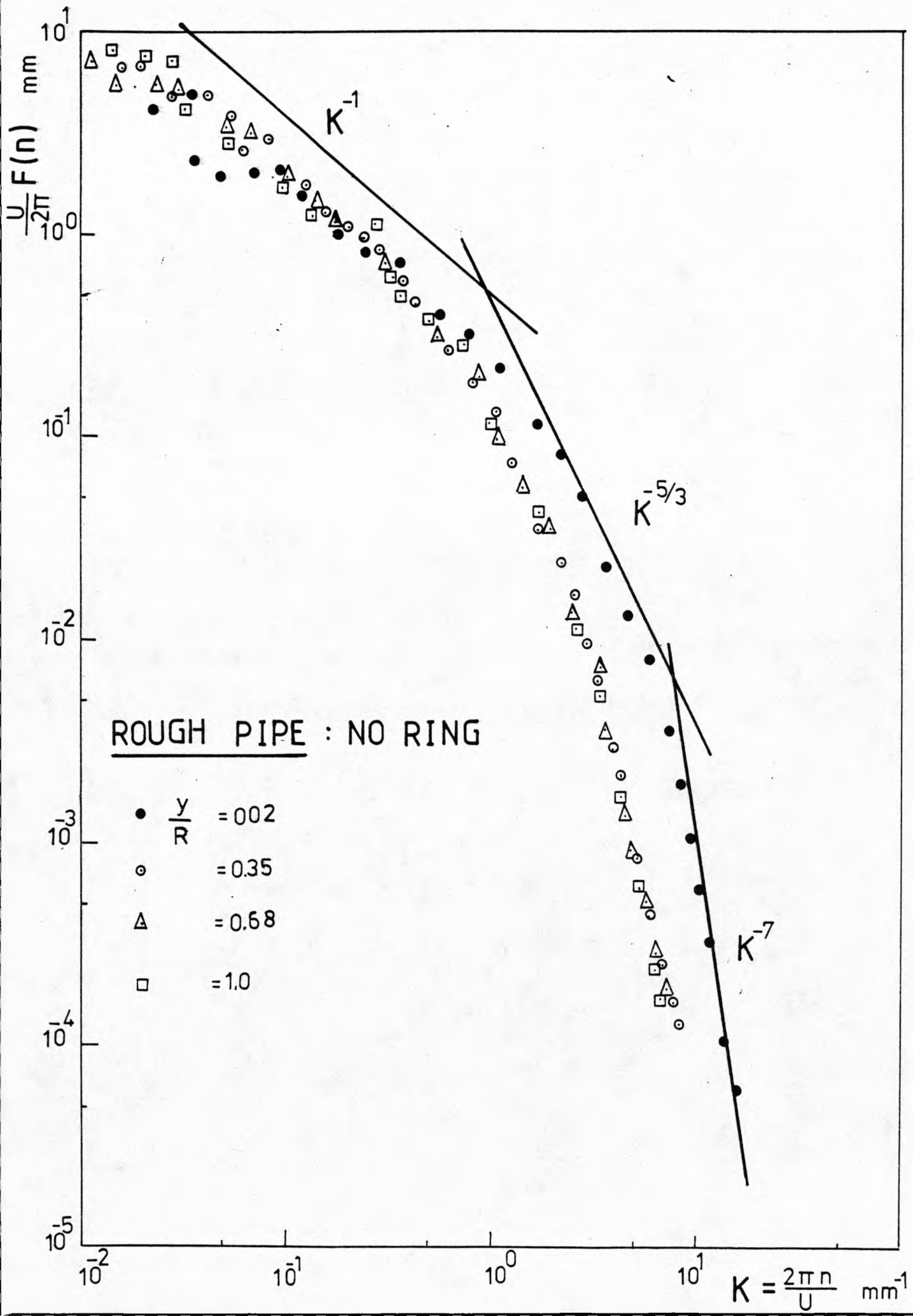

FREQUENCY SPECTRA OF $\overline{u^2}$ AT x/h = 11.9 DOWNSTREAM OF RING IN SMOOTH PIPE

FIG. (5.17a)

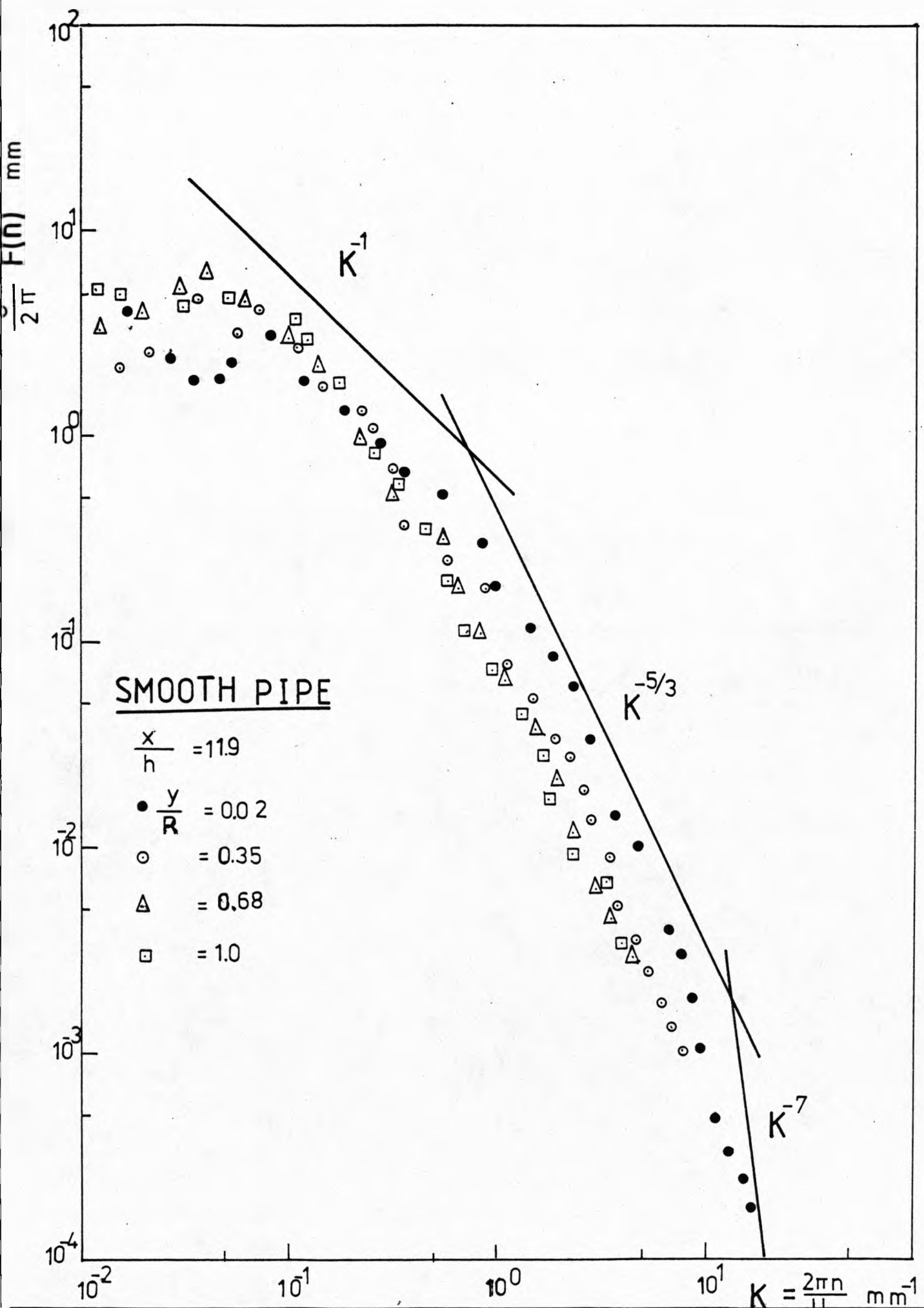

FIG.(5.17b)

FREQUENCY SPECTRA OF $\overline{u^2}$ AT x/h = 35.6 DOWNSTREAM OF RING IN SMOOTH PIPE

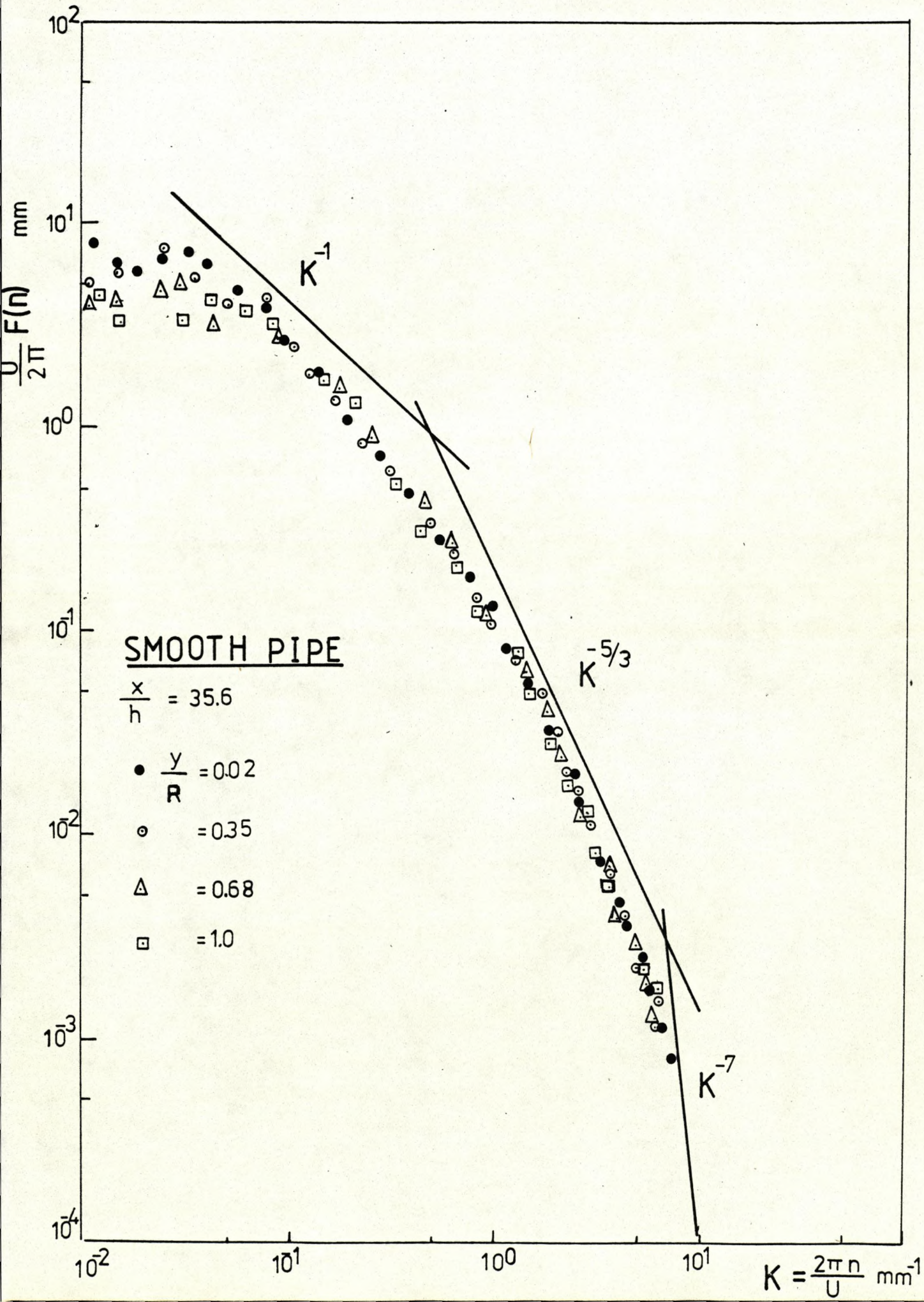

FREQUENCY SPECTRA OF $\overline{u^2}$ AT x/h = 63.3 DOWNSTREAM OF RING IN SMOOTH PIPE

FIG. (5.17c)

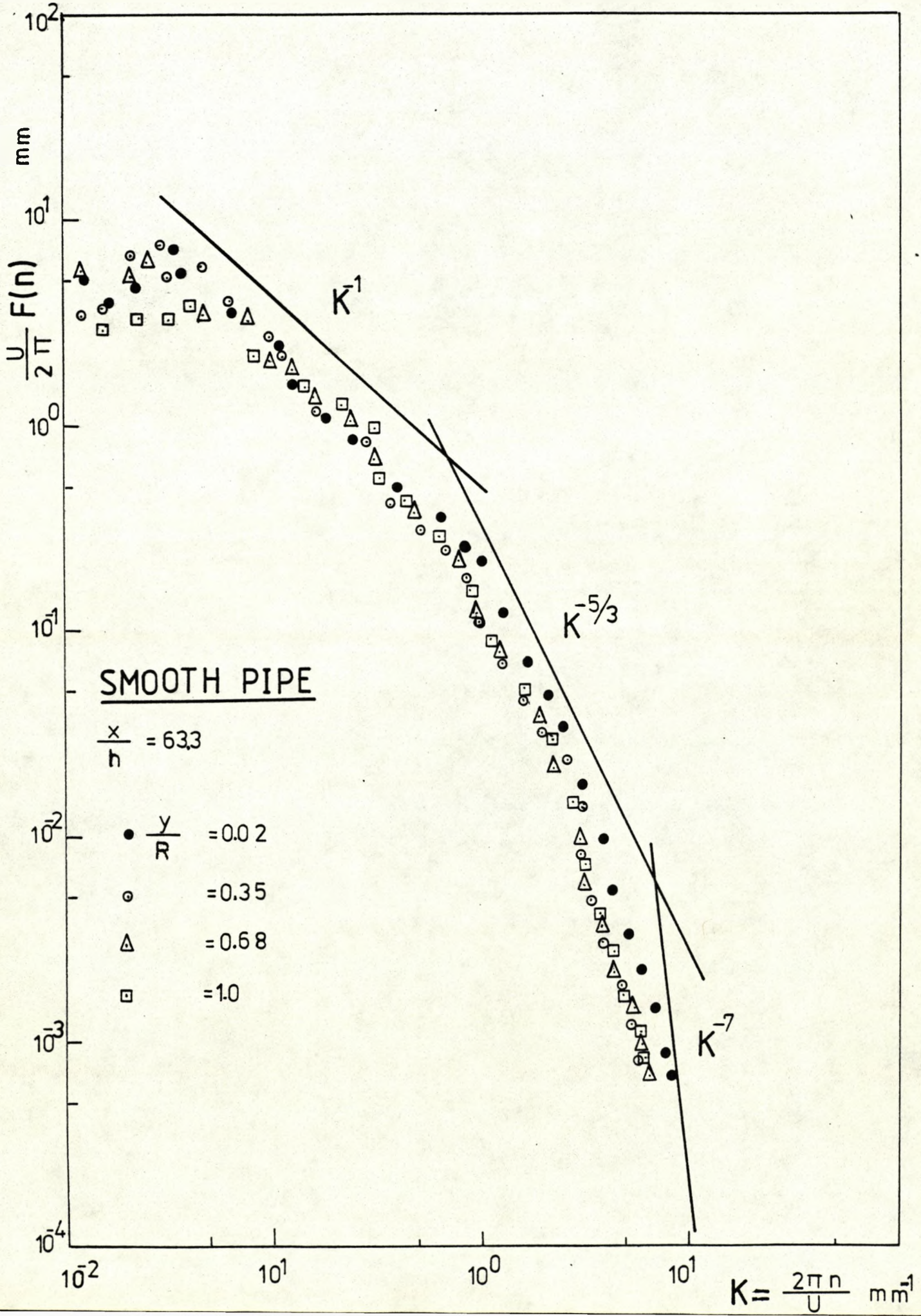

FIG.(5.17d)

FREQUENCY SPECTRA OF $\overline{u^2}$ AT x/h = 126.6 DOWNSTREAM OF RING IN SMOOTH PIPE

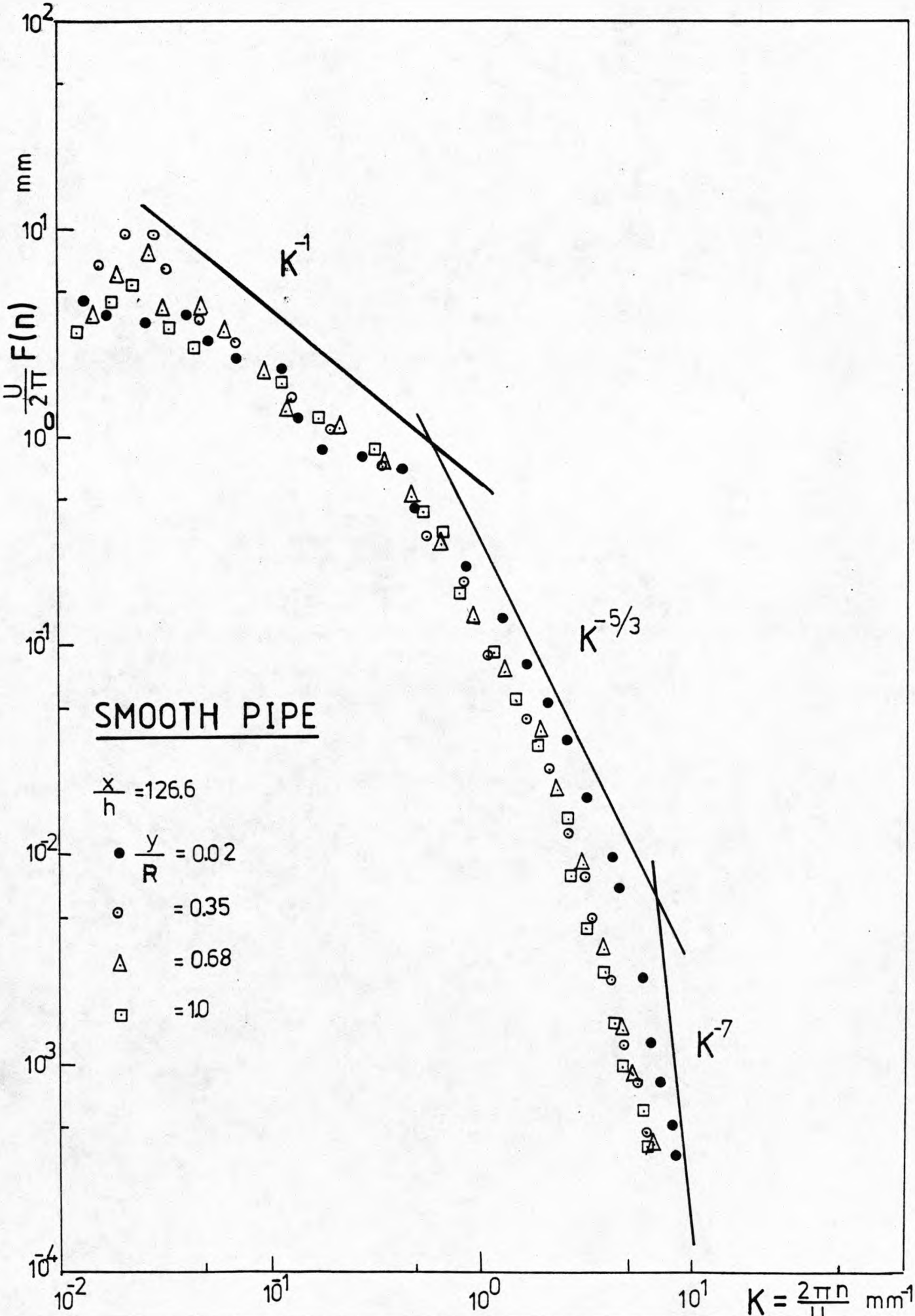

FIG.(5.17e)

FREQUENCY SPECTRA OF $\overline{u^2}$ FOR SMOOTH PIPE WITHOUT RING

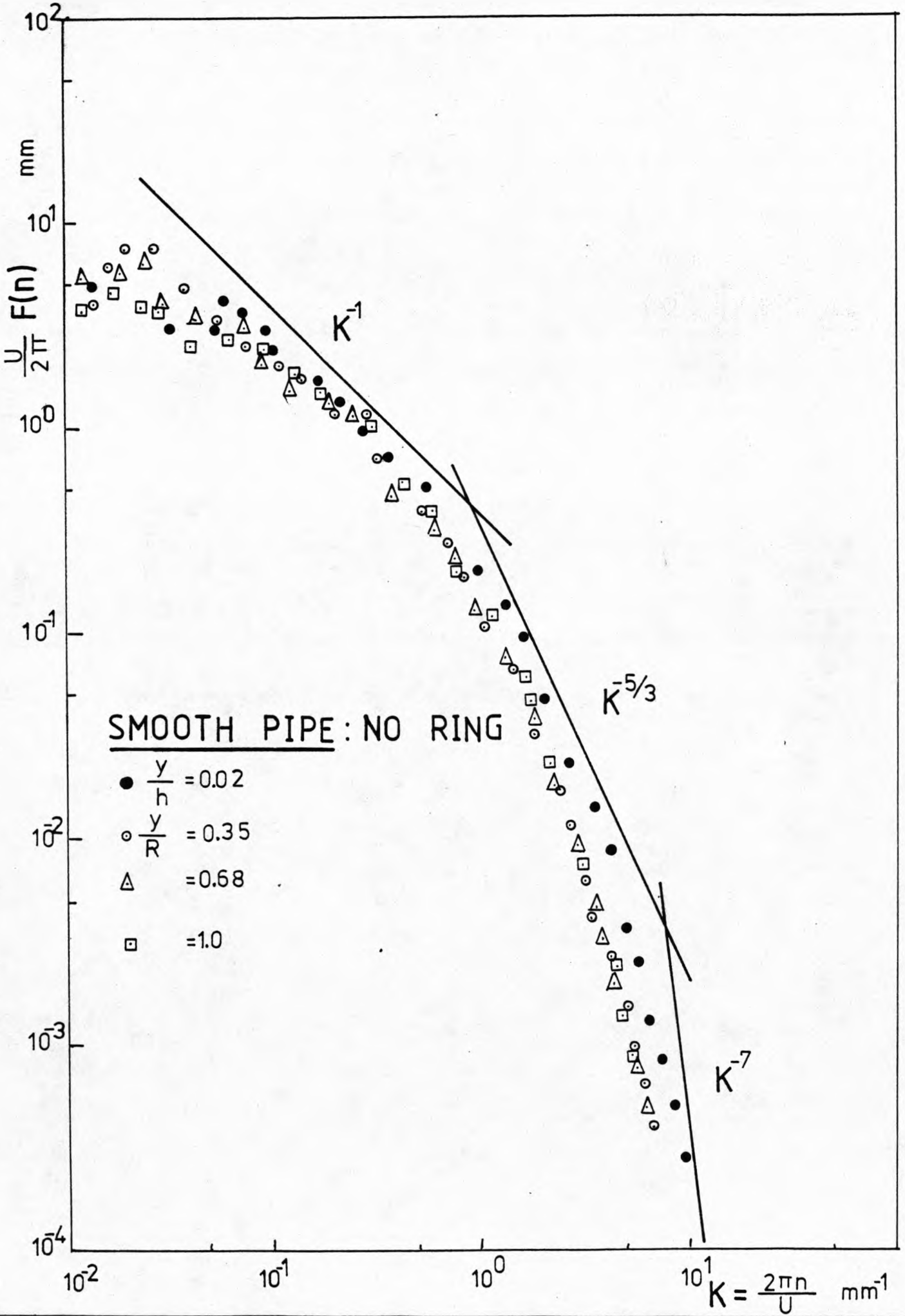

SECOND MOMENTS OF FREQUENCY SPECTRA OF $\overline{u^2}$ AT x/h = 11.9 DOWNSTREAM OF RING IN SMOOTH AND ROUGH PIPES

FIG.(5 1.8a)

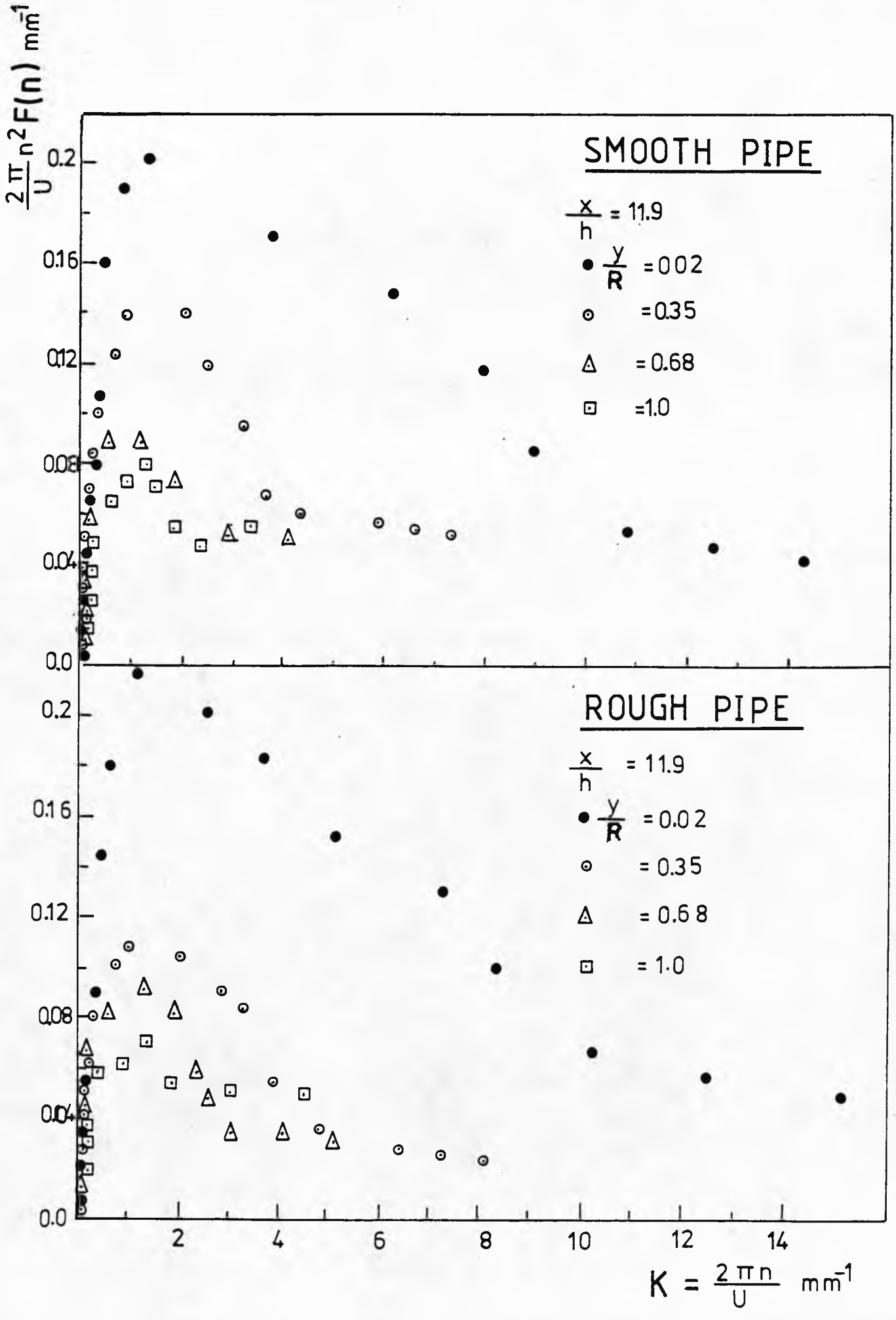

FIG.(5.18b)

SECOND MOMENTS OF FREQUENCY SPECTRA OF $\overline{u^2}$ AT $x/h = 35.6$ DOWNSTREAM OF RING IN SMOOTH AND ROUGH PIPES

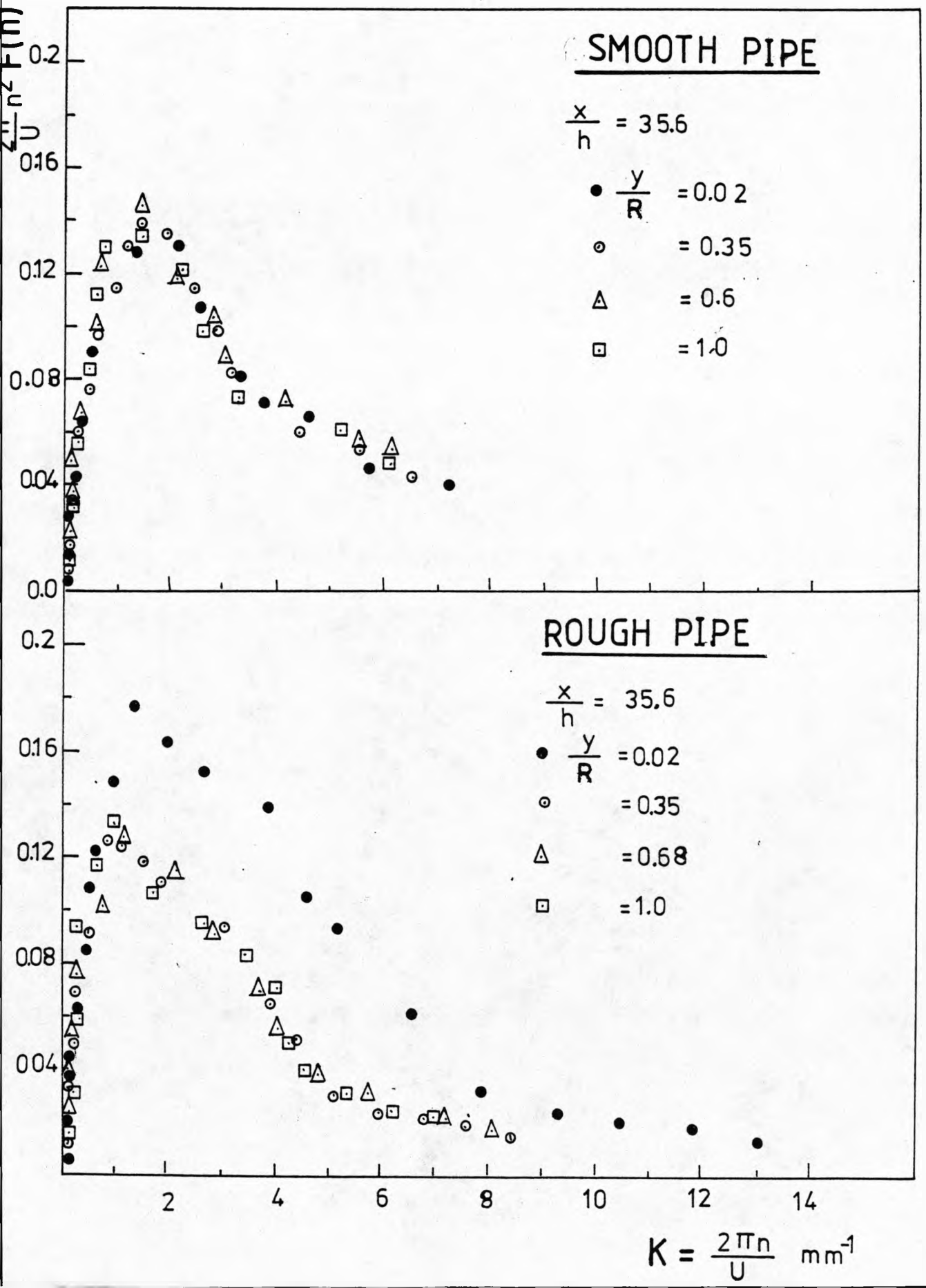

FIG.(5.18c)

SECOND MOMENTS OF FREQUENCY SPECTRA OF $\overline{u^2}$ AT x/h = 63.3 DOWNSTREAM OF RING IN SMOOTH AND ROUGH PIPES

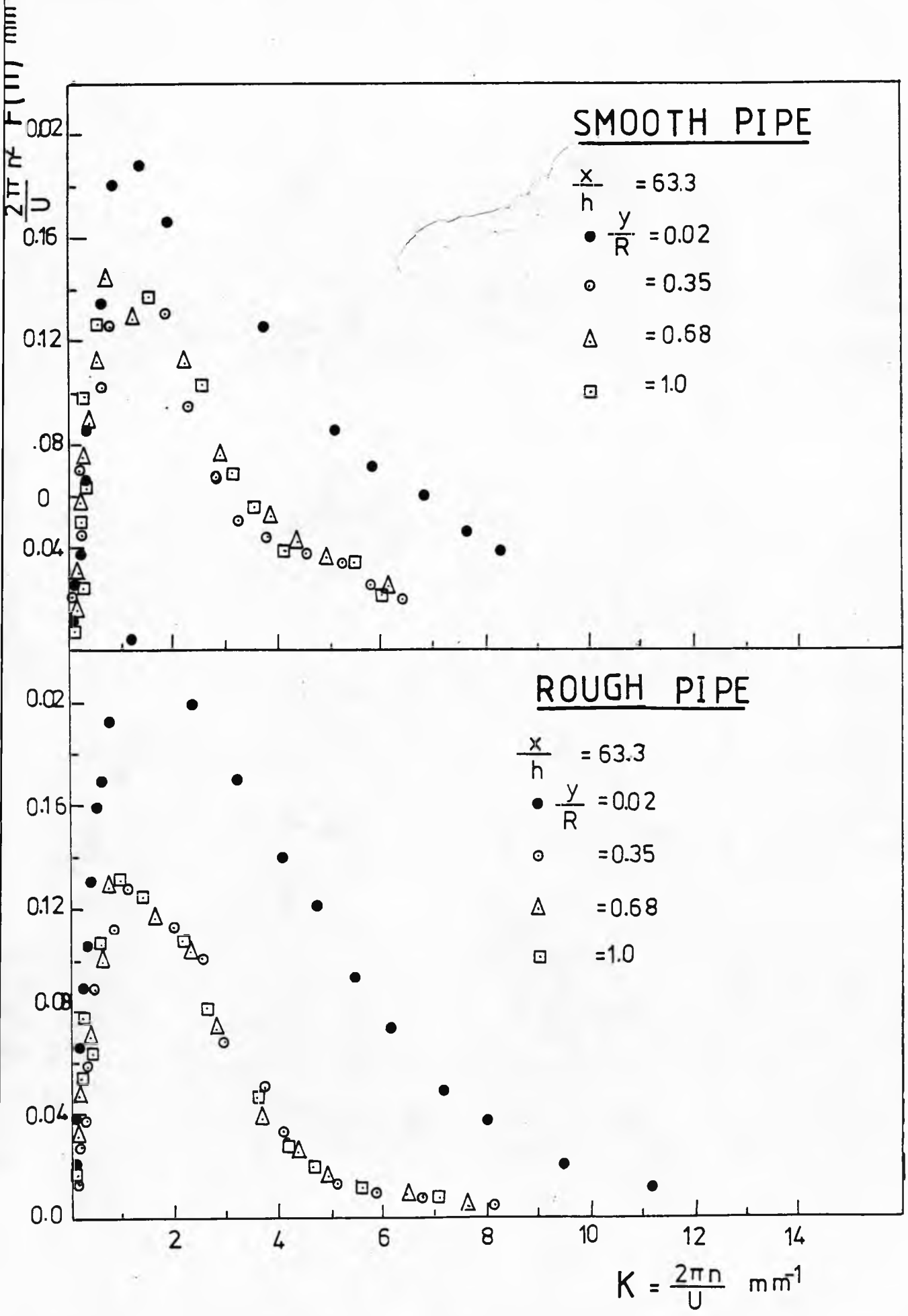

FIG. (5.18d)

SECOND MOMENTS OF FREQUENCY SPECTRA OF $\overline{u^2}$ AT x/h = 126.6 DOWNSTREAM OF RING IN SMOOTH AND ROUGH PIPES

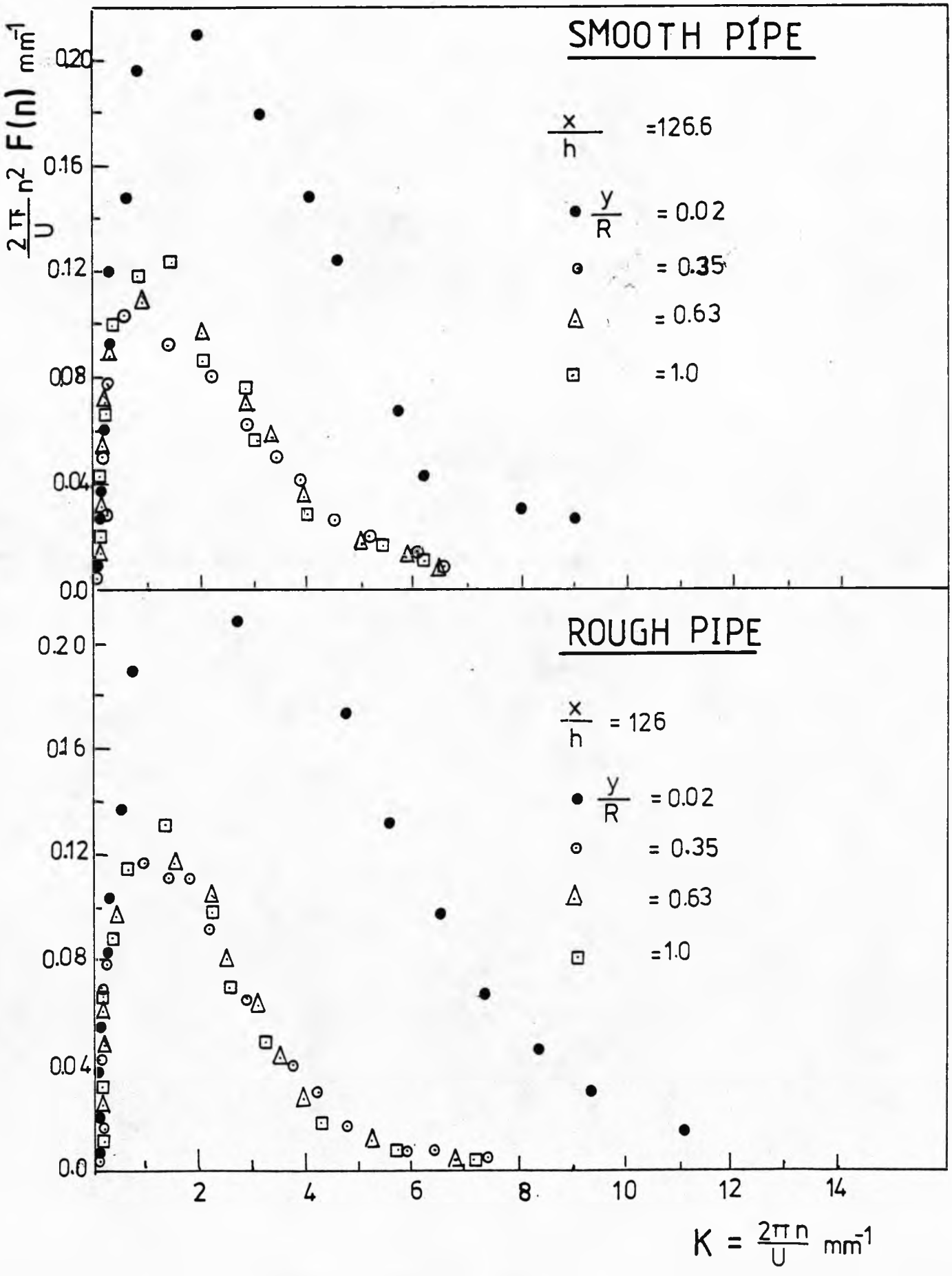

FIG.(5.18e)

SECOND MOMENTS OF FREQUENCY SPECTRA OF $\overline{u^2}$ FOR SMOOTH AND ROUGH PIPES WITHOUT RING

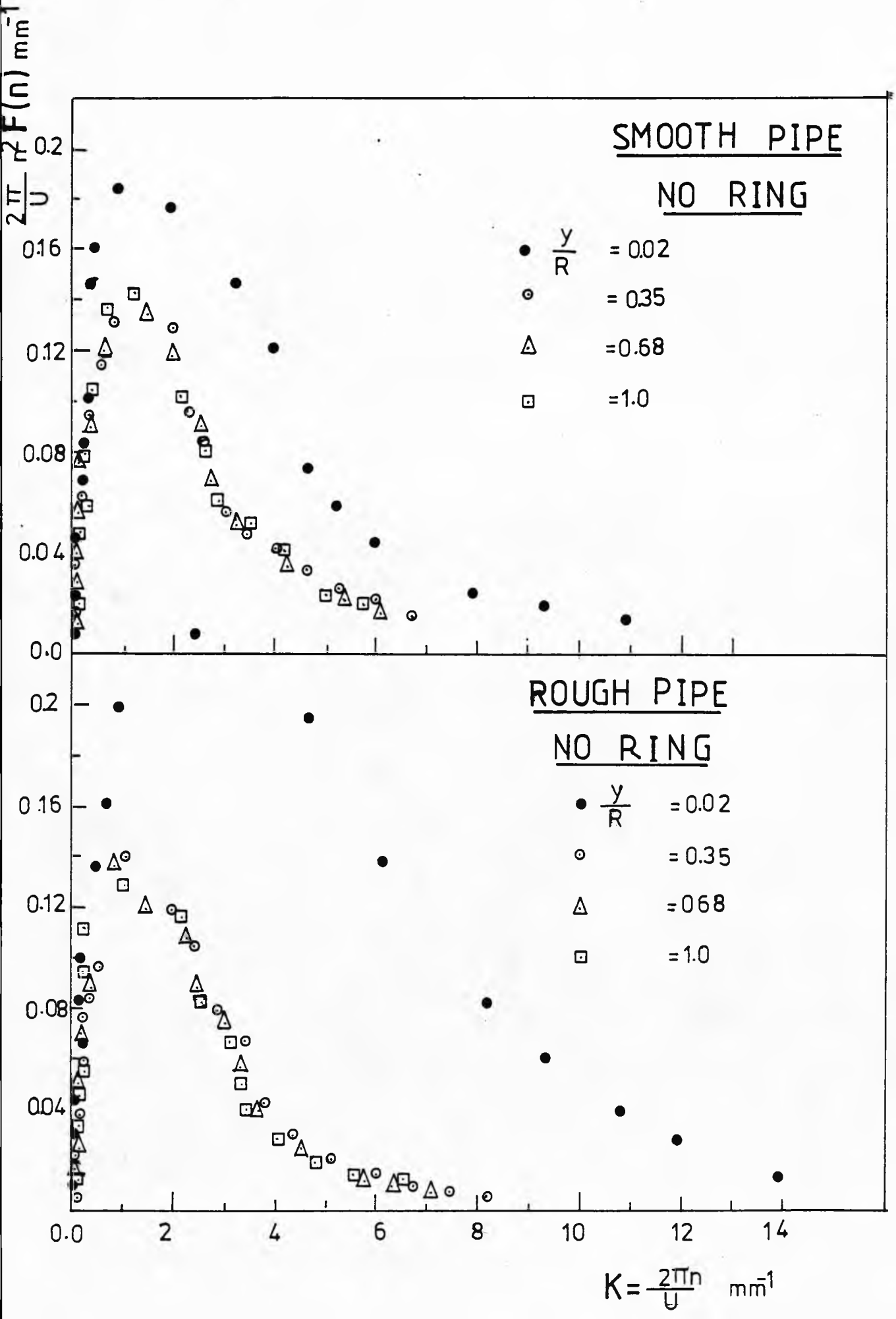

LONGITUDINAL SPATIAL CORRELATION COEFFICIENT AT
x/h = 11.9 DOWNSTREAM OF RING IN ROUGH AND SMOOTH PIPES

FIG.(5.19a)

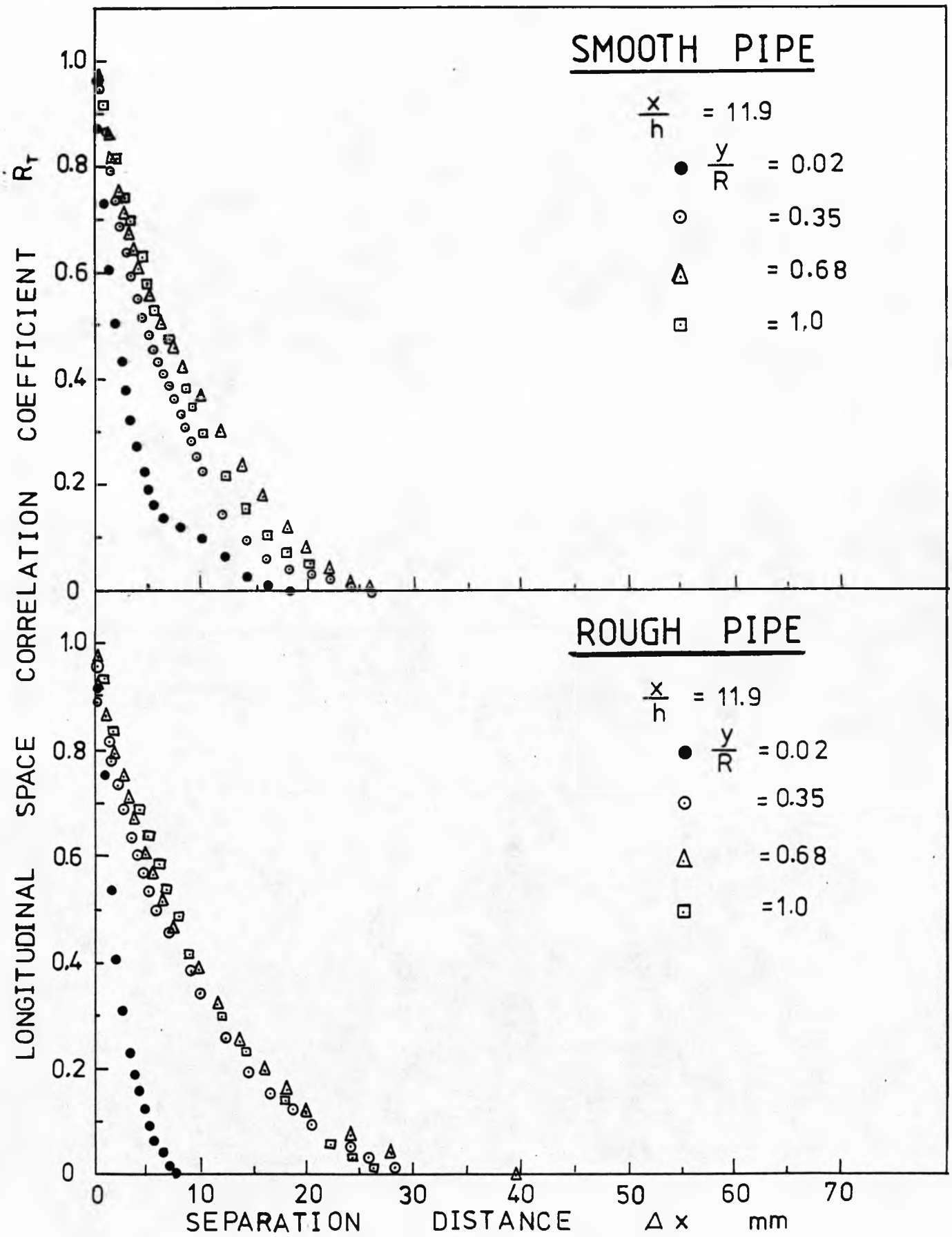

FIG.(5.19b)

LONGITUDINAL SPATIAL CORRELATION COEFFICIENT AT
x/h = 35.6 DOWNSTREAM OF RING IN ROUGH AND SMOOTH PIPES

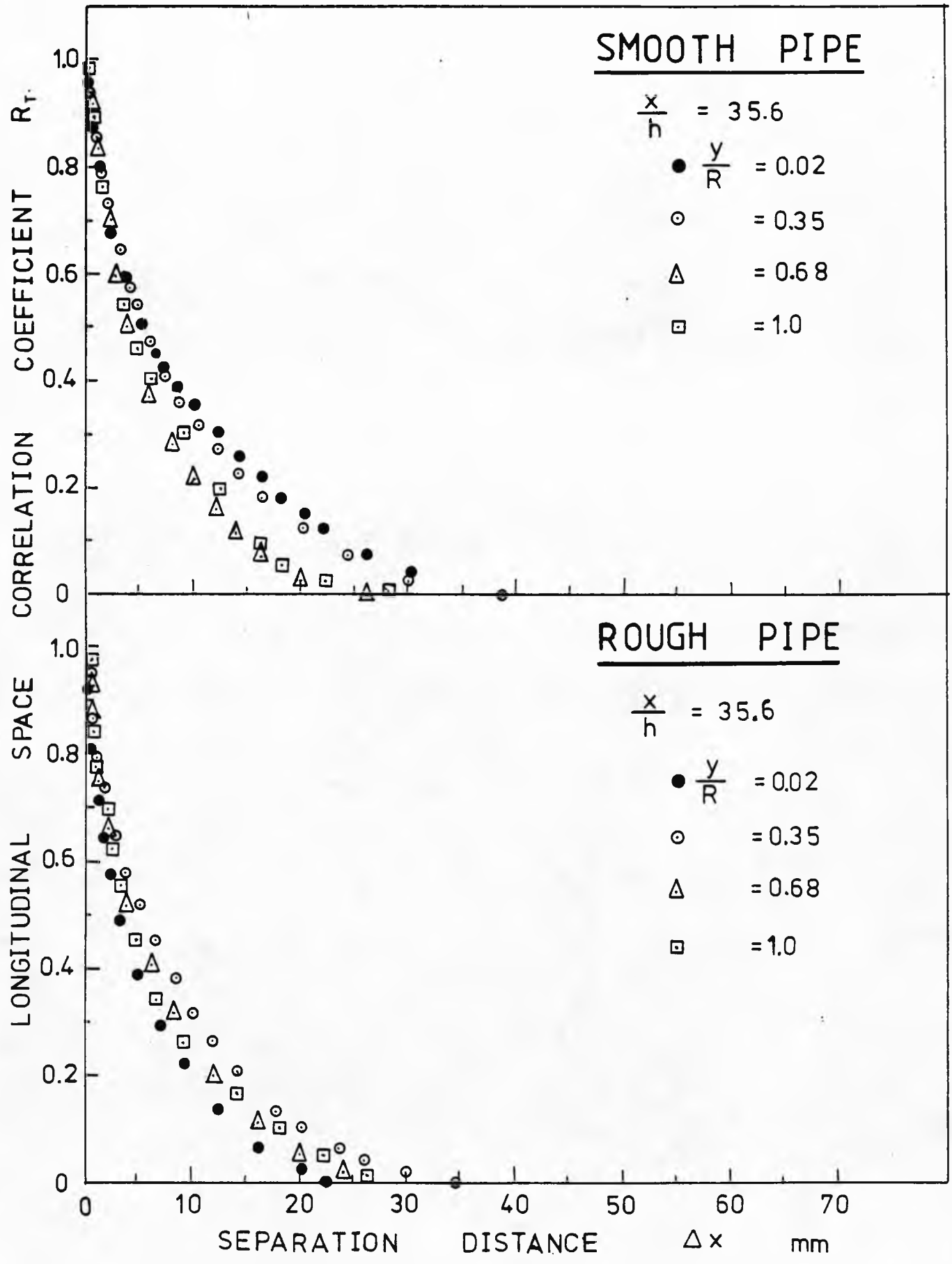

FIG.(5.19c)

LONGITUDINAL SPATIAL CORRELATION COEFFICIENT AT
x/h = 63.3 DOWNSTREAM OF RING AND ROUGH AND SMOOTH PIPES

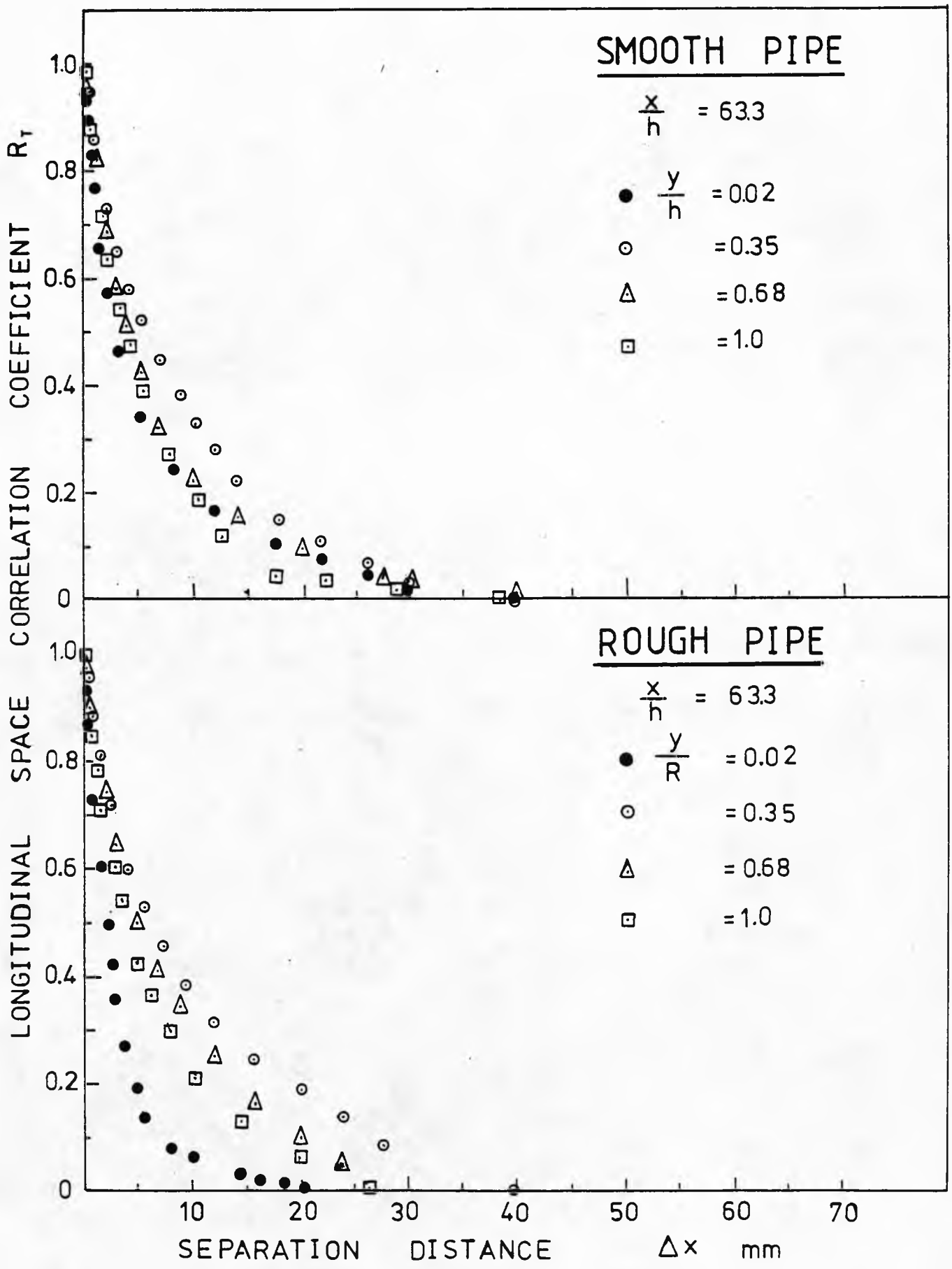

FIG.(5.19d)

LONGITUDINAL SPATIAL CORRELATION COEFFICIENT AT
x/h = 126.6 DOWNSTREAM OF RING IN ROUGH AND SMOOTH PIPES

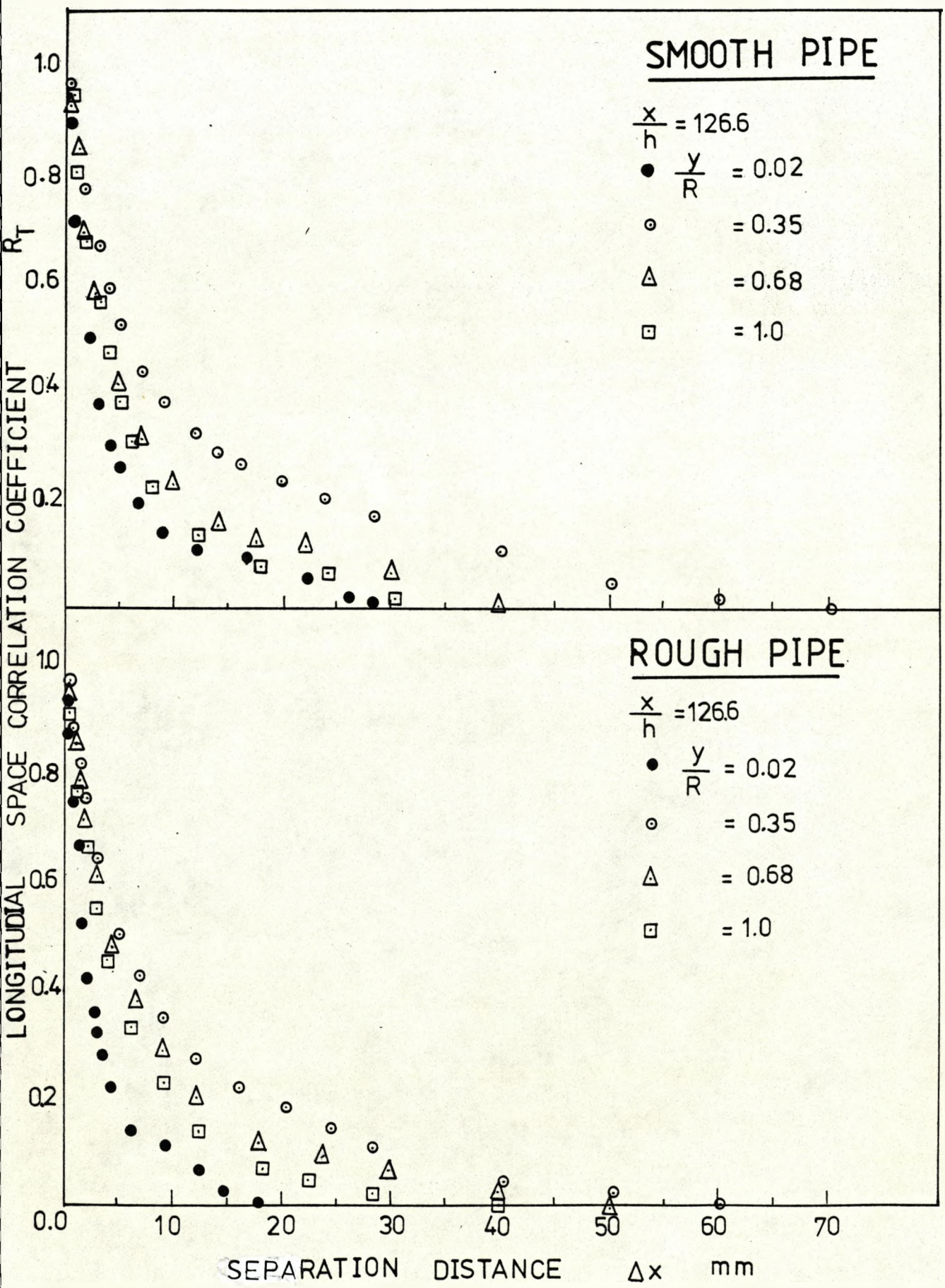

LONGITUDINAL SPATIAL CORRELATION COEFFICIENT IN ROUGH AND SMOOTH PIPES WITHOUT RING

FIG.(5.19e)

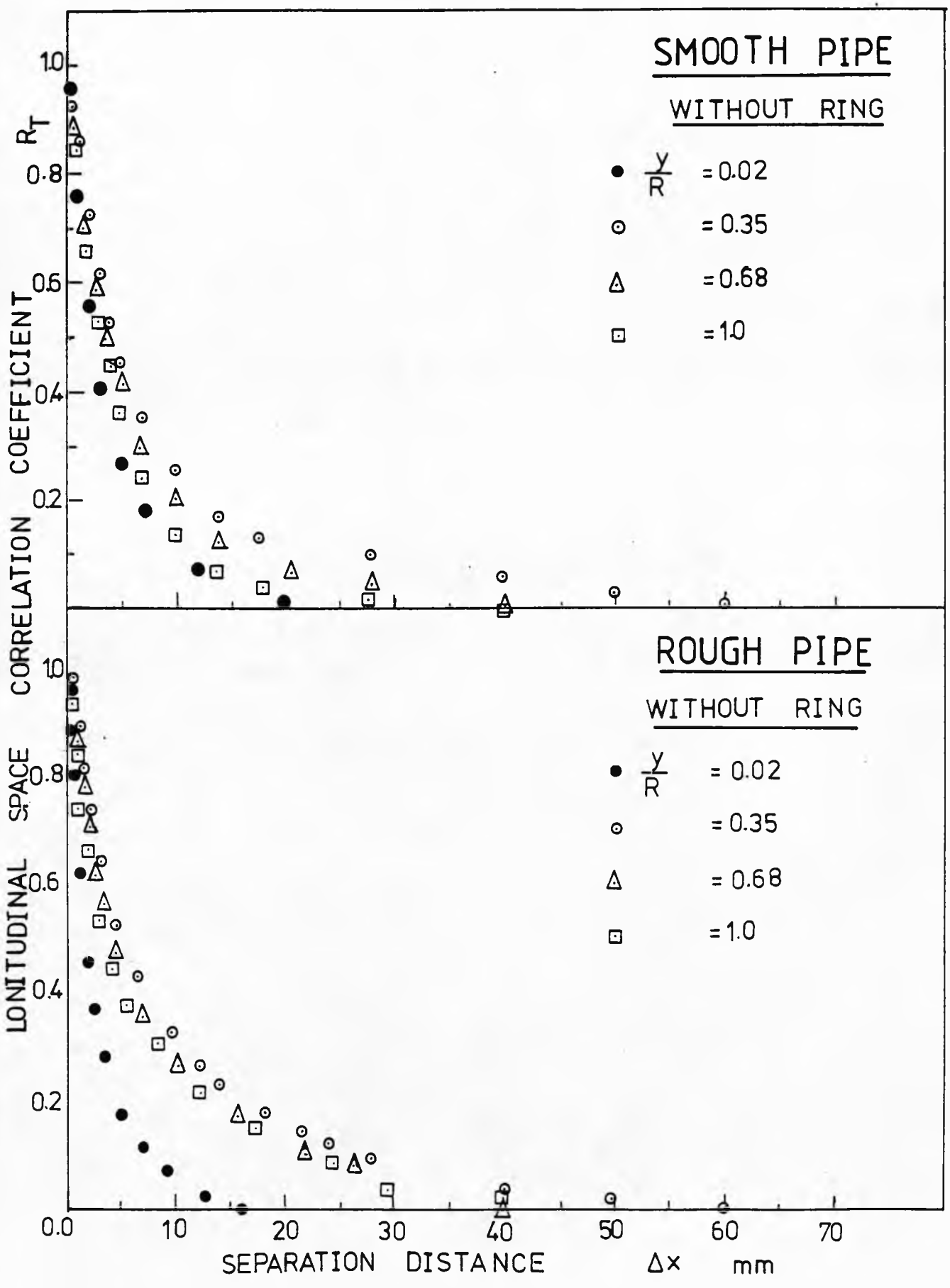

FIG:(5.20a)

MICRO-SCALE OF TURBULENCE DOWNSTREAM OF RING IN ROUGH AND SMOOTH PIPES

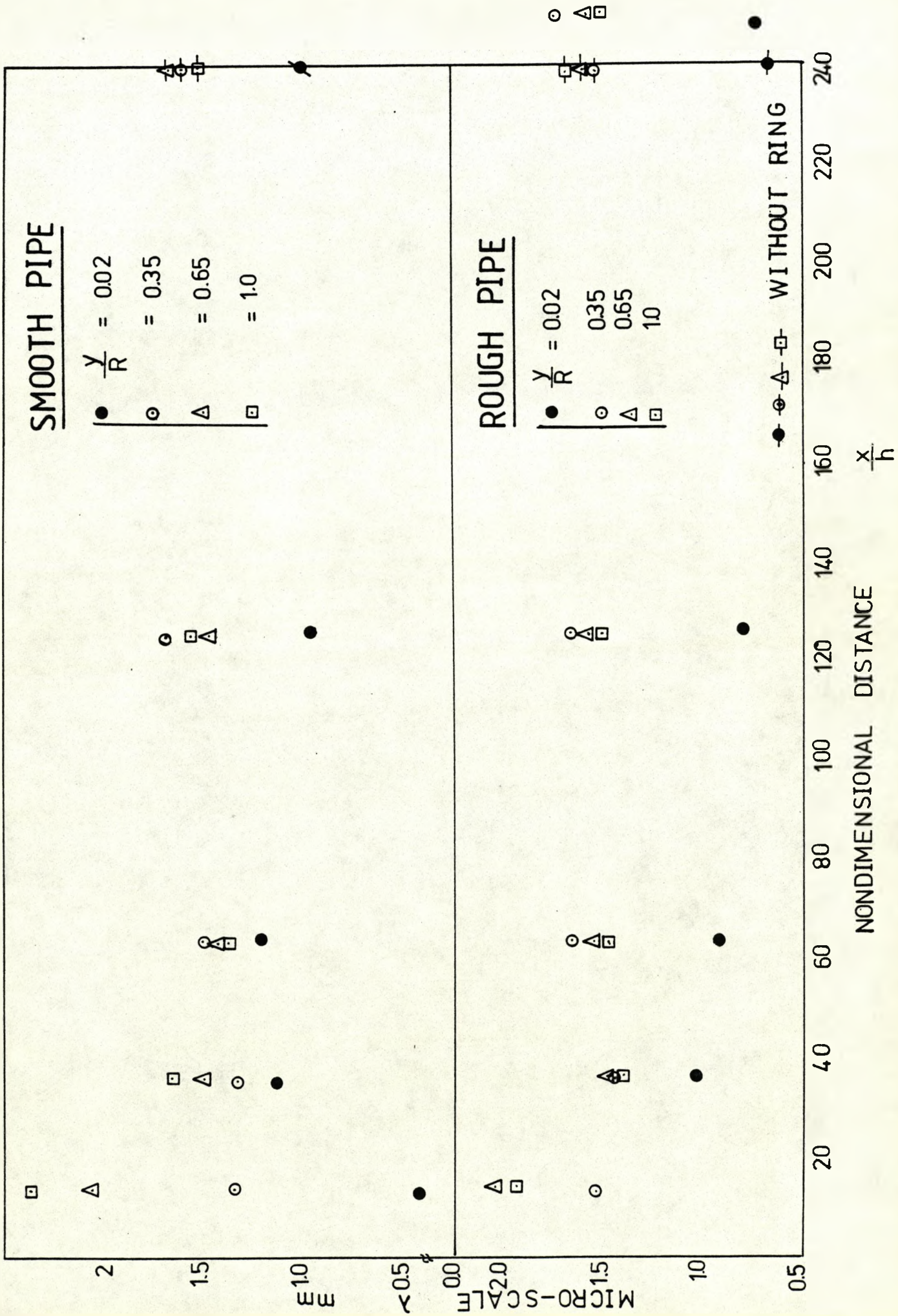

FIG.(5.20b)

MACRO-SCALE OF TURBULENCE DOWNSTREAM OF RING IN ROUGH AND SMOOTH PIPES

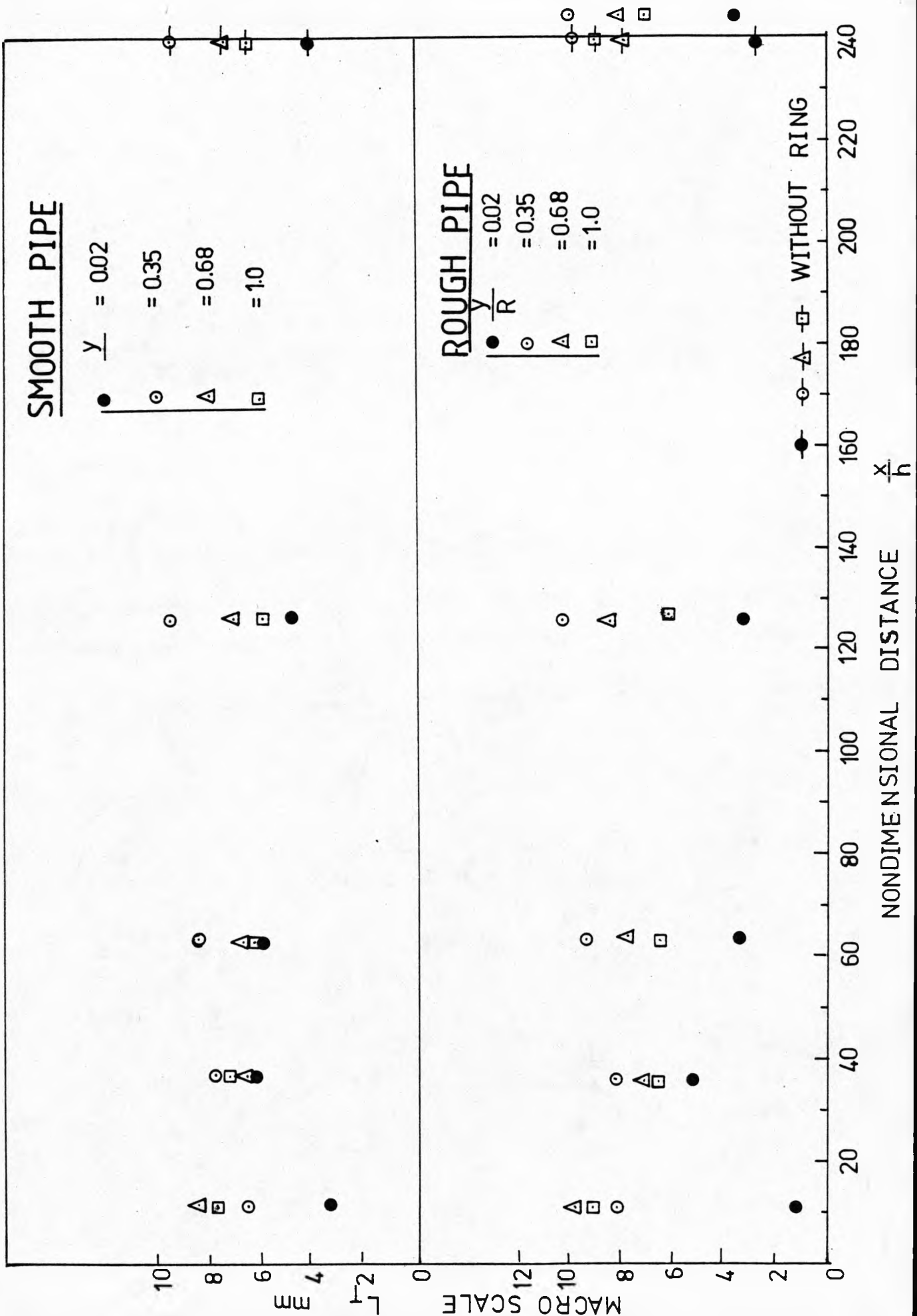

TURBULENT EDDY VISCOSITY DOWNSTREAM OF RING IN ROUGH AND SMOOTH PIPES

FIG.(5.21a)

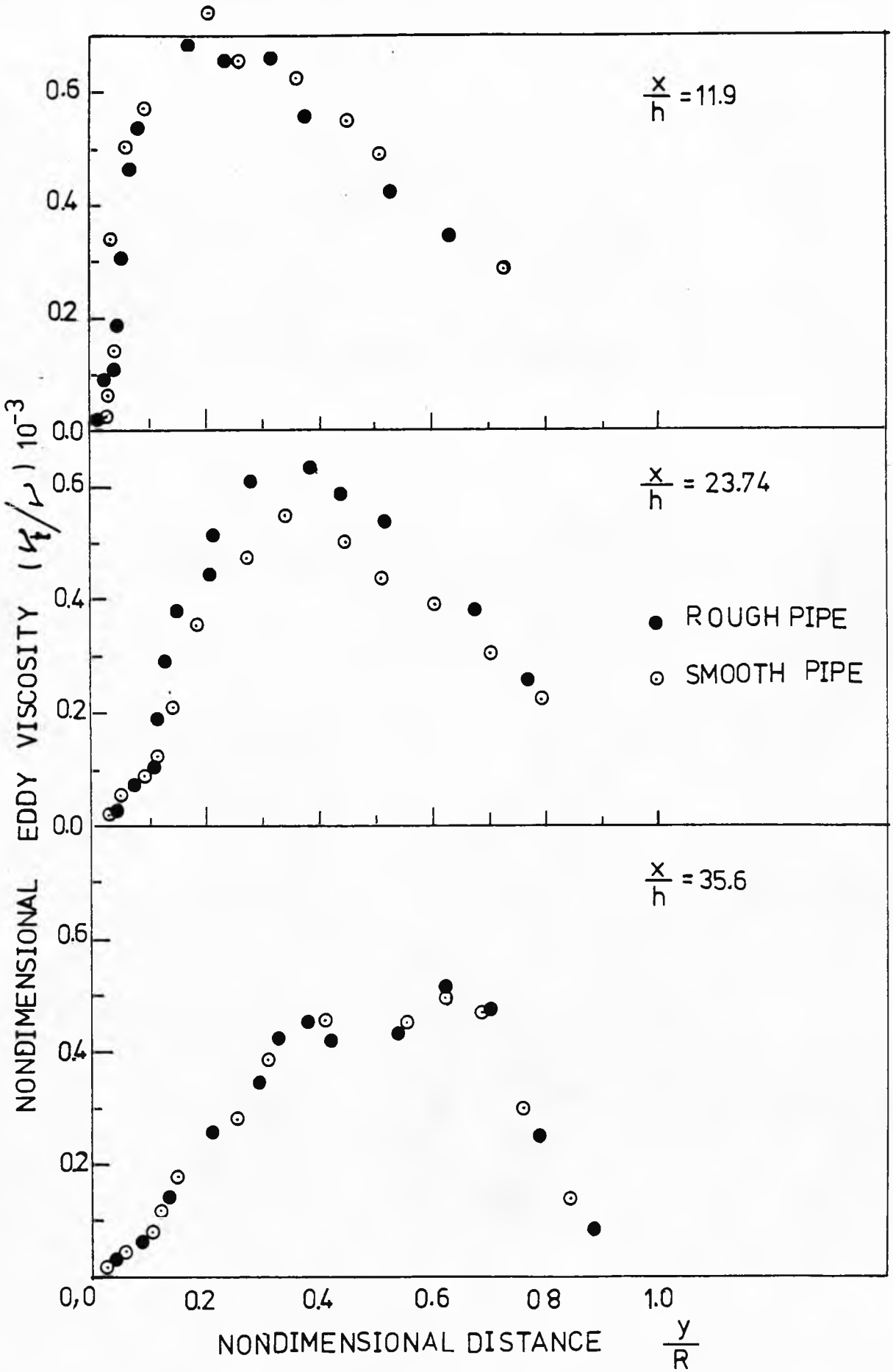

TURBULENT EDDY VISCOSITY DOWNSTREAM OF RING
IN ROUGH AND SMOOTH PIPES

FIG.(5.21b)

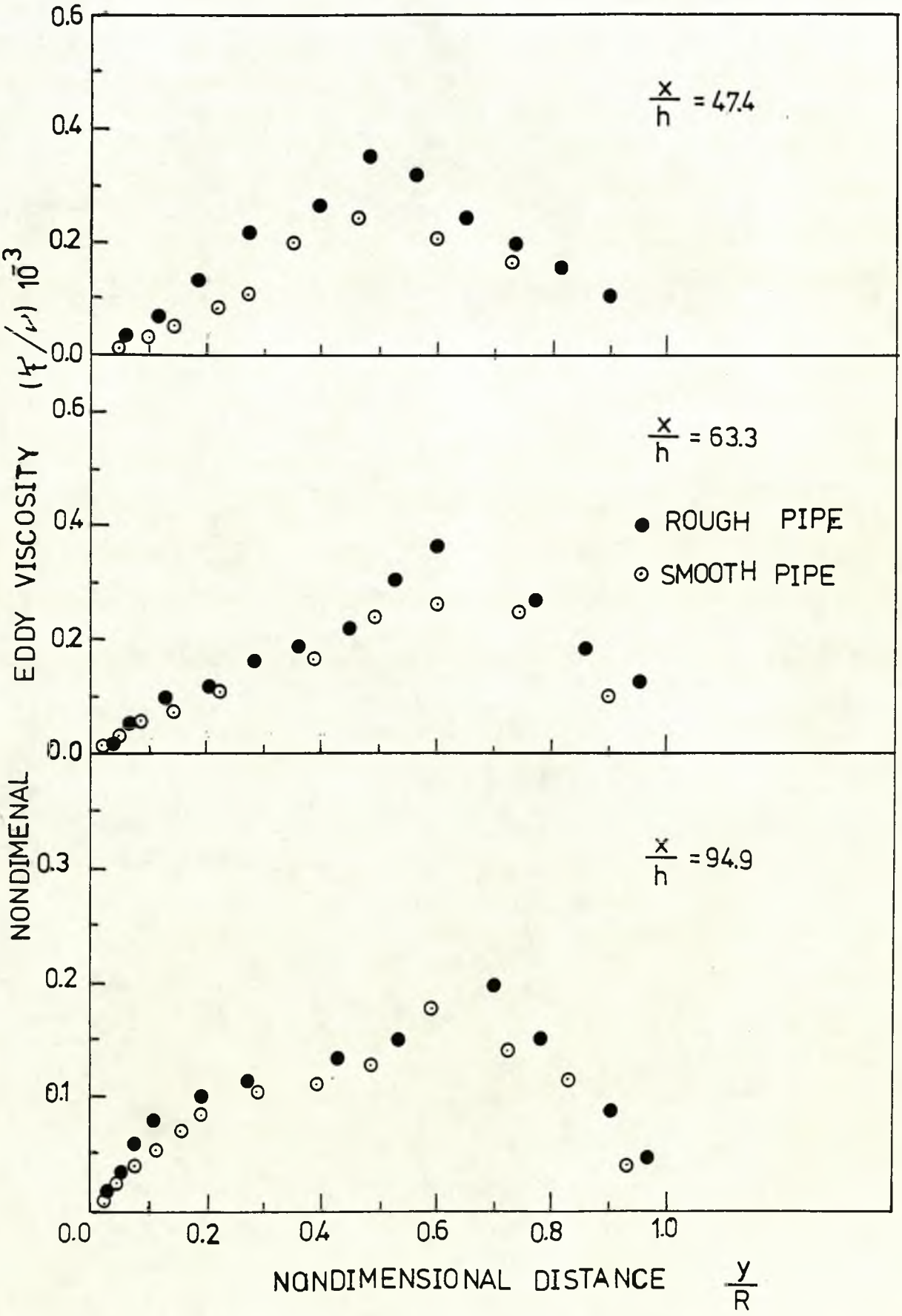

TURBULENT EDDY VISCOSITY DOWNSTREAM OF RING IN ROUGH AND SMOOTH PIPES

FIG.(5.21c)

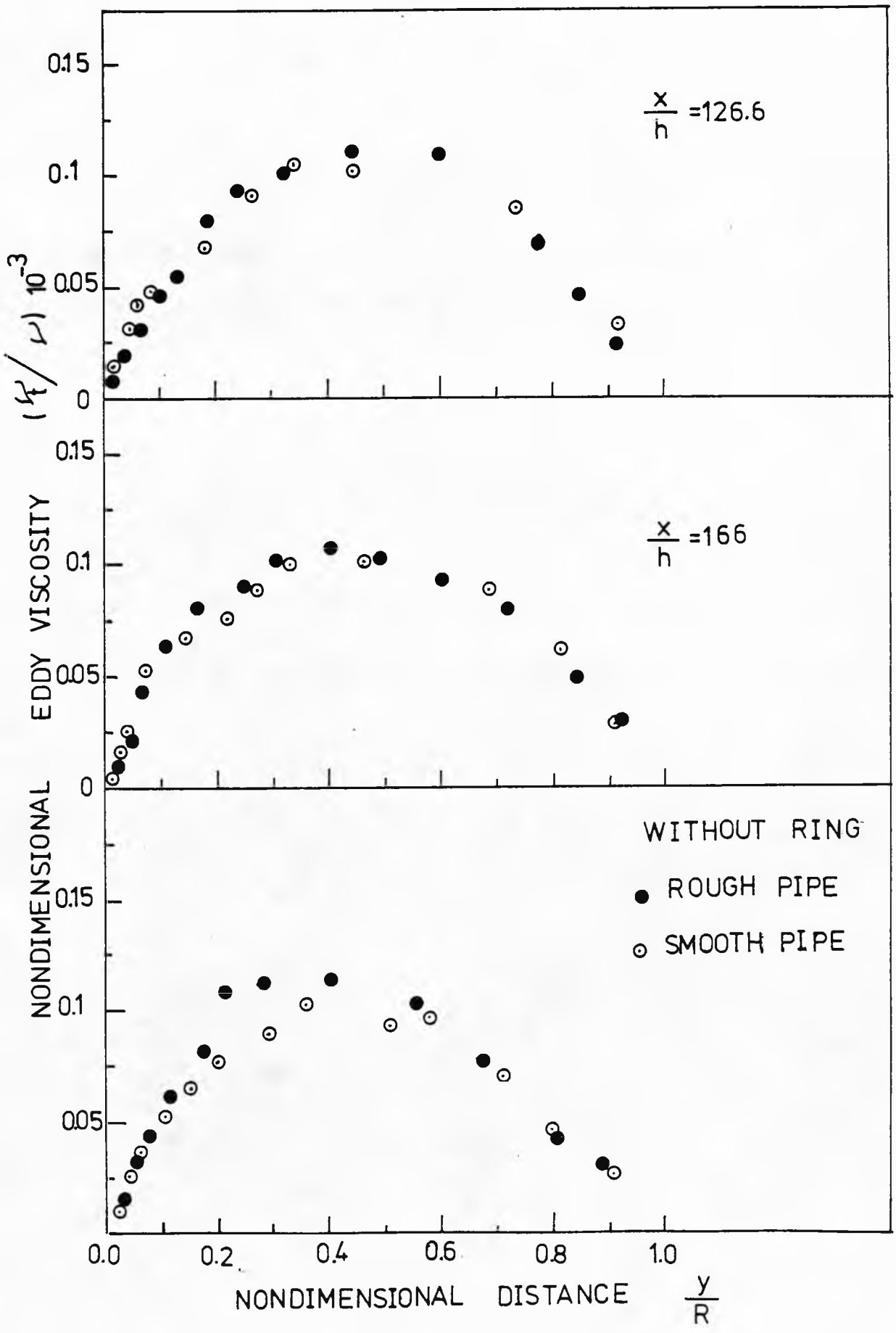

FIG.(5.22a)

MIXING LENGTH DISTRIBUTIONS DOWNSTREAM OF RING IN ROUGH AND SMOOTH PIPES

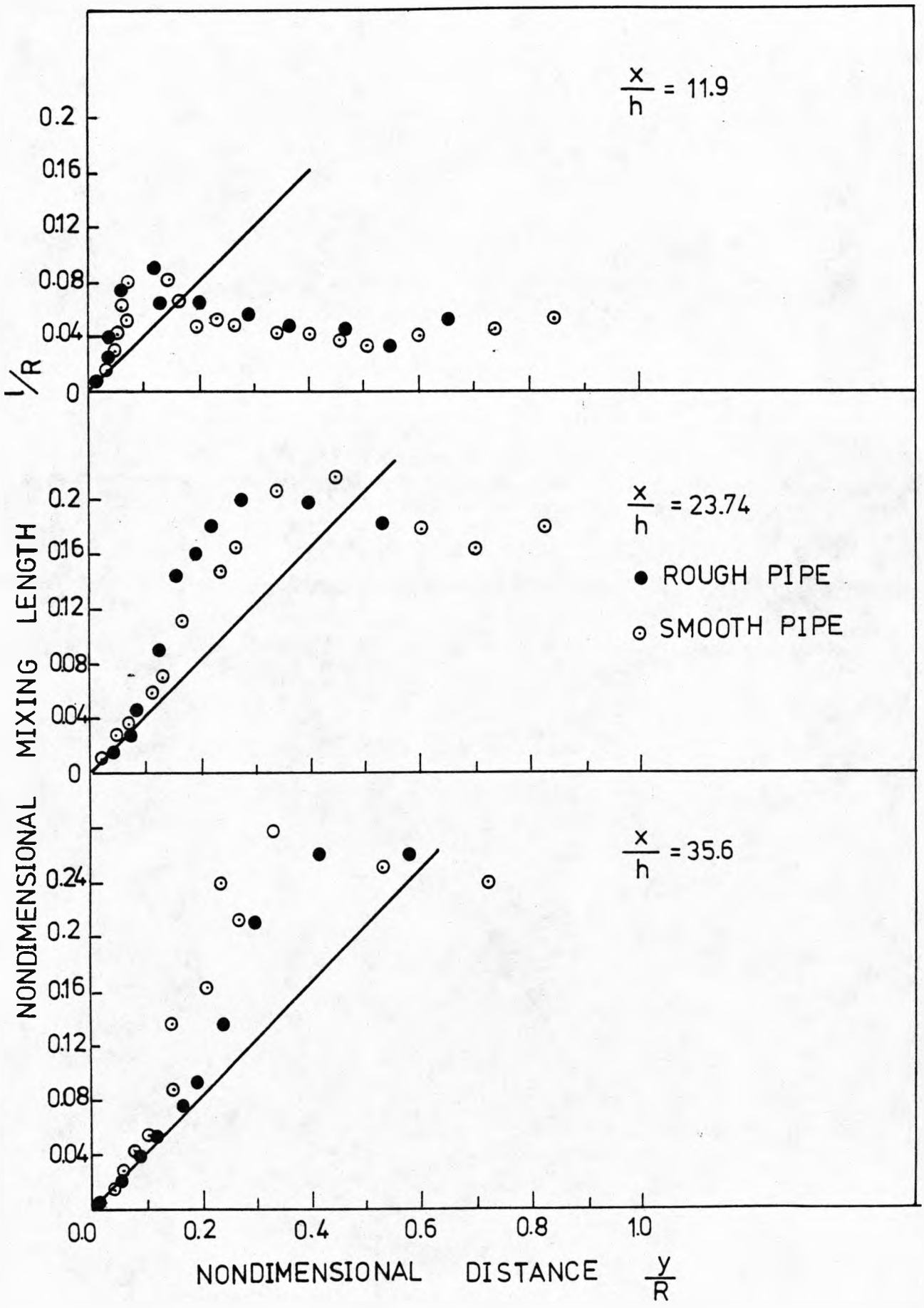

MIXING LENGTH DISTRIBUTIONS DOWNSTREAM OF RING IN ROUGH AND SMOOTH PIPES

FIG.(5.22b)

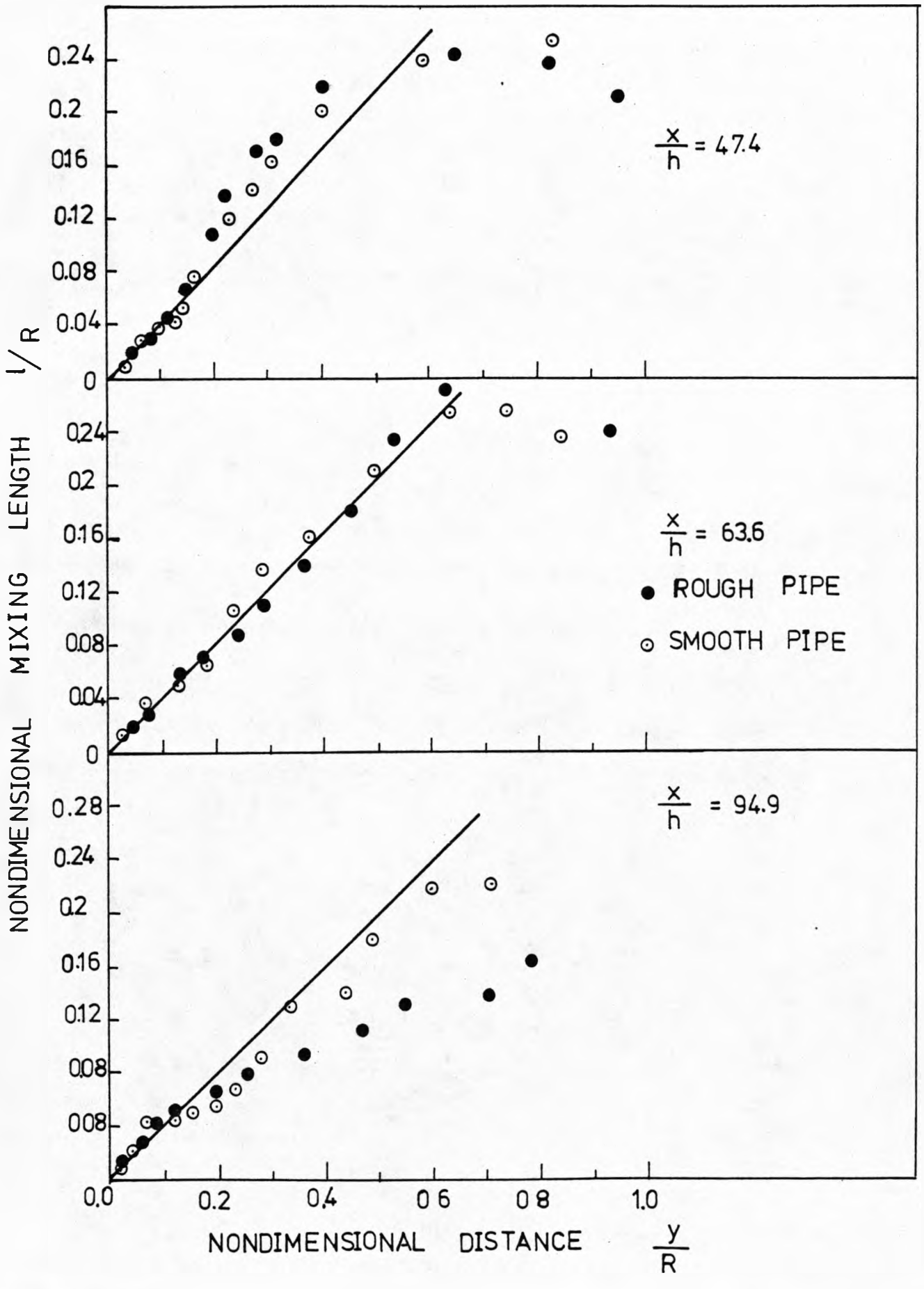

MIXING LENGTH DISTRIBUTIONS DOWNSTREAM OF RING IN ROUGH AND SMOOTH PIPES

FIG.(5.22c)

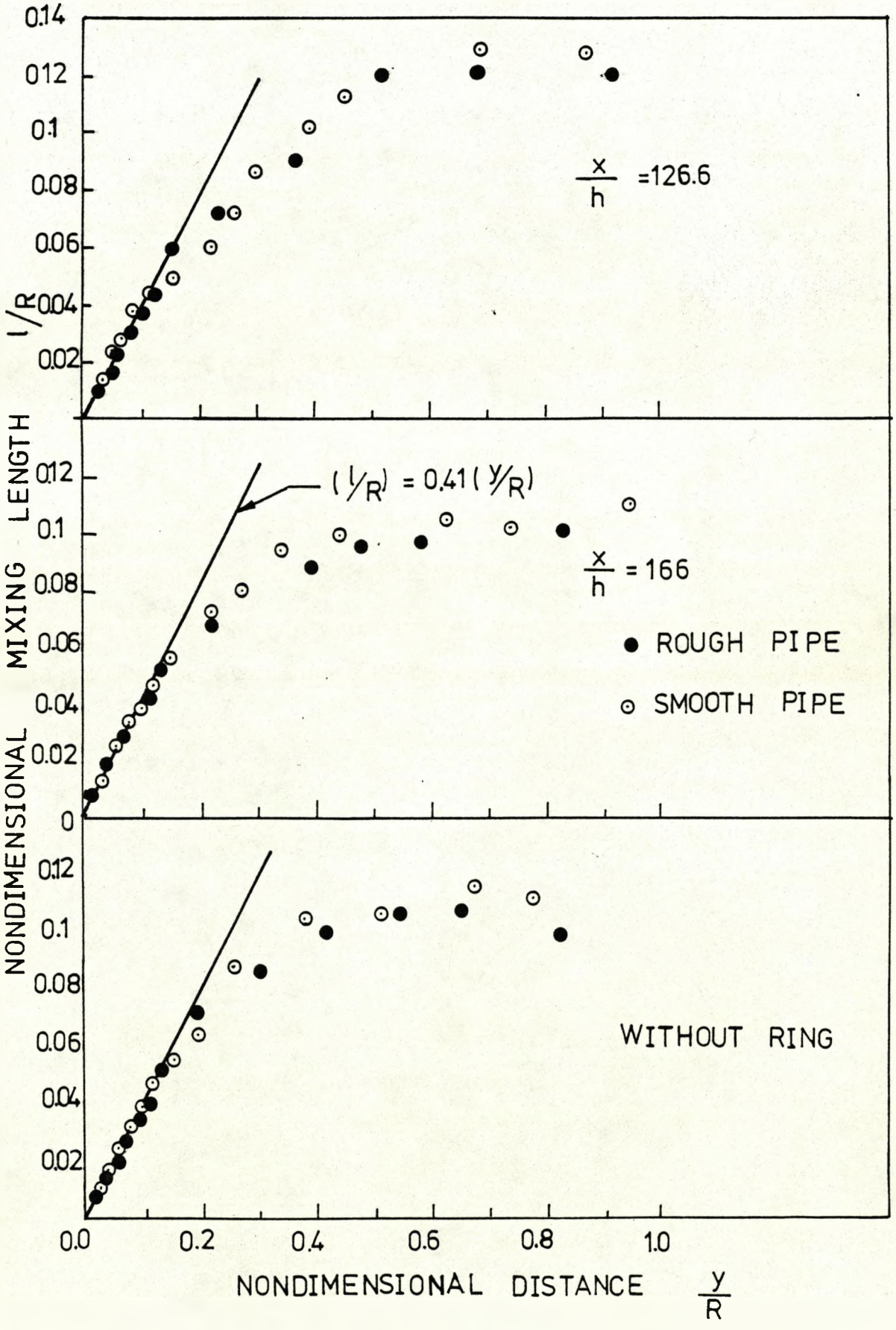

a - Finte - Difference Grid

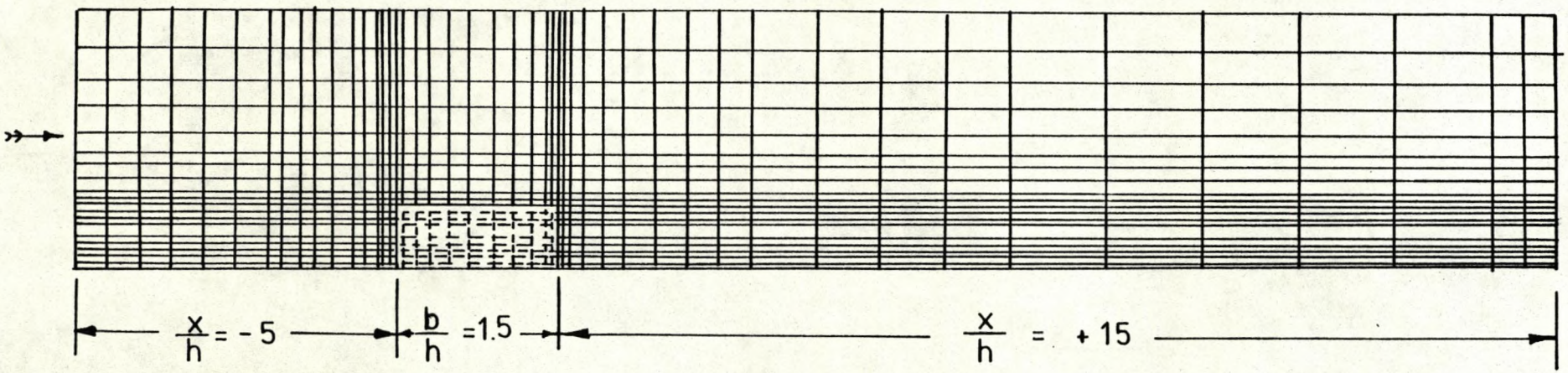

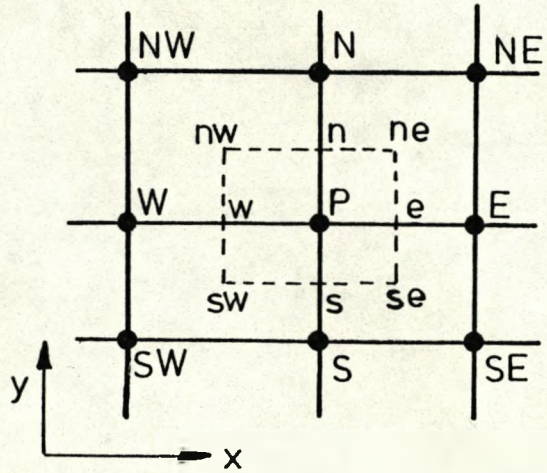

b - Illustration of a cell of the Finite Differnce Grid

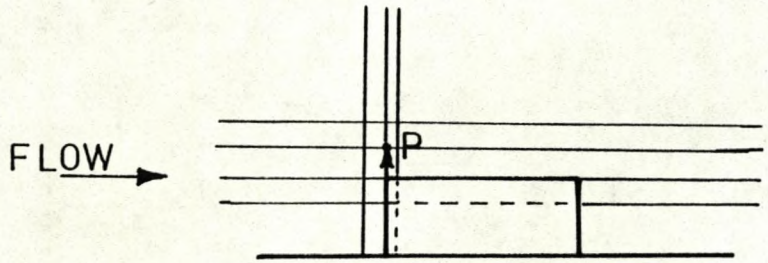

c - A Fixed Separated Stream Line

FINITE-DIFFERENCE GRID AROUND THE TWO-DIMENSIONAL OBSTACLE (RIDGE)

FIG.(6.1)

FIG.(6.2)

STREAM LINE PATTERNS IN THE RECIRCULATING FLOW REGION UPSTREAM AND DOWNSTREAM OF THE OBSTACLE ATTACHED TO ROUGH AND SMOOTH PLATES

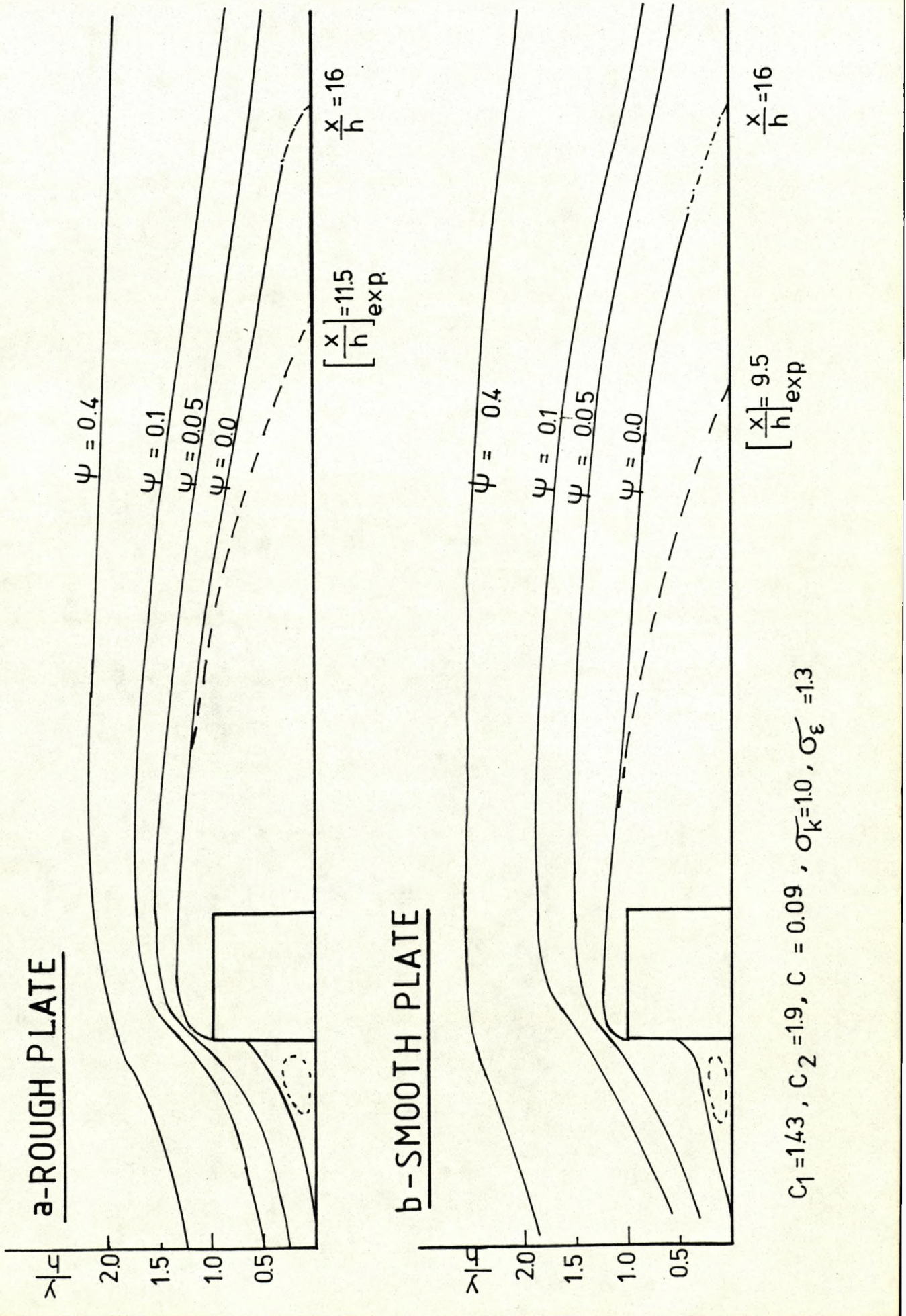

STREAM LINE PATTERNS IN THE RECIRCULATING FLOW REGION UPSTREAM AND DOWNSTREAM OF THE OBSTACLE ATTACHED TO ROUGH AND SMOOTH PLATES (WITH DIFFERENT VALUES OF THE CONSTANTS C_1, C_2, σ_k AND σ_ε)

FIG.(6.3)

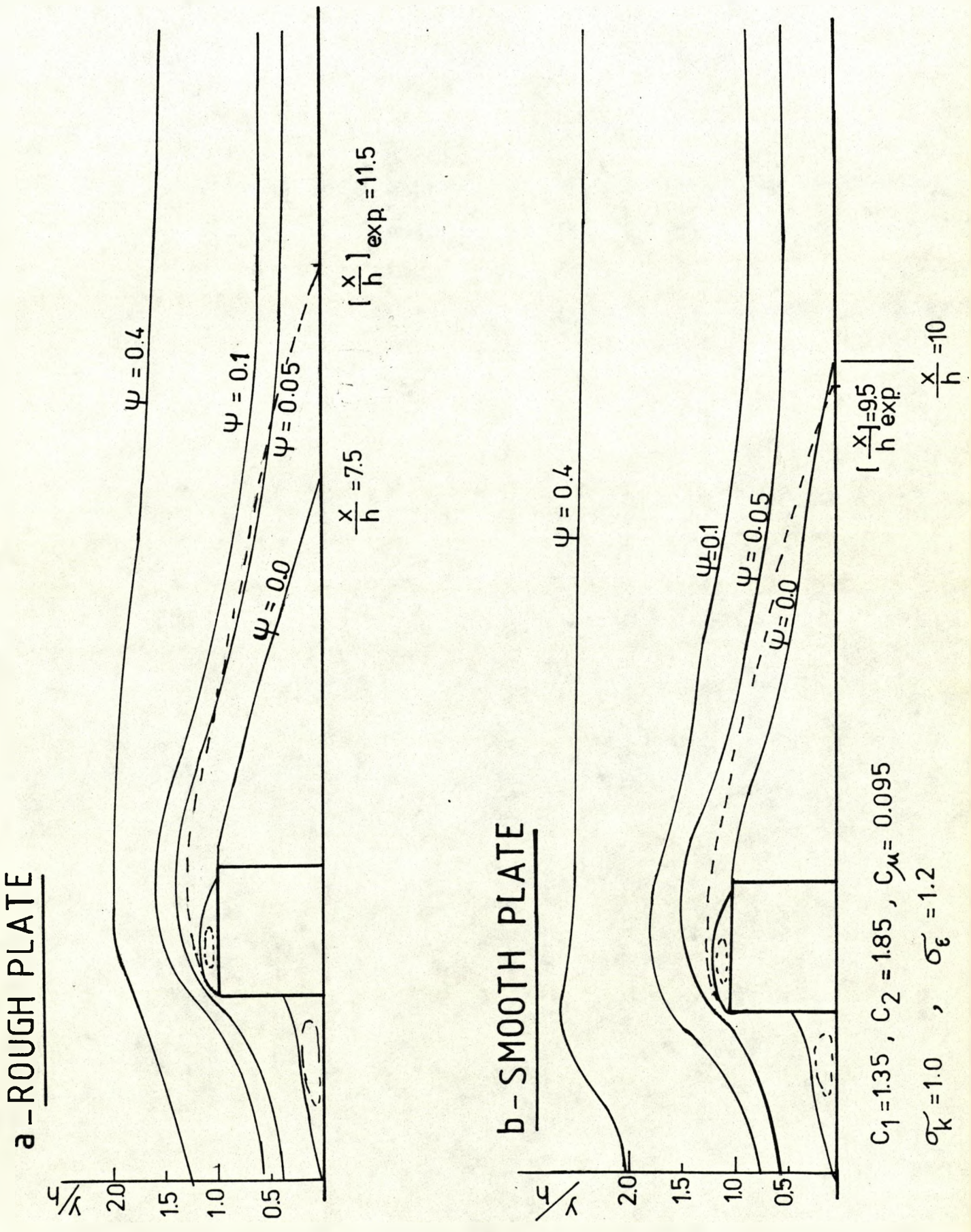

STREAM LINE PATTERNS IN THE RECIRCULATING FLOW REGION UPSTREAM AND DOWNSTREAM OF THE RIDGE ATTACHED TO SMOOTH PLATE (WITH DIFFERENT VALUES OF THE CONSTANTS C_1, C_2, σ_k and σ_ε)

FIG.(6.4)

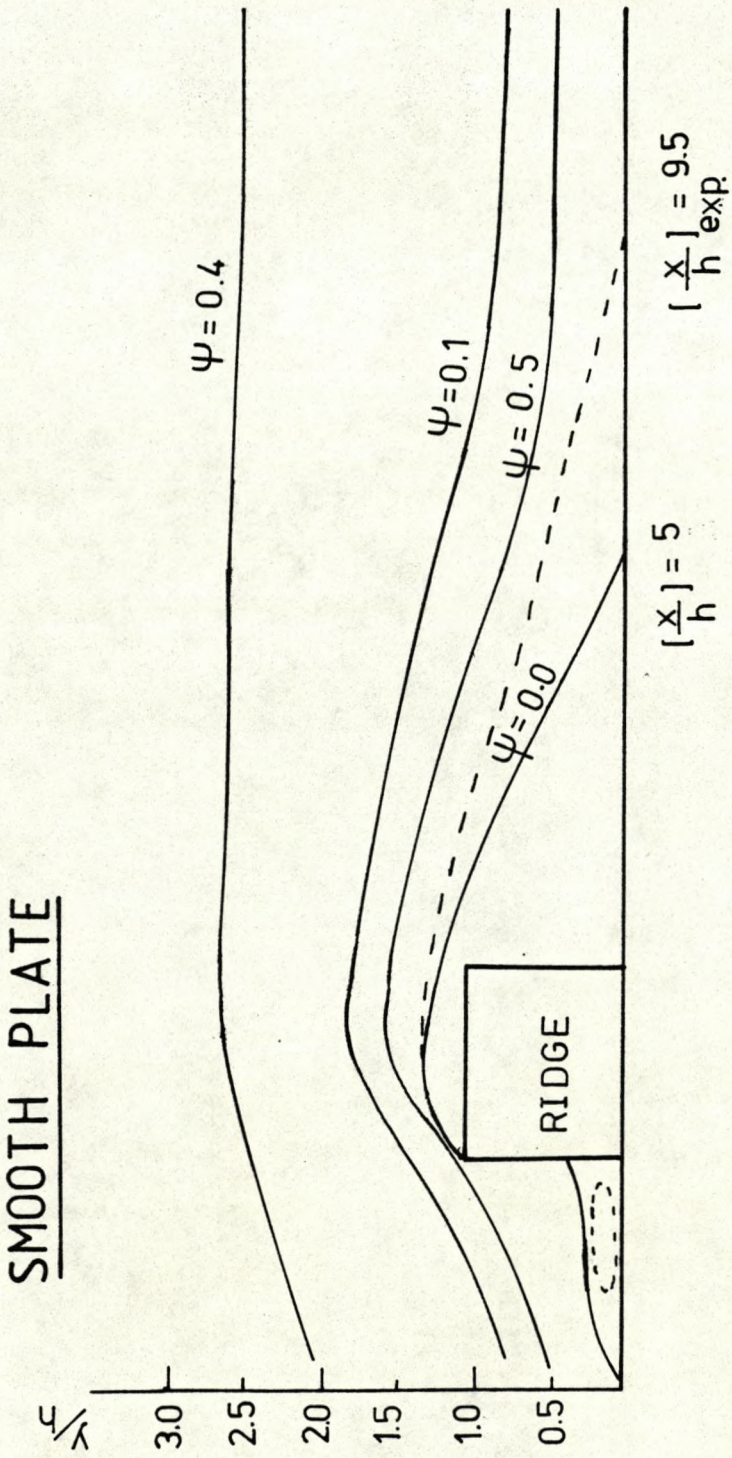

FIG.(6.5)

COMPARISON BETWEEN PREDICTED AND EXPERIMENTAL MEAN VELOCITY DISTRIBUTIONS DOWNSTREAM OF THE RIDGE ATTACHED TO ROUGH AND SMOOTH PLATES

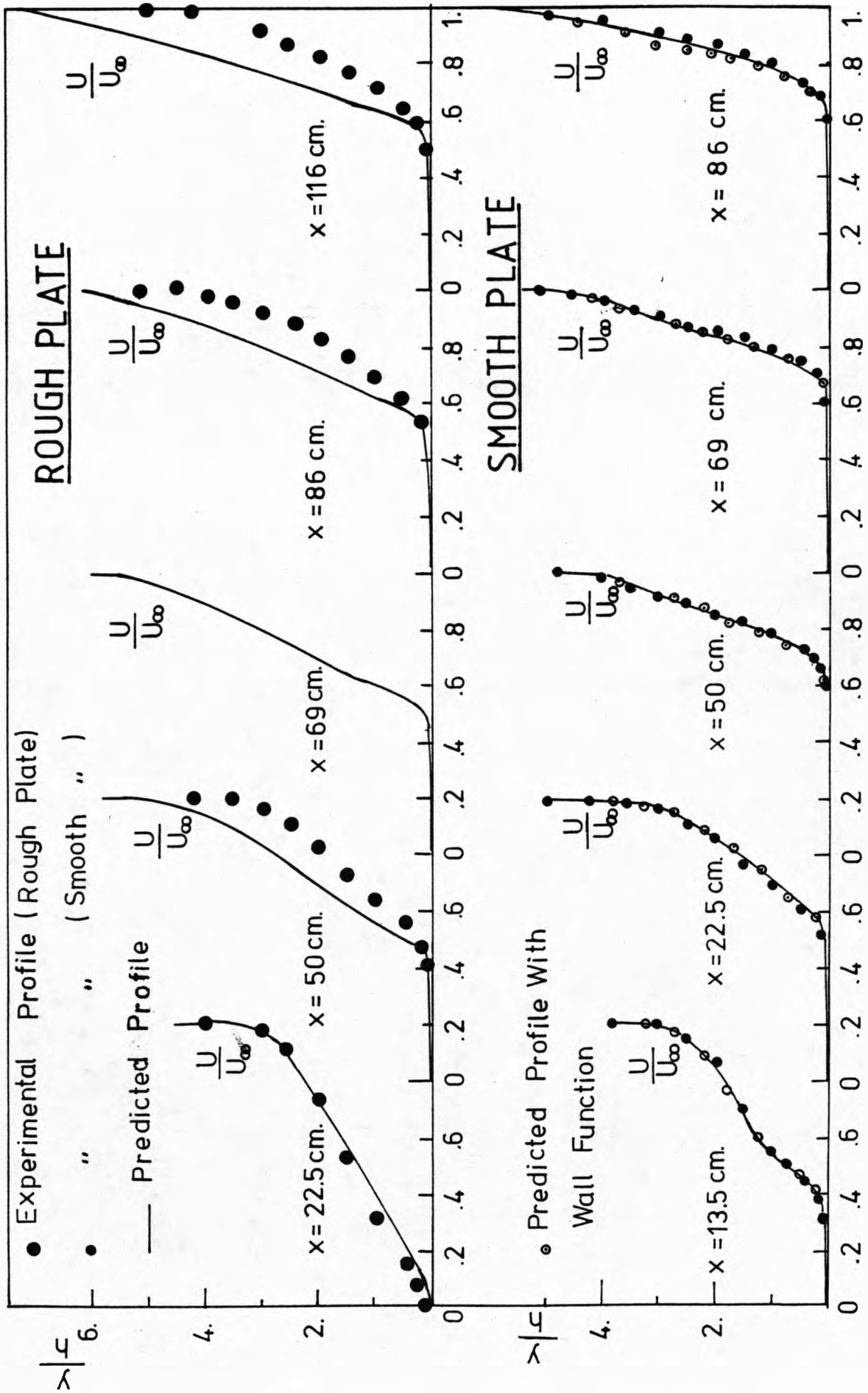

FIG.(6.6)

COMPARISON BETWEEN PREDICTED AND EXPERIMENTAL WALL FRICTION COEFFICIENT c_f DOWNSTREAM OF THE RIDGE ATTACHED TO SMOOTH PLATE

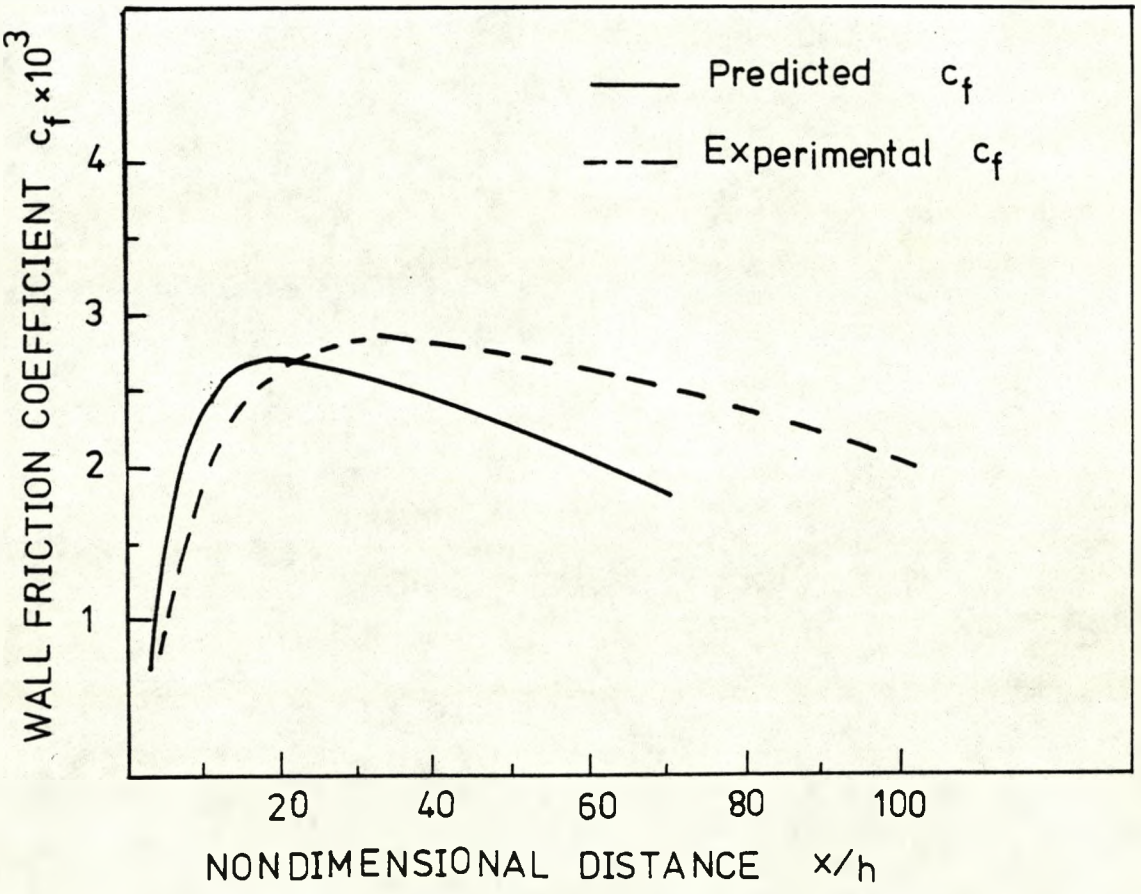

COMPARISON BETWEEN PREDICTED AND EXPERIMENTAL KINETIC ENERGY DISTRIBUTIONS DOWNSTREAM OF THE RIDGE ATTACHED TO ROUGH AND SMOOTH PLATES

FIG.(6.7)

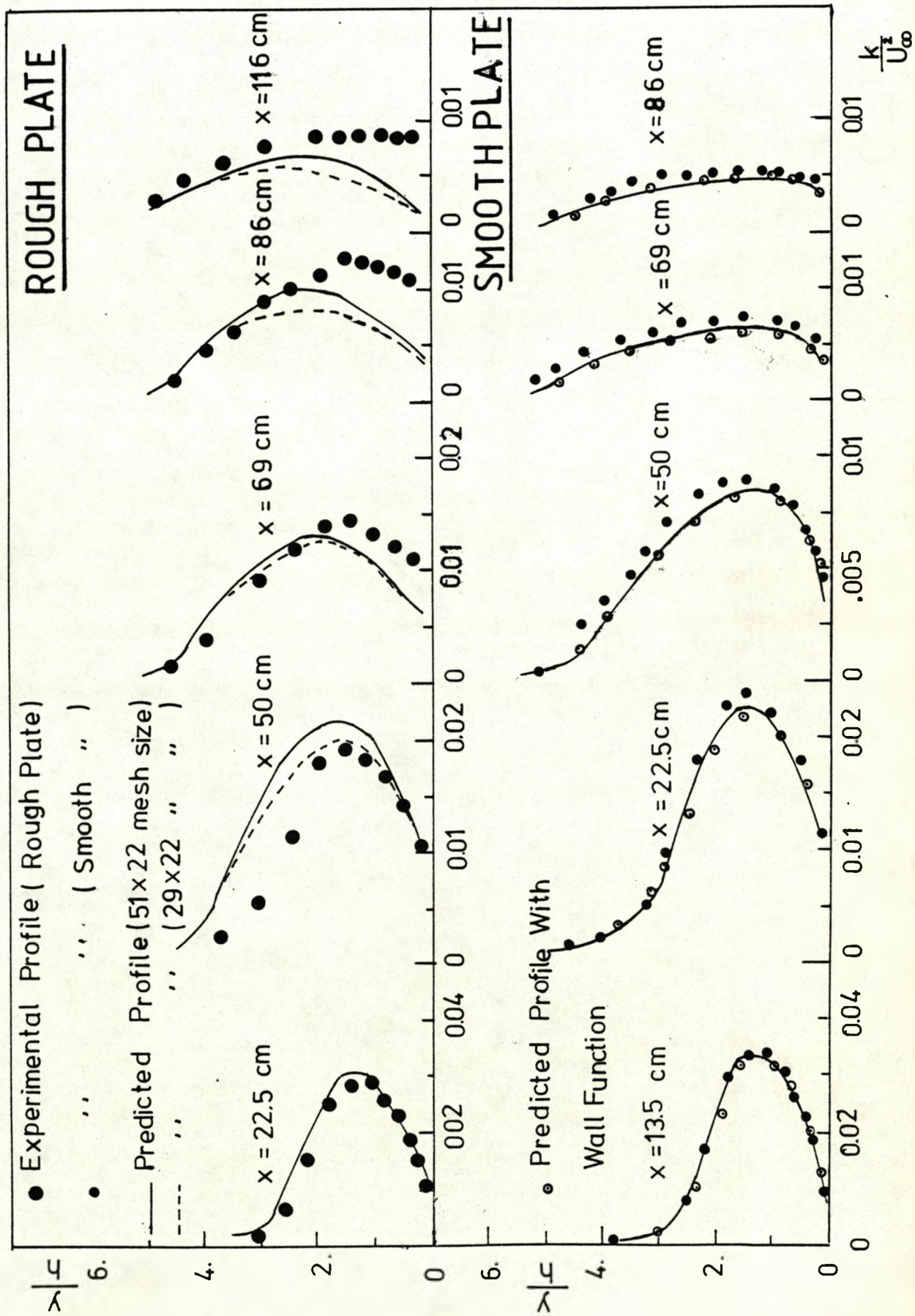

FIG.(6.8)

COMPARISON BETWEEN PREDICTED AND EXPERIMENTAL BOUNDARY-LAYER INTEGRAL THICKNESSES δ^*, θ AND SHAPE PARAMETER H DOWNSTREAM OF THE RIDGE ATTACHED TO ROUGH AND SMOOTH PLATES

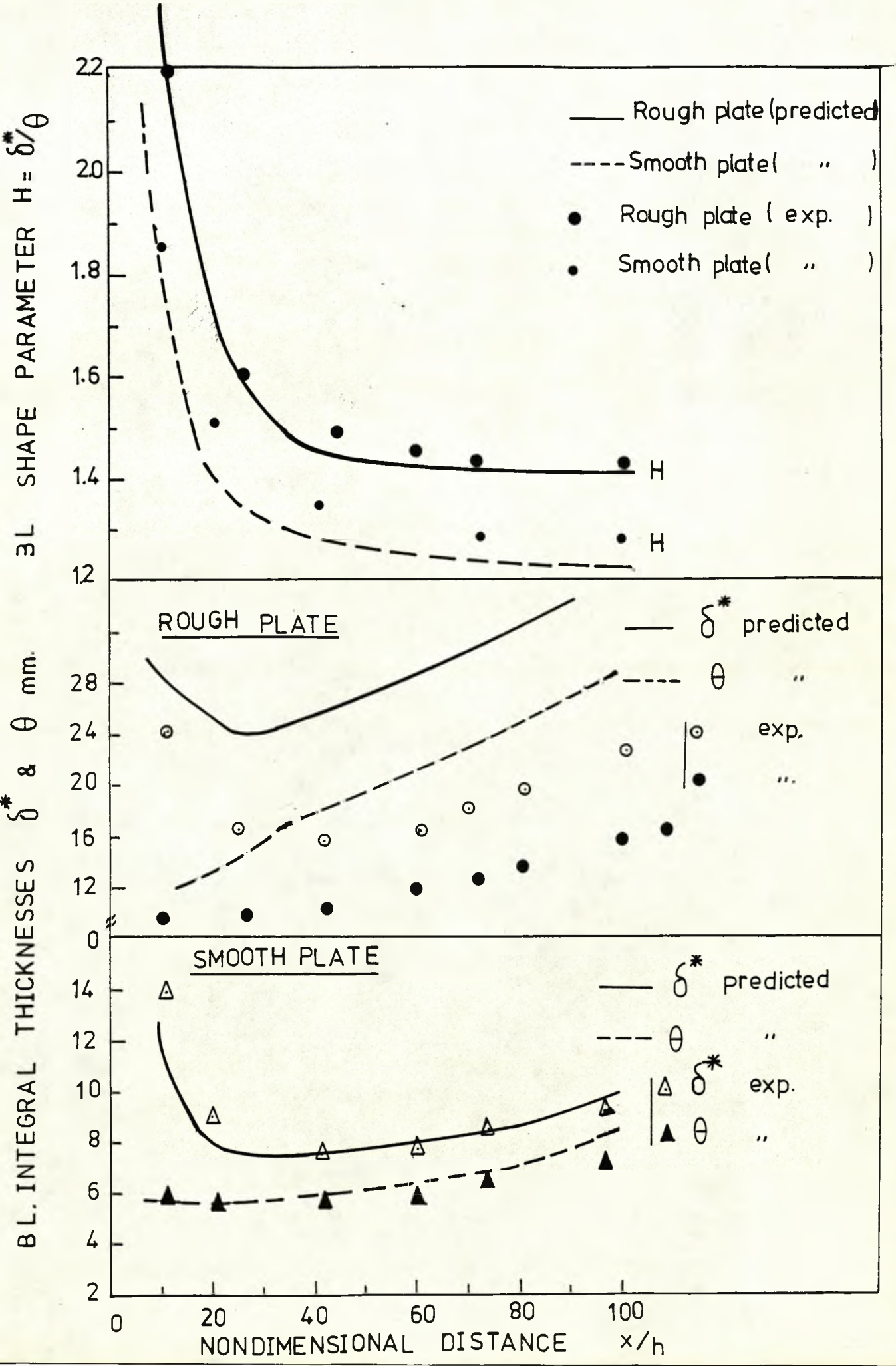

FIG.(A.1)

PROFILES FOR THE IRREGULAR ROUGH PLATE USED IN THE PRESENT EXPERIMENTS

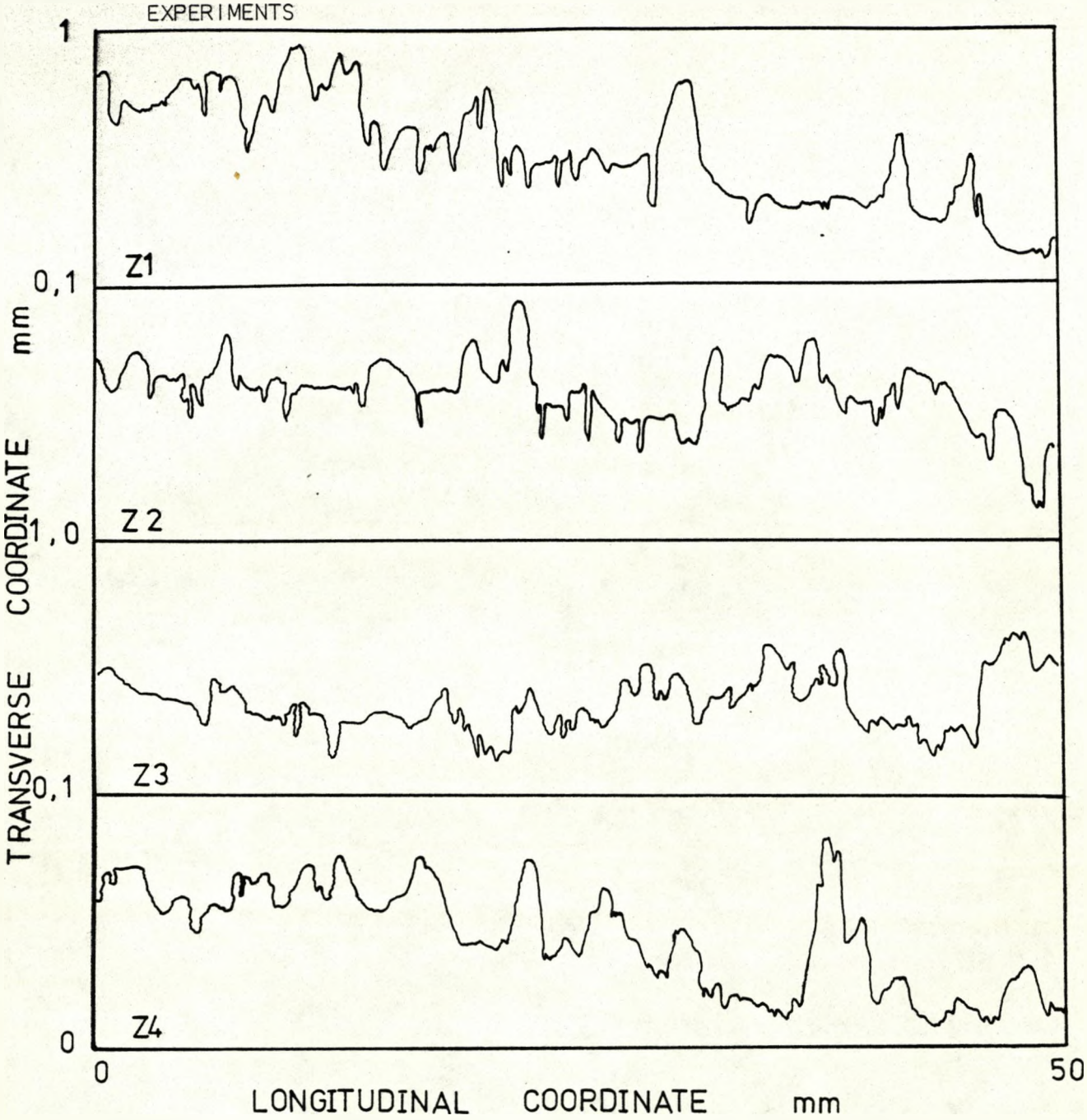

Average Statistical Charactertistics
(All values in μm)

Peak-to-Valley Height	1095
10-Point-Height	980
Centre Line Av. Height	136
Std. Deviation	180
Max. Peak from Mean	608
Min. Valley from Mean	488
Skewness	0.72
Flatness	4.03